Analysis, Design, Fabrication, and Testing of a MEMS Switch for Power Applications

by

Jo-Ey Wong

B.S., National Chiao Tung University (1990)
S.M., Massachusetts Institute of Technology (1993)

SUBMITTED TO THE DEPARTMENT OF MECHANICAL ENGINEERING IN PARTIAL FULFILLMENT OF THE REQUIREMENTS FOR THE DEGREE OF

DOCTOR OF PHILOSOPHY

at the

MASSACHUSETTS INSTITUTE OF TECHNOLOGY

June 2000

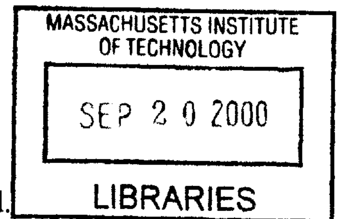
MASSACHUSETTS INSTITUTE OF TECHNOLOGY
SEP 2 0 2000
LIBRARIES

© Massachusetts Institute of Technology 2000. All rights reserved.

Signature of Author..
Department of Mechanical Engineering
May 22, 2000

Certified by.............................. ....
Nam. P. Suh
Professor and Head of Mechanical Engineering Department
Thesis Supervisor

Certified by..
Jeffrey H. Lang
Professor of Electrical Engineering and Computer Science
Thesis Supervisor

Certified by..
Martin A. Schmidt
Professor of Electrical Engineering and Computer Science
Thesis Supervisor

Certified by..
Ain A. Sonin
Chairman, Department Committee on Graduate Students

Analysis, Design, Fabrication, and Testing of a MEMS Switch for Power Applications

by

Jo-Ey Wong

SUBMITTED TO THE DEPARTMENT OF MECHANICAL ENGINEERING IN PARTIAL FULFILLMENT OF THE REQUIREMENTS FOR THE DEGREE OF DOCTOR OF PHILOSOPHY

ABSTRACT

This thesis reports an electrostatic MEMS switch for power applications. The proposed switching system consists of an array of single-switch cells, and a parallel transistor-based protection circuit for *arcless* switching. Such a system design enables the switch development to focus on a normally-open single-pole-single-throw modular MEMS switch cell, which operates under cold-switching conditions. This leaves arcing-related issues, integration with of control/protection electronics, and more complicated switch configurations to higher system-level design.

Achievable off-state standoff voltages of a switch cell are investigated through experimental measurements of electrical breakdown in micron-sized air gaps. Breakdown voltages exceeding *300 V* are demonstrated across clean air gaps as small as *0.5 μm*. Based on this, design theories and criteria are discussed for power switching applications. The goals for this application are low on-state resistance, low power consumption, high current capacity, and high off-state standoff voltage. Common geometries and actuation mechanisms for MEMS actuators are compared and the electrostatic actuation of a diaphragm switch cell is chosen because of its low actuation voltage and power, its compatibility with mainstream CMOS processing technologies, and its good thermal performance. Pneumatic actuation is used as a secondary tool for the validation of diaphragm integrity. The mechanical analysis of axisymmetric thin plates is studied and two diaphragm designs are proposed: a single-crystal silicon diaphragm of uniform thickness and a highly-tensile-stressed LPCVD nitride diaphragm. Switch prototypes employing vertically-moving bulk-micromachined single-crystal silicon or LPCVD nitride diaphragms with highly-doped poly-silicon actuation electrodes and metal contacts are fabricated with an 8-mask IC-friendly process.

Mechanical and electrical models of the MEMS switch cells are established analytically and are validated experimentally. Various characterization tests are executed to understand the behavior and the performance of the prototype switch cells. The switch cells can be switched electrostatically with *20 V* or less, pneumatically with *1200 Pa*, or through combined actuation. Metal-to-metal contact resistance measurements, performed using a four-point-probe technique, are normally below *50 mΩ* and sometimes approach *15 mΩ* while the current capacity in excess of *400 mA* per switch cell in either current direction is demonstrated. An off-state resistance greater than *30 MΩ* is achieved. The lowest un-damped resonant frequency of one of the diaphragm designs is calculated to be 19.8 kHz. The effects of the compressible air in the gap dominate the device switching speed as the squeeze-film characteristic time constant of this high radius-to-separation ratio gap is calculated to be 54 ms. Switching time are found to be on the order of 20-50 ms, which agrees with the squeeze-film characteristic time. Cyclic operation of the device is demonstrated without significant performance degradation. The switch cells exhibit

essentially zero power consumption during stead state because of the nature of electrostatic actuation.

Thesis Supervisor: Jeffrey H. Lang
Title: Professor of Electrical Engineering and Computer Science
Associate Director of Laboratory for Electromagnetic and Electronic Systems

Thesis Supervisor: Martin A. Schmidt

Title: Professor of Electrical Engineering and Computer Science
Director of Microsystems Technology Laboratories

ACKNOWLEDGEMENT

As they say, one has to go through adversity to get better. Then I guess I am leaving MIT a little better than when arrived, only maybe too much betterment than I was looking for. I was really fortunate in having an enormous amount of support, encouragement, and patience from my family, advisors, friends, and colleagues along my journey of graduate study at MIT. I couldn't have done it without them. These two pages belong to you.

I would like to first acknowledge Professor Jeffrey Lang for his extraordinary level of support and patience. I will always remember those countless hours he spent with me in the trenches debugging hardware problems, deciphering experimental data, or just offering words of wisdom. I would also thank Professor Martin Schmidt for his encouragement, inspiration and positive thinking when I needed them the most. In this roller coaster ride to my doctorate, his helping and dependable hands have kept things from derailing many a time. Thank you Marty and Jeff for your intellectual guidance and moral support over the past five years. I would like to also take this opportunity to thank Professor Nam Suh for agreeing to serve as the chairman of my thesis committee and for his insightful comments over the course of this thesis.

This project was supported mainly by C. P. Clare Corporation and Packard Electric Division of General Motors Corporation. I am thankful to Scott Jones, Nestor Polce, and Robert Andosca from Clare for intriguing discussions we had together and the fabrication support on the bottom wafers of the final switch design.

A warm thank you goes to fellow Schmidt Group members residing in the northwest corner on the fifth floor of Building 39: Christine Tsau, Samuel Schaevitz, Joel Voldman, Dye-Zone Chen, Chi-Fan Yung, Samara Firebaugh, Rebecca Braff and Xue'en Yang. They have been there for me through thick and thin. Your pat-on-the-backs and high-fives in the dugout meant a lot to me. The joint work I did with Christine in the development of smooth gold deposition and in the wafer-level packaging project has been rewarding and pleasurable. Joel has made the Schmidt Group Lab a pleasant work place where I spent innumerate nights. I am particularly grateful for Zony's support on computer-related issues. It is a shame that I could not attend as many MEMS Salons, which are made possible thanks to Samara, as I would like to.

My association with other fellow graduate students and research staff members has been a great learning experience. Steven Nagle, Arturo Ayon, Ravi Khanna, Luc Frechette, Tom Takacs, Amitav Mehra, Joyce Wu, Xin Zhang and Hanqing Li were nice enough to share their invaluable knowledge and experience with me and to be my lab buddies from time to time. I would like to acknowledge Steve, who indirectly influenced my career decision (see you in a month), and Arturo, from whom I learned a great deal on deep RIE and align-bonding. My discussions with Mathew Varghese, Yao-Joe Yang, and Kuo-Shen Chen on various subjects were very informational and I very much appreciated them.

Former Schmidt Group members, Aravind Padmanabhan, Ravi Srinivasan, Lalitha Parameswaran, Errol Arkilic, Charles Hsu, Chuang-Chia Lin, Roberto Devoto and Kei Ishihara all have helped me while we were together. Especially I would like to thank Lalitha and Charles for being the go-to persons whenever I had questions. I am still amazed that more often than not they would have exactly the answers to the unusual questions I was asking.

I would like to thank my Taiwanese buddies, especially Kuang-Han Chen, Henry Hwu, Tza-Jing Gung, and Chien-Ning Yu. The memories we had together through numerous championship pursuits in sports events have left permanent marks in my heart.

Thanks also go to all MTL staff for their assistance and support in the cleanrooms. Vicky Diadiuk, Paul Tierney, Kurt Broderick, Joe DiMaria, Bernard Alamariu, Joe Walsh, Dan Adams, Wayne Price, Ron Stoute, and Patricia Burkhart all have made my MTL experience a memorable one. Particularly I wish to thank Octavio Hurtado, who retired two years ago, for his incredible patience in answering my not-so-smart questions.

I would like to thank Professor Stephen Senturia for my initiation into MEMS, otherwise I would probably become just an unhappy control engineer somewhere else.

I would like to thank Professor Anuradha Annaswamy, Professor David Trumper, and Professor Lionel Kimerling, having teaching experiences in different MIT courses with them is not only enlightening but also enjoyable. A warm thank you goes to Anne Wasserman, Patricia Varley, Karin Janson-Strasswimmer, and Kiyomi Boyd for making a seamless connection between MIT bureaucracy and graduate students.

I want to thank my parents for their understanding and support to let their only son be thousands of miles away from home. Their love and sacrifices will not be forgotten. I can never repay what they have given me and will make sure my future children feel the same way about me. And I am very thankful for the love and the long-distance professional medical advises I got from my sister.

Finally, I dedicate this thesis to Yu-Huai, whom I have no words to thank enough.

CONTENTS

Acknowledgement....5
Contents....7
List of Figures....10
List of Tables....13
Chapter 1 Introduction....15
1.1 Background....15
1.2 Other Micro Relays/Switches....17
1.3 Power MEMS Switches: Motivation and Goal....18
1.4 System Viewpoint....19
1.4.1 Arcless Switching Scheme....19
1.4.2 Switch Cell Array Configuration....20
1.4.3 Quick Summary on Device Performance....20
1.5 Thesis Overview....21
Chapter 2 Electrical Breakdown in Narrow Air Gaps....23
2.1 Introduction....23
2.2 Electrical Breakdown in Gases....24
2.2.1 Paschen's Law....25
2.2.2 Townsend Mechanism....26
2.2.3 Streamer Mechanism....28
2.2.4 Summary of Breakdown Theories....28
2.3 Discussion of Electrical Breakdown in Narrow Air Gaps....29
2.4 Fabrication and Testing of Breakdown Test Device....33
2.5 Summary and Future Work on Electrical Breakdown....37
2.5.1 Breakdown Test Results Summary....37
2.5.2 Suggestions on Future Breakdown Strength Study....38
Chapter 3 Theory and Design....41
3.1 Introduction....41
3.2 Actuation Scheme....42
3.2.1 Piezoelectric actuation scheme....43
3.2.2 Thermal actuation....43
3.2.3 Magnetostatic Actuation....45
3.2.4 Pneumatic Actuation....46
3.2.5 Shape-Memory Alloy Actuation....47
3.2.6 Electrostatic Actuation....48
3.2.7 Actuation Scheme of Choice: Electrostatics....49
Pull-in voltage....49
Release voltage....50
3.3 Design of Mechanical Structure....50
3.3.1 Overview....50
Elasticity....51
Bulk Micromachining....51
Surface Micromachining....52
Circular or Rectangular Diarphagm Design?....53
3.3.2 Bossed Circular Diaphragm....54
Timoshenko Plate Theory....55
3.3.3 Uniform-Thickness Circular Diaphragm....59
Timoshenko Plate theory....60
Energy method....64

3.4 Electrical Breakdown Strength....67
3.4.1 Off-state breakdown strength across contacts....68
3.4.2 Breakdown strength associated with actuation....68
3.5 Contact Resistance....69
3.5.1 Contact surface....71
3.5.2 Constriction resistance....74
3.6 Switching speed....76
3.6.1 Resonant frequency....76
Stress dominant case (membrane)....77
Bending dominant case (plate)....78
3.6.2 Squeeze-film effects....78
3.7 Design of electrostatic MEMS switch....80
3.7.1 Actuation Scheme....80
3.7.2 Actuation voltages....81
3.7.3 Micromachining technologies....82
3.7.4 Mechanical structure....82
3.7.5 Breakdown....83
3.7.6 On-state Resistance....83
Constriction resistance, $R_{constriction}$....84
Resistance of the metal films, R_{metal}....85
Resistance of the metal-semiconductor contact interface, $R_{contact}$....85
Resistance in the bulk of the silicon substrates, R_{bulk}....85
Resistance within the diaphragm structure, $R_{diaphragm}$....85
Film resistance, R_{film}....85
3.7.7 Switching speed....85
3.7.8 Prototype Design/Performance....86
Chapter 4 Device Fabrication....87
4.1 Introduction....87
4.2 Earlier Generations....87
4.2.1 The Bottom Wafer....88
4.2.2 Generation 1 Top Wafer....89
4.2.3 Generation 2 Top Wafer....90
4.2.4 Generation 3 Top Wafer....91
4.2.5 Final Generation Top Wafer....93
4.3 Process Flows....94
4.3.1 Bottom wafer....95
4.3.2 Top wafer....98
Silicon diaphragm....98
Nitride diaphragm....99
4.4 Fabrication Issues....100
4.4.1 Die-level thermocompression bond....100
4.4.2 Diesaw....101
4.4.3 Gold evaporation....102
4.4.4 Miscellaneous Issues....103
Gold agglomeration....103
Stress gradient of diaphragm....104
Packaging....104
Deep RIE etch non-uniformity....104
4.5 Summary and suggestions....104
Use of wet etchant for diaphragm micromachining....105
Replacing diesaw with deep-trench-etch-and-cleave....105

Reduction in device density ... 105
Chapter 5 Testing and Characterization ... 107
5.1 Introduction ... 107
5.2 Instrumentation ... 107
5.2.1 Why dual actuation schemes? ... 108
5.2.2 Packaging issues for pneumatic actuation ... 108
5.2.3 Software ... 111
5.2.4 Hardware ... 111
5.3 Electrical Model ... 116
5.4 Mechanical Model ... 123
5.4.1 Diaphragm deflection profile (Scenario-I) ... 123
"Approaching" phase ... 126
"Spreading" phase ... 129
"Conforming" phase ... 132
5.4.2 Pressure-capacitance model and discussions (Scenario-I) ... 136
5.4.3 Diaphragm deflection profile (Scenario-II) ... 139
5.5 Pneumatic Actuation ... 143
5.6 Electrostatic Actuation ... 145
5.7 Combined Actuation ... 146
5.8 Contact resistance ... 150
5.9 Switching time ... 153
5.9.1 Electrostatic switching ... 154
5.9.2 Pneumatic switching ... 155
5.10 Current capacity ... 157
5.11 Cyclic Operation ... 158
Insulation oxide breakdown ... 159
5.12 Summary ... 161
Chapter 6 Summary, Conclusions, and Suggestions for Future Work ... 163
6.1 Summary ... 163
6.2 Conclusions ... 165
6.3 Recommendations for Future Work ... 166
6.3.1 Ultra-high standoff voltage ... 167
6.3.2 Protection arcless-switching circuit ... 167
6.3.3 Switch cell array ... 168
6.3.4 Thicker insulation oxide ... 168
6.3.5 Other design possibilities ... 168
Appendix A Diaphragm buckling ... 171
Appendix B Detailed Process Travelers ... 173
Appendix C Mask Layouts ... 191
Appendix D Test fixture design ... 199
Appendix E Poly-silicon surface roughness measurement ... 201
Appendix F LabVIEW® programs ... 203
Appendix G MATLAB® Script for Circular Clamped diaphragms ... 209
Bibliography ... 215

LIST OF FIGURES

Figure 1.1 Arcless switching scheme 20
Figure 1.2 Four-by-four switch cell array configuration 20
Figure 2.1 Typical Paschen curves for hydrogen and air [36] 25
Figure 2.2 V-I plot of two parallel plates (Townsend electrical breakdown mechanism [33]) 27
Figure 2.3: The effect of electrode material on breakdown in argon [36] 30
Figure 2.4: Device for Measuring Electrical Breakdown in Narrow Air Gaps 33
Figure 2.5: Process flow for upper and bottom wafers of Breakdown Test Device 33
Figure 2.6: Circuit for measuring electrical breakdown 34
Figure 2.7: Breakdown voltage v.s. Gap separation 36
Figure 2.8 Charging/breakdown transient curves of different devices: {pedestal #, pedestal diameter, air gap} = (a) {1, 100 μm, 0.5 μm}, (b) {1, 100 μm, 1 μm}, (c) {19, 200 μm, 1.5 μm}, (d) {19, 200 μm, 1.5 μm} 36
Figure 3.1 A schematic drawing of a micro electromagnetic actuator 45
Figure 3.2 A schematic drawing of a micro electrostatic actuator 48
Figure 3.3 Typical process flow of bulk-micromachining a diaphragm 52
Figure 3.4 Typical process flow of surface-micromachining a beam 53
Figure 3.5 Drawing of annular diaphragm with central boss 55
Figure 3.6 Plot of deflection correction factor due to stress, g, as a function of ζ^2 [57]. See Equations (3.28) and (3.29). (a) ζ^2 in linear scale, and (b) ζ^2 in log scale. 59
Figure 3.7 Moment equilibrium of a plate element (vertical deflection and slope not shown) 61
Figure 3.8 Diaphragm deflection in a thick-film model 65
Figure 3.9 Contact gap, actuation gap, and insulation layers of the MEMS switch 69
Figure 3.10 Contact areas (apparent, load-bearing, and conducting) 72
Figure 3.11 Asperity-based rough surface model. (a) Geometry model of rough contact surfaces, (b) Elastically deformed asperity ($\omega_e \leq \omega_c$), and (c) Partially plastically deformed asperity ($\omega_p > \omega_c$) 72
Figure 3.12 Effects of spreading out a-spots on constriction resistance [42] 75
Figure 3.13 Schematic drawing of a circular clamped diaphragm under electrostatic actuation and pneumatic actuation. 77
Figure 3.14 MEMS switch design (not to scale) 80
Figure 3.15 Lumped model for electrostatic actuation: Electrostatic forces (dotted lines) and mechanical force (solid line) vs. gap 81
Figure 4.1 First modification on bottom substrate 88
Figure 4.2 Second modification on bottom substrate 89
Figure 4.3 MEMS switch design – Generation 1 90
Figure 4.4 MEMS switch design – Generation 2 91
Figure 4.5 MEMS switch design – Generation 3 92
Figure 4.6 Micrograph of a Generation 3 top wafer 92
Figure 4.7 Latest MEMS switch design - silicon diaphragm 94
Figure 4.8 Latest MEMS switch design – nitride diaphragm 94
Figure 4.9 Bottom wafer process sequence 96
Figure 4.10 Micrograph of sixteen i-pedestals in a ring of *300 μm*-radius. 97
Figure 4.11 Micrograph of a close-up of a *3 μm*-pedestal contact. 97
Figure 4.12 Top wafer process sequence (silicon diaphragm) 98
Figure 4.13 Top wafer process sequence (nitride diaphragm) 99
Figure 4.14 Crack propagation in overly dried photoresist 102
Figure 4.15 Gold spheres on deposited gold film (courtesy of C. Tsau) 103

Figure 5.1 Top view of the test device. Testing window needs to be *open* and circular diaphragm needs to be *completely sealed* after packaging. 109
Figure 5.2 Packaging scheme (side view) 109
Figure 5.3 Packaging procedure (perspective view) 110
Figure 5.4 Pressure control scheme 112
Figure 5.5 Four-point-probe resistance measurement 113
Figure 5.7 Device cross-section drawing of one single switch cell (electrical model) 116
Figure 5.8 Distributed system circuit model of a single switch cell 116
Figure 5.9 Further simplified electrical model of a single switch cell. 117
Figure 5.10 Generalized representation of the simplified electrical model 117
Figure 5.11 Electrical model for impedance analyzer: A resistor and a capacitor in parallel 118
Figure 5.12 Low-frequency circuit model of a single switch cell in OFF-state 118
Figure 5.13 Apparent air-gap capacitance $C_{air\text{-}gap}$ vs. variable $C_{air\text{-}gap}$ and apparent resistance *R*' vs. variable $C_{air\text{-}gap}$ as computed numerically 119
Figure 5.14 Apparent resistance (*R*') and apparent capacitance (*C*'): Measurement data vs. Model simulation 120
Figure 5.15 Low-frequency circuit model of a single switch cell in ON-state 121
Figure 5.16 Discontinuity in capacitance measurement: An indication of change in switch state 122
Figure 5.17 The three proposed phases as diaphragm deflecting downward onto a bottom contact pedestal, (1) "approaching", (2) "spreading", and (3) "conforming". (Scenario-I) 125
Figure 5.18 Clamped circular thin plate under uniformly distributed pressure 126
Figure 5.19 Plate deformation profile in "approaching" phase. Each curve represents a 0.05psi pressure increment. 128
Figure 5.20 Incremental capacitance between deformed plate and ground 129
Figure 5.21 Capacitance-pressure curve in "approaching" phase 129
Figure 5.22 Dimension definitions in "spreading" phase 130
Figure 5.23 Plate deformation profile in "spreading" phase. 131
Figure 5.24 Capacitance-pressure curve in "spreading" phase (solid line) and "approaching" phase (dash-dot line). 132
Figure 5.25 Dimension definitions in "conforming" phase 133
Figure 5.26 Plate deformation profile in "conforming" phase. Each curve represents a 0.05psi pressure increment. 135
Figure 5.27 Capacitance-pressure curve in "conforming" phase. 136
Figure 5.28 Complete capacitance-pressure plot in Scenario-I. 137
Figure 5.29 Pressure-capacitance curve comparison: Experimental data (solid lines) vs. Scenario-I model (dashed line) 137
Figure 5.30 The two phases of diaphragm deflecting downward onto a bottom contact pedestal, (1) "approaching", (2) and "spreading". (Scenario-II) 139
Figure 5.31 Plate deformation in Scenario-II. "Approaching" phase (dashed): each curve represents 0.05psi increment. "Spreading" phase (solid): each curve represents 50μm increment in touchdown radius. 142
Figure 5.32 Pressure-capacitance curve comparison: Experimental data (solid lines) vs. Scenario-I model (dashed line) 143
Figure 5.33 Pneumatic actuation test result 144
Figure 5.34 Electrostatic actuation: capacitance vs. actuation voltage 145
Figure 5.35 Actuation current of the switch 146
Figure 5.36 Electrostatic test result 146
Figure 5.37 Combined actuation: Simulated $V_{pull\text{-}in}$ (squares) vs. measured $V_{pull\text{-}in}$ (diamonds) ... 148
Figure 5.38 Pneumatic pressure, electrostatic pressure, and total pressure under combined actuation 149

Figure 5.39 Resistance measurements of a device with insufficient metal height........................150
Figure 5.40 Contact resistance vs. pressure........................152
Figure 5.41 Contact resistance vs. current (positive current flows from bottom to top)..............153
Figure 5.42 Hardware setup for switching time test........................154
Figure 5.43 Switching time (device switching electrostatically)........................155
Figure 5.44 Switching time (device switching pneumatically)........................156
Figure 5.45 Current capacity for one single switch cell........................157
Figure 5.46 Contact resistance vs. cycles........................158
Figure 5.47 First 30 cycles in cyclic operation test........................159
Figure 5.48 Insulation oxide breakdown test (350°C, 2min. thermal treatment)........................160
Figure 5.49 Insulation oxide breakdown test (no thermal treatment)........................160
Figure 6.1 Other MEMS switch design: A vertically-moving structure deflects down and electrically connects with two pedestal contacts........................168
Figure A.1 Buckling of thin bossed silicon diaphragms........................171
Figure A.2 Buckling of thin bossed silicon diaphragms coated with nitride film........................172
Figure C.1 Mask ID: BTM-NI........................191
Figure C.2 Mask ID: BTM-ND........................192
Figure C.3 Mask ID: BTM-NB........................193
Figure C.4 Mask ID: BTM-NG........................194
Figure C.5 Mask ID: BTM-NM........................195
Figure C.6 Mask ID: TOP-NB........................196
Figure C.7 Mask ID: TOP-NM........................197
Figure C.8 Mask ID: TOP-NI........................198
Figure D.1 Drawing for the sealing fixture design........................199
Figure D.2 Drawing for the alignment jig design........................200
Figure E.1 Surface condition of bottom substrate (measured by *WYKO* surface profiler).........201
Figure E.2 Surface roughness of the top surface on poly-silicon actuation electrode.............202
Figure F.1 Front panel of a LabVIEW® program used for device characterization while sweeping actuation voltage at biased pressures........................203
Figure F.2 Block diaphragm of the LabVIEW® program shown in Figure F.1. (1 of 5)..........204
Figure F.3 Block diaphragm of the LabVIEW® program shown in Figure F.1. (2 of 5)..........205
Figure F.4 Block diaphragm of the LabVIEW® program shown in Figure F.1. (3 of 5)..........206
Figure F.5 Block diaphragm of the LabVIEW® program shown in Figure F.1. (4 of 5)..........207
Figure F.6 Block diaphragm of the LabVIEW® program shown in Figure F.1. (5 of 5)..........208

LIST OF TABLES

Table 1.1 Advantages of switching devices: Solid-state transistor vs. Electromagnetic relays 17
Table 1.2 Specification requirements of switching devices: Signal switching vs. Power switching 17
Table 1.3 Selected micro switching devices published recently 18
Table 1.4 Summary on device performance 21
Table 2.1: Breakdown voltage measurements 35
Table 3.1 Gold properties 83
Table 3.2 Derivation of constriction resistance 84
Table 3.3 Design and target specifications 86
Table 4.1 Comparison of anisotropic silicon etchant systems 105
Table 5.1 Electrostatic pull-in voltage under pneumatic pressure bias 147

Chapter 1 INTRODUCTION

This thesis presents a MEMS[1] electrostatic actuator for power switching applications. This normally-open SPST[2] switch prototype employs a vertically moving bulk-micromachined diaphragm structure, features metal-to-metal electrical contact, and can be alternatively actuated with pneumatic pressure. The underlying physics in key aspects of a power switch are investigated and the results are used as general design guidelines for the MEMS switch. The design theories are realized through fabricated devices with good agreement between the theory prediction and the experimental data. Our design of a MEMS power switch employs a two-wafer stack structure with a clamped circular diaphragm as the moving structure. This hockey-puck power paradigm also possesses favorable features such as good heat dissipation and easy packaging.

Section 1.1 contains the historic background of micro switching devices, the device attributes, and applications. In Section 1.2, other micro switch/relay works published recently are surveyed and listed in for a side-by-side comparison. Section 1.3 briefly describes the project motivation and goal. In Section 1.4, a system viewpoint is provided to explain why SPST switch cell under cold-switching scenario will be considered in the thesis. Finally, Section 1.5 outlines the framework structure of the thesis.

1.1 Background

Relays and *switches* are often regarded as interchangeable terms for electromechanical devices that alternate, under a controlled fashion, between two (sometimes more) configurations of electrical connections. Generally, a relay is a *four-terminal* device having two isolated ports. A pair of the terminals, or port, is powered to *control* the *state* of the device. The other port makes

[1] Micro-Electro-Mechanical Systems
[2] Single-Pole-Single-Throw

or breaks its connectivity, depending on the *state* of the device. Therefore, it is possible to control high power flows using a relay driven by relatively low actuation power. The most commonly seen relays are magnetically driven and the simplest magnetic relay consists of an electromagnet, an armature, a mechanical spring, and a set of electrical contacts.

In other switching devices, one of the *control* terminals and one of the *line* terminals share a common electrical potential and merge into one, and the *three-terminal* switching device is conventionally called a *switch.* The first appearance of an *electronic* device of this kind in history dates back in early twentieth century when the *audion* (triode) was invented [1]. The *audion* was encapsulated in a vacuum and made up of a heated wire (the *filament*) that emitted electrons, a closely separated metallic plate, and a third electrode (the *grid*) inserted in between the filament cathode and the plate. The grid voltage controls the charge flow between plate and cathode. The invention of such *grid-controlled* vacuum-tube rectifiers marked the dawn of the vacuum tube era spanning over the first half of the twentieth century. Bipolar and field-effect semiconductor switching devices, which operate *without heated filaments* and *do not* need to reside in a vacuum, were invented in the 1940-50's and soon gained popularity to open the *transistor era* that lasts to date. The initial applications of the electronic devices were to telephone and radio communication. Nowadays, information processing and signal transmission remain the dominant applications of electronics but the technological breakthroughs have also benefited *power* engineering whose major concerns are *power* processing and *power* transmission. Basic semiconductor power switching devices include diodes (bipolar and Schottky), transistors (BJT[3] and MOSFET[4]), and thyristors[5] [2] [3]. The success of microelectronics is empowered by the advancements of semiconductor fabrication technologies that continuingly make possible smaller and better devices. *Silicon*, the most popular semiconductor material and probably *the* most exhaustively studied material on Earth, with the availability of a complete machining tool set for selective material addition/subtraction and planar pattern definition on a substrate on a greatly reduced yet precise dimension scale, has made itself a legitimate structural material for *micro-machines* [4]. Similar to what miniaturization of silicon *electronic* devices has brought to the world, silicon *micro-machines* can lead to technological revolutions of unprecedented magnitude. Such *micro-machines* are often referred to as *MEMS devices.*

---

[3] Bipolar Junction Transistor
[4] Metal-Oxide-Semiconductor Field-Effect Transistor
[5] Thyristor is a class of latching bipolar devices initially known as the Silicon Controlled Rectifier, or SCR.

Solid-state transistors and conventional electromagnetic relays have been extensively used in various industrial applications as switching devices to make or break circuits. The advantages of each type of the switching devices are listed in Table 1.1.

Solid state transistors	**Magnetic relays**
Small size	Low *on-state* resistance
Mass Producibility	High *off-state* blocking voltage
Easy on-chip integration	High current capacity
Fast switching speed	Good control/signal isolation
Low actuation power	

Table 1.1 Advantages of switching devices:
Solid-state transistor vs. Electromagnetic relays

The choice of one type of switching device over the other depends on application-specific requirements. The two most prevalent applications of the switching devices are *signal routing* and *power routing*. In addition to common requirements, such as long lifecycle, robust operation, high open-contact and control-to-contact breakdown voltages, and minimal bouncing effects, etc., the two major applications of the switching devices, *signal* and *power* redirectioning, also call for fairly distinct specifications on the switches as illustrated in Table 1.2.

Signal switching (High-fidelity)	**Power switching (High-efficiency)**
Low insertion loss	Low *on-state* voltage drop
Wide frequency bandwidth	High current capacity
Low signal cross-talk	Low *off-state* leakage current
Low parasitic impedance	—

Table 1.2 Specification requirements of switching devices:
Signal switching vs. Power switching

1.2 Other Micro Relays/Switches

The emergence of MEMS technologies has brought global attention to the possibility of merging conventional macroscopic relay attributes with MEMS device attributes into a new family of switching devices: MEMS based relays/switches. One of the earliest MEMS devices is an electrostatic switch developed two decades ago [5]. Electrostatic actuation remains the most popular actuation scheme, but other methods of actuation have also been broadly investigated. Most MEMS relay/switch studies found in the literature either focus on signal switching applications, such as automatic test equipment [6-10], telecommunications [11-18], and logic

operation [19], or are oriented toward technology demonstration [5, 20-25]. Few [26] have addressed the need for a MEMS-based relay/switch tailored for power applications, and that is the gap this thesis is trying to fill. In Table 1.3, a selected collection of recent publications on micro switches/relays is illustrated. Cronos Integrated Microsystems Inc.[6] has unveiled a thermally actuated micro relay as the company's first commercial product. However, not much device detail has been revealed to the public so far.

Year	Organization	Actuation	Act Pwr/Volts	Contact	Current	Speed	Application	Cycles	Ref.
1979	IBM	Electric	-	5 Ω	-	40 μs	AC signal	-	[5]
1994	Neuchatel	Electric	50-75V	-	-	4 μs	Signal	1e9	[27]
1995	EG&G	Electric	50-100 V	3 Ω	-	20 μs	ATE	1e8	[6]
1995	NTT	TCMA[1]	>300mA	3 Ω	-	10ms	-	-	[21]
1995	CWRU	Electric	35-150V	<20Ω	150mA	5-40kHz	-	-	[23]
1995	Rockwell	Electric	28V, 1.4uW	0.22Ω	200mA	30 μs	Telecomm.	-	[12]
1996	TI	Electric	50-300V	-	-	6-8 μs	Microwave	-	[28]
1997	Omron	Thermal	27V, 25mA	-	-	-	-	-	[29]
1997	GA Tech	Magnetic	180mA,33mW	2-3Ω [2]	1.2A	1-5ms	Automotive	3e5	[30]
1997	NEU	Electric	30-400V	50mΩ [3]	5mA	-	ATE	1e9	[7]
1998	CSEM	Magnetic	8mA, 14mW	0.4Ω	-	0.2-0.3ms	Signal	>1.5e7	[8]
1998	UCLA	Electric	35V	1kΩ	10mA	4 Hz	-	-	[25]
1998	NJIT	Thermal	12mW + 10mW	2.1-35.6Ω	-	0.1-0.5ms	Signal	1e5	[31]
1999	NTT	Electric	15V	5Ω	-	10kHz	Signal	-	[19]
1999	CSEM	Magnetic	2V, 16mW	0.4Ω	-	1ms	Signal	1e7	[10]

Table 1.3 Selected micro switching devices published recently

[1] Thermally Controlled Magnetization Actuation
[2] Minimum resistance measurement: 0.85Ω
[3] Resistance measurement made with manual contact closure.

1.3 Power MEMS Switches: Motivation and Goal

One of the promising high power applications of MEMS switches is automotive relay replacement. Fifteen million automobiles are manufactured per year in the U.S. and an average car uses approximately 15 relays which is increasing rapidly to as many as 50 per car. This puts the automotive relay market at 225 million relays per year in the U.S. alone. Thus, one important target application for a MEMS switch would be in the replacement of the conventional relay block in an automobile. The intent there is to embed MEMS switches at the point of use instead of running wire harnesses across the engine compartment to a relay block. Embedding relays at

[6] JDS Uniphase Corporation has just announced its acquisition of Cronos Integrated Microsystems, Inc.

the point of use reduces car weight and power line loss, and improves fuel economy and automobile performance. Another equally promising market for the power MEMS switch is application in residential circuit breakers.

The goal of this thesis is the development of a MEMS switching device for automotive, residential, and/or other power distribution applications. The power MEMS switching device should possess the key attributes of a power switch, such as high current-carrying capacity and low on-state resistance for efficient power transmission with low loss. Unlike signal switches that need to deliver/receive information with high data transmission rate and high fidelity, requirements on switching speed, on-state insertion loss, off-state parasitic capacitive coupling, signal cross-talking noises, and so on are not major issues for the power switches to be studied in this thesis. As with signal switches, the power MEMS switches call for high off-state resistance and high standoff voltage.

1.4 System Viewpoint

It is believed that the lifetime of the mechanically moving MEMS switch is dictated more by the wear of its contacts than by the failure of the moving member itself. Since arcing is a well-known cause of contact wear, we propose a protective circuit to parallel the power MEMS switch device as described in Section 1.4.1. This scheme enables us to focus on *cold switching* in the study of the MEMS power switch behavior. Moreover, to scale up the current capacity and to facilitate different switch configurations with SPST switch cells at the packaging level, Section 1.4.2 proposes a four-by-four switch cell array design.

1.4.1 Arcless Switching Scheme

The protective switching scheme is shown in Figure 1.1 where the MEMS switch is paralleled with a solid-state-transistor based circuit and the circuit turns on before and turns off after the MEMS switch. In this way, the contacts of the MEMS switch are protected from being brought into close vicinity with a high potential difference across them thereby preventing arcing due to hot switching. Moreover, any inductive energy stored behind the switch is dissipated by the protective circuit thereby protecting the thermally vulnerable switch contacts. This protective circuit can be incorporated with the MEMS switches via on-chip integration or off-chip packaging and will be the subject of future investigation.

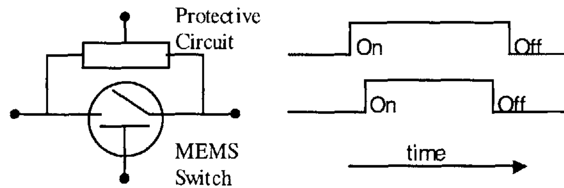

Figure 1.1 Arcless switching scheme

1.4.2 Switch Cell Array Configuration

The purpose of the switch cell array design is *two-fold*: in addition to the apparent current capacity boost, such switch cell arraying permits a simple SPST switch cell design and leaves more complicated switch configurations to packaging-level connections. Furthermore, if the protective/control circuit mentioned in Section 1.4.1 is to be implemented off chip, it can realized by replacing one of the cells in the array with a circuit cell. Figure 1.2 shows the cell array schematically.

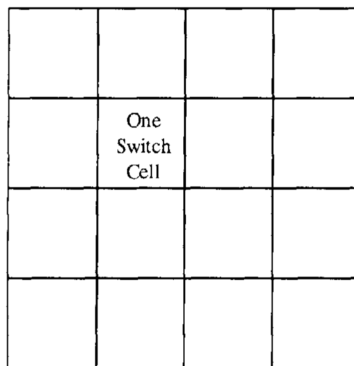

Figure 1.2 Four-by-four switch cell array configuration

1.4.3 Quick Summary on Device Performance

To put the device in perspective with other micro relay/switch work, and with the power switch requirements discussed earlier, this section tabulates in Table 1.4 an upfront summary of the performance of the power MEMS switch investigated in the thesis. This device exhibits *on-state* characteristics among the best of its kind and, more significantly, the current capacity per cell appears promising for power applications.

Actuation Scheme	Electrostatic	Zero actuation power during steady state.
Actuation Voltage	Turn-on: *20 V* Turn-off: *14 V*	Lowest turn-on voltage: *15 V*.
Mechanical Design	*2.4-mm* diameter diaphragm	Good heat dissipation.

$R_{contact}$	Generally < *50 mΩ*	Lowest resistance: *14 mΩ.*
Current Capacity	*400mA*	Current/actuator area: *90 mA/mm²*. With 4×4 array design: > *6 A*.
$V_{breakdown}$	> *300 V*	Sufficiently high for automotive applications.
t_{switch}	Turn-on: *5 ms* Turn-off: *20 ms*	Limited by squeeze-film damping; can be improved.
Cyclic Operation	> 4000 operations	Not much performance degradation observed.

Table 1.4 Summary on device performance

1.5 Thesis Overview

The remainder of the thesis is organized as follows. Chapter 2 investigates theories and experimental results of electrical breakdown in narrow air gaps. This work establishes guidelines for the MEMS switch design Chapter 3 analyzes various switch designs and settles on a promising candidate design. Chapter 4 addresses the fabrication techniques of different device generations and their behavior. Chapter 5 discusses various device performance characterizations, how tests are implemented, and their results. Finally, a summary, conclusions, and suggestions for future work are given in Chapter 6.

Chapter 2 ELECTRICAL BREAKDOWN IN NARROW AIR GAPS

2.1 Introduction

This chapter focuses on two main subjects. First, the underlying physics of electrical breakdown phenomena in micron-scale air gaps are summarized. Second, an empirical study of the standoff voltages achievable in such narrow air gaps is presented. Acquiring the knowledge of electrical breakdown through experimental results on actual devices, along with the experience gained in the course of design, fabrication, and experimentation of breakdown test devices is an important step toward the design of actual MEMS switches. Therefore, an investigation of electrical breakdown in narrow air gaps is chosen to be the first challenge of this thesis.

Various factors must be taken into account in an in-depth study of the electrical breakdown in gases. They include gas pressure, gas temperature, gap spacing between electrodes, electrode shape, electrode surface condition, material of electrodes, composition of the gas, radiation in the space, and uniformity of electrical field. The atomic, molecular, electronic, ionic, and photon collision processes in the gas and at the electrodes, which can be involved in the various mechanisms of breakdown, are themselves of fundamental physical interest. A full-scale study of electrical breakdown in micron-scale gaps can make up a doctoral thesis in fundamental physics in its own right and is impossible to carry out here. Our simplified experimental approach will consider only gap separation and contact patterns as variables. Also, issues such as how fast gases respond to the electrical field and break down, and how fast gases recover from a heavy current carrying state back to their original insulating state after an applied potential is removed are not addressed in this thesis.

In what follows, Section 2.2 develops a basic understanding of the electrical breakdown in air gaps from our everyday observations and some existing theories of electrical breakdown found in

the literature such as [32-35] are discussed. These references are good introductory reading for readers interested in much more detail than can be presented here. Section 2.3 comments on the electrical breakdown theories especially in the case of very narrow air gaps. Section 2.4 discusses the fabrication of breakdown test devices employed here, the test hardware as well as the test results. Lastly, Section 2.5 concludes what we learn from the electrical breakdown test and presents the author's suggestions for further studies in improving the breakdown strength of MEMS devices.

2.2 Electrical Breakdown in Gases

Our perception of gas has always been a nearly perfect insulator and it is generally true in our everyday life experience. Under certain conditions, however, when an electric field of sufficient intensity is applied across two electrodes, the gas could suddenly become relatively conductive. The transition from insulating to conducting states is a physical change often referred as the electrical breakdown of the gas. This transitional process occurs in very short times varying from milliseconds to nanoseconds.

The most commonly seen occurrences of electrical breakdown are lightning, fluorescent lamps, and sparks between hands and doorknobs in dry winter days. Electrical breakdown in gases is a very involved phenomenon and, in general, requires electron avalanche. It has to do with a sudden and dramatic change of gas dielectric property as the collision of sufficiently high-energy particles ionizes material molecules and produces a large number of free current carriers. To achieve a self-sustaining discharge, any ionization on average must produce some means for at least one new ionization to occur. The condition under which such transition takes place is a function of a variety of parameters as briefly described in Section 2.1. The following section will describe the typical process of electrical breakdown and provide an introduction to electrical breakdown theories.

Scientists have studied the electrical breakdown of gases for over a hundred years in order to answer two main questions. *Firstly,* is it possible to explain and to predict, from our understanding of collision processes, the lowest voltage at which electrical breakdown will occur for a given set of electrodes at a given gap separation in a given gas at a given pressure? In other words, is it possible to elucidate a mechanism of breakdown and derive a criterion for the breakdown voltage? Secondly, is it possible to establish a theoretical explanation, based on collision processes, to account for the breakdown process from the first few electrons that must always be present to initiate breakdown to the final form of the discharge? The following sections

will describe, in a very simplified way, the breakdown phenomenon and summarize the generally accepted theories that have been established to answer these questions.

2.2.1 Paschen's Law

As mentioned earlier, there are various factors that must be taken into account in studying the breakdown in gases, such as gas temperature, gas pressure, the shape, surface condition, and material of electrodes, the gap spacing between electrodes, the composition of the gas, radiation, and the uniformity of the electrical field. An empirical criterion found by Paschen in 1889 [32] states that over a certain pressure and temperature range in a static uniform field, using parallel plate electrodes, the breakdown voltage of a gas depends on the product of gas pressure and gap separation. Thus,

$$V_s = f(pd) \tag{2.1}$$

where V_s is the sparking potential, or breakdown voltage, p is the gas pressure at a given temperature, d is the gap spacing, and f is a function of pd only. This criterion has been shown to hold for a wide range of conditions up to a pressure of about 150 psi and is now known as Paschen's Law. Sometimes, Paschen's Law is also stated as

$$V_s = f(Nd) \tag{2.2}$$

where N is the gas density in molecule number per unit volume. This latter form of the law is useful when considering a sealed system where pressure increases with temperature but N remains constant, so the breakdown strength remains unchanged. The breakdown voltages for gases decrease as the product of p and d is reduced, and reach a minimum at a value of pd on the order of *1* to *10mm-Hg* × *cm* [34, 35].

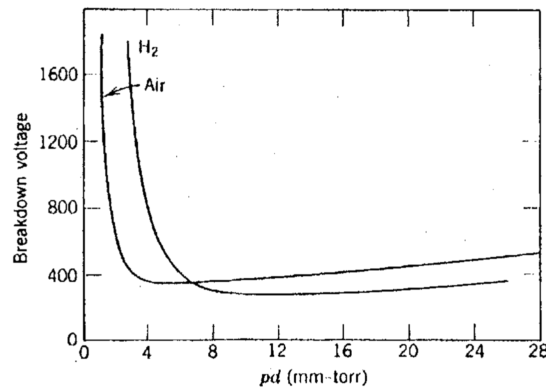

Figure 2.1 Typical Paschen curves for hydrogen and air [36]

At present, two fundamental breakdown mechanisms have been established to account for this relationship. The first is a relatively slow mechanism, which needs a large number of generations to produce breakdown. This is referred to as the Generation Mechanism or Townsend Mechanism. The second is a rapid mechanism, which develops directly from the first avalanche to breakdown. This is referred to as the Streamer Mechanism or Kanalaufbau. There also exist variations of these mechanisms, which can be understood as transitions between them. These two mechanisms are briefly discussed next.

2.2.2 Townsend Mechanism

Townsend's paper in 1910 [33] illustrates this theory by examining the current between parallel plate electrodes under increasing electric force; see Figure 2.2. As the electric field increases, the leakage current between the plates first increases accordingly. This leakage current very quickly saturates at a certain value, *Io*. After that, any further potential increase does not change the leakage current very much over a wide range of electric potential. As electric potential is increased still further, the rate of leakage current increase suddenly jumps to an appreciable value. Townsend explains this as follows. Under low electric field, a dielectric gas is in its normal state and electrically non-conductive because there is no significant number of free electrons or ions to carry electrical current between the electrodes. However, there is always a small number of low-energy charged particles present in the gas due to environmental radioactivity and cosmic radiation. This limited amount of free electrons accounts for the leakage current, *Io*, at low electric field. A single free electron could ionize a gas molecule by collision, producing two free electrons and a positive ion. The higher the electric field intensity, the more electrons colliding with ions which generates more charge particles. This cumulative process eventually produces a swarm of free electrons and ions, generally called "electron avalanche", the gas then becomes conductive. Secondary avalanches may be produced at the cathode by the impact of positive ions or photons from an ongoing avalanche. This in turn initiates more avalanches, creating a self-sustaining discharge. This electrical breakdown model is known as the *Townsend theory of breakdown.*

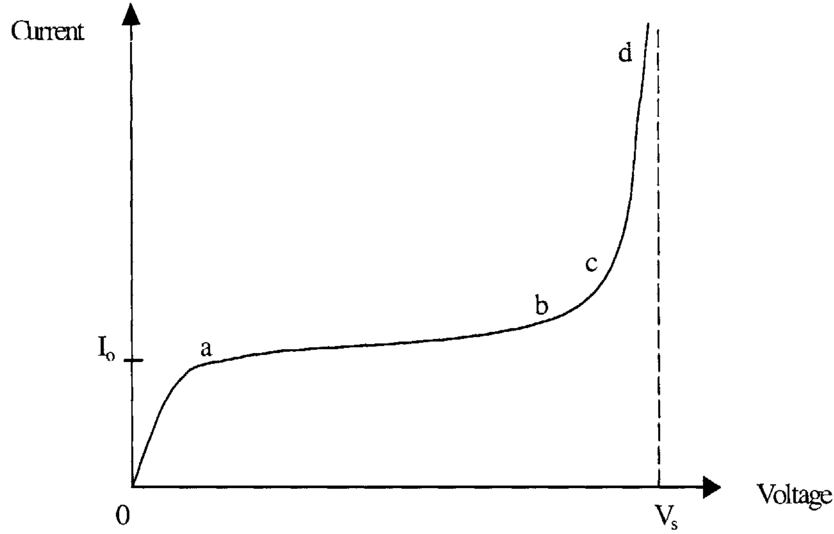

Figure 2.2 V-I plot of two parallel plates (Townsend electrical breakdown mechanism [33])

Townsend's theory of breakdown is good for low *pd*, between 200 torr-cm and 1000 torr-cm [37], where p is the gas pressure between the parallel plates and d is their separation distance. Townsend also develops the following formula and finds good agreement with experimental data.

$$i = \frac{i_0 e^{\alpha x}}{1 - \gamma(e^{\alpha x} - 1)} \tag{2.3}$$

where i_0 is the saturated leakage current, α is the so-called first Townsend multiplication coefficient, and γ is the so-called second Townsend ionization coefficient. Physically, the first Townsend coefficient, α, indicates the number of new electrons created by a traveling electron through a path of length 1 cm. It is concerned with the electron multiplication by primary ionization. The second Townsend coefficient, γ, is also called the *generalized secondary ionization coefficient* and represents the efficiency of production of secondary electrons per ion pair formed in the gas. Breakdown then occurs when the denominator becomes zero, or

$$\gamma^{-1} = e^{\alpha x} - 1 \tag{2.4}$$

References [33-35] provide a more thorough understanding of Townsend's description of gas breakdown phenomena.

2.2.3 Streamer Mechanism

There exists another breakdown mechanism that progresses much faster than the Townsend Mechanism described in the preceding section. The most striking differences of this mechanism compared with the Townsend breakdown mechanism are as follows.

1. There is no cathode or gas secondary ionization process as in a Townsend type breakdown mechanism, thus the breakdown potential is independent of the nature of the cathode surface. Additionally, photons from the avalanche head produce free electrons by photo-ionization.
2. High field distortion, due to space charge at the avalanche head, moves the free electrons toward the avalanche head and generates further cumulative avalanches. When the space charge suddenly distorts the field, breakdown suddenly occurs. The criterion that sets the value of breakdown potential is uniquely determined by space-charge distortion of the electric field.
3. It is feasible that breakdown could take place in a very short time, less than *0.1 μs* for a *1 cm* gap, and that luminous streamers can cross the gap in less than an electron transit time.

The Streamer theory applies when the number of electrons in the average avalanche reaches a critical value, generally taken as 10^8. The transition from a Townsend mechanism, which operates at the lower pd values, to a Streamer mechanism takes place when $pd > 200$ torr-cm, where p is the gas pressure between the parallel plate electrodes and d their gap separation distance.

In conventional relays or MEMS switches/relays, the open contact separation ranges from millimeters down to micrometers, and the product of gas pressure and electrode separation (pd), is normally well below 200 torr-cm. Therefore, the Streamer mechanism does not apply in such small air gaps. Readers with more interest in Streamer breakdown mechanism should refer to [34, 35] for further discussion.

2.2.4 Summary of Breakdown Theories

In essence, electrical breakdown can be seen as a competition between the recombination/absorption rate and the generation/multiplication rate of such free electrons and ions. When the former dominates, the gas is nonconductive; when the latter dominates, electrical breakdown occurs. The experimental data of electrical breakdown found in the literature affirm Paschen's criterion, which is now well accepted and referred to as *Paschen's Law,* Equation (2.1) or (2.2).

Paschen's Law says that the dependencies of breakdown potential between parallel plates on pressure (*p*) and on gap-distance (*d*) are linearly linked with each other and appear as their product (*pd*).

Two breakdown models are established to explain the fundamental physics of Paschen's Law in different *pd* ranges: the Townsend breakdown model for the lower *pd* range, and the Streamer breakdown model for the higher *pd* range. Secondary ionization at the cathode plays an important role in the Townsend breakdown mechanism, as the positive ions and photons colliding with the cathode provides the self-sustaining discharge. Therefore this breakdown phenomenon is more dependent on the characteristics of the cathode. In the Streamer breakdown theory, local electron avalanche causes photo-ionization and field distortion by space charge, driving free electrons toward the avalanche head and initiating more avalanche, more photo-ionization, more field distortion, and more free electrons into the cloud. The gas can respond to an electric field in a very short time and spark under streamer breakdown model.

The transition from a lower *pd*-valued Townsend breakdown mechanism to a higher *pd*-valued Streamer breakdown mechanism takes place when $pd \approx 200$ *torr-cm*. If we fix the air pressure at atmospheric pressure, $p = 760$ *torr*, Townsend breakdown theory is applicable to cases with electrode separated less than *2.6 mm*. Generally, the off-state contact separation, *d*, is orders of magnitude less than *2.6mm* for MEMS-based devices. From this point of view, the Townsend breakdown mechanism seems to be a more appropriate model to explain the breakdown process in MEMS relay/switch applications at atmospheric pressure due to the small gap separation in MEMS devices.

2.3 Discussion of Electrical Breakdown in Narrow Air Gaps

The limits of Paschen's law in terms of *pd* ranges is still an open question. However, with the assumption that Paschen's law applies well into very-low *pd* realm, it is possible to investigate electrical breakdown in narrow air gaps by examining into Paschen's curves in the ultra-low pd range. Under this assumption, the data in the low *pd* regime of the Paschen curves, which are taken in vacuum pressures, can be employed to predict the electrical breakdown in very narrow air gaps at atmospheric pressure. This is the reason why the experimental data for electrical breakdown voltages in the ultra-low *pd* ranges found in the literature were primarily obtained with gap separations in the centimeter range and air pressure brought down in the vacuum range. In other words, low *pd* values were achieved by pumping the air pressure down to the *m-torr* range while keeping the electrode separation fixed at a fair distance [35]. This is understandable

since well-developed vacuum technology makes it more manageable to pump down and control pressures at vacuum levels than to bring two exceptionally planar polished electrodes into very close proximity while maintaining uniform and precise gap separation in micron range.

Figure 2.1 in Section 2.2.1 shows typical Paschen curves of hydrogen and air. If the curve for air in this figure is chosen to study the breakdown of air in narrow gaps, it can be seen that the breakdown voltage for air decreases as *pd* is reduced, reaching a minimum of 360 V at *pd* = 5 torr-mm, and then increases. This means that, other conditions being the same, the minimum breakdown voltage of air at *760 torr* atmospheric pressure, should take place at 360 V when the electrodes are 6.6 μm apart. Note that the field emission of electrons limits the electric field to about 10^9 V/m or lower. The breakdown voltage should rise with either closer or wider gap spacing.

Before examining whether Paschen's law provides a good prediction of the breakdown voltage of the micrometer-scale air gaps in MEMS-based devices, consider the following issues.

(1) Surface roughness

Figure 2.3 shows another plot of breakdown voltage curves with different electrode materials. It can be seen that a variation of breakdown voltage occurs with different types of electrode materials as *pd* reduces. This is not surprising since secondary cathode ionization is a significant mechanism in Townsend breakdown theory, which is the predominant breakdown model in the low *pd* regime. The lower the *pd* value, the more important role the electrode surface plays in the electrical breakdown mechanism. At higher *pd*, surface condition has negligible effect.

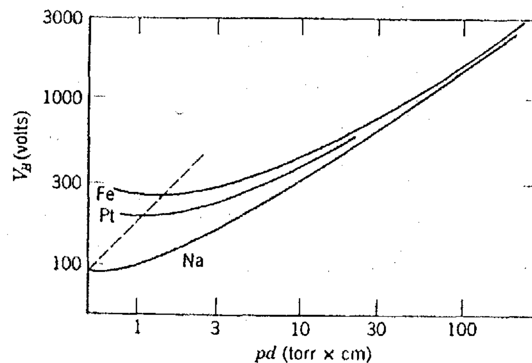

Figure 2.3: The effect of electrode material on breakdown in argon [36]

Remember that the data in the low *pd* range were obtained with experiments in vacuum pressure and with relatively large gap separations. Surface roughness of electrodes, which might not be of importance at such considerable gap distance, can now become a even more important factor in the case of very narrow separation at atmospheric pressures. In other words, a higher dependency of breakdown voltage of air at atmospheric pressure on the electrode conditions in very narrow gap separation should be expected, especially surface roughness. A uniform electric field might no longer be a valid assumption. This is important because locally distorted fields due to surface roughness can enhance ionization, and pointed protrusions can support electron emission. These surface roughness effects can be of importance in the electrical breakdown between very closely separated electrodes.

(2) Collision number

The collision count that an ion or electron will encounter traveling across a voltage-biased gap is linearly proportional to the length of travel (gap spacing) as well as the collision probability along the travel (air density or pressure). Since the atomic, molecular, electronic, ionic, and photon collision processes in the gas are crucial physical events that lead to eventual electrical breakdown, it can be argued that one rationale behind Paschen's law, Equation (2.1) or Equation (2.2), is that the electrical breakdown voltage across two parallel electrodes is a function of total particle collision number along the gap. Therefore, to first order approximation, a constant product of travel length (*d*) and collision probability (*p*) dictates a certain number of collisions a particle would see crossing the gap.

From the discussion of *surface roughness*, it has been argued that the surface condition of electrodes can be of greater consequence for narrower gap separation. This follows from the secondary ionization at the cathode as proposed by Townsend [33]. The frequency of particle collisions at the cathode electrode is still a linear function of air density or pressure, but its dependency on gap spacing, if any, is very weak. In other words, Paschen's criterion relates the breakdown potential of air with particle collision counts *within* the electrodes, which is a function of *pd*; however, as gap separation gets closer, collisions *at* the electrode, which is a function of only pressure (*p*) but not gap distance (*d*), plays a more important role. Therefore it would be reasonable to expect more deviation from predictions based on Paschen's law for narrower gap separations.

(3) Collision energy

Electrical breakdown is a phenomenon that turns gases from insulators to conductors with the continual creation of charged particles. Charged particles come from ionization, which in turn is induced by collision of energized particles. The kinetic energy of the colliding particle is prescribed by the accelerating distance between collisions (mean-free-path, $\lambda_{m.f.p.} \propto 1/p$) and the acceleration rate (proportional to electric field, $E = V/d$), among other factors such as the charge and mass of the particle. The accelerating distance ($\lambda_{m.f.p.}$) and acceleration are inverse proportional to pressure (p) and gap separation (d), respectively. Therefore, the product pd dictates not only the total number of collisions along the gap as discussed earlier, but also the kinetic energy of the colliding pair at each collision occurrence.

For air at room temperature and atmospheric pressure, $\lambda_{m.f.p.} \approx 700$ Å [38]. Statistically this means that 63% of particles undergo collisions in a distance less than $\lambda_{m.f.p.}$, and about 0.6% travel more than $5\lambda_{m.f.p.}$ before collisions, assuming $d \gg \lambda_{m.f.p.}$. The more the gap (d) reduces to the order of the mean-free-path ($\lambda_{m.f.p.}$), the higher percentage of the collisions will have the accelerating distance capped by the gap separation. This again suggests more deviation from Paschen's model for narrower gaps.

Experiments of the electrical breakdown of atmospheric air with gaps down to the air mean-free-path range have been done [39], but the rising branch at the left side of the minimum was not observed. Breakdown occurred at voltages as low as *50 V*, smaller than the *360 V* as predicted by Paschen. This inconsistency with Paschen's law suggests that there are effects that were not considered in the initial breakdown theory of Paschen's law when the gap becomes very narrow. Which effects these are is not yet clear and not much discussion of this subject is available in the literature.

The above discussions of *(1) surface roughness, (2) collision number*, and *(3) collision energy* are the author's qualitative arguments to explain the deviation from Paschen's law in the limiting scenario of very narrow air gaps. More analytical work in fundamental physics and experimental data will be needed to validate these speculations. Because of this complicated nature of electrical breakdown, the experimental exploration of the electrical breakdown voltage of a MEMS switch is both justified and essential.

2.4 Fabrication and Testing of Breakdown Test Device

Breakdown test devices such as the one shown in Figure 2.4 are employed to mimic the close separation between two deposited metal contacts in a real MEMS switch, and to measure the voltage at which electrical breakdown occurs under such condition. The test devices are fabricated from upper and lower wafers that are separately processed, diced and cleaned. Individual upper and lower dice are then bonded using a metal-to-metal bond to form individual devices. Figure 2.4 shows the cross-sections of upper and lower wafer just prior to the bond. The fabrication of the devices is briefly explained here.

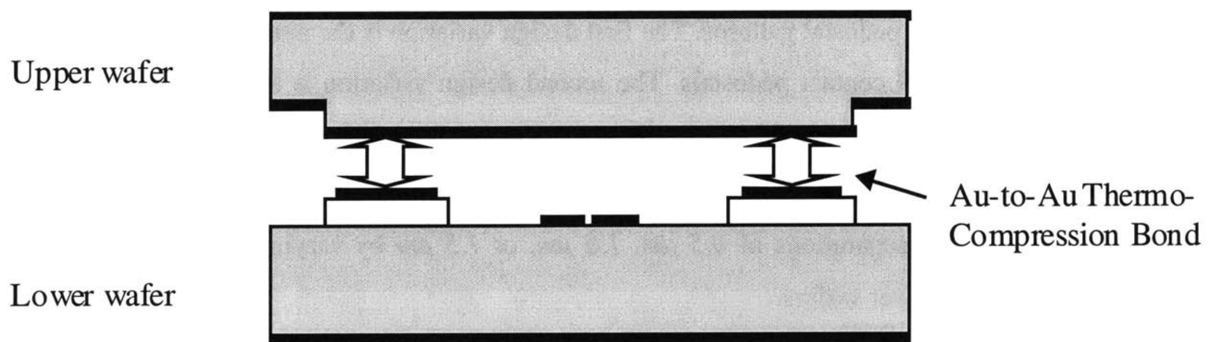

Figure 2.4: Device for Measuring Electrical Breakdown in Narrow Air Gaps

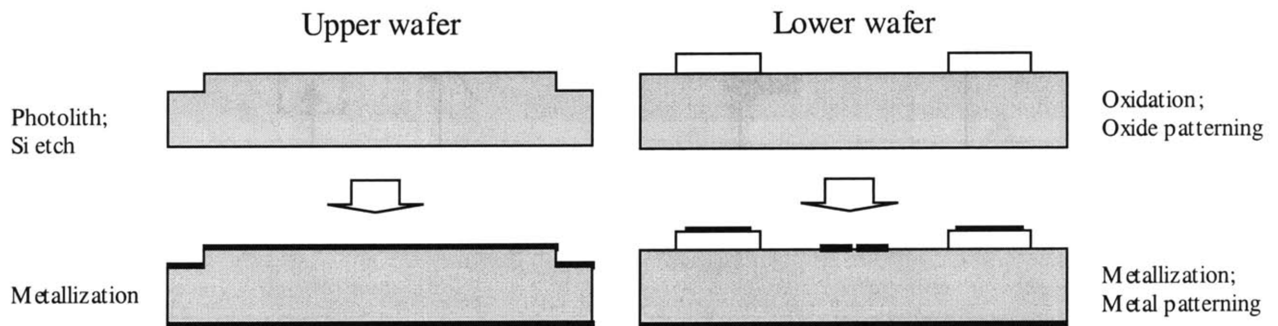

Figure 2.5: Process flow for upper and bottom wafers of Breakdown Test Device

The upper wafers are first etched along the periphery of each device to prevent electrical breakdown from occurring there. The wafers are then coated with 0.5 μm of gold on the front sides and 0.5 μm of aluminum on the back sides. The aluminum coating facilitates electrical contact to the devices. The gold coating forms one side of the contacts and also participates in the

metal-to-metal thermo-compression bond with dice from the lower wafers. Finally the upper wafers are diced and solvent-cleaned.

The lower wafers are first oxidized and then a photolithography step follows to pattern the silicon dioxide film. The thickness of the oxide determines the gap separation in the finished devices. The wafers are then coated with 1 μm of gold on the front sides and 1 μm of aluminum on the back sides. The gold is patterned by lift-off to form contact pedestals in the center of the device and rings on top of the oxide for bonding purpose. Finally, the lower wafers are diced and solvent-cleaned. Individual upper and lower dice are thermo-compression-bonded to form finished devices.

There are six contact pedestal patterns. The first design variation is the number of pedestals; each device has 1, 7 or 19 contact pedestals. The second design variation is the pedestal radius and spacing; pedestals are either *100 μm* in diameter separated by *200 μm*, or they are *200 μm* in diameter and separated by *200 μm*. In addition to varying the contact geometry, devices are fabricated with gap separations of *0.5 μm*, *1.0 μm*, or *1.5 μm* by varying the thickness of the oxide layer on the lower wafers.

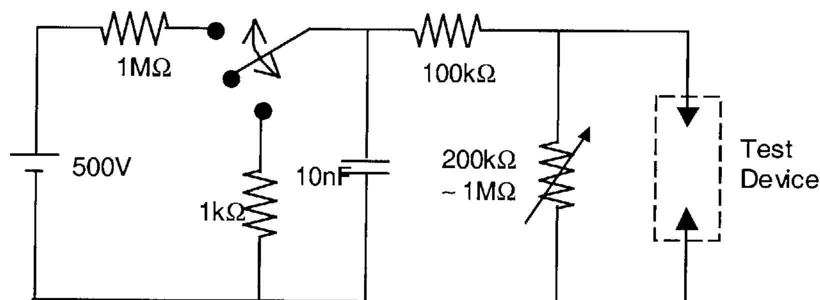

Figure 2.6: Circuit for measuring electrical breakdown

The voltage at which electrical breakdown occurs in a test device is measured using the circuit show in Figure 2.6. To execute a test, the switch is first set to the lower position to completely discharge the capacitor; then, the switch is positioned to connect to the voltage source so as to charge the capacitor. As the voltage rises, the increasing voltage is scaled by a voltage divider and applied the test device. At a certain voltage, the test device will finally break down. The charging/breakdown transient is measured with a storage oscilloscope, and the breakdown voltage is taken to be the peak voltage of the transient. The results of the tests are listed in Table 2.1 and

shown graphically in Figure 2.7. Typical curves for such charging/breakdown transients for different devices are shown in Figure 2.8.

Gap Separation	Pedestal Number	Pedestal Diameter	Breakdown Voltage
0.5 μm	1	100 μm	156 V
			170 V
			314 V
0.5 μm	1	200 μm	54 V
0.5 μm	19	100 μm	116 V
1 μm	1	100 μm	292 V
			330 V
1 μm	1	200 μm	156 V
1 μm	7	100 μm	42 V
			334 V
1 μm	7	200 μm	176 V
1 μm	19	200 μm	284 V
1.5 μm	1	100 μm	8 V
			270 V
1.5 μm	1	200 μm	62 V
			140 V
1.5 μm	7	200 μm	9 V
			314 V
			314 V
			316 V
1.5 μm	19	100 μm	296 V
			320 V
1.5 μm	19	200 μm	40 V
			342 V
			342 V

Table 2.1: Breakdown voltage measurements

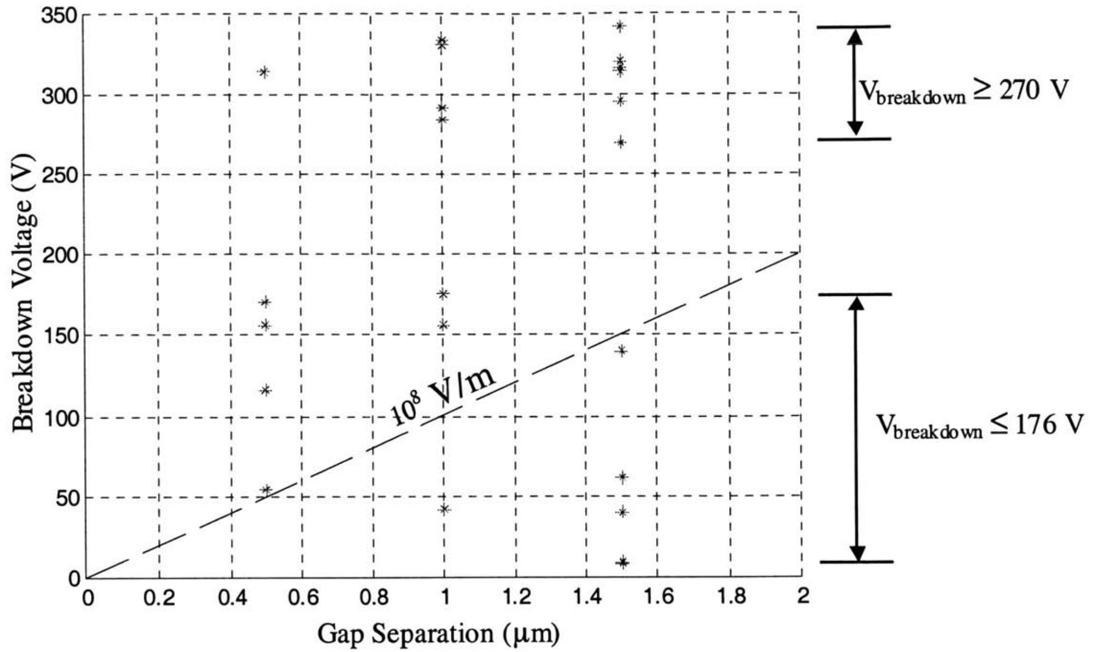

Figure 2.7: Breakdown voltage v.s. Gap separation

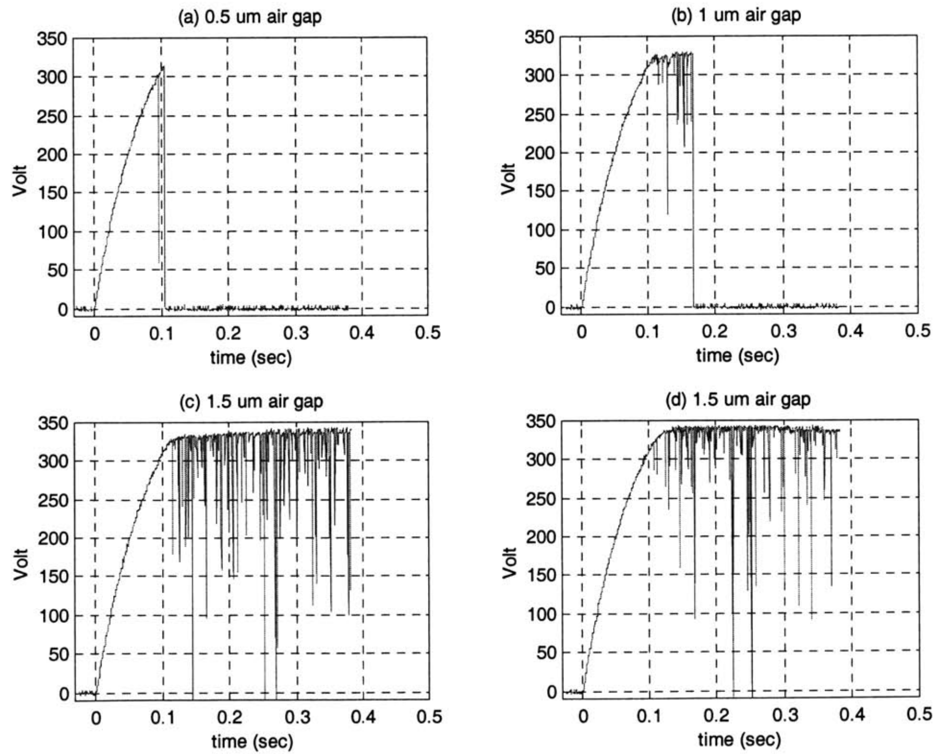

Figure 2.8 Charging/breakdown transient curves of different devices: {pedestal #, pedestal diameter, air gap} = (a) {1, 100 μm, 0.5 μm}, (b) {1, 100 μm, 1 μm}, (c) {19, 200 μm, 1.5 μm}, (d) {19, 200 μm, 1.5 μm}.

2.5 *Summary and Future Work on Electrical Breakdown*

This section summarizes the breakdown test results. Additionally, it offers suggestions for future improvement of the breakdown experimentation.

2.5.1 Breakdown Test Results Summary

It is interesting to note from Table 2.1 or

Figure 2.7 that all breakdown voltages are either less than or equal to 176 V, or greater than or equal to 270 V. We believe that those contacts which broke down at voltage less than or equal to 176 V were contaminated with diesaw slurry, as discussed below, and that those breakdown voltages which were greater than or equal to 270 V are indicative of what can be achieved with clean contacts. Given this, it is important to note that breakdown voltages exceeding 300 V have been observed for 1.5 μm-gap, 1 μm-gap as well as 0.5 μm-gap devices.

A lesson learned during the course of fabricating the test devices is the importance of cleaning prior to die-level bonding. The die-level bonding process sequence exposes the contact surfaces to diesaw slurry and particles which could either short the devices or cause premature electrical breakdown if the devices are not thoroughly cleaned, prior to bonding. At first, a cleaning was performed in an ultrasonic solvent bath after the wafers were diced but before they were bonded. About 90% of these bonded devices were shorted due to diesaw slurry or particle contamination. However, the non-shorted devices exhibited leakage resistances in excess of 20 MΩ, which is the limit of the ohmmeter used to measure the leakage resistance. To address this problem, subsequent wafers were coated with a protective layer of photo-resist on the bonding side after the wafer-level processes were completed and before dicing. Then, the diced wafers were immersed in acetone, methanol, iso-propanol, and DI water, in that order, with ultrasonic agitation for photo-resist removal and cleaning. The yield improved significantly to 50% with this die-level bonding protocol.

Breakdown test results were very encouraging since the goal of accomplishing a breakdown voltage of 300 V was achieved. As long as the contact surfaces are sufficiently cleaned, it is safe to conclude that *250 V* breakdown strength can be repeatedly demonstrated. These results suggest that a gap as small as 1 μm or even 0.5 μm should be sufficient in the MEMS switch design to withstand *250 V* breakdown voltages. A die-level metal-to-metal thermo-compression bond process protocol was also established to minimize the diesaw slurry/dust contamination problem

due to the fact that breakdown test devices were fabricated from wafers first diesawed and then bonded.

2.5.2 Suggestions on Future Breakdown Strength Study

Our experiments with electrical breakdown strength in narrow gaps are carried out exclusively in atmospheric air, mostly because that current metal-to-metal thermo-compression bonding technology does not assure hermetic sealing. Potentially, a gas-sealing metal-to-metal wafer bonding technology or packaging scheme would facilitate the use of other dielectric gases at different pressures bringing forth a new dimension in terms of improving breakdown strength of the MEMS switches.

According to Paschen's Law (Section 2.2.1), pumping up the gas pressure inside the gap has the same effect on the electrical breakdown phenomenon as raising the gap separation distance in a linearly proportional manner. Therefore, it can be argued that either increasing or decreasing the gap pressure can be implemented to move further away from *pd* point corresponding to the minimum breakdown potential in the Paschen breakdown curve (Figure 2.1) and thus improves the breakdown strength until field emission.

The fact that the rising branch at the left of the minimum has not been consistently observed in micron-scale gaps suggests that pumping up the gap pressure might be the preferred approach. On the other hand, one might favor vacuum pressure since the squeeze-film damping effect which slows down the approaching speed of two closely spaced contacts can be lessened with reduced pressure. Empirical investigations need to be done to find an optimum pressure for a particular design.

Generally, dielectric gases can be classified as follows [40]: *simple gases*, such as air, nitrogen, hydrogen, helium, and oxygen; *oxide gases,* such as carbon dioxide and sulfur dioxide; *hydrocarbon gases,* such as methane, ethane, propane, butane, and hexane; *electronegative gases*, such as sulfur hexafluoride (SF_6), dichlorodifluoromethane (CCl_2F_2, Freon 12, Genetron 12) and so on. The formation of negative ions in electronegative gases reduces the density of free electrons and thus renders better electrical breakdown strength. Among these listed above as electronegative gases, sulfur hexafluoride (SF_6) [40] is preeminent because: it suppresses carbonization; it is useful over the normal range of utility operating conditions; it has the best obtainable arc-interrupting properties; it has excellent dielectric properties; it is nontoxic and easy to handle; it is chemically inert; it has good heat transfer properties; and it is highly electronegative. However, its price is relative higher than other dielectric gases.

The breakdown test results were successful, since breakdown voltages over *250-300 V* are normally sufficient in many power applications. Our experimental study suggests that an aggressive gap separatio, such as *1 μm* or below, can be designed to gain advantages in electrostatic actuation force. If, nevertheless, higher breakdown voltages are required in some particular applications, it is possible to improve the breakdown strength of narrow air gaps in MEMS devices with air sealing bonding/packaging technologies. Optimal gas pressures and/or choice of dielectric gases should be investigated experimentally for any specific device design.

Finally, the next generation of automotive electrical system will raise its voltage from *14 V* to *42 V* and the power transistors used in automotive applications will have a *60 V* rating with a *60 V* clamping protection. The impacts of this voltage change on the MEMS switch design are the availability of *higher* actuation voltages and *lower* standoff voltage requirement, both of which are favorable. As demonstrated experimentally in the electrical breakdown tests, 25*0 V* of breakdown strength is achievable with micron-sized gaps and well exceeds the future *60 V* requirements of automotive power devices.

Chapter 3 THEORY AND DESIGN

3.1 Introduction

Design is a combination of art and science. In areas where facts and rules are not clearly understood or elucidated, design practice resembles an art that requires intuition for perfection. On the other hand, when a sound knowledge base in all relevant domains has been well established, there is an axiomatic approach that a design engineer can follow to optimize the invention [41]. Due to the multi-disciplinary nature and the relatively short history in the still-evolving field, however, many MEMS device design problems are backed with a somewhat limited knowledge base, and become more or less an ad hoc activity that almost inevitably must go through a trial-and-error stage. In some cases, the problem statement is all but constant and the project objective is a continually moving target since discoveries of limitations and possibilities in MEMS technologies are still being constantly learned. This chapter is the author's effort to provide guidance to decision-making in the design process of MEMS switches so that unacceptable designs can be avoided, and to contribute to the knowledge base so that the endeavor of design in the young multi-disciplinary MEMS field can be more like science than art.

This chapter discusses the theories used in the design of the MEMS power switch and it is broken down as follows. In Section 3.2, actuation schemes commonly seen in MEMS devices are briefly introduced, and the selection of an electrostatic scheme is explained. Discussion and analysis of two different mechanical diaphragm structures, a bossed circular diaphragm and a uniform-thickness circular diaphragm, are given in Section 3.3. Design concerns associated with electrical breakdown are reviewed in Section 3.4; the theories of electrical breakdown in narrow air gaps were provided in Chapter 2. Section 3.5 is dedicated to the discussion of metal-to-metal contact resistance particularly in the case of small-force small-area micro contacts. Finally, in Section 3.6, the squeeze action damping of the air film bounded between the moving diaphragm and the

stationary bottom substrate is described and its effects on the device switching speed are examined.

3.2 Actuation Scheme

Various actuation schemes have been proposed for different micro actuator applications. In the case of the MEMS relay/switch, the characteristics of primary interest are the attainable force and displacement, power consumption, and ease of fabrication. The actuation force at closure provides the squeezing pressure against the contacts, and higher pressure results in a larger a-spot, a widely accepted term used in tribology representing the actual conducting areas between contacts [42]. Therefore high contact force is preferred for good on-state performance. On the other hand, the actuation displacement would be the stroke that the moving contact electrode has to travel between its on-position and off-position. The longer this travel the wider the gap separating the contacts becomes during the off state, and thereby rendering a higher off-state electrical breakdown strength. Consequently, a longer actuation displacement is preferred from the off-state breakdown strength point-of-view. Low actuation power consumption is favorable not only for economic reasons, but also for heat generation considerations. Overheating of a MEMS switch could lead to undesirable change of mechanical properties, such as contact melting, thermal stresses, non-uniform thermal expansions, metal softening and contact sticking, etc. There are two internal sources of heat generation in a micro switch: (1) ohmic heating in power lines and (2) ohmic heating in control lines. Ohmic heating in the power lines is inevitable for power switches which carry significant currents, but can be minimized with designs of low on-state resistances (Section 3.5). Heating in the control lines can be reduced with the design of a low-power actuation scheme. For a given design of a MEMS switch, there is a certain bound on its overall heat dissipation capability. The lower heat generation in actuation lines gives more room for heat dissipation in power transmission, and thus raises the current carrying capacity with fewer thermally-related uncertainties. Ease of fabrication and compatibility with mainstream CMOS processing are fabrication-related design factors that must be taken into account, especially in cases where applications necessitate on-chip integration with other electronic components and/or when a CMOS friendly process is requested by a foundry service provider.

3.2.1 Piezoelectric actuation scheme

Piezoelectric materials deform under the application of an electric field, or conversely, develop an electric field under the action of an applied strain. The strain, ε, in a piezoelectric material under the action of an applied electric field is given by

$$\varepsilon = \sigma s + Ed, \tag{3.1}$$

where ε is the strain in the material, s is the elastic compliance constant, E is the electric field, and d is the piezoelectric strain constant. In general, the stress, σ, and the piezoelectric strain constant, d, are both third-rank tensors. For typical materials, the piezoelectric strain coefficients, d_{ij}, are on the order of *1* to *3Å/Volt* maximum, which are relatively small values, resulting in very small displacements. The displacements can be made substantial by increasing the physical size of the piezoelectric actuator, or by the use of a displacement amplifier. The former is incompatible with the goal of miniaturization and the latter is achieved at the price of a small actuation force. Typical values of displacement for macro-scale piezoelectric actuators of a few centimeters in length are 250 ~ 500 Å/Volt.

The forces generated by piezoelectricity are reasonable if the sample is held at zero strain. But decrease as the piezoelectric material expands. This can be seen by rewriting Equation (3.1) as

$$\sigma = -P = \frac{1}{s}(\varepsilon - Ed) \tag{3.2}$$

where P is the reaction pressure the material applies to its surroundings. From Equation (3.2), it is apparent that the maximum pressure can only be achieved by having zero strain. This property makes it impossible to achieve a large actuation and a large displacement at the same time. Furthermore, actual material properties limit the amount of achievable deformations unless piezoelectric actuators of relatively large physical size are put into use, which defeats the goal of miniaturizing the device. In short, piezoelectric mechanisms cannot provide enough displacement without using an actuator of relatively large size due to limitations of real material properties.

3.2.2 Thermal actuation

Thermal actuators utilize the property of thermal expansion to produce motion. When a current is applied across the actuator, it heats up and thermal expansions occur. Parameters such as member geometry, size, and overall configuration may be tuned to achieve optimal deflection. As

temperature changes, a normal stress develops within a constrained solid or liquid according to the following relationship [43]:

$$\delta\sigma = E(\alpha\delta T - \frac{\delta V}{V}) \tag{3.3}$$

where $\delta\sigma$ is the thermal stress increase, E is the bulk modulus of elasticity, α is the thermal coefficient of expansion, V is the volume, and δV is the volume change. As can be seen from Equation (3.3), the thermal stress of a constrained solid or liquid increases in proportion to the bulk modulus of elasticity. Also, it rises with the thermal coefficient of expansion and the change in temperature, and falls with the differential volume change per unit volume. If the heated structure is not constrained and has certain degrees of freedom to expand, it will relieve the thermal stress and settle to a lower energy state with thermal expansion. Typical values of thermal coefficient of expansion for materials commonly used in the MEMS structures range from 0.1×10^{-6} °C^{-1} to 5×10^{6} °C^{-1}.

Another type of thermal actuation scheme uses a gas sealed inside a chamber. Upon heating of the enclosed gas, the pressure will rise according to ideal gas law,

$$\delta p = \frac{nR\delta T}{V} \tag{3.4}$$

where n is the moles of the gas, R is the ideal gas constant, δT is the temperature change, and V is the volume of the chamber. Such pressure rise or thermal expansion of the gas is then in turn used directly or indirectly for actuation.

The response time of a thermally actuated device is determined by the product of the thermal resistance and the thermal capacitance of the system. For faster thermal response, one must lower the thermal resistance and/or thermal capacitance. On the other hand, it will take higher actuation power with a lower thermal resistance. Therefore, for a given thermal capacitance, there is a trade-off between the thermal response time and the power consumption [44].

Thermal actuation of bi-stable mechanisms may lead to the ability to use micro bi-stable mechanisms as switches. With an appropriate design, it could provide the desirable large force and large displacement. The heating action takes place as currents flowing through resistors built in to the mechanically moving structures. A favorable design must the address the trade-off between thermal response time and power consumption, possibly by minimizing the thermal capacitance of the system. The fabrication of such thermal actuators is no more complicated than

other types of actuators, but might use materials not typically seen in standard CMOS process to optimize the thermal expansion characteristics.

Because of a wide temperature range in automotive environments, thermal actuation is *not* a favorite choice, as the issues of thermal drift and non-uniform temperature distribution on the change of device characteristics must be taken into account especially in automotive applications.

3.2.3 Magnetostatic Actuation

Magnetostatic actuation is commonly employed in macro-scale relays in power or signal routing applications. The magnetostatic actuation force is directly linked to coil currents. Therefore, for applications in which high actuation force is strongly desired while high actuation power is not a major concern, magnetostatic actuation is one of the better choices.

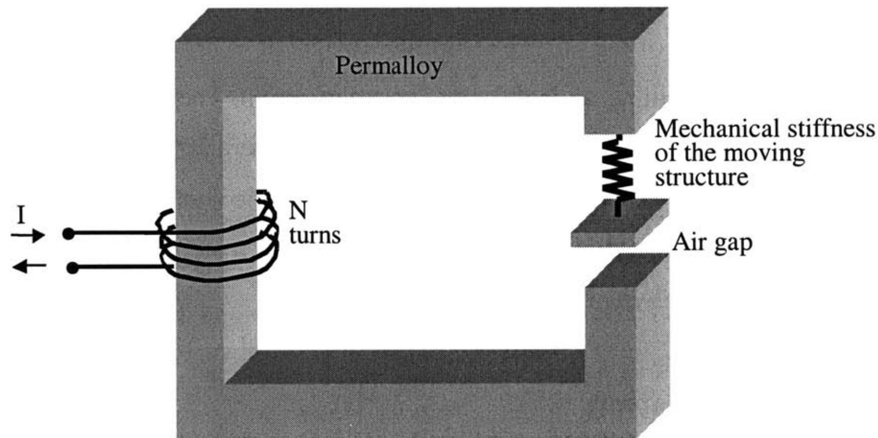

Figure 3.1 A schematic drawing of a micro electromagnetic actuator

The design of micro electromagnetic actuators usually takes the form of a magnetic circuit with a variable air-gap reluctance [10, 26, 45] as shown schematically in Figure 3.1. An efficient magnetic actuator requires simultaneous optimization of interdependent variables, such as magnetic permeability, air gap reluctance, magnetic core reluctance, and mechanical stiffness of the moving structure. It can be shown that using the energy method and Maxwell's Equations [46], the force generated at the air gap is given by Equation (3.7)

$$|F_{magnetic}| = \frac{dE_{magnetic}}{dl} = \frac{1}{2}\left(\frac{NI}{R_m}\right)^2 \frac{dR_m}{dl} \tag{3.5}$$

where $$R_m = R_{m,core} + R_{m,gap} = \frac{l_{core}}{\mu_{core} A_{core}} + \frac{l_{gap}}{\mu_{gap} A_{gap}} \tag{3.6}$$

so that $$\lfloor F_{magnetic} \rfloor = \frac{1}{2\mu_0 A_{gap}} \left(\frac{NI}{R_{m,core} + R_{m,gap}} \right)^2 \tag{3.7}$$

where $F_{magnetic}$ is the gap magnetic force, $E_{magnetic}$ is the magnetic energy, l is the length, A is the cross-sectional area, N is the number of coil turns, R_m is the magnetic reluctance, μ is the magnetic permeability, and I is the coil current.

It can be seen that, to achieve large actuation magnetic force, *low* magnetic circuit reluctance and *large* amp-turns are favorable. To reduce magnetic reluctance requires using a high magnetic permeability material. If the reluctance of the magnetic circuit becomes dominated by the low-permeability material instead of the air gap reluctance, magnetic energy stored within the air gap would become negligible resulting an inefficient force generation. Therefore, magnetic actuators using low permeability material are inefficient and will consume a large coil power to generate moderate magnetic force. Other challenges are parasitic magnetic flux leakage losses, geometry constraints of MEMS devices, limited choices of thin-film materials available for micro-fabrication, and CMOS process compatibility.

3.2.4 Pneumatic Actuation

With an external pressure source, an on-chip micro-pump, or an on-chip gas/liquid chamber that has built-in heating elements to thermally raise pressure [47], pneumatic actuation is a legitimate option for MEMS actuators. However, few MEMS switches/relays have employed this actuation scheme [48] and there are reasons for that. First, the inherent complication with such an actuation scheme lies in the integration of pneumatic lines with electronic lines. Normally, electronically controlled micro-valves must be implemented to be the bridge between the electronics and the pneumatics, and this unnecessarily increases the complexity of the MEMS switch design. If an external pressure source is to be used, the packaging design must address the need for additional pneumatic connections. And if an on-chip heating chamber or a micro-pump is to be used as a built-in pressure source, the complexity of the switch design reaches a very undesirable level for a MEMS switch. Further, pneumatic actuation is in general slow compared with the electrical/mechanical time constant of the system.

There are a few advantages of the pneumatic actuation scheme, nevertheless. First of all, due to its non-electric nature, signal coupling between the electric lines and the pneumatic control channels are minimal. Additionally, for small-deflection situations in which materials behave elastically, there is a linear relationship between the actuation pressure and the displacement with no hysteresis. This linearity and the fact that only mechanical properties of materials need be considered in the design stage greatly simplify the analysis and modeling of the actuator's mechanical behavior. In some pressure control applications where pneumatic sources are part of the system, pneumatics becomes a natural choice for actuation, such as pressure switches. However, pneumatic actuation does *not* seem to be an appropriate option in automotive applications, considering that *12V* batteries are the only power source and there is *no* convenient pneumatic source available in a car for general distribution.

3.2.5 Shape-Memory Alloy Actuation

Utilization of the shape-memory effect of materials for actuation purposes is a recent development in micro-actuators [49] and has been realized in a few MEMS devices. By heating the shape-memory alloy (SMA) above the transformation temperature, or cooling the material below it, the alloy undergoes a change between its martensite and austenite phases, and deformation occurs due to such phase-transformation.

SMA actuation schemes can potentially provide high force, high displacements in a restricted space and are highly attractive in some applications where high actuation work density is demanded. An optimum use of the SMA requires specific designs with homogeneous spatial stress profiles for a given load pattern [50], which can be a non-trivial challenge. In terms of work output and power consumption, optimal SMA device thicknesses range between 30-100 μm, which are difficult to fabricate by traditional micro-fabrication technologies. Therefore, other technologies like cold-rolling for thickness adjustment, electrolytic photoetching and laser cutting for material removal has been used [51]. Actuation performance, hysteresis, slow response, and additional mechanical design for motion linearization are the disadvantages of the SMA actuation scheme.

In terms of automotive applications, SMA has a fatal drawback: the phase-transformation of most alloys occurs well *below* the 120°C temperature requirement in the automotive industry. As a result, an SMA scheme is *not* considered in the design of the MEMS switch.

3.2.6 Electrostatic Actuation

Electrostatic actuation is one of the most common force-generation schemes used in micro actuators. When an electric field is excited between two parallel plates, there will be an attractive force acting on both plates to bring them closer and minimize the electrical potential energy of the system. This electrostatic force is given by

$$f_{electrostatic} = -\frac{\partial U^*}{\partial g} \tag{3.8}$$

$$U_e^* = \frac{1}{2}CV^2 = \frac{\varepsilon_0 A V^2}{2g} \tag{3.9}$$

so that $$f_{electrostatic} = \frac{\varepsilon_0 A V^2}{2g^2} \tag{3.10}$$

where U_e* is the electrical co-energy in the system, C is the capacitance of the parallel plates, g is the gap separation distance between the plates, ε_0 is the dielectric constant of air (8.854×10^{-12} F/m), and V is the potential difference across the plates.

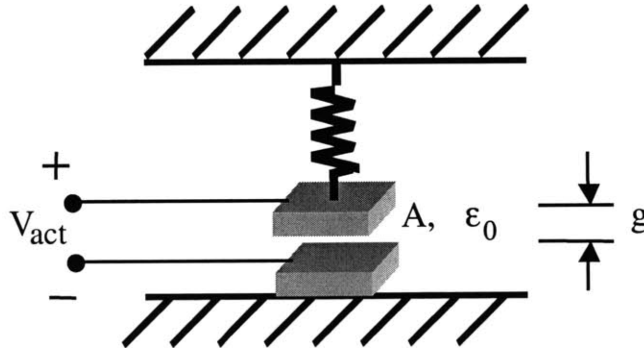

Figure 3.2 A schematic drawing of a micro electrostatic actuator

Thus, the electrostatic attractive pressure between two capacitor plates separated in air, neglecting the fringing effects on the periphery, is given by

$$p_{electriostatic} = \frac{f_{electrostatic}}{A} = \frac{1}{2}\varepsilon_0 E^2 \tag{3.11}$$

where E is the electrical field and $E = \frac{V}{g}$. For micron-sized air-filled gaps, the maximum electrical field before breakdown is approximately 10^8 V/m and therefore the maximum electrostatic pressure is limited to about 44kPa (≈ 6.5psi or 0.44 atm). In addition, for a fixed voltage, the electrostatic force or electrostatic pressure is inversely dependent on the separation

squared between the capacitor plates. This means that the electrostatic force drops significantly as the plates get farther apart. This force is also linearly proportional to the plate area. The requirement of a large area with a close gap separation for the purpose of generating force of significant magnitude imposes fabrication difficulties. Finally, if the allowable travel of the movable plate is larger than one third of the air gap, there will be a snap-through motion due to the unstable nature of electrostatic actuation. In order to release the movable plate from electrostatic seizure, the applied voltage has to reduce well below the voltage at which such snap-through motion occurs. This hysteresis can be avoided by restricting the displacement of the movable plate within g/3. However, the hysteresis snap-through motion can be favored in the MEMS switch operation for the consideration of higher actuation force.

3.2.7 Actuation Scheme of Choice: Electrostatics

Our choice of actuation mechanism for the MEMS switch is electrostatic actuation of a deformable diaphragm, with pneumatic actuation as a secondary means. Gas pressure actuation requires special packaging to assure air-tight sealing and is used here only as a supplemental tool for quantitative characterization of the diaphragm mechanics. With minor design modification, our switch is also applicable in pressure control applications that require pressure switches with tunable threshold pressures controlled by a voltage bias.

The design geometries and materials chosen for the MEMS switch are such that the diaphragm, under small deflection assumptions, has a linear relationship between the applied pressure, either electrostatic or pneumatic, and the diaphragm deflection.

Pull-in voltage

Consider the lumped parallel-plate spring-mass system shown in Figure 3.2. When a voltage under a certain threshold is applied, an electrostatic attractive force brings the plate closer to the ground while the displacement-induced mechanical restoring force balances the electrostatic force, and system equilibrium is reached when the two forces equate. However, the electrostatic and mechanical forces have different dependencies on the displacement of the plate, and when the voltage exceeds the threshold level, the mechanical force cannot balance the electrostatic force. The plate experiences a *positive* force gradient and accelerates away from that particular equilibrium point. This threshold voltage is the pull-in voltage. If the design of the contact gap separation is larger than one third of the design of the actuation gap, the MEMS switch would be electrostatically turned ON under an instability condition, which is advantageous for contact force

consideration. A closed-form expression for the pull-in voltage ($V_{pull\text{-}in}$) in the case of a clamped circular diaphragm [52] is

$$V_{pull-in} = \sqrt{\frac{\gamma_1 \sigma_0 E t g_0^{\ 3}}{(1-\nu^2)\varepsilon_0 a^2 f(\gamma_2, k, a)}} \tag{3.12}$$

where g_0 is the actuation gap separation, ε_0 is permittivity of air, γ_1= 1.55, γ_2= 1.65, k = $\sqrt{12(1-\nu^2)/Et^2\sigma_0^{\ 2}}$, and $f(\gamma_2, k, a) = 1 + 2[1-\cosh(\gamma_2 ka/2)]/(\gamma_2 ka/2)\sinh(\gamma_2 ka/2)$. If the design of the diaphragm mechanics is such that it is dominated by stress, then Equation (3.12) can be approximated as

$$V_{pull-in} = \sqrt{\frac{\gamma_1 \sigma_0 t g_0^{\ 3}}{\varepsilon_0 a^2}}. \tag{3.13}$$

To switch off electrostatically, the actuation voltage must drop below a voltage significantly less than $V_{pull\text{-}in}$ due to the hysteretic nature of electrostatic actuation.

Release voltage

Both electrostatic pull-in and release take place in a *snap-through* fashion. This is because both pull-in and release correspond to the transition between *stable* and *unstable* equilibrium solutions of the force-balancing equations of Newton's first law. However, unlike electrostatic pull-in, there is no closed-form analytical expression for the prediction of electrostatic release voltage available for distributed mechanical systems. The electrostatic release voltage can be numerically obtained with the help of finite element software capable of analyzing coupled electromechanical systems [53]. In this thesis, an approach using lumped model approximation is demonstrated in 3.7.2 for the estimation of the release voltage in the design example at the end of this chapter.

3.3 Design of Mechanical Structure

3.3.1 Overview

One of the most important tasks in the design of a MEMS transducer is to understand the mechanics of the movable structure, as it serves as the link to the mechanical domain in a multi-energy-domain system. Commonly seen designs of mechanically movable structures in MEMS devices are fix-fix beams, cantilever beams, clamped diaphragms, and torsional plates, among

others. Because of the desired electrostatic actuation scheme, it is preferred to have a large actuation area and therefore a *planar* mechanical structure is favored. Additionally, in order to take advantage of pneumatic actuation for the experimental study of diaphragm mechanics analysis, the favored design would be some movable structure that can be deflected by static air pressure. Clamped diaphragms would be the choice given such objectives.

Elasticity

Single-crystal silicon and its ceramics, such silicon nitride and silicon carbide, are considered brittle materials, which yield catastrophically rather than deform plastically when bearing stresses exceeding their material yielding strengths at room temperature. The brittle to ductile transition temperature for undoped silicon is 660°C [54]. The maximum stress, σ_{max}, in a clamped diaphragm under uniform pressure loading p occurs at the edge and is given by

$$\sigma_{\max} = \frac{3}{4}\frac{pa^2}{h^2} \tag{3.14}$$

where a and h are the diaphragm radius and thickness, respectively [55]. If this maximum stress is kept under the yielding strength, it is safe to say that the brittle material is within the elastic range. For example, the yielding strength for silicon is 7 *Gpa* [4], a clamped silicon diaphragm of *1200 μm* radius and *10 μm* thickness will go beyond elastic limit at a pressure load of *648 kPa*, more than 6 times the atmospheric pressure.

Bulk Micromachining

A good mechanical design of a MEMS device cannot be brought about without taking fabrication constraints into consideration. In general, there are two predominant micro fabrication technologies used in creating micron-scale movable structures, namely surface-micromachining technologies and bulk-micromachining technologies.

In bulk micromachining, MEMS mechanical structures are formed by selectively etching away single-crystalline substrates. Anisotropic wet etching and dry DRIE (deep reactive ion etching) techniques are the two commonly used silicon-etching methods. In many cases, bulk-micromachined devices use two-sided processing with one side exposed to the environment and the other side enclosed by wafer bonding or packaging. Simple mechanical structures such as diaphragms and cantilever beams are being commercially fabricated using such technologies.

There are various bonding techniques which can be performed at the wafer level or chip level to stack samples and form more complicated microstructures. Extreme surface cleanliness is crucial to successful wafer bonding and at times the alignment of the bonding pair can be nontrivial.

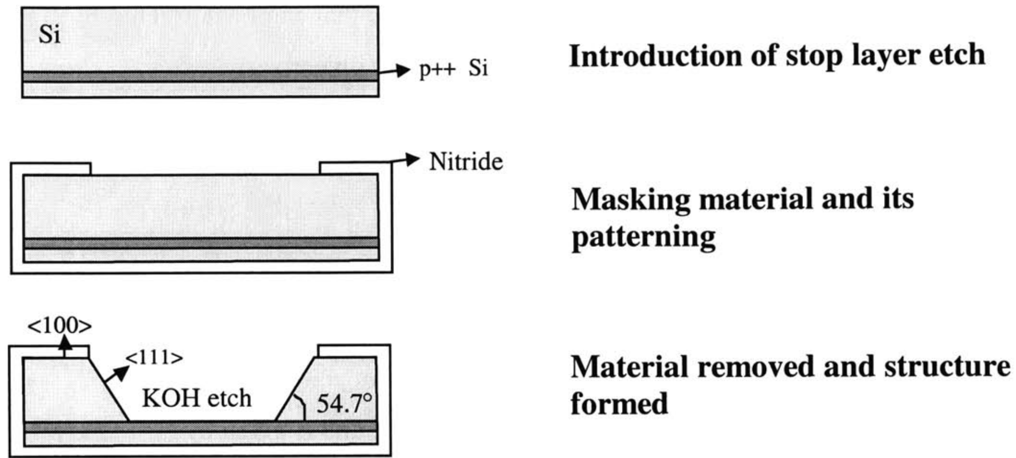

Figure 3.3 Typical process flow of bulk-micromachining a diaphragm

Figure 3.3 illustrates an example of using bulk-micromachining to create a diaphragm structure. A (100) silicon wafer is heavily boron-doped on one side to define the diaphragm, and then the wafer is protected by a thin layer of nitride except where silicon will be deep-etched. Through etching in a heated alkaline solution, such as potassium hydroxide, sloped sidewalls will be formed along the {111} plane while the <100> etch front progresses until stopping at the *p++* layer. Stripping the protective nitride, which is shown in the figure, leaves a clamped silicon diaphragm structure.

Surface Micromachining

Surface micromachined structures are constructed entirely from deposited thin films. A variety of thin films are available for the structural materials, such as silicon dioxide, silicon nitride, single-crystal or polycrystalline silicon, aluminum, and some organic materials. To form a freestanding structure using surface micromachining, there must exist (1) processing technologies to deposit and pattern structural layers and sacrificial layers, and (2) etchants that can preferentially remove sacrificial materials without attacking structural materials too much. Figure 3.4 shows an example of surface-micromachining: the creation of a beam. First a spacer layer, or sacrificial layer is deposited and patterned on a substrate, and then a structural layer is deposited on top and patterned. Finally, the structure is released by the selective removal of the spacer material leaving a free structure.

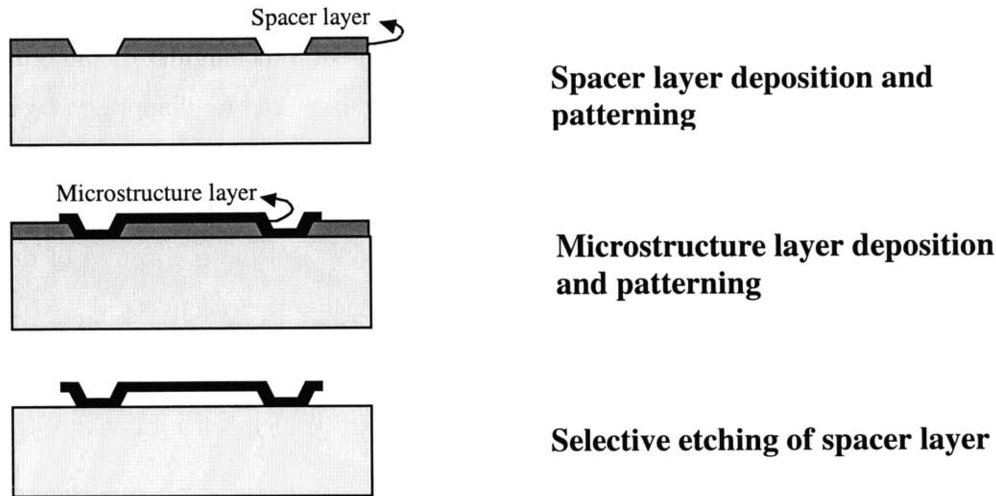

Figure 3.4 Typical process flow of surface-micromachining a beam

One of the challenges in the early stages of the structural design of MEMS devices is to overcome the limitations of micro-machining technologies since arbitrary 3-D structure *cannot* be micro-fabricated. Neither bulk- nor surface-micromachining technologies render true 3-D structures. Only a certain set of 2½-D structures can be realized. In addition to the geometric constraints, there are limited materials to choose from and limited fabrication technologies to process the materials, although efforts to enlarge this set of available geometries and materials are on going research activities all over the world.

Bulk-micromachined structures are normally bigger than surface-micromachined ones. Therefore, one of the advantages of surface-micromachining is in its improved device density. Also, surface-micromachining permits the fabrication of more structurally complex devices by stacking and patterning layers of thin films while multi-layered bulk-micromachined structures are more difficult to construct. However, there are reasons why bulk micromachining is still the more dominant technology in industry. First, single-crystal materials used in bulk micromachining have well-defined properties in contrast to those have amorphous or polycrystalline thin films, hence yielding devices with more reproducible characteristics. In addition, many thin film materials used in surface micromachining often have internal residual stresses that can affect the mechanical integrity of the devices. Under these considerations, bulk-micromachining is preferred to micro-fabricate the MEMS switch in this thesis.

Circular or Rectangular Diarphagm Design?

As for the geometric shape of the clamped diaphragm, two natural choices are a circular-shaped diaphragm and a rectangular-shaped diaphragm. The advantages of a rectangular diaphragm design are easy mask layout design and low-cost deep silicon wet-etch technology (potassium

hydroxide etch [56]) readily available. However, the analysis of the mechanics is usually left to finite element analysis because the theoretical mechanics analysis of a rectangular diaphragm is relatively complicated compared with that of a circular diaphragm. A circular diaphragm design will greatly reduce the complexity level of the mechanics analysis because of the axisymmetric property. Well-developed theories can be found in solid mechanics textbooks and other references for a variety of axisymmetric diaphragm structures [55]. But the realization of deep silicon etch of non-rectangular shapes usually requires more expensive equipment such as a deep RIE silicon etcher.

Our design will be a circular diaphragm design due to the simplicity of its mechanics analysis.

3.3.2 Bossed Circular Diaphragm

Two types of circular diaphragm structures have been considered in this thesis. One is an annular diaphragm with a central boss structure; the other is a circular diaphragm of uniform thickness. Discussion and analysis of the former structure design will be given here in 3.3.2 and that of the latter will be given in 3.3.3.

If the vertical deflection is much smaller than the annular diaphragm thickness, which, in turn, is much smaller than the thickness of the central boss, then the annular diaphragm part may behave like a linear spring and the analysis of such a structure can be closely approximated with that of a circular rigid plate with a linear spring. Such approximation will greatly simplify the electrical capacitor model of the device as well as the mechanical model of the movable structure. As depicted in Figure 3.5, the structure of an annular diaphragm with a rigid center boss, when actuated, will move like a plunger with most of the material strain confined within the annular diaphragm as the central boss moves rigidly. Electrically, the device can be modeled as a parallel-plate capacitor with a variable gap, and the effective capacitor area would be the boss area especially if the central gap is much smaller than the outer gap. Mechanically, such a movable structure under the small deflection assumption would behave as a piston with a linear spring. The task is to quantitatively understand the relationship between applied actuation pressure and the resulting deflection, or equivalently the spring constant.

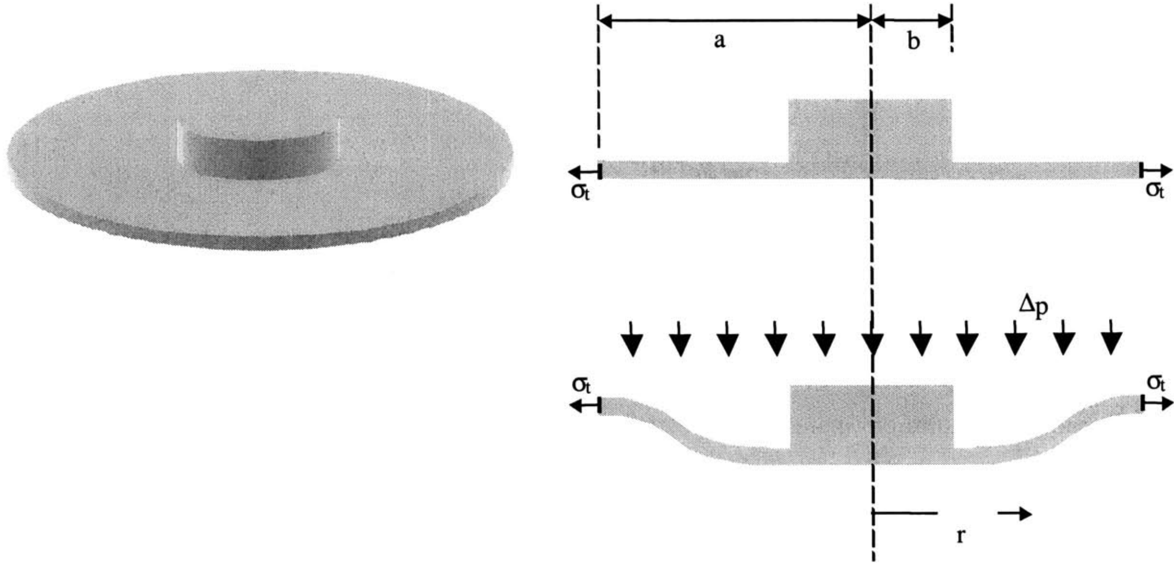

Figure 3.5 Drawing of annular diaphragm with central boss

Timoshenko Plate Theory

The structure of an annular diaphragm with a rigid boss has been presented in other MEMS devices [57, 58]. The following paragraphs discuss the mechanical analysis of such a structure. Note that effects of shear stresses are not taken into account, as they are considered insignificant in diaphragms with thickness-to-radius ratios of less than 0.15 [59]. Because of the axisymmetry of a circular diaphragm, the central deflection, δ, of the diaphragm depends only on the radial distance, r, from the center. Consider the case when the diaphragm is subjected to a uniform transverse pressure, Δp, and a uniform initial tensile stress, σ_t, applied normal to the periphery and in the plane of the diaphragm. The analysis is based on the classic small-deflection theory and starts with the following ordinary differential equation governing the slope, ϕ, of the deformed diaphragm [55].

$$\frac{d^2\phi}{dr^2}+\frac{1}{r}\frac{d\phi}{dr}-(\frac{N_t}{D}+\frac{1}{r^2})\phi=-\frac{q(r)}{D} \tag{3.15}$$

where ϕ is the slope the deformed diaphragm, q is the radial shearing force per unit length in the cross section at the radial position r due to transverse load along; D is the flexural rigidity of the diaphragm; and N_t is the in-plane peripheral tension per unit length. Furthermore,

$$\phi=-\frac{dw(r)}{dr} \tag{3.16}$$

$$D = \frac{Eh^3}{12(1-\nu^2)} \tag{3.17}$$

$$q(r) = \frac{\Delta p}{2\pi}\int_0^r 2\pi r dr = \frac{1}{2}\Delta p r \tag{3.18}$$

$$N_t = \sigma_t h = \varepsilon_t \frac{E}{(1-\nu)} h \tag{3.19}$$

where w is the deflection of the diaphragm, E and ν are the Young's modulus and Poisson's ratio of the annular diaphragm material, respectively, h is the thickness of the diaphragm, and ε_t is the residual in-plane tensile strain. The general solution of Equation (3.15) takes the form below

$$\phi(r) = c_1 I_1(\zeta \frac{r}{a}) + c_2 K_1(\zeta \frac{r}{a}) + \phi_p(\frac{r}{a}) \tag{3.20}$$

where c_1 and c_2 are constants which depend on boundary conditions, I_1 is the modified Bessel function of the first kind of order one, K_1 is the modified Bessel function of the second kind of order one, ϕ_p is a particular solution, and

$$\zeta \equiv \frac{N_t a}{D} = 12\varepsilon(1+\nu)\left(\frac{a}{h}\right)^2 \tag{3.21}$$

is a dimensionless quantity designated as the stiffness ratio.

If $\zeta^2 > 100$, the diaphragm has no significant bending stiffness and the transverse load is solely counteracted by the membrane stiffness. In this range, the diaphragm can be modeled as a membrane. If $\zeta^2 < 1$, membrane stiffness can be ignored and the diaphragm can modeled as a plate. Typical values of the stiffness ratio for micro-machined structures are in the range from 1 to 100, i.e., the transition-range from membranes to plates.

The particular solution is chosen to be

$$\phi(r/a) = \frac{\Delta p\, a}{2N_t}(r/a) = \frac{\Delta p\, a^3}{24\sqrt{3}D}\frac{12\sqrt{3}}{\zeta^2}(r/a) = \phi_o \frac{12\sqrt{3}}{\zeta^2}(r/a), \text{ for } b \le r \le a \tag{3.22}$$

where b denotes the outer radius of the boss, $\phi \equiv \Delta p a^3 / 24\sqrt{3}D$ denotes the maximum slope occurring at the inflection point of a flat stress-free diaphragm subjected to transverse pressure Δp. It is evident that the slope is zero for $0 \le r \le b$. The constants c_1 and c_2 can be found after formulating the boundary conditions, which for a rigidly clamped diaphragm are

$$\phi(b/a) = 0$$
$$\phi(a/a) = 0 \tag{3.23}$$

Introducing the above boundary conditions into Equation (3.20), leads to the general solution

$$\phi(\frac{r}{a}) = \phi_0\left(\frac{12\sqrt{3}}{\zeta^2}\right)\left(\frac{r}{a} - \frac{\left[K_1(\zeta\frac{b}{a}) - \frac{b}{a}K\ \ (\zeta)\right]I_1(\zeta\frac{r}{a}) + \left[\frac{b}{a}I_2(\zeta) - I_2(\zeta\frac{b}{a})\right]K_1(\zeta\frac{r}{a})}{I_1(\zeta)K_1(\zeta\frac{b}{a}) - I_1(\zeta\frac{b}{a})K_1(\zeta)}\right) \tag{3.24}$$

The expression for the transverse deflection w(r/a) can be obtained by integrating the above equation with respect to r/a,

$$w(r/a) = -a\int\phi(r/a)d(r/a)$$
$$= c_3 - \left(\frac{\Delta pa^4}{64D}\right)\left(\frac{32}{\zeta^2}\right)\left(\frac{1}{2}\left(\frac{r}{a}\right)^2 - \frac{1}{\zeta}\frac{\left[K_1(\zeta\frac{b}{a}) - \frac{b}{a}K_1(\zeta)\right]I_0(\zeta\frac{r}{a}) + \left[\frac{b}{a}I_1(\zeta) - I_1(\zeta\frac{b}{a})\right]K_1(\zeta\frac{r}{a})}{I_1(\zeta)K_1(\zeta\frac{b}{a}) - I_1(\zeta\frac{b}{a})K_1(\zeta)}\right) \tag{3.25}$$

where I_0 is the modified Bessel function of the first kind of order 0, K_0 is the modified Bessel function of the second kind of order 0 and c_3 is a constant. The second boundary condition for a clamped edge is $w = 0$ at $r = a$, and it determines the unknown constant c_3.

$$c_3 = \left(\frac{\Delta pa^4}{64D}\right)\left(\frac{32}{\zeta^2}\right)\left(\frac{1}{2}\left(\frac{r}{a}\right)^2 - \frac{1}{\zeta}\frac{\left[K_1(\zeta\frac{b}{a}) - \frac{b}{a}K_1(\zeta)\right]I_0(\zeta) + \left[\frac{b}{a}I_1(\zeta) - I_1(\zeta\frac{b}{a})\right]K_1(\zeta)}{I_1(\zeta)K_1(\zeta\frac{b}{a}) - I_1(\zeta\frac{b}{a})K_1(\zeta)}\right) \tag{3.26}$$

An important design parameter of a bossed diaphragm is the rigidity ratio b/a, which is the ratio of the boss and diaphragm ratio. Two other independent design parameters are the diaphragm aspect ratio *a/h*, and the residual strain, ε_r. The latter two parameters can sometimes conveniently be combined into the stiffness ratio, ζ^2, as defined in Equation (3.21). In the following discussions, the performance characteristics of the bossed diaphragm will be evaluated as a function of these parameters.

Now we are ready to investigate and discuss the effects of stress on the deflection of such a structure. Due to the transverse pressure Δp, the deflection of the diaphragm will take an S-shape profile, as shown in
Figure 3.5. It is evident that the maximum deflection will occur at the center of the circular diaphragm. To compare the maximum deflection of a bossed diaphragm with in-plane tension with the maximum deflection of a flat stress-free diaphragm, the maximum deflection w_o is written as

$$w_0 = \left(\frac{\Delta p a^4}{64D}\right) g(\zeta, b/a) \tag{3.27}$$

where $(\Delta p a^4/64D)$ is the maximum deflection of a uniform-thickness stress-free diaphragm, clamped around the perimeter and subjected to a transverse pressure Δp [55], and the function g is given by

$$g(\zeta, b/a) = \left(\frac{32}{\zeta^2}\right)\left[\frac{1}{2} - \frac{1}{2}\left(\frac{b}{a}\right)^2 - \frac{1}{\zeta}\frac{\left[K_1(\zeta\frac{b}{a}) - \frac{b}{a}K_1(\zeta)\right]\left[I_0(\zeta) - I_0(\zeta\frac{b}{a})\right] - \left[\frac{b}{a}I_1(\zeta) - I_1(\zeta\frac{b}{a})\right]\left[K_0(\zeta) - K_0(\zeta\frac{b}{a})\right]}{I_1(\zeta)K_1(\zeta\frac{b}{a}) - I_1(\zeta\frac{b}{a})K_1(\zeta)}\right] \tag{3.28}$$

In a similar way as discussed in [60] for flat diaphragms with in-plane loads, the function g can be approximated for bossed diaphragm as

$$g(\zeta, \frac{b}{a}) \approx \frac{1 - \left(\frac{b}{a}\right)^4 - 4\left(\frac{b}{a}\right)^2 \ln\left(\frac{1}{(r/a)}\right)}{1 + N_t/N_{cr}} \approx \frac{1 - \left(\frac{b}{a}\right)^4 - 4\left(\frac{b}{a}\right)^2 \ln\left(\frac{1}{(r/a)}\right)}{1 + (\zeta/\zeta_{cr})^2} \tag{3.29}$$

where N_{cr} and $\zeta_{cr} \equiv N_{cr}a^2/D$ denote the critical load for buckling and stiffness ratio, respectively. The critical stiffness ratio can be determined by letting the denominator of Equation (3.28) be zero as expressed below

$$J_1(\zeta)Y_1(\zeta\frac{b}{a}) - J_1(\zeta\frac{b}{a})Y_1(\zeta) = 0 \quad \Rightarrow \quad \zeta = \zeta_{cr}$$

where J_1 is the Bessel function of the first kind of order one and Y_1 is the Bessel function of the second kind of order one. Performing a curve fit using a cubic polynomial yields the approximated solution of the critical stiffness of a circular bossed diaphragm below

$$\zeta_{cr} \approx \frac{\zeta_{cro}}{1 - 0.44918\left(\frac{b}{a}\right) - 2.9138\left(\frac{b}{a}\right)^2 + 2.5213\left(\frac{b}{a}\right)^3} \tag{3.30}$$

where $\zeta_{cro}=14.682$ is the critical stiffness ratio of a circular flat diaphragm [55]. The function $g(\zeta, b/a)$ is a dimensionless quantity and is completely determined by the stiffness ratio and the rigidity ratio. A plot of g *vs.* ζ^2 is shown in Figure 3.6, where ζ is the stress ratio as defined in Equation (3.21).

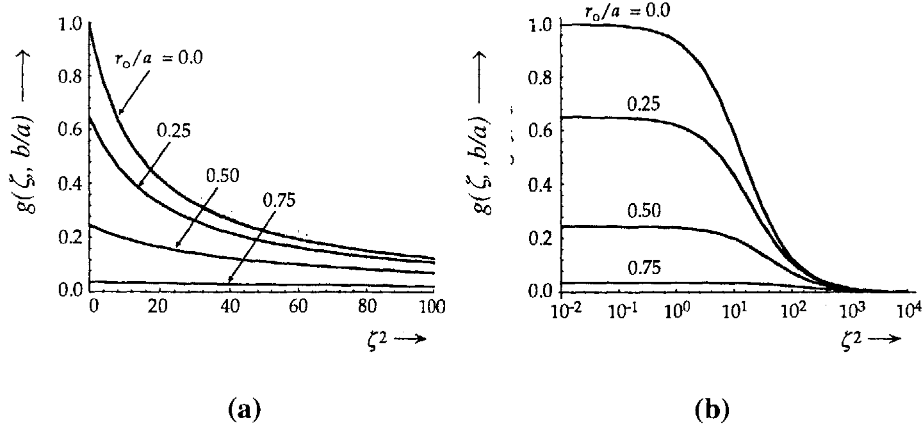

Figure 3.6 Plot of deflection correction factor due to stress, g, as a function of ζ^2 [57]. See Equations (3.28) and (3.29). (a) ζ^2 in linear scale, and (b) ζ^2 in log scale.

As both the stiffness ratio and the rigidity ratio approach zero, the ratio g approaches unity. Higher values of both the stiffness ratio and the rigidity ratio will lower the quantity g. The stiffness contribution brought about by the bossed over the non-bossed diaphragm is expressed by the numerator of Equation (3.30). The denominator of Equation (3.30) represents the stiffness contribution due to the in-plane initial tension. It is pointed out that Figure 3.6 is a little misleading. It suggests that an increase of the stiffness ratio results in a decrease of the maximum deflection. This is true as long as the increase of the stiffness is a result of a *higher in-plane tension*. If on the other hand, the increase of the stiffness ratio is a result of a *higher aspect ratio*, *a/h*, the maximum deflection w_o will increase, while the ratio g will decrease.

The bossed diaphragm structure is a *preferred* design for the MEMS switch device because the motion of the central boss can be modeled as a rigid body and the continuous diaphragm structure can be approximated as a discrete spring-mass system. In addition to the simplification in modeling, it is also advantageous that the central boss, when it touches other objects, does *not* conform to the topography of other objects and thereby concentrated contact force can be achieved. However, due to unexpected fabrication difficulties to be explained in Chapter 4, an alternative diaphragm structure of uniform thickness is proposed and discussed in the next section.

3.3.3 Uniform-Thickness Circular Diaphragm

The second type of movable structure considered in this thesis is a clamped circular diaphragm of *uniform* thickness. A uniform thickness design greatly reduces the complexity of the mechanics

analysis as well as the fabrication of the device. In this section, the analytical model of the diaphragm load-deflection behavior will be derived first through Timoshenko plate theories [55], and secondly through an energy minimization approach [61].

The discussions of Timoshenko plate theory starts with force and moment balance of an infinitesimal plate element and ends with an expression for plate deformation primarily due to bending. The effect of residual stress is incorporated into the deformation expression as a modifier. This analysis provides the buckling stress given the diaphragm geometry in (3.38).

Timoshenko Plate theory

In Timoshenko plate theory, the discussion of plate mechanics is grouped into three cases according to the deflection of the plate in comparison with its other dimensions. These three cases are, (1) thin plate with small deflection, (2) thin plate with large deflection, and (3) thick plate.

The device structure of interest here will have a relatively high radius-to-thickness ratio, $a/t >> 1$, therefore case (3) does not apply. Therefore, our discussion can reasonably be restricted under thin plate assumption and will not consider the shearing stress factor due to plate thickness. This leaves us with cases (1) and (2). The difference between the two thin plate cases lies in the stretching effects in the middle plane of the diaphragm. In case (1), thin plate with small deflections, the stress in the middle plane of the plate is assumed to be neutral, while in case (2), thin plate with large deflection, non-negligible stretching effects in middle plane of the diaphragm must be taken into consideration.

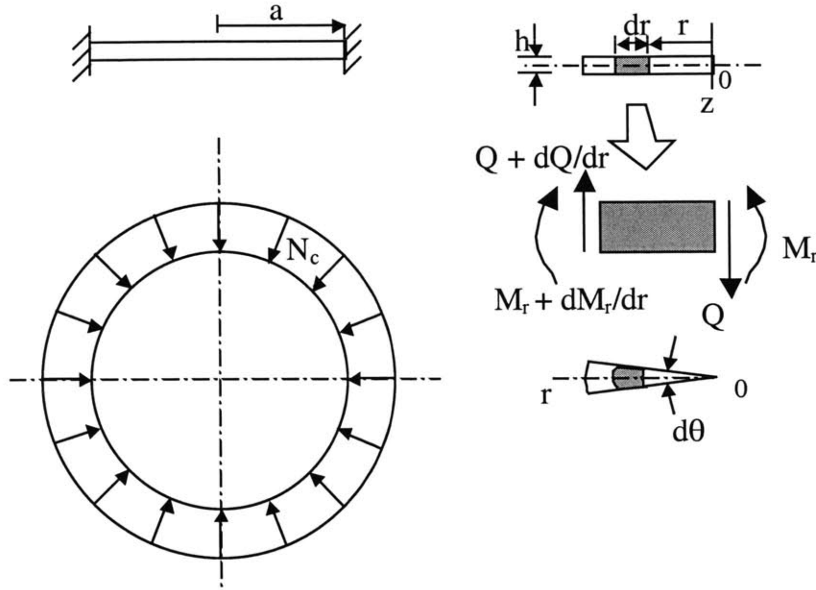

Figure 3.7 Moment equilibrium of a plate element (vertical deflection and slope not shown)

The diaphragm design of the MEMS switch in this thesis is such that diaphragm deflection is *not* necessarily much less than the diaphragm thickness. This implies that it should belong to the second case of thin plates with large deflections. However the discussion here will assume that the stretching of the middle plane in the diaphragm can still be ignored and, therefore, limit our discussion to case (1), thin plate with small deflection. Later in the energy method, this assumption will be justified, as the diaphragm is so highly tensile stressed by design that the stretching effects as well as bending effects both become negligible. By assuming small deflection, the diaphragm analysis can be carried out without considering the correction factor usually used to include the strain of the middle plane of the plate.

The discussion of a clamped thin circular plate of uniform thickness under the combined action of uniform pressure and residual compressive stress [55] starts with a differential equation for a circular plate similar to Equation (3.16). Owing to the slope, ϕ, of the deformed plate, the radial compression due to residual stress at the edge of the plate, N, gives a transverse component, $N\,d\phi/dr$, which must be added to the shearing force Q due to the lateral stress; see Figure 3.7. Hence, the modified differential equation becomes,

$$\frac{d^2\phi}{dr^2}+\frac{d\phi}{rdr}+\left(\frac{k^2}{a^2}-\frac{1}{r^2}\right)\phi=-\frac{Q}{D} \tag{3.31}$$

in which

$$k^2 = \frac{N_c a^2}{D}. \tag{3.32}$$

The general solution of Equation (3.31) is of the form

$$\phi = C_1 J_1\left(\frac{kr}{a}\right) + \phi_0 \tag{3.33}$$

where J_1 is the Bessel function of first kind of order one, ϕ_0 is a particular solution of Equation (3.31) depending on Q, and C_1 is the integration constant depending on boundary conditions of the plate. In the case of uniform load density, q, take the particular solution to be

$$\phi_0 = -\frac{qa^2 r}{2k^2 D} = -\frac{qr}{N_c} \tag{3.34}$$

and therefore

$$\phi = \frac{dw}{dr} = C_1 J_1\left(\frac{kr}{a}\right) - \frac{qr}{N_c}. \tag{3.35}$$

By integration of the Equation (3.35), it follows that the solution of the deflection, w, is

$$w = \frac{C_1 a}{k} J_0\left(\frac{kr}{a}\right) - \frac{qr^2}{4N_c} + C_2 \tag{3.36}$$

where J_0 is the Bessel function of first kind of order zero and C_2 a second integration constant. The clamped boundary conditions at the edge of the plate require $\phi(a)=0$ and $w(a)=0$ which can be used in calculations for constants C_1 and C_2. The final form of the solution can be expressed as

$$w(q,r,N_c) = \frac{qa^4\left[J_0\left(\frac{kr}{a}\right) - J_0(k)\right]}{2k^2 J_1(k) D} - \frac{qa^2(a^2 - r^2)}{4k^2 D}. \tag{3.37}$$

The deflection $w(q,r,N_c)$ becomes infinite when $J_1(k)$ in the denominator of the above solution becomes zero.

Denote the zeros of $J_1(k)$ in order of their magnitude as j_1, j_2, j_3, j_4,..., etc. When $k=j_1$, the corresponding N_c is the critical compressive stress. When the compressive stress rises beyond this value, a buckling instability occurs at

$$N_{critical} = \frac{Dj_1^2}{a^2} \tag{3.38}$$

Now, for the function $J_1(k)$, we have the following expression

$$J_1(k) = \frac{k}{2}\left(1 - \frac{k^2}{j_0^2}\right)\left(1 - \frac{k^2}{j_1^2}\right)\cdots \tag{3.39}$$

in which $j_1=3.83171$, $j_2=7.01559$, ... Considering the fact that $k<j_0<j_1<...$, the terms k/j_i^2 can be neglected starting from the second parentheses, $i \geq 1$. With this approximation, and the relationship

$$\frac{k^2}{j_0^2} = \frac{N_c}{N_{critical}} \tag{3.40}$$

which is derived from Equations (3.32) and (3.38), an approximate expression for the Bessel function of the first kind of order one is

$$J_1(k) = \frac{k}{2}(1-\alpha) \tag{3.41}$$

where

$$\alpha \equiv \frac{N_c}{N_{critical}} \tag{3.42}$$

Taking advantage of this approximation, we can obtain an expression for the central deflection ($r=0$) of the clamped circular plate to be approximately

$$w_{(r=0)} = \frac{w_{q(r=0)}}{1-\alpha} \tag{3.43}$$

where w_q is the central deflection of a stress-free circular plate due to load Q only. The beauty of this approximation method is that we can calculate the plate deflection as if it is stress-free and the residual stress effect comes in as a scaling factor of $1/(1-\alpha)$. If we take a another look at Equation (3.43), it can be seen that as the compressive stress N_c gets closer to $N_{critical}$, the buckling limit, α gets closer to unity, and a larger plate deflection results. Therefore, the presence of the compressive residual stress has a decreasing effect on the plate stiffness. On the other hand, what if the residual stress is *tensile*? Timoshenko's plate theory suggests that this approximation method can still apply to the tensile stress case with a minor modification. [55]

$$w_{(r=0)} = \frac{w_{q(r=0)}}{1+\alpha'} \quad (3.44)$$

where

$$\alpha' \equiv \frac{N_t}{N_{critical}} \quad (3.45)$$

As expected, the presence of tensile residual stress will have a plate stiffening effect as the central deflection is scaled down by a factor of $1/(1+\alpha')$.

There is a great deal of approximation in this mathematical derivation made to attain the diaphragm deflection under combined effects of the bending, stretching, and residual-stress. However, their individual contributions to the stiffness of the diaphragm is *not* explicitly formulated. In the next few paragraphs, a energy approach starts with a estimation of the diaphragm deflection profile and ends with a pressure balance equation using principle of virtual work is presented.

Energy method

A second approach to the load-deflection behavior analysis is carried out using an energy method [55, 61]. Only the circular thick-film diaphragm case is discussed here. A few assumptions will be made to carry out this analysis. First, plane stress is assumed. That is, the stress is entirely in the plane of the diaphragm as the diaphragm is deflected. Second, the residual stress of the diaphragm is constant and is bi-axially distributed in the plane of the diaphragm. Residual stress is also assumed to be uniform throughout the thickness of the diaphragm. Finally, the diaphragm is assumed to stay in a linear elastic regime as it is deflected.

The first step of this energy minimization approach is to calculate the total strain energy of a deflected structure by assuming the shape of the deformation. For a thick-film model, the strain functions for the thick deflected film are thickness dependent, i.e. the strain on the top surface of the diaphragm can be different from that on the bottom surface. Therefore, the displacement in the r-direction is assumed to be a function of the z-axis coordinate and the z-direction deflection is assumed to be invariant across the thickness so that the lines perpendicular to the diaphragm surface across the thickness remain perpendicular to the surface after deflection, as shown in Figure 3.8.

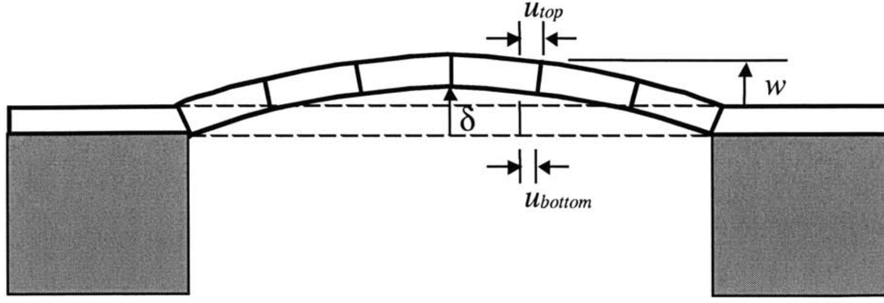

Figure 3.8 Diaphragm deflection in a thick-film model

To generate a z-dependent function for the displacement function, it is assumed that the difference of lateral displacement in z-direction is a linear function of z and is proportional to the partial derivative of the vertical displacement w with respect to r. Therefore the displacement functions w and u are assumed to have the expressions

$$u = r(a-r)(k_1 + k_2 r) - z\frac{dw}{dr} = r(a-r)(k+kr) + \frac{2zr\delta}{a^2} \tag{3.46}$$

$$w = \delta\left(1 - \frac{r^2}{a^2}\right) \tag{3.47}$$

where δ is the maximum deflection at the center ($r=0$) of the circular diaphragm. In the case of a very thin diaphragm, these displacement functions can still be employed with z set to zero. The strain in the r-direction, e_r, and the strain the transverse direction, e_t, are given by

$$\varepsilon_r = \frac{\partial u}{\partial r} + \frac{1}{2}\left(\frac{dw}{dr}\right)^2 = k_1 a + 2(k_2 a - k_1)r - 3k_2 r^2 + \frac{2z\delta}{a^2} + \frac{2r^2\delta^2}{a^4} \tag{3.48}$$

$$\varepsilon_t = \frac{u}{r} = (a-r)(k_1 + k_2 r) + \frac{2z\delta}{a^2} \tag{3.49}$$

The strain energy due to the elastic stretching of the membrane becomes

$$V_{elastic} = \frac{\pi E}{1-\nu^2}\int_{-t/2}^{t/2}\int_0^a \left(\varepsilon_r^2 + \varepsilon_t^2 + 2\nu\varepsilon_r\varepsilon_t\right) r\,dr\,dz. \tag{3.50}$$

Substituting the strain terms into Equation (3.50) and carrying out the integration yields

$$V_{elastic} = \frac{\pi Et}{1-\nu^2}\left(\frac{k_1^2 a^4}{4} + \frac{3k_1 k_2 a^5}{10} + \frac{7k_2^2 a^6}{60} + \frac{(\nu-3)k_1 a\delta^2}{5} + \frac{2(\nu-3)k_2 a^2\delta^2}{15} + \frac{2\delta^4}{3a^2}\right) + \frac{\pi Et}{1-\nu}\left(\frac{t\delta^2}{3a^2}\right). \quad (3.51)$$

The strain energy due to the residual stress is,

$$V_{residual} = 2\pi\sigma_0 \int_{-t/2}^{t/2}\int_0^a (\varepsilon_r + \varepsilon_t) r\,dr\,dz \quad (3.52)$$

Performing the integration yields

$$V_{residual} = \pi\sigma_0 t\delta^2 \quad (3.53)$$

This total strain energy consists of the elastic stretching contribution and the residual stress contribution and thus

$$V = V_{eleastic} + V_{residual} \quad (3.54)$$

The constants, k_1 and k_2, can now be determined using the assumption that the total strain energy of the diaphragm at the equilibrium position is a minimum energy. Hence, from the principle of the virtual displacement, it follows that

$$\frac{\partial V_{system}}{\partial k_1} = \frac{\partial V_{system}}{\partial k_2} = 0 \quad (3.55)$$

$$\frac{\partial V_{system}}{\partial \delta} = 0 \quad (3.56)$$

where the system potential energy function V_{system} is given by

$$V_{system} = V - \int_A Pwrdrd\theta \quad (3.57)$$

Differentiation of Equation (3.57) and use of Equation (3.56) yields

$$\frac{\partial V}{\partial \delta} = \frac{\pi Pa^2}{2} \quad (3.58)$$

Next, from Equations (3.55), two linear equations for k_1 and k_2 are obtained,

$$\begin{aligned} 5k_1 a^3 + 3k_2 a^4 + 2(\nu-3)\delta^2 = 0 \\ 9k_1 a^3 + 7k_2 a^4 + 4(\nu-3)\delta^2 = 0 \end{aligned} \quad (3.59)$$

and their solutions are

$$k_1 = \frac{(3-\nu)\delta^2}{4a^3} \qquad k_2 = \frac{(3-\nu)\delta^2}{4a^4} = \frac{k_1}{a} \tag{3.60}$$

Now, substituting Equations (3.51), (3.53), and (3.60) into Equation (3.54) yields the expression for total strain energy,

$$V = \frac{\pi \varepsilon t \delta^4 (7-\nu)}{24a^2(1-\nu)} + \frac{\pi E t^2}{(1-\nu)}\left(\frac{t\delta^2}{3a^2}\right) + \pi \sigma_0 t \delta^2 \tag{3.61}$$

From the principle of virtual displacement, it follows that

$$\frac{\partial V}{\partial \delta} = \frac{\pi P a^2}{2} \tag{3.62}$$

Finally, substituting Equation (3.61) into Equation (3.62), the pressure-deflection relationship of a clamped circular diaphragm takes the form,

$$P = \frac{Et}{(1-\nu)}\left(\frac{7-\nu}{3a^4}\right)\delta^3 + \frac{4Et^3\delta}{3a^4(1-\nu)} + \frac{4\sigma_0 t\delta}{a^2} \tag{3.63}$$

Equation (3.63) can also be viewed as an equilibrium equation in which the term on the left side is the applied external pressure and the three terms on the right are the resultant stresses whose sum balances the external pressure. The first term on the right is due to the stretching of the middle plane and has a non-linear P-δ relationship. The second term on the right is due to diaphragm bending and it has a higher dependency on thickness. This is why deformations of thicker diaphragms are usually dominated by bending effects. The third term has a σ_o in its numerator and is directly linked to residual stress.

Note that this approach is very forgiving in the initial displacement profile guess. The energy method provides the contribution of the bending, stretching, and residual-stress of the diaphragm, individually as formulated in Equation (3.63), but does *not* have the deflection profile since it only considers the maximum deflection at diaphragm center. This is the formulation used later in the Section 5.5.

3.4 Electrical Breakdown Strength

Chapter 2 of this thesis discusses of the theories and experimental data of electrical breakdown across very narrow air gaps. This section will not repeat that discussion but will only address the design issues in terms of electrical breakdown strength considerations. There are three electrical

breakdown strength issues in this MEMS switch: (1) the breakdown strength in the air gaps across the two contacts, (2) the breakdown strength associated with the isolation of the actuation electrodes from the substrate, and (3) the breakdown strength of the air gaps between the actuation electrode and the moving structure. The first breakdown voltage will be the highest off-state voltage the device can sustain before arcing short-circuits the contacts, the second one dictates the highest actuation voltage that can be applied to turn on the MEMS switch, and the third one limits the actuation electric field that can turn into effective electrostatic pressure by the air breakdown strength. The following two sub-sections will discuss these breakdown strengths.

3.4.1 Off-state breakdown strength across contacts

The design parameter that affects the off-state breakdown strength of the device is predominantly the air gap separation between the contacts, while other design parameters might also have certain degree of minor effects. Based on the discussions in Chapter 2, breakdown voltages in excess of 250 V are achievable for air gaps as small as *0.5 μm*, as long as contact cleanliness is ensured. According to Paschen's Law (Chapter 2), this breakdown strength increases as the air gap separation widens. And also the wider the air gap, the less susceptible it is to particle contamination in terms of particle-induced pre mature breakdown. However, there are design constraints that limit the maximum air gap separation there can be between the MEMS switch contacts. As the electrostatic force is inversely proportional to the actuation air gap separation, a wider actuation gap separation will raise the actuation voltage necessary to close the contacts in a dramatic manner.

Considering current thin film technologies and bulk-micromachining technologies, air gaps on the order of 0.5 μm to 5 μm are reasonably feasible geometries. In order to actuate the device with manageable voltages, the lower end of this range is preferable.

3.4.2 Breakdown strength associated with actuation

The actuation electrode of the electrostatically actuated MEMS switch must be electrically isolated from the power lines. To actuate the device, the potential of the actuation electrode is raised with respect to the moving diaphragm until the electrostatic force brings the electrically grounded diaphragm, which serves as the movable electrode, into physical contact with the stationary electrode. This actuation voltage cannot be arbitrarily large and, among other constraints, is restricted by two breakdown strength limits.

The first actuation-limiting electrical breakdown strength is the electrical breakdown strength of the dielectric material that provides the insulation between the actuation electrode and the substrate. This breakdown strength is directly related to the thickness of the dielectric material and its material properties. Thermally grown oxide is a widely accepted choice whose electrical breakdown field is predicted to be 13MV/cm in the thick-oxide theory [62]. However, considering practical issues such as the weakest-link nature of the dielectric breakdown process and the oxide degradation due to voltage stresses, it is not uncommon that a safety factor of 3 be used in industry. The second actuation-related breakdown issue is the air breakdown across the actuation air gap. As discussed earlier in Section 3.2.6, the maximum electrical field in air for a micron-sized gap separation is approximately 10^8 V/m before breakdown occurs. Our experimental observations, as shown in Figure 2.7, agree with this limit. Therefore the maximum electrostatic pressure, $\frac{1}{2}\varepsilon_0 E^2$, is limited to about 44kPa ($\approx$ 6.5psi or 0.44 atm). Therefore, the mechanical design of any electrostatic device should be such that it can be actuated under a pressure of 44kPa. The maximum achievable actuation voltage is the lower of the two limits. An electric breakdown in either the insulation layer or the actuation air gap will result in *less* actuation than expected, or sometimes device failure.

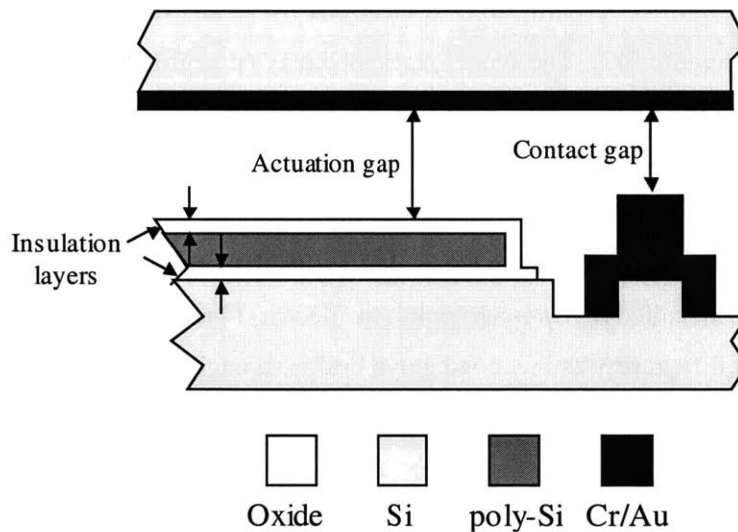

Figure 3.9 Contact gap, actuation gap, and insulation layers of the MEMS switch

3.5 Contact Resistance

Contact resistance is one of the most crucial characteristics of the power MEMS switch because it is directly linked to the power handling capability of the device. Joule heating at the contact

interface can lead to thermally related wear, sticking and fatigue problems. The ON-resistance of a complete switch device will consist of (1) interfacial resistance between the packaging connectors and the device, (2) bulk resistance in the substrates, and (3) contact resistance at the interface of the two contacting members. The focus in the thesis will be on the third resistance; the first two resistances can be optimized with proper choices of packaging schemes and starting materials.

The study of contact resistance of micron-sized contacts has been of great interest recently [63-66] in light of rising interests in micro-relays and micro-switches. Most of this work is a collection of experimental data. Attempts to model the contact resistance of small contacts showed overly optimistic predictions by orders of magnitude [65], which is not surprising since the seemingly simple electrical contacts can be a very complicated physical system. The inaccuracy can result from certain simplifications and assumptions made to keep the complexity of the problem at a manageable level. Also, the thermo-electric effect can be another source of deviation [63]. Furthermore, contact surface cleanliness is a physical property that is difficult to quantify and maintain over the course of an experiment. Its effects on contact resistance can be dominant and, worse yet, fluctuating under different conditions. When there exists an alien film that is thin enough, <20 Å, to be permeable to electrons by means of tunneling, the contact surface is called *quasi-metallic* [42]. The tunnel resistance may be negligible at high mechanical loads; but if the load is of the order of *0.01 N* or less and the contact area correspondingly small, this resistance may surpass the constriction resistance and render inconsistent measurements. The contacts of most micro-relays and micro-switches certainly fall in this small-force small-area category. What complicates the case even more is that an insulating tarnish film could become conductive by a mechanism called *A-fritting*, which is an electrical breakdown that occurs when a sufficiently high electrical field results in a conductive bridge through the film or even in a small conducting spot [42]. A common example of fritting an ordinary plug and socket is given. When their contact is examined by a small e.m.f., such as 1V, the pair may appear insulating; but this feature is not noticeable in service because the ordinary line voltage is high enough to *frit* the contact.

This section will not attempt to provide an exact model for the prediction of the contact resistance of micron-sized contacts. Instead, only general contact theories will be presented here and used to develop design guidance. Modeling of the contact resistance can be broadly divided into two steps: determining the distribution and sizes of the conducting areas at the contact interface as a

function of the contact force (Section 3.5.1), and determining the contact resistance as a function of the distribution and sizes of the conducting contact areas (Section 3.5.2.).

3.5.1 Contact surface

Electrical contact refers to a releasable junction between two contact conductors, or simply contacts. The conductor through which the positive current enters is called *anode*; the other conductor is the *cathode*. The force that presses the contact members together is the load, F. Infinitely hard contact pairs when brought together under the load will have no more than three contact points. Actual materials have finite hardness and are deformable. The points become enlarged into small areas and simultaneously new contact points may set in. The sum of these areas or spots is the *load bearing area,* A_b, over which the local pressure, p, is finite. It is possible that A_b is generated merely by elastic deformation. But, due to the surface unevenness and waviness, even though the contact surfaces may be nominally flat, they actually touch each in areas that are more or less *plastically* deformed. The load, F, the average pressure $\overline{p}$, and the load-bearing area, A_b is related by

$$F = \overline{p}A_b = \xi H A_b \tag{3.64}$$

where usually $0.2 < \xi < 1$ and H is the *contact hardness*. For a given load F, the smoother and flatter the contact surface, the larger the load-bearing area, A_b, and the lower the average contact pressure, $\overline{p}$, would be. The local pressure, p, may vary from point to point with elastic deformation in some spots and plastic deformation in others. However, it is difficult to polish contact surfaces so as to attain an average pressure as small as $0.05H$ and it is usually not lower than 0.2 of the contact hardness [42].

The load-bearing area, A_b, is usually *much* less that the apparent contact area, A_a. From the aspect of current conduction, the load-bearing area may consist of three different parts, (1) metallic contact spots, (2) quasi-metallic spots, and (3) insulating spots. Areas (1) and (2) constitute the conducting spots, short-named *a-spots* referring to the radius a of a circular contact area. Area (3) is normally covered with thick insulating films not permeable by electron tunneling. Figure 3.10 shows different contact areas. Theoretically, if two *ultra* clean and smooth metal surfaces are brought into contact with sufficiently high load that plastically deforms all surface asperities, it may happen that $A_a = A_b = A_c$. However, the inconsistency in contact resistance experimental data and the difficulty in accurate resistance prediction for small-force small-area contacts, as the case for micro-relays and micro-switches, have a lot to do with the lack of the knowledge in the contact

area ratios. To better control and predict the contact area ratios, a micro-relay that uses contact between liquid mercury and a solid conductor has been proposed [48], although no significant improvement in contact resistance is reported.

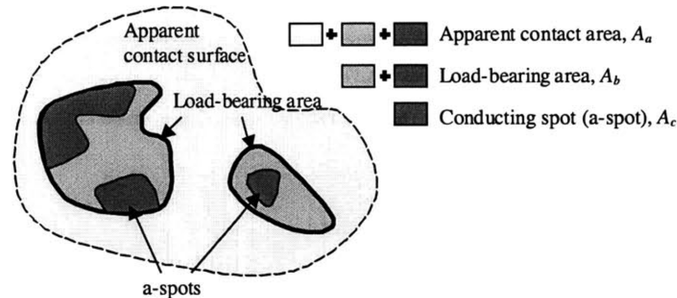

Figure 3.10 Contact areas (apparent, load-bearing, and conducting)

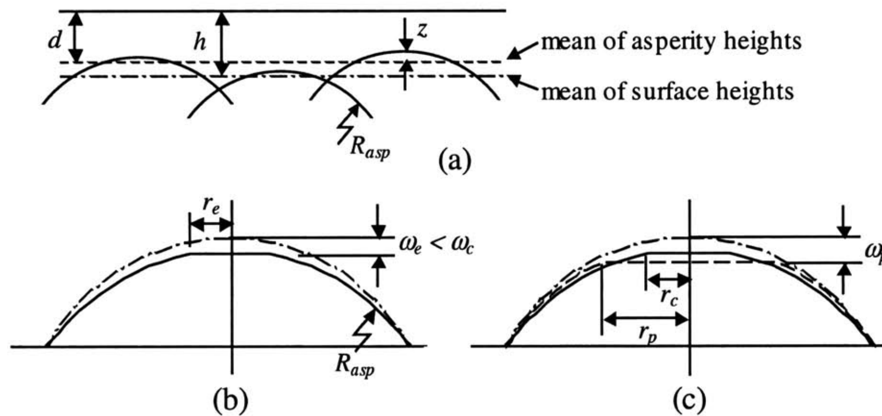

Figure 3.11 Asperity-based rough surface model.

(a) Geometry model of rough contact surfaces, (b) Elastically deformed asperity ($\omega_e \leq \omega_c$), and (c) Partially plastically deformed asperity ($\omega_p > \omega_c$).

Quantitative analysis of the distribution and sizes of the load-bearing contact areas is usually performed with fractal surface modeling. The basic elastic contact model, or "asperity-based model," was first introduced in 1966 [67], in which the rough surfaces are represented by a collection of asperities of prescribed shape. The asperities are scattered over a reference plane and their heights have a statistical distribution. It is assumed that the contacting asperities deform *elastically* according to Hertz theory [68]. An *elastic-plastic* model for the contact of rough surfaces was proposed in [69]. This model is a refinement of the previous asperity-based model and is based on volume conservation of the asperity control volume during plastic deformation. A brief summary of this elastic-plastic model [69] is given in the following paragraphs.

The effective Young's modulus for the system, *E'*, is defined as

$$\frac{1}{E} = \frac{1-\nu_1}{E_1} + \frac{1-\nu_2}{E_2} \tag{3.65}$$

where E_1, E_2, ν_1, and ν_2 are Young's moduli and Poisson's ratios of the contacting surfaces, respectively. For an elastically deformed asperity as shown in Figure 3.11 (b), the radius and area of the contact spot, r_e and A_e, respectively, the vertical elastic deformation of the asperity, ω_e, and the local force on the asperity, $\overline{F}$, are related by

$$\overline{F} = \frac{4}{3} E R_{asp}^{1/2} \omega^{3/2} \text{ , } A_e = \pi r_e^2 = \pi \left(\frac{3\overline{F} R_{asp}}{4E} \right)^{2/3} \text{ , and } r_e = \sqrt{R_{asp}\omega} \tag{3.66}$$

where R_{asp} is the radius of curvature of the asperity.

Plastic yielding is assumed to occur when the local contact pressure exceeds $\xi_p H$, where H is the hardness of the softer contact material, and $\xi_p H$ is the yield strength. From the work of [70], the value of ξ_p is shown to be 0.5. At this onset of plastic deformation, the vertical deformation, w_c, is

$$\omega_c = \left(\frac{\pi \xi_p H}{E} \right)^2 R_{asp} \tag{3.67}$$

Equation (3.66) is good for an elastically deformed asperity and no longer holds when the asperity is partially plastically deformed.

An elastic-plastic model for rough contact surfaces based on control volume conservation of the deformed asperity, as depicted in Figure 3.11(b), is proposed to model the deformation behavior [69]. This model establishes

$$\overline{F} = \xi_p H A_p = \xi_p H \pi r_p^2 = \xi_p H \pi \left(2 - \frac{\omega_c}{\omega_p} \right) \tag{3.68}$$

as the relations between the local contact force, $\overline{F}$, the area of the contacting spot, A_p, the radius of the contacting spot, r_p, and the vertical deformation, ω_p. Therefore, given a vertical deformation ω_p, Equation (3.68) can be used to determine the local contact force $\overline{F}$ and the size of the contact spot A_p. Note that the contact area A_p of this partially plastically deformed asperity is just the *load-bearing* area of one single asperity. Total load-bearing area, A_b, is the sum of all A_p's of contacting asperities. How much percentage of A_b is metallic or quasi-metallic and can be

treated as conducting area A_c depends on the cleanliness of the contact surface, the contact force, and the voltage across the contacts.

3.5.2 Constriction resistance

Subsection 3.5.1 dealt with the relationships among the vertical deformation of a single asperity, the size of the conducting area, and the corresponding contact force based on volume conservation. In this subsection, the goal is to determine the constriction resistance of the contacts assuming the size of the conducting contact spots is known. To elucidate the theory without the confusion of too much detail, the following assumptions are made to simplify the problem:

1. constant resistivity, ρ;
2. same isotropic material for both contacts;
3. no thermoelectric effects;
4. long constrictions, i.e. the contacting area, A_c, is small compared with the dimensions of the contact members;
5. symmetric contacts with a circular a-spot (see Section 3.5.2), A_c, of known radius; and
6. clean metal contact, i.e. no need to consider film resistance.

The circular conducting a-spot is assumed to be an equipotential due to symmetry. The constriction resistance of such a contact system is sought by calculating the resistance between A_c and another equipotential surface A_l belonging to the same contact member [42]. One method often applied to solve this problem is the following. Considered A_c as a current source and A_l as a sink, and consider the region between them to be free from sources and sinks. The current vector can be expressed as the gradient of a potential function, φ, which satisfies the Laplacian equation in the respective region

$$\Delta\varphi = 0 \tag{3.69}$$

and the mathematical task is to find solutions of this equation with certain boundary conditions.

This problem is identical to the electrostatics problem of determining the capacitance between electrodes A_c and A_l in vacuum with similar boundary conditions, and is treated in many textbooks. Since the treatment of such a mathematic problem is given in Section §4 in [42], and since the details of its calculations are lengthy, only the final result of the derivation is given. The

constriction resistance of a circular a-spot satisfying the assumptions made earlier in this subsection is

$$R_{constriction} = \frac{\rho}{2a_p} \tag{3.70}$$

where a_p is the radius of the current-constricting a-spot.

It is interesting to note that the formula for the constriction resistance, Equation (3.70), contains the factor $1/a_p$ instead of $1/a_p^2$. A simple explanation for this is that an electrical resistance is proportional to the length and inversely proportional to the cross-section of the current path. The dominating part of the constriction resistance is in the neighborhood of the conducting contact surface, a-spot. The order of magnitude for the length and the cross-section area of the a-spot are a_p and a_p^2, respectively. Hence the factor in Equation (3.70) is $a_p/a_p^2 = 1/a_p$.

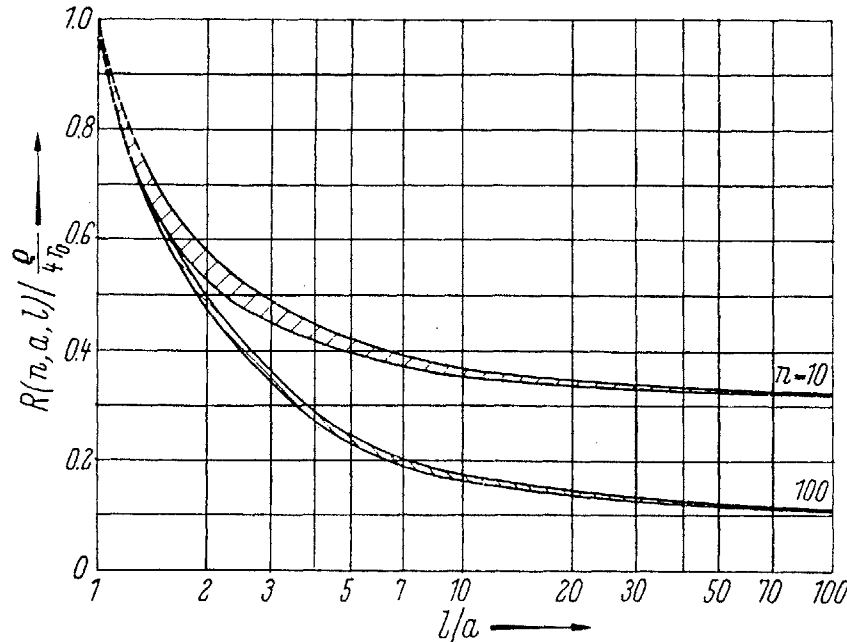

Figure 3.12 Effects of spreading out a-spots on constriction resistance [42].

Finally, another interesting point worth mentioning is the effect on constriction resistance of spreading out a-spots with their total area fixed. Shown in Figure 3.12 [42] is the comparison of the constriction resistance of n uniformly distributed a-spots and the constriction resistance when

all spots are united into one conducting area $A_0 = \pi r_0^2$. The average radius of the a-spot is denoted as a, distance between neighboring a-spots as l, and total number of a-spots as n. It can be seen that, for a constant total conducting area, lower constriction resistance can be achieved by increasing n (dividing into more yet smaller a-spots) and/or increasing l (spreading out the a-spots). Experimental investigations of the contact resistance are discussed in Section 5.8.

3.6 Switching speed

The switching speed of the MEMS switch is dictated by two factors: (1) the un-damped natural frequencies of the diaphragm, and (2) the squeeze-film damping effects. The structural damping due to the internal stress and the hysteresis of the material are *not* considered. The following two subsections discuss the characteristic times of these two speed-limiting phenomena.

3.6.1 Resonant frequency

The complete governing equation for the dynamics of the un-damped circular clamped diaphragm under electrostatic and pneumatic pressures can be written as:

$$\rho t_d \frac{\partial^2 g}{\partial t^2} = -D\nabla^4 g + \sigma_t t_d \nabla^2 g - \frac{\varepsilon_0 V_{act}^2}{2g^2} - p_{act} \tag{3.71}$$

where ρ is the mass density of the diaphragm material, t_d is the diaphragm thickness, g is the gap distance, D is the flexural rigidity, σ_t residual tensile stress in the diaphragm, ε_0 is the permittivity of free space, V_{act} and p_{act} are the actuation voltage and pressure, respectively, and ∇^2 is the Laplace operator in polar coordinates, $\nabla^2 = \frac{\partial^2}{\partial r^2} + \frac{1}{r}\frac{\partial}{\partial r} + \frac{1}{r^2}\frac{\partial^2}{\partial \theta^2}$ and $\nabla^4 = \nabla^2\nabla^2 = \left(\frac{\partial^2}{\partial r^2} + \frac{1}{r}\frac{\partial}{\partial r} + \frac{1}{r^2}\frac{\partial^2}{\partial \theta^2}\right)\cdot\left(\frac{\partial^2}{\partial r^2} + \frac{1}{r}\frac{\partial}{\partial r} + \frac{1}{r^2}\frac{\partial^2}{\partial \theta^2}\right)$. Note that Equation (3.31) in Section 3.3.3 is a steady-state variation of Equation (3.71). The θ derivatives vanish because of axisymmetry. The boundary conditions for a clamped diaphragm, whose radius is a, are

$$g(a, \theta) = g_0, \text{ where } g_0 \text{ is initial gap, and}$$
$$\left.\frac{\partial g(r,\theta)}{\partial r}\right|_{r=a} = 0. \tag{3.72}$$

The only term on the left of Equation (3.71) is the inertia term; on the right are, in order, the bending term, the residual-stress term, the electrostatic pressure, and the pneumatic pressure. Figure 3.13 schematically shows such diaphragm dynamic system.

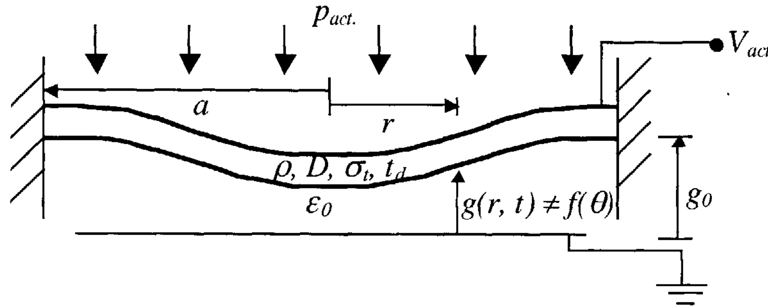

Figure 3.13 Schematic drawing of a circular clamped diaphragm under electrostatic actuation and pneumatic actuation.

The switching speed depends not only on the diaphragm characteristics but also on the actuation forces and its exact solution can be obtained by solving Equation (3.71). Theoretically the diaphragm deflection, its spatial distribution, and its time derivatives can be obtained by solving Equation (3.71); however, the analytical formulation for the solution of this particular form of partial differential equation is not available and the numerical approach is overwhelmingly computation intensive. Therefore, instead of solving for exact un-damped response of an actuated diaphragm, we consider the *free vibration* of two limiting cases, a stress-dominant circular membrane and a bending-dominant circular plate.

Stress dominant case (membrane)

The free vibration differential equation for a circular clamped membrane is

$$\rho \frac{\partial^2 g}{\partial t^2} = \sigma_t \nabla^2 g \tag{3.73}$$

whose boundary conditions are the same as given in Equation (3.72). Equation (3.73) is a two-dimensional *wave equation* in polar coordinates and is treated in many textbooks for advanced engineering mathematics, e.g. [71]. The solution of Equation (3.73) can be represented as a sum of an infinite set of orthogonal frequency functions, *Bessel functions*, called natural modes. The frequencies of the natural modes can be determined by the zeros of the first kind of Bessel

function of order zero, $J_0(\frac{\omega_n a}{\sqrt{\sigma_t/\rho}}) = 0$. The zeros of the Bessel function have been numerically found and the smallest value corresponds to the lowest fundamental frequency,

$$\omega_1 = \sqrt{\frac{\sigma_t}{\rho}}\frac{2.405}{a}. \qquad (3.74)$$

Bending dominant case (plate)

The governing differential equation for the free vibration of a circular clamped plate is

$$\rho t_d \frac{\partial^2 g}{\partial t^2} = -D\nabla^4 g \qquad (3.75)$$

whose boundary conditions are the same as in Equation (3.72). The solution of Equation (3.75) is discussed in [72] and, as in the previous membrane case, the frequencies of the natural modes can be determined by the solutions of a set of characteristic equations,

$$I_m(\beta a)J_{m-1}(\beta a) - J_{m-1}(\beta a)I_m(\beta a) = 0 \qquad (3.76)$$

where I_m is the first kind of *hyperbolic* Bessel function of order m, J_m is the first kind of Bessel function of order m, $\beta^4 = \frac{\omega_n^2 \rho t_d}{D}$, and ω_n is the nth natural frequency. The zeros of the characteristic equations in Equation (3.76) must be determined numerically and the lowest natural frequency is found to be

$$\omega_1 = 1.105^2 \frac{\pi}{a^2}\sqrt{\frac{D}{\rho t_d}}. \qquad (3.77)$$

If the diaphragm is neither a stress-dominant membrane nor a bending-dominant plate, then the higher natural frequency obtained from Equations (3.74) and (3.77) can be used as a lower bound to the actual natural frequency of the real dynamics system since both Equations (3.74) and (3.77) are limiting cases and do not consider *all* diaphragm stiffening factors.

3.6.2 Squeeze-film effects

The MEMS switch is operated in an atmospheric environment and the air film trapped between the clamped diaphragm and the stationary substrate gives rise to a pressure force against the diaphragm motion known as *squeeze-film damping*. The dynamic behavior of the clamped

diaphragm can be profoundly influenced by squeeze-film damping due to the high radius-to-separation device geometry. The governing equation of parallel rigid-body plates under squeeze-film effects is the compressible isothermal Reynold's equation derived from Navier-Stokes equation, the continuity equation, and the equation of state. Under assumptions that (1) the inertia effect in the Navier-Stokes equation is negligible, (2) the pressure distribution across the gap is uniform, and (3) the fluid velocity component perpendicular to plate surface is negligible, a non-dimensional form of this compressible isothermal Reynold's equation can be written as [73]

$$\nabla \cdot \left(PH^3 \nabla P\right) = \tau_{sqfm} \frac{\partial (PH)}{\partial t} \tag{3.78}$$

where the normalized gap, $H = \frac{h}{h_0}$, is the ratio of the gap distance, h, to initial gap distance, h_0; the normalized pressure, $P = \frac{p}{p_a}$, is the ratio of the gap pressure, p, to ambient pressure, p_a; and the characteristic time constant, $\tau_{sqfm} = \frac{12\mu_a L^2}{p_a h_0^2}$, is a function of the air viscosity, μ_a, the plate length, L, the ambient pressure, p_a, and the initial gap distance, h_0. Most squeeze-film studies [74-76] in the literature focus on cases of small plate motion magnitude with respect to gap distance in order to linearize Equation (3.78), which is a time-dependent nonlinear parabolic partial differential equation. Relaxation of small motion-to-gap assumption can be achieved by numerically solving Equation (3.78) [77]. To further model the compliance of the plate requires finite element analysis using some commercial packages with specialty solvers for fluidic problems [53].

The characteristic time constant in the compressible isothermal Reynold's equation can be used as a quick estimation of the effects of squeeze-film damping without solving the nonlinear partial differential equation. For parallel circular plates, the plate length, L, can be replaced with the plate diameter and therefore the characteristic time constant can be rewritten as

$$\tau_{sqfm} = \frac{48\mu_a a^2}{p_a h_0^2} \tag{3.79}$$

where a is the radius of the circular plates.

3.7 Design of electrostatic MEMS switch

This section summarizes the discussion in the previous sections and proposes a switch design shown in Figure 3.14. The following subsections explain the criterions used to reach the design. The design parameters and the estimation of device performance are printed ***in bold***.

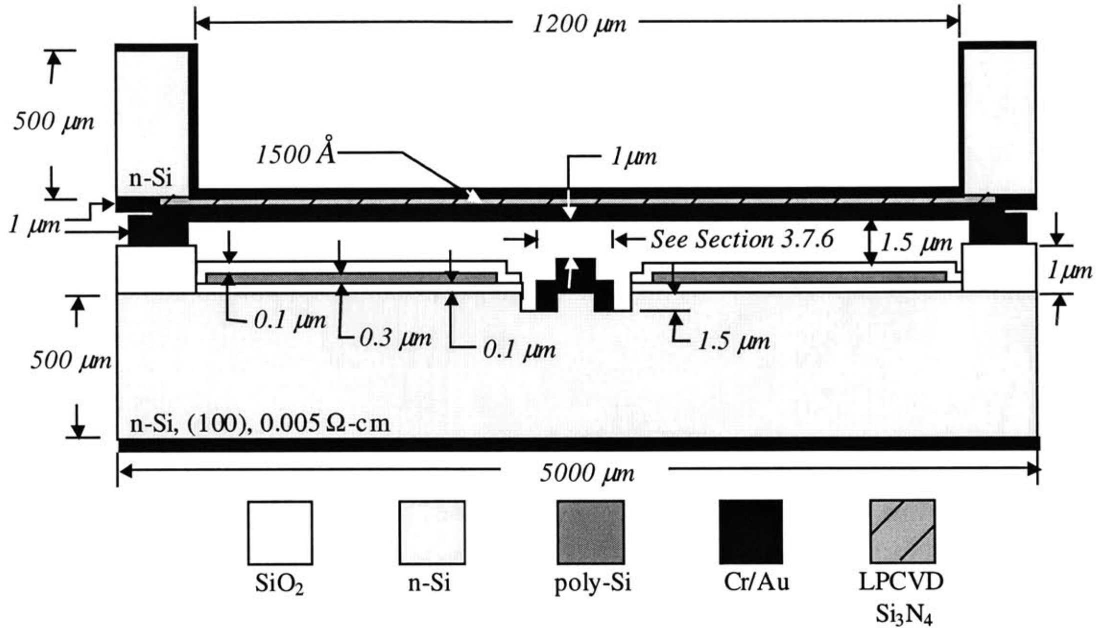

Figure 3.14 MEMS switch design (not to scale)

3.7.1 Actuation Scheme

In Section 3.2, actuation methods commonly implemented in micro actuators were critiqued on their suitability for automotive power switching applications and their MEMS processing facility. *Piezoelectric* mechanisms cannot provide enough displacement without using an actuator of relatively large size owing to limitations of real material properties. This could conflict the purpose of device miniaturization for point-of-load applications. *Thermal* actuation is *not* an optimal choice because device characteristics could deviate over the wide temperature range of normal automotive operations both in time and in location in the vehicle. The appealing feature of *magnetostatic* actuation is that the force generated is solely controlled by the actuation coil current, as indicated in Equation (3.7), for a specific actuator design. Its major adversity is the difficulty in microfabricating a high-efficiency magnetic circuit due to the scarcity of high permeability CMOS-process-compatible permalloy materials and constraints on the MEMS realization of *large* amp-turns. As a result, magnetostatic micro actuators appear to be more power hungry than electrostatic ones. *Pneumatic* actuation does *not* seem to be an appropriate

option in automotive applications, considering that *12V* batteries are the only power source and there is *no* apparent pneumatic source available in cars. In terms of automotive applications, *Shape-Memory Alloy* actuation has a fateful drawback: most of the alloy phase-transformation occurs *below* the 120°C temperature requirement in automotive industry. Therefore, an SMA scheme is *not* considered in the design of the MEMS switch.

Almost by elimination, the choice of actuation scheme for the MEMS switch is ***electrostatics***. Its advantages are low power consumption and CMOS compatible materials and processes. The major disadvantage is the requirement of a large area with a close gap separation for to generate force of significant magnitude.

3.7.2 Actuation voltages

Because the design of the contact gap separation is wider than one third of the actuation gap separation (Figure 3.14), the electrostatic actuation will occur in a snap-through motion, assuming that electrostatic actuation behavior of a diaphragm and that of a plate are similar. If the thin diaphragm is electrically grounded, the minimum voltage applied to the poly-silicon electrode for the diaphragm to snap close the contacts is the electrostatic pull-in voltage of the device. Substitution of design parameters into Equation (3.12) yields ***7.85 V*** as the actuation voltage and the polarity of this voltage does *not* matter.

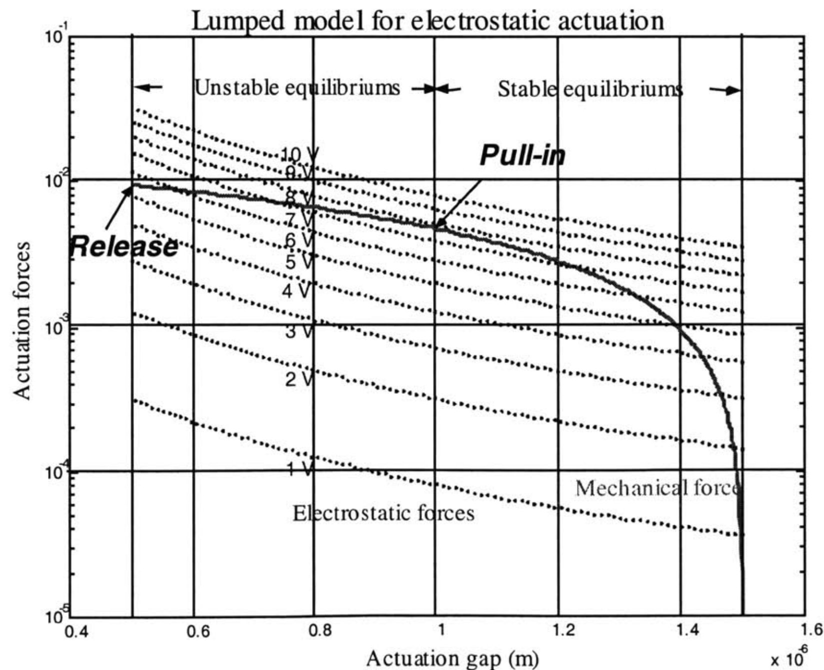

Figure 3.15 Lumped model for electrostatic actuation:
Electrostatic forces (dotted lines) and mechanical force (solid line) vs. gap

The estimation of the release voltage is implemented using a lumped model approximation. The radius of the circular rigid-body plate, *1200 μm*, and the gap distance, *1.5 μm*, for the lumped model are carried forward directly from the geometry design of the thin diaphragm. The plate size, the gap distance, and the calculated *7.8 V* pull-in voltage can be used to calculate the effective spring constant. Figure 3.15 shows the electrostatic force of different actuation voltages and the mechanical force as a function of the gap distance. The intersections of the two forces indicate possible equilibrium solutions at the corresponding voltages. By increasing the voltage, it can be seen that the gap slowly decreases until $V_{pull\text{-}in} = 7.8\ V$ is reached, and that there is no intersection for voltages above $V_{pull\text{-}in}$. The only possible equilibrium location for $V > V_{pull\text{-}in}$ is at contact closure where a strong repulsive force is exerted on the plate by the opposing contact. This repulsive force is the difference between the mechanical force and the electrostatic force of the corresponding voltage at minimum gap actuation distance of *0.5 μm*. In order to *release* the plate from this minimum gap position, or maximum plate deflection, the voltage needs to drop well below $V_{pull\text{-}in}$ to a point where the physical repulsive force vanishes. Based on Figure 3.15, one can see that such electrostatic release occurs at $\boldsymbol{V_{release} = 5.6\ V}$.

3.7.3 Micromachining technologies

The advantages of surface-micromachining technologies are the smaller device footprint and higher structural complexity. However, multi-layered bulk-micromachined structures have been demonstrated in various devices (e.g. [78]). More importantly, the single-crystal materials used in bulk-micromachining technology have well-defined and precisely-controlled properties. In contrast, tremendous effort must be made in surface-micromachining to control the residual-stress of deposited films. As a result, ***bulk-micromachining technology*** is chosen for its more reproducible material characteristics.

3.7.4 Mechanical structure

The requirements of a large electrostatic actuation area and high surface-to-volume ratio for heat dissipation consideration make a vertically-moving diaphragm structure a favorable choice. ***Circular-shaped*** diaphragms are chosen over rectangular-shaped ones because of the simplicity of their axisymmetric mechanics analysis.

A bossed diaphragm design enables simplification of device behavior modeling with a spring-mass mechanical model and a parallel-plate capacitor electrical model. In addition, the determination of actual contact force is more straightforward with a bossed design. Therefore, a

bossed diaphragm is *preferred to* a uniform-thickness one. However, the unexpected fabrication complexities discussed in Chapter 4 lead us to the alternative design of a ***uniform-thickness diaphragm***. The lumped-parameter models are no longer applicable; but, because of their simplicity, they are still employed in some cases for a rough first-order estimation. If the device is pneumatically actuated, it follows from Equation (3.63) that the clamped circular uniform-thickness diaphragm will deflect and touch the bottom pedestal contacts at a pressure of ***417 Pa***.

3.7.5 Breakdown

Based on the experimental observations presented in Section 2.5, a breakdown voltage above 300 V can be achieved in a clean $1\mu m$-gap. It is reasonable to target the *off-state standoff voltage* at ***270 V***.

The *1000 Å* thermal oxide insulation layers are expected to sustain ***100 V*** of electrical bias. The electric field established by this maximum *100V* actuation across the 1.5µm actuation gap is 6.7×10^7 V/m, which is below the 1×10^9 V/m field emission limit of electron for micron-sized gaps. Therefore, the *100 V* actuation voltage is ***within the safe operating range*** in terms of electrical breakdown.

3.7.6 On-state Resistance

The on-state resistance of the MEMS switch can be expressed as the sum of *all* resistances in the electrical path shown in Equation (3.80).

$$R_{on} = R_{constriction} + R_{metal} + R_{contact} + R_{bulk} + R_{diaphragm} + R_{film} \tag{3.80}$$

where $R_{constriction}$ is the constriction resistance, R_{metal} is the resistance of the metal films, $R_{contact}$ is the semiconductor-metal contact resistance, R_{bulk} is the resistance in the bulk of the silicon substrates, $R_{diaphragm}$ is the resistance of the diaphragm structure, and R_{film} is the resistance of any insulating films. Gold is chosen as the contact metal because of its high conductivity and its key properties as listed in Table 3.1.

Gold (Au)	
Young Modulus	*78 GPa*
Brisnell Hardness	245 GPa
Resistivity	$2.2\times 10^{-8}\ \Omega\text{-}m$

Table 3.1 Gold properties

The resistances in Equation (3.80) are treated individually and summed in the end to obtain the total on-state resistance.

Constriction resistance, $R_{constriction}$

The constriction resistance is the dominant resistance near the contact region between the top diaphragm and the bottom pedestals. We define the theoretically semi-infinite contact dimension to be confined within the $1\mu m$-radius of the diaphragm and the contact pedestals. In addition to the *six* assumptions made in Section 3.5 discussions, the following assumptions are made to further simplify the problem to a manageable level:

1. a parallel-plate spring-mass lumped-parameter model is valid;
2. the coefficient ξ_p defined in Equation(3.64) is 0.5;
3. 50% of the load-bearing area is actually conductive;
4. the contact surface roughness is $10\ nm$;
5. the radius of curvature of the asperity is approximated by surface roughness;
6. the radius of the local contacting spot is approximated by vertical deformation of the partially deformed asperity; and
7. individual conducting spots behave as parallel resistors

With these assumptions, the parameters shown in Table 3.2 can be determined. The predicted constriction resistance for this contact system, $4.71 \times 10^{-19}\ \Omega$, might be overly optimistic. Experimental study of this constriction resistance is discussed in Section 5.8.

Parameters	Derivations
Total contact force $F = 5.485 \times 10^{-4}\ (N)$	Equation (3.10) and Assumption 1
Total load-bearing area, $A_b = 4.478 \times 10^{-13}\ (m^2)$	Equation(3.64) and Assumption 2
Asperity vertical deformation, $\omega_c = 2.43 \times 10^{-12}(m)$	Equation(3.67) and Assumptions 4 and 5
Radius of contacting spot of a single asperity, $r_p = 2.43 \times 10^{-12}(m)$	Assumption 6
Total number of contacting spots, N = 9.61 × 10^{19}	$A_b/(\pi r_p^2)$
Constriction resistance, $R = 4.71 \times 10^{-19}\ (\Omega)$	Equation(3.70), r_p, and Assumption 7

Table 3.2 Derivation of constriction resistance

Resistance of the metal films, R_{metal}

The resistance across the thin metal film is negligible because of the low-resistivity characteristic of metals, large areas on the device surface, and thin metal thickness; thus $R_{metal} = 0\ \Omega$.

Resistance of the metal-semiconductor contact interface, $R_{contact}$

The semiconductor is assumed to be degenerately doped and a perfect *Ohmic contact* is formed across the metal-semiconductor interface. There is no Schottky diode and the contact resistance is ignored. Thus, $R_{contact} = 0\ \Omega$.

Resistance in the bulk of the silicon substrates, R_{bulk}

To simplify the calculation, the top wafer and bottom wafers are assumed to be *identical* with 5mm × 5mm die size, *0.005 Ω-cm* resistivity, and *500 μm* in thickness. Therefore, the bulk resistance of the *top* and the *bottom* wafers can be obtained $R_{bulk} = 2\times \rho_{Si}\frac{(thickness)}{(die\ area)} = 0.2\Omega$.

Note that R_{bulk} can be improved with substrates of even lower resistivities.

Resistance within the diaphragm structure, $R_{diaphragm}$

Since the structural silicon nitride is an insulator, the current flows *radially* inward or outward the *1200 μm*-radius diaphragm within the metal film. For the central *1μm*-radius portion, the resistance is dominated by the constriction resistance. For the outer 1 *μm* – *1200* μm portion, the resistance can be calculated by integration, $R_{daiphragm} = \int_{1\mu m}^{1200\mu m} \rho_{Au}\frac{dr}{2\pi r(thickness)} = 24.8\ m\Omega$.

Film resistance, R_{film}

It is assumed that the contacts are clean and *free* of insulating films, therefore $R_{film} = 0\Omega$.

Summing all the resistances discussed, the on-state resistance is estimated to be $R_{on} = 0.225\Omega$. Note that R_{on} is dominated by the *bulk resistance of the substrates*. As a result, low-resistivity starting substrates are preferred in terms of on-state resistance performance.

3.7.7 Switching speed

The LPCVD nitride diaphragm is highly tensile stressed and therefore can be treated as a membrane. Before using Equation (3.74) for the calculation of the lowest natural frequency, it

should be noted that the both sides of the *1500Å* tensile-stressed nitride membrane are coated with *1 μm* of stress-free gold metal. The consequence of this is that the inertia of the membrane is dominated by the metal films while the stress is dictated by the nitride. As a result, in order to account for this aberration, Equation (3.74) is modified as

$$\omega_1 = \sqrt{\frac{\sigma_{t,nit} t_{nit}}{\rho_{Au} t_{Au}}} \frac{2.405}{a} \tag{3.81}$$

where t is the film thickness of the corresponding material denoted by the subscript. Substitution of the design parameters into Equation (3.81) shows that the lowest resonant frequency of the circular membrane is *19.9 kHz*. In other words, the un-damped mechanical time constant of the membrane is *50.3 μs*.

Equation (3.79), the characteristic time constant of the compressible isothermal Reynold's equation, is used for the estimation the switch time under the influence of the squeeze-film damping and is found to *be* τ_{sqfm} = ***54.5 ms***. Compared with the time constant based on un-damped membrane mechanics, it is obvious the switch time is limited by the squeeze-film damping effects.

3.7.8 Prototype Design/Performance

A summary of the device design choices and target specifications are listed in Table 3.3.

Actuation scheme	Electrostatics
Structure design	Bulk-micromachined, clamped circular diaphragm
Device Dimensions	Refer to Figure 3.14
Turn-on Voltage	*7.85 V*
Turn-off Voltage	*5.6 V*
Turn-on Pressure	*417 Pa*
Stand-off Voltage	*270 V*
Max. Actuation Voltage	*100 V*
On-state Resistance	*0.225 Ω*
Switch time	*54.5 ms*

Table 3.3 Design and target specifications

Chapter 4 DEVICE FABRICATION

4.1 Introduction

This chapter discusses the fabrication details of the MEMS switch and related issues. The MEMS switch shown in Figure 3.14 is fabricated from a bottom wafer and a top wafer bonded together. The fabrication processes for both the bottom and top wafers are compatible with that for silicon based integrated-circuits until metallization and are carried out separately before the final bonding. For the bottom wafer, a 5-mask process is designed that bears considerable similarity with mainstream microelectronics processes. The top wafer, which is fabricated with a 3-mask process, features a classic bulk-micromachined diaphragm, and extreme handling care must be taken once the delicate structures are formed.

Section 4.2 first reviews the experience gained during the course of the device development. The latest design of the MEMS switch device is presented in Section 4.3 where process descriptions are provided for both the bottom wafer and the top wafer. Section 4.4 discusses the fabrication issues that are not commonly encountered in conventional microelectronics processing. A brief summary and suggestions for future improvement are given in Section 4.5. Detailed process travelers for both the top wafer and the bottom wafer are listed in Appendix B.1 and Appendix B.2, respectively, and the corresponding mask layouts are provided in 0.

4.2 Earlier Generations

Before detailing the process sequence and mask layouts for the final switch, this chapter opens with an introduction to the development history of the MEMS switch. A few example designs preceding the current one are presented in chronological order and each design is followed by a brief discussion of its the complications.

4.2.1 The Bottom Wafer

The MEMS switch consists of a *bottom* substrate, which contains the stationary bottom contacts and actuation electrode, and a *top* movable electrode, which has a circular plate structure. Over the course of this thesis, there was not much change in the design of bottom substrate except for two minor modifications. The first modification for the bottom substrate, as depicted in Figure 4.1, is the extension of the insulation oxide over the gap between the poly-silicon actuation electrode and the field oxide area. This covers the otherwise exposed single-crystal silicon substrate in the gap just outside the actuation electrode to ensure good electrical insulation between the bottom substrate and top diaphragm.

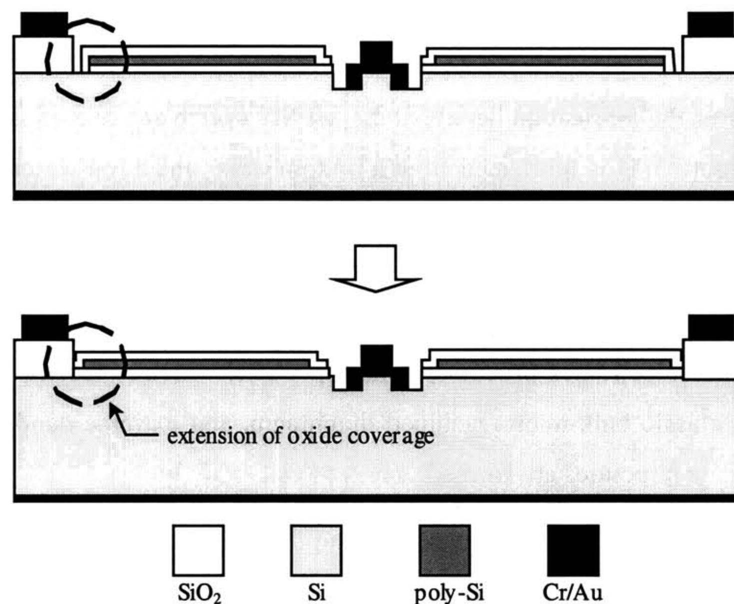

Figure 4.1 First modification on bottom substrate

The second modification, as illustrated in Figure 4.2, is the addition of an oxide insulation layer underneath the metal lead used to access the contact pedestals. This long and thin lead is required for a four-point-probe resistance measurement as described in Section 5.2.4. Our experience showed that, if the metal lead-out line is in direct contact with the bottom substrate, the contact resistance measurement will have a strong dependence on the current directionality. After reviewing the design, it was diagnosed that a series of rectifying Schottky diodes have been accidentally fabricated along the metal/semiconductor interface, as the bottom substrate is highly but not thoroughly degenerately doped. When a not-degenerately-doped semiconductor is brought into intimate contact with a metal, after thermal equilibrium is reached, the difference in work functions between the semiconductor and the metal will cause energy band bending, resulting in a energy barrier that gives rise to the rectifying characteristic [79]. The other option is to

degenerately dope the bottom substrate exhaustively to ensure ohmic contact. However, perfectly ohmic metal-to-semiconductor contact is hard to implement, if not unrealizable. Therefore, an insulation layer was inserted underneath the long lead to eliminate the rectifying effects at the metal-semiconductor interface.

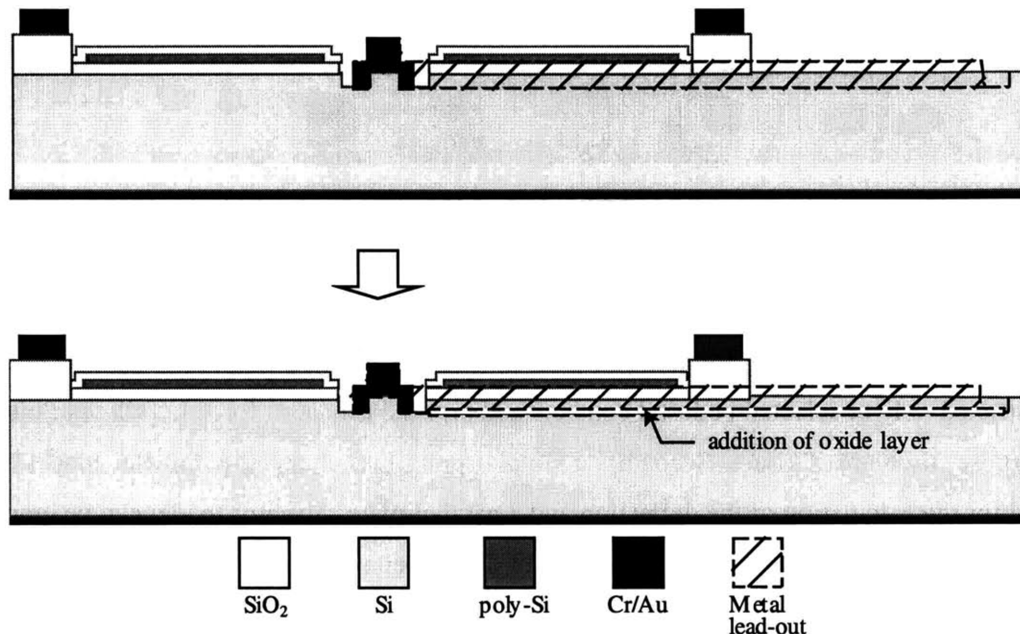

Figure 4.2 Second modification on bottom substrate

The following subsections discuss the evolution of the design of the *top* wafer containing the diaphragm of the MEMS switch; the geometric design and functionality of the bottom substrate essentially remains unchanged through this evolution.

4.2.2 Generation 1 Top Wafer

The first generation of the MEMS switch features a three-wafer stack design as shown in Figure 4.3. Wafer 3 is the bottom substrate briefly discussed earlier. The fabrication process for the movable diaphragm starts with Wafer 2 as an SOI (silicon-on-insulator) wafer. The front side of Wafer 2 is trench-etched twice to define the bossed structure before being fusion-bonded to Wafer 1 for structural support, and the backside is completely bulk-micromachined away in an alkaline-based wet etchant to form the diaphragm. Venting channels for pressure balancing are created before metallization. Finally, a metal-to-metal thermocompression bond is applied to hold the bottom substrate and top diaphragm substrate tightly together.

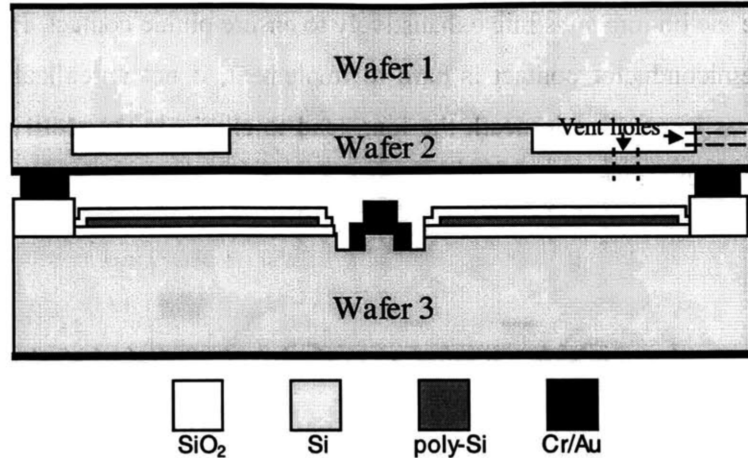

Figure 4.3 MEMS switch design – Generation 1

The purpose of the circular *bossed* structural design is twofold. First, most of the deformation will take place in the more compliant annular region and the thicker central boss will translate in a rigid-body-like motion. Therefore, contacts made between the diaphragm and bottom substrate are restricted only at selected pedestal contacts and thus the actuation force is fully exploited for the purpose of contact closure. Secondly, a simple spring-mass lumped-parameter model can be applied for the calculation of the deflection and a parallel-plate capacitor model can be employed for electrostatic analysis. The complexity level of device behavior analysis can be greatly reduced with these simplified models.

The vent holes schematically drawn on the diaphragm are actually *not* on the diaphragm but fabricated indirectly. These air passages are crucial for the pressure equilibrium on both sides of the diaphragm but pose serious fabrication challenges: (1) a photolithography process needs to be performed *after* fragile diaphragms are formed, and (2) *no* wet cleaning is allowed after the vent-holes are opened otherwise liquids might be drawn into cavities by capillary effects resulting in sticking problems. Moreover, the 3-wafer stack design seems unnecessarily complicated. Therefore, modifications are made to simplify the fabrication of the bossed circular diaphragm as discussed in the next subsection.

4.2.3 Generation 2 Top Wafer

The second generation of the MEMS switch inherits the circular bossed diaphragm structure from previous generation but has it inverted upside down as depicted in Figure 4.4. Wafer 1 is an SOI wafer whose device-side is trench-etched to define the central boss. The handle side of Wafer 1 is etched with a deep RIE (reactive-ion etch) etcher and the etch stops on the buried oxide layer to form the diaphragm. The exposed buried oxide is removed before metallization on both sides.

Wafer 2 is the same bottom substrate that has the bottom pedestal contacts and the poly-silicon actuation electrode.

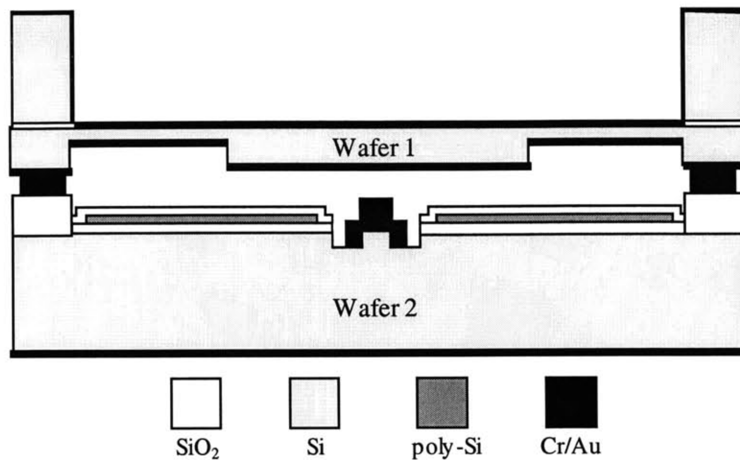

Figure 4.4 MEMS switch design – Generation 2

Having the boss-defining trench-etch performed on the contact side of the diaphragm eliminates the need of fusion-bonding to a third handle wafer for structural support. In addition to this apparent gain in process simplification, this design also enables the application of pneumatic pressure on the diaphragm whose topside is fully exposed to atmosphere. The advantages of being able to actuate the switch pneumatically are discussed in Section 5.2.1. On the other hand, the drawbacks of the second-generation design are: (1) that the less-than-optimal metal step coverage on the contact surface of the top diaphragm results in *poor* on-state resistance performance, and (2) *lower* electrostatic force can be attained due to a wider gap distance between the thinner annular diaphragm and the bottom actuation electrode. The next actions taken to address these problems are discussed in the next subsection.

4.2.4 Generation 3 Top Wafer

Figure 4.5 shows the cross-sectional drawing of the third generation of the MEMS switch. Generation 3 returns to the three-wafer stack structure as in the design of Generation 1. Another similarity between the first and the third generations is the *flat* contact surface on the top diaphragm. Other features are the exposed diaphragm enabling pneumatic actuation retained from Generation 2 and the bossed circular diaphragm from Generation 1. In fact, the only difference between Generations 1 and 3 is that air-venting passages on the Wafer 2 level (Figure 4.3) have been replaced with a through-wafer opening on Wafer 1 level (Figure 4.5). The bottom substrate, denoted as Wafer 3 in this case, remains unchanged.

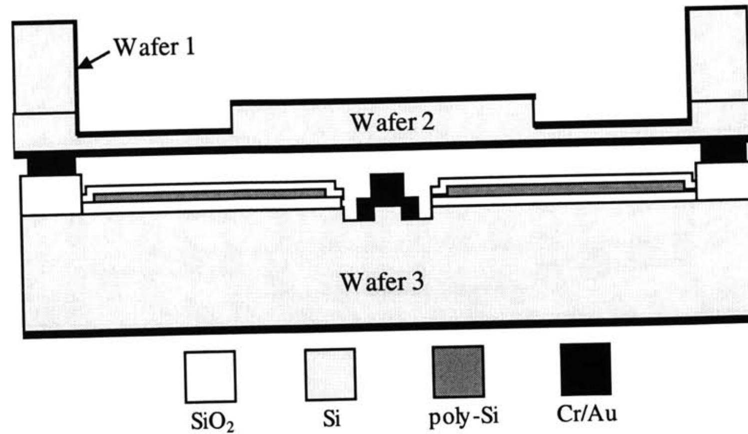

Figure 4.5 MEMS switch design – Generation 3

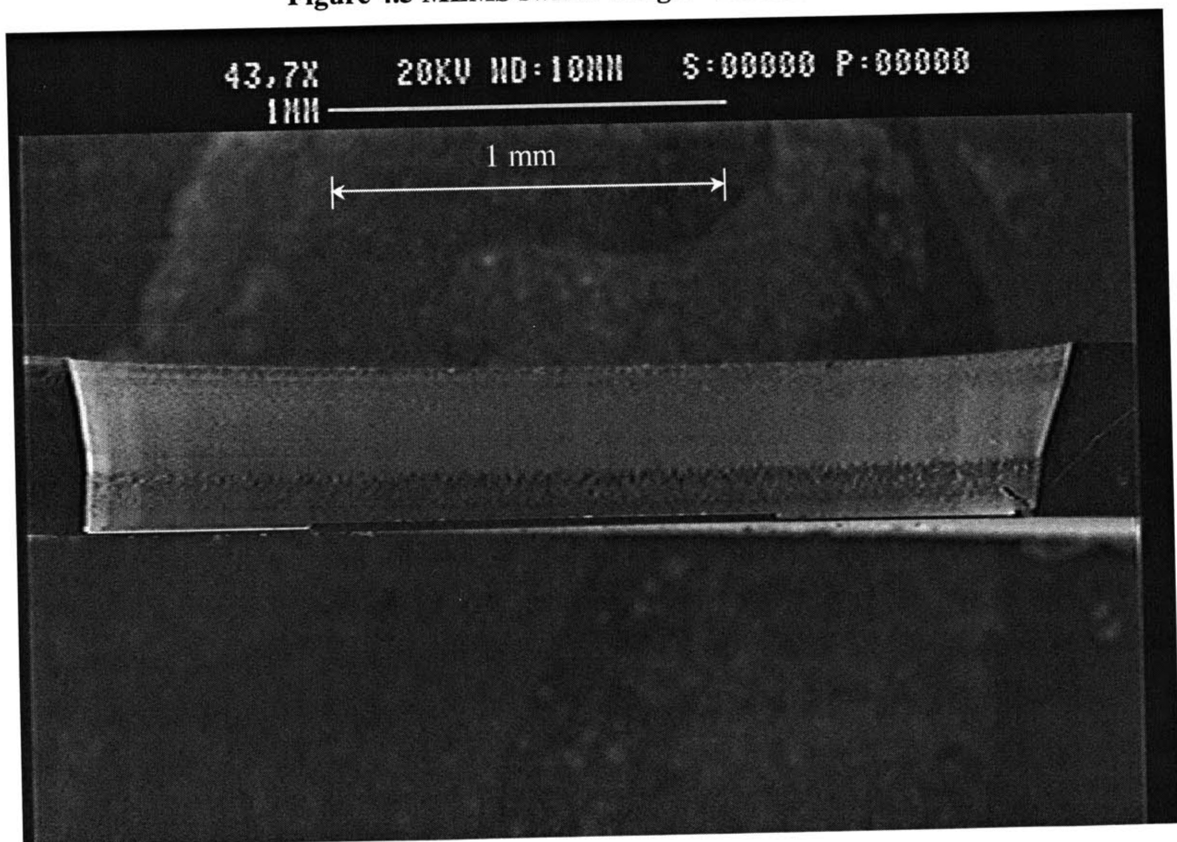

Figure 4.6 Micrograph of a Generation 3 top wafer

One baffling problem with this switch is the unexpected buckling of the diaphragm after the diaphragm structure is formed (see Appendix A). Calculations show that for a *1200 μm*-radius, *10 μm*-thick, and *900 μm*-radius-boss diaphragm structure, the compressive in-plane stress for buckling to occur has to exceed a critical value of 72 MPa [57]. A highly tensile-stressed LPCVD (low-pressure chemical vapor deposition) stoichiometric silicon nitride film (Si_3N_4) was deposited

on the top side of the diaphragm to remedy the buckling situation but the effort was in vain. Under the assumption that the starting SOI wafers are stress–free, either or both of the following scenarios are speculated to cause the buckling.

The presence of large holes in Wafer 1 could give rise to non-uniformity in the thermal shrinkage between Wafers 1 and 2 when cooling down from the 1100 °C anneal temperature of the fusion-bond. Such shrinkage mismatch will be dominated by the much thicker Wafer 1 and the thinner Wafer 2 will yield to the supporting structure inducing a compressive in-plane stress in the diaphragm.

In addition to the absolute in-plane compressive stress level, a *transverse stress-gradient* could also lead to buckling, especially for the diaphragm structure in this case because of its high radius-to-thickness ratio. It is conceivable that a considerably slender diaphragm with a transverse stress-gradient would easily relax itself into a curved profile and settle to a lower energy equilibrium state. Due to the difference in thermal expansion coefficient between the buried oxide and silicon layer, stress-gradient could be introduced into the diaphragm layer near the oxide-silicon interface during the anneal cool-down.

Based on these postulations, changes are made to further modify the design of the device with minimal high-temperature processes as presented in Section 4.2.5.

4.2.5 Final Generation Top Wafer

The latest prototype design preserves the pneumatic actuation capability and the flat diaphragm contact surface from earlier generations. However, in an effort to eliminate the need for the fusion bond and thus the high-temperature anneal, a uniform-thickness diaphragm design is chosen over the bossed diaphragm structure. This is a compromise to trade the preferred bossed structure for a low-temperature process. To fabricate a *bossed* structure with a flat contact surface, the SOI wafer *must* be fusion-bonded to another wafer for structural support after trench-etching its boss patterns and before the removal of the SOI handle substrate. There is no way around this unless a reliable photolithography technology applicable to wafers with full-wafer-depth features becomes available. The consequences of *not* having a bossed structure are: (1) a much more complicated modeling and analysis for the distributed system, (2) a reduction in contact force, and (3) difficulty in obtaining contact-force information. Nevertheless, these are worthwhile sacrifices because a buckle-free diaphragm is of higher priority.

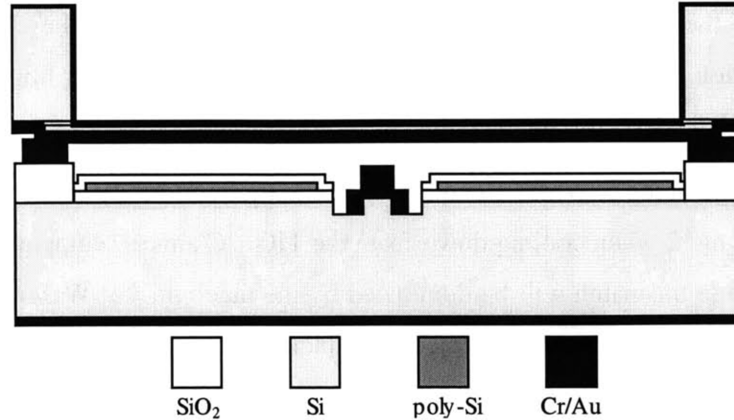

Figure 4.7 Latest MEMS switch design - silicon diaphragm

Figure 4.7 shows the cross-section of the latest design where the silicon diaphragm is formed by selectively etching away the handle substrate of an SOI wafer. The bottom substrate remains the same as in earlier generations. Figure 4.8 shows a design variation that has a LPCVD tensile-stressed diaphragm. Instead of starting with a SOI wafer, a double-side-polished silicon wafer is first deposited with a thin film of stoichiometric silicon nitride on one side and selectively deep-etched on the other side. Advantages of a tensile-stressed nitride diaphragm design are lower-cost starting substrates and less susceptible to unpredicted stress deviations.

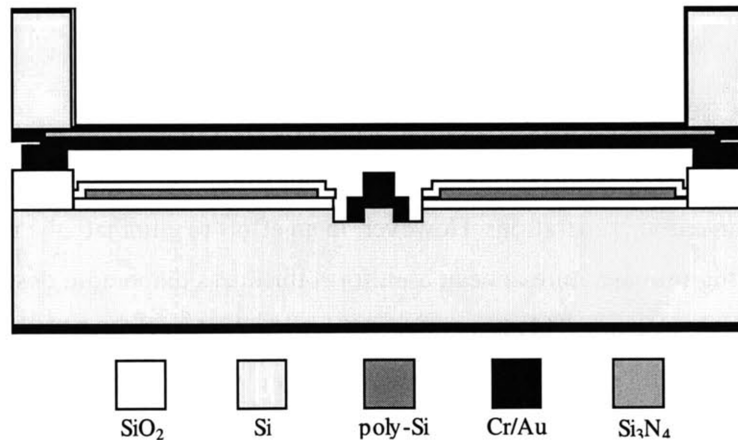

Figure 4.8 Latest MEMS switch design – nitride diaphragm

4.3 Process Flows

The final design, as discussed in Section 4.2.5 and depicted in Figure 4.7 or Figure 4.8, consists of a top wafer and a bottom wafer. The main role of the top wafer is to provide a structure that acts both as the movable part of an actuator and as a contact member of the switch. The bottom wafer contains the stationary actuation electrode and the other contact member. The top and

bottom wafers are processed *separately* before bonding together, and their fabrication considerations are rather distinct. The processing for the bottom wafer is very much similar to that for mainstream electronic devices except for the choice of contact metal, while the top wafer features classic bulk-micromachined structures. The processing sequences for the bottom wafer and top wafer are discussed in following subsections.

4.3.1 Bottom wafer

Detailed process descriptions for the bottom wafer are provided in Appendix B and the corresponding mask layouts in 0. This subsection discusses only the major process steps for bottom wafer as illustrated in Figure 4.9.

The starting substrate is a single-side polished silicon wafer. First, a field oxide is grown thermally and then patterned to define active device areas. The thickness of this oxide and any additional growth during subsequent high-temperature processes will ultimately set the gap between the contacts when the MEMS switch is open. A thin dry-oxide is grown next and then a layer of LPCVD poly-silicon is deposited and patterned. The poly-silicon is the stationary actuation electrode of the device and the oxide underneath provides the electrical isolation between the actuation electrode and the bottom substrate. An ion-implantation is performed to heavily dope the poly-silicon and another thin layer of dry-oxide is thermally grown on the poly-silicon to fully enclose the poly-silicon actuation electrode and activate the implanted dopants. The insulation oxides are patterned, and the exposed silicon substrate is then trench-etched to shape the bottom contact pedestals. Finally, metallization on both sides of the substrate is performed and a lift-off process is used to pattern the front-side metal.

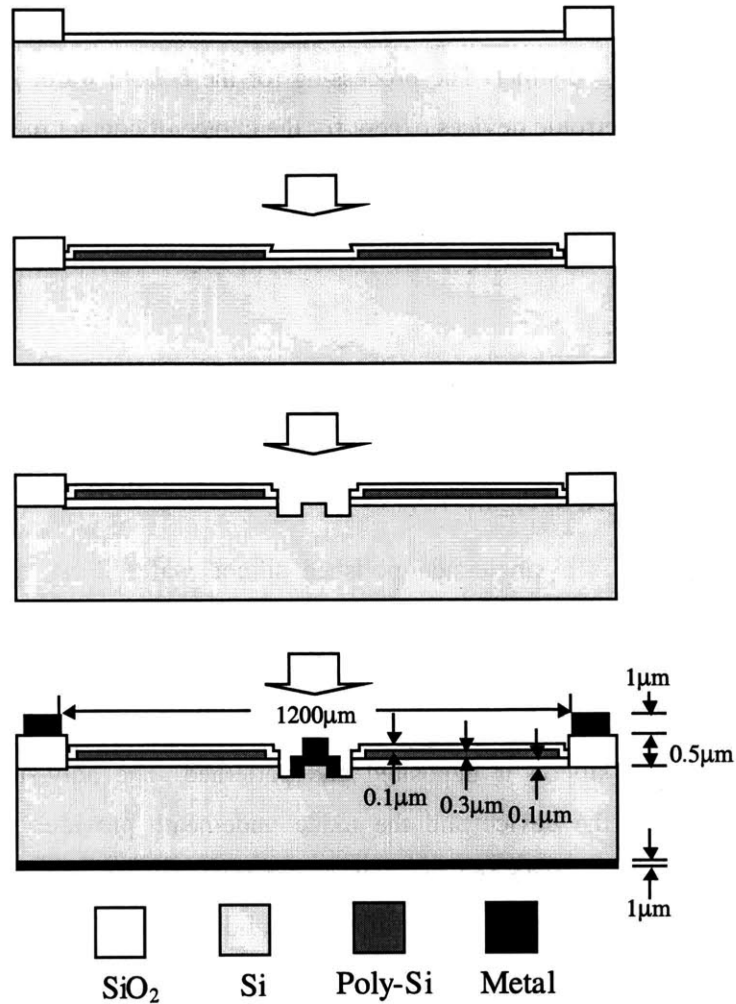

Figure 4.9 Bottom wafer process sequence

The field oxide thickness has two variations: *0.5 μm* and *0.75 μm.* The poly-silicon is also deposited in two different thicknesses: *3000 Å* and *5000 Å*. The poly-silicon actuator has openings in the center of the device area to accommodate the bottom contact pedestals. Drawings in Figure 4.9 show only one contact pedestal, but there are actually four variations in the bottom contact pedestal design: two different bottom contact patterns and two different pedestal sizes. As can be seen in the mask design, (mask ID: *BTM-NG* or *BTM-NB* in 0), the two patterns are: (1) a cluster of seven pedestals with *100 μm*-spacing between each individual pedestal and (2) a *300 μm*-radius ring of *16* pedestals. The two sizes are *3 μm* and *30 μm* in diameter (Figure 4.10 and Figure 4.11).

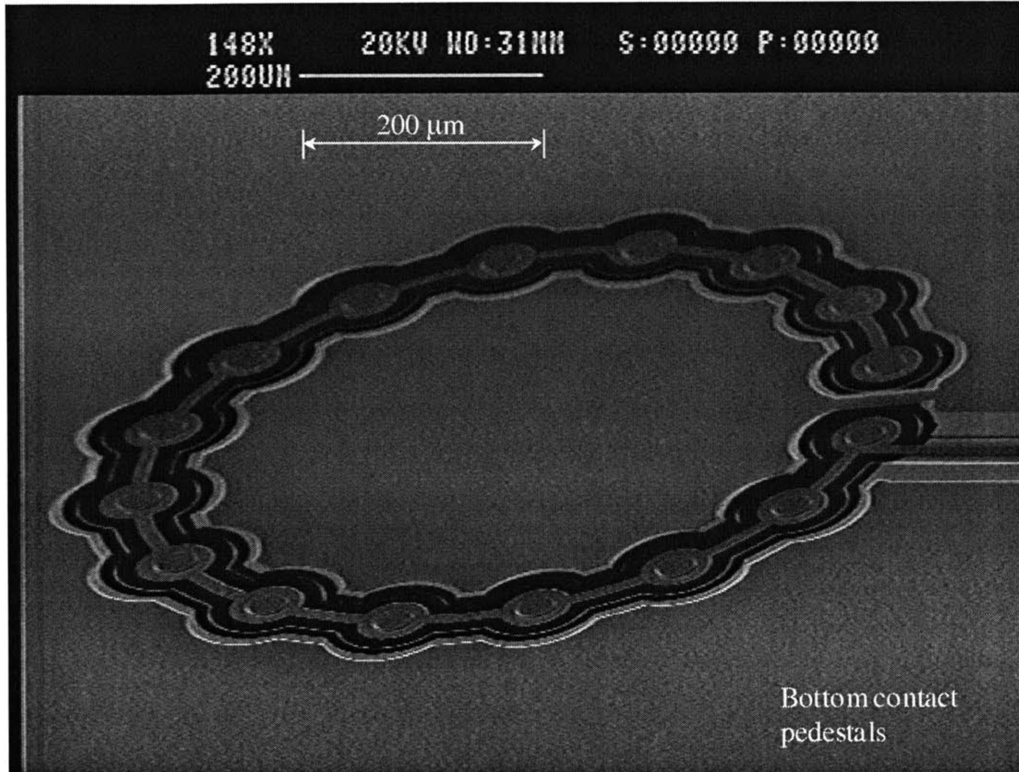

Figure 4.10 Micrograph of sixteen i-pedestals in a ring of *300 μm*-radius.

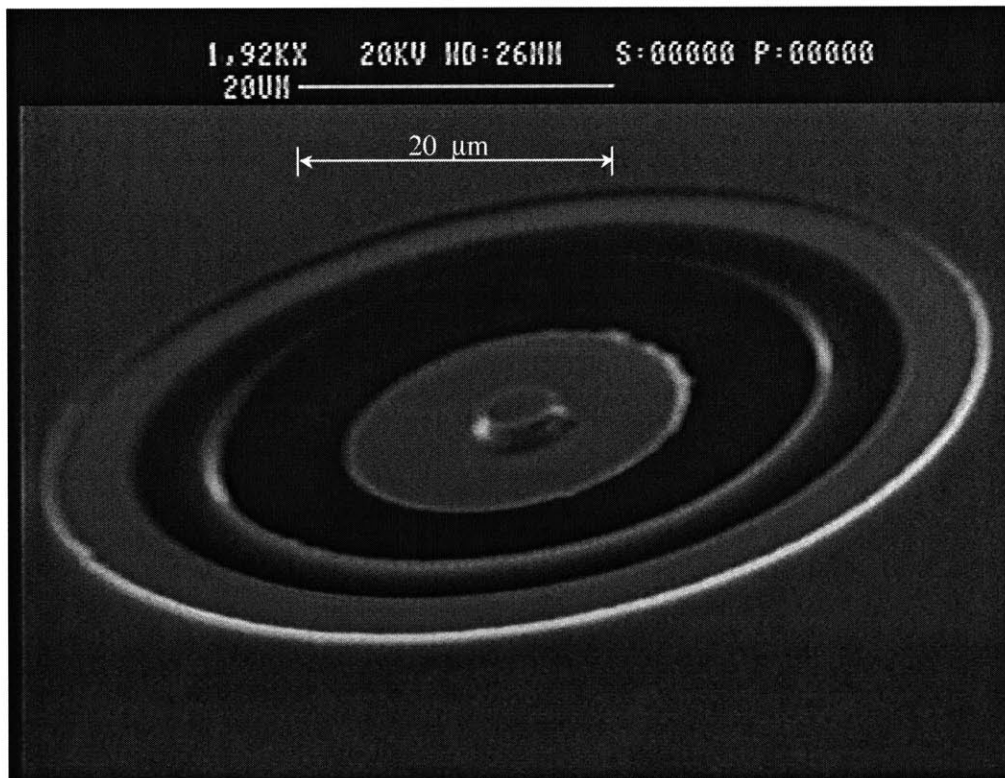

Figure 4.11 Micrograph of a close-up of a *3 μm*-pedestal contact.

4.3.2 Top wafer

This subsection provides a *brief* description of the fabrication of the top wafer. An expanded process sequence and mask layout design are given in **Appendix B** and **0**, respectively. There are two designs of the top wafer structure — one with a single-crystal silicon diaphragm and one with a LPCVD nitride diaphragm. Their processing sequences are different and will be discussed individually.

Silicon diaphragm

The fabrication of the *silicon* version of the top wafer starts with a heavily-doped *double-side-*polished SOI wafer. Three different thicknesses of SOI wafers were used: *10 μm*, *17.5 μm*, and *25 μm*. The SOI layer thickness determines the final diaphragm thickness. A photolithography step is performed on the handle side of the SOI wafer followed by a shallow trench etch to define the alignment marks. This etch is not shown in the simplified process sequence drawing in Figure 4.12. A second photolithography step is then performed on the SOI side of the substrate followed by a plasma silicon-etch stopping on the buried oxide to pattern the bonding pads, the diesaw cut lines, and the diaphragms. The first and second masks are aligned using *IR* (infra-red) through-wafer photolithography.

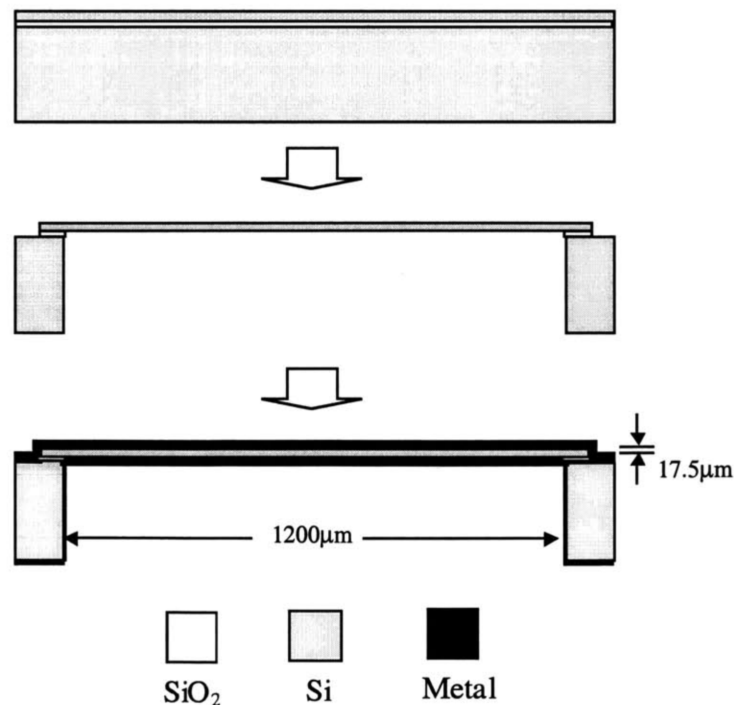

Figure 4.12 Top wafer process sequence (silicon diaphragm)

A third photolithography is performed on the handle side of the SOI wafer with a *thick* photoresist coating. The bulk of the handle-side silicon is etched away using a deep RIE etcher and the etch stops on the buried oxide layer. The exposed oxide is removed in BOE (buffered oxide etchant) solution and this completes the formation of the silicon diaphragm. Finally, metal deposition on both sides of the wafer is performed.

Nitride diaphragm

The starting material for the nitride version of the top wafer is a *double-side*-polished silicon wafer. First, the wafer is heavily phosphorus-doped using $POCl_3$ followed by a quick HF dip to remove the phosphosilicate glass. A thin layer (530Å) of dry oxide is then grown thermally for etch-stop purposes. A thin film of LPCVD silicon nitride is deposited with one of three different thicknesses (1000 Å, 1500 Å, or 2000 Å). This LPCVD silicon nitride film provides the structure material of the diaphragm. A photolithography step is performed on the backside of the wafer followed by a shallow trench etch to define the alignment marks. This etch is not shown in the simplified process sequence drawing in Figure 4.13.

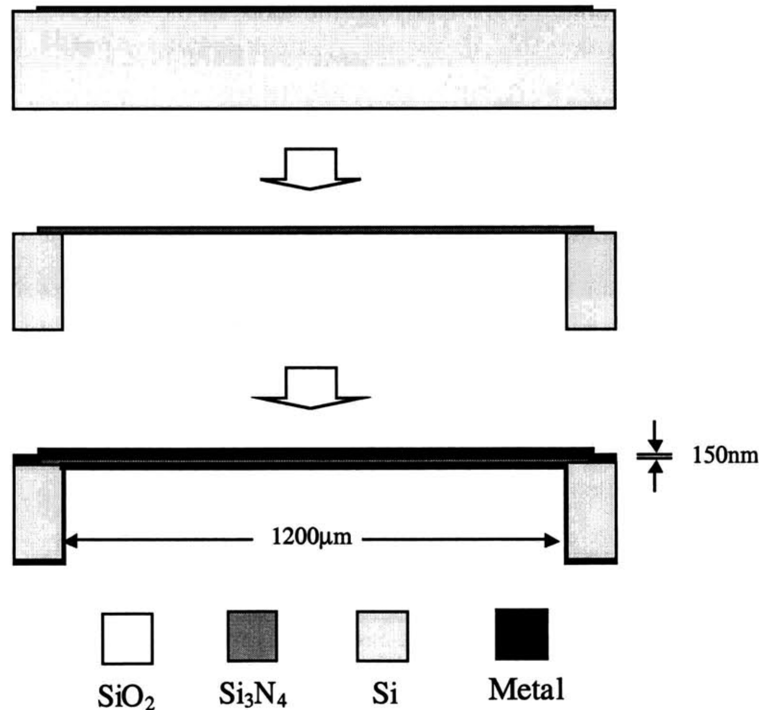

Figure 4.13 Top wafer process sequence (nitride diaphragm)

A second photolithography is then performed on the front side of the substrate followed by plasma etches to pattern the oxide and nitride films. The un-etched dielectric films define the bonding pads, the diesaw cut lines, and the diaphragms. Moreover, since the nitride film is not

electrically conductive, this etch is necessary because it allows parts of the underneath silicon substrate to expose thereby making the electrical connection between the contact metal, which is to be deposited later, and the substrate. The first and second masks are aligned using *IR* (infra-red) through-wafer photolithography. A third photolithography is performed on the handle side of the backside of the wafer with a *thick* photoresist coating. The bulk of the silicon is etched away using a deep RIE etcher and the etch stops on the oxide layer grown earlier. The exposed oxide is removed in BOE (buffered oxide etchant) solution. Finally, metal deposition on both sides of the wafer is performed.

4.4 Fabrication Issues

This section is dedicated to the discussions on fabrication problems that might seem trivial but could have devastating consequences if not properly treated. Physical explanations or postulations of the causes of these problems are made in order to reach solutions or alternatives. Some solutions and alternatives suggested here are *not* optimized *nor* are they the only available answers to the specific problems. More investigations are needed to achieve a full-scale understanding of the problem and are beyond the scope of the thesis.

4.4.1 Die-level thermocompression bond

The gold-to-gold thermocompression bond of the top wafer to the bottom wafer is undertaken at the *die-level*. This presents a nontrivial problem in particle contamination control as the wafers are diced and the bonding surfaces are exposed to diesaw slurries *before* bonding. The cleanliness of the bonding surfaces is crucial to the bond integrity as well as to the control the contact air-gap. Therefore, a special cleaning treatment is exercised to ensure the cleanliness of the bonding surfaces. First, a layer of photoresist is coated and soft-baked before the wafer is brought out of the cleanroom environment for diesawing. During the dicing, this layer of photoresist protects the sensitive bonding surfaces from being in direct contact with the diesaw slurries. A solvent wet clean followed by an ultraviolet-ozone dry clean is performed *after* the dicing. The solvent clean comprises of a sequence of acetone, methanol, and iso-propanol baths in that order followed by a *DI* (de-ionized) water rinse. For the bottom wafers, such solvent wet clean can be carried out with *ultrasonic* agitation to enhance the shake-off of particle contaminants. As for the top wafers, the wet solvent clean can only be performed with some gentle stirring at most, as extreme care must be taken in handling the top wafers once the delicate diaphragms are formed.

Besides the post-diesaw pre-bond cleaning, other complications of the *die-level* bonding process are (1) the alignment between the top die and the bottom die, (2) the uniform application of pressure during bonding, and (3) the handling of dice on a heated hot plate. The die-level alignment is achieved with the help of an L-shaped alignment jig since the top die and the bottom die are of the same size. The compression pressure during bonding is realized by physically pressing the top and the bottom wafers together with a pointed tool. A dummy die is stacked on top of the device die as a buffer between the pointed tool and the device during bonding. This buffer dummy die helps diffuse the force from a concentrated source into more uniformly distributed pressure. Finally, a *4"* silicon wafer is employed as a platform, upon which die-level alignment and thermocompression bond of the dice are conducted, to facilitate handling and transportation of the device die.

4.4.2 Diesaw

Coating the device wafer with a layer of photoresist before diesaw for particle contamination control can backfire if it is not cautiously done. This is especially true for wafers with the highly tensile-stressed nitride diaphragm structures. The protective photoresist is coated and moderately baked (90°C for 10 minutes) but *not* to be hard-baked. In addition, effort should be made to minimize the storage time during the photoresist-coating/dicing/solvent-clean process. Hard-baking or long storage time would make the photoresist overly crispy and create cracking problems as shown in Figure 4.14. This sample has a layer of photoresist coated and soft-baked before diesaw and then kept in a dry storage box for more than three months. As the photoresist gets over-dried over the long storage time, cracks initiate from the cut edges and propagate within the coated photoresist layer. Normally this would not be a problem if the diaphragm structure can sustain cracks on the surfacial photoresist. For the ultra-thin tensile-stressed nitride diaphragm, the cracks in the coated photoresist layer transfer to the diaphragm structure causing permanent damage as can be seen on the left side of Figure 4.14 where part of a circular nitride diaphragm is shown.

Additionally, to avoid direct contact between the delicate diaphragms and the diesaw mounting tape, it is desirable to have the diesaw performed on the device side of the top wafer with the blade-cooling wafer jet turned down to lower its physical impact on the diaphragms. In processes where dicing must be done on the handle side, extreme care must be taken because the fragile diaphragms can break by roughly mounting wafers onto the tape, and can peel off with the diesaw tape when dismounting. UV-dismountable tapes are recommended in such cases.

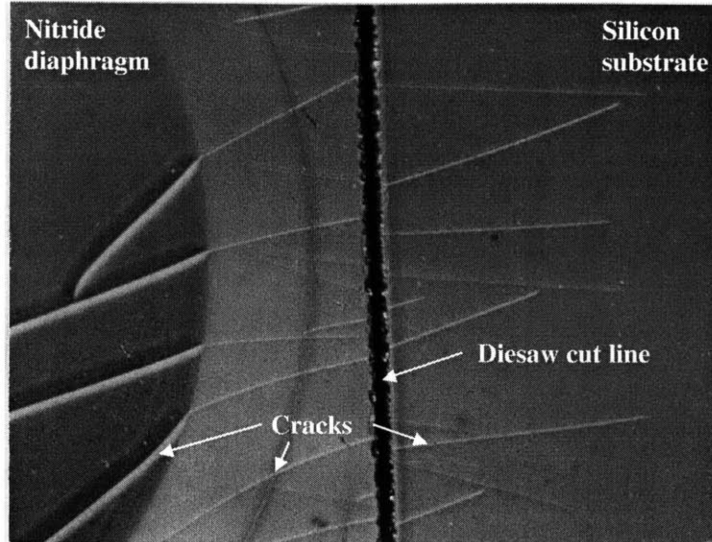

Figure 4.14 Crack propagation in overly dried photoresist

4.4.3 Gold evaporation

Gold (*Au*) is chosen as the contact metal for the MEMS switch because of its low resistivity and packaging considerations. Surface quality of the gold film has a decisive impact on the switch performance. An electron-beam evaporative deposition system is employed for the gold film deposition. In the earlier stages of the device process development, micron-sized gold spheres were observed to be scattered all over the surface of the deposited gold film; see Figure 4.15. It is believed that the formation of such gold spheres is closely linked to the choice of crucible material. Noticeable gold spheres were observed if the deposition was carried out with a *graphite* crucible containing the gold source but *not* with a *tungsten* crucible.

Deposition of a smooth gold film relies on well-controlled heating of the source material generating uniform gaseous gold vapor. It is conceivable that gold spheres can be rendered when such evaporating conditions are not optimized resulting in *spitting* of tiny liquid gold droplets onto the wafers. The underlying physics of the connection between the crucible material and gold spitting is not fully understood, but the following two scenarios are hypothesized based on discussions with students and staff members.

It is known that melted liquid gold *does not* wet the graphite surface. Such non-wettability between melted gold and the graphite crucible allows out-gassing of the crucible to take place near that non-wetting wide-angle gold-graphite contact interface. As the gas jet enters and leaves the liquid gold, bubbles are created in the melted gold causing gold spitting. With a tungsten

crucible, melted gold will wet the crucible sidewall leaving the crucible out-gassing to occur further away from the melted region without bubble generation.

Tiny carbon powders can be generated when the graphite crucible is hit by the electron beam and these can be re-deposited on the surface of the melted gold source. The presence of such carbon powders on the melted gold source yields non-uniform heating and stirring during the evaporation, and in turn produces gold spitting. With a tungsten crucible, there is no powder generated and therefore it is preferred for smooth gold film deposition.

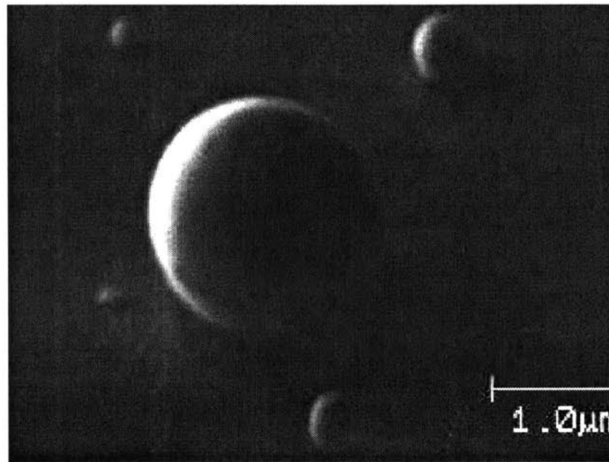

Figure 4.15 Gold spheres on deposited gold film (courtesy of C. Tsau)

From the viewpoint of producing smooth gold films, tungsten crucibles are favored. On the other hand, from the experience of the MTL staff, tungsten crucibles tend to crack more frequently and create more maintenance problems than graphite crucibles. A solution to this problem is to have a smaller tungsten crucible *inside* a regular-size graphite crucible. Lower evaporation power and tighter beam focus are also called for in this modified process.

4.4.4 Miscellaneous Issues

In this subsection, other fabrication issues and their solutions or alternatives are discussed.

Gold agglomeration

Gold does *not* adhere to a silicon substrate very well and usually a thin (30~100 Å) layer of chromium (*Cr*) or titanium (*Ti*) is deposited first for adhesion purposes. The thermocompression bond is performed at a temperature (300~350 °C) just below the *Au-Si* eutectic temperature of 363°C. It has been observed that the mirror-smooth surface quality of the metal on the diaphragm region degrades after this moderate thermal cycle for *Cr/Au* metal films. Such surface roughening is speculated to results from metal agglomeration or grain coalescence. With titanium as an

adhesion material, this agglomeration effect is not as apparent and therefore *Ti/Au* is a preferred combination.

Stress gradient of diaphragm

One of the advantages in bulk-micromachining technologies over surface-micromachining is the capability to construct stress-free single-crystal silicon microstructures. However, care must be taken in the process design to minimize high-temperature cycles as stress gradients can be introduced leading to undesirable outcomes. More discussion can be found in Section 4.2.4.

Packaging

The MEMS switch device can be actuated *both* electrostatically and pneumatically. Several tricky packaging issues must be considered to interface the device with external electronics and pneumatics. These packaging complications are addressed in Section 5.2.2.

Deep RIE etch non-uniformity

Fabrication of the diaphragm structure is realized by etching the silicon through the substrate and stopping on a thin oxide layer. A time-multiplexing Bosch process is employed to achieve etch sidewall profiling. One of the issues in the deep silicon etch is the non-uniformity of this etch over the wafer as the etch rate is higher near the wafer periphery and lower near the center. A problem with this etch non-uniformity and a thin oxide etch-stop is the difficulty to end the deep etch all over the wafer on the etch-stop layer, as the oxide etch-stop might be thinned and eventually etched through in higher-etch-rate regions. To ensure that the deep etch ends on the thin oxide etch-stop throughout the wafer, it is necessary to switch to a etch recipe with a *higher* silicon-to-oxide etch selectivity at the end of the etch process. Because the MEMS switch device does not require highly precise sidewall control, it is therefore possible to sacrifice anisotropy for selectivity in order to accommodate etch non-uniformity.

4.5 Summary and suggestions

This chapter focuses on the fabrication of the MEMS switch device and several of its complications. Earlier generations of the prototype are first introduced and their design considerations are explained. The process descriptions for final versions of the device are then given. Various fabrication issues are discussed and solutions and/or alternatives are suggested. Detailed process travelers and mask layouts are presented in Appendix B and 0, respectively. As

discussed in Section 3.3, a bossed diaphragm has several desirable features such as simplification in device modeling and straightforward contact force calculations but is prohibited due to stress-related fabrication issues. The latest MEMS switch prototype devices exhibit promising results as presented in Chapter 5. Nevertheless, in the interest of future improvements, the following suggestions are made:

Use of wet etchant for diaphragm micromachining

The diaphragm structure of the MEMS switch is formed by removing the bulk of the silicon handle substrate using a lower throughput deep-RIE technology (Section 4.3.2). A more economical approach would be the use of anisotropic silicon wet etchant systems enabling batch fabrication. There are three common anisotropic wet etchant systems used to bulk-micromachine silicon structures. Each has its advantages and disadvantages as listed in Table 4.1 [80-82].

Etchant	Alkaline-hydroxide (*KOH* or *NaOH*)	Ethylene-diamine/pyrocatechol (*EDP*)	Hydrazine (N_2H_4)
Diluent	Water (H_2O)	Water (H_2O)	Water (H_2O)
Adv.	• High (100)/(111) etch rate ratio	• High selectivity over various masking materials	• Low SiO_2 etch rate
Disadv.	• Alkali contamination • Relative high SiO_2 etch rate	• Optically dense • Carcinogenic possibilities	• Low (100)/(111) etch rate ratio • Gas explosiveness

Table 4.1 Comparison of anisotropic silicon etchant systems

Replacing diesaw with deep-trench-etch-and-cleave

The die-level thermocompression bond in the very last step of the process calls for dicing *preceding* the bond and thus, as discussed in Section 4.4.2, raises particle contamination concerns. Diesaw tape mounting/dismounting can also create complications. Another approach of dicing that could lessen the above-mentioned problems is to deep-trench-etch the dicing lines and then cleave them. This is a commonly used practice but adds complications in handling the fragile wafers after the deep-etch. New masks and process sequences would be required, and these might take some trial and error to optimize.

Reduction in device density

Many pneumatic packaging problems (Section 5.2.2) originate from the tight space between the test window, which must be open, and the diaphragm structure, which must be tightly sealed. This is *not* a problem if the MEMS switch is only to be electrostatically actuated. However, as a

diagnostic tool, pneumatic actuation is employed to characterize the mechanical integrity of the diaphragm and packing the device density unnecessarily raises the pneumatic packaging difficulties.

Chapter 5 TESTING AND CHARACTERIZATION

5.1 Introduction

This chapter contains the results of experiments performed on the MEMS switch. The prototype switch has gone through several evolutions and not all tests are performed with the same type of switch. In the discussion of each individual test, an effort will be made to specify the type of switch being investigated. It is worth mentioning that such design modifications are made to facilitate some actuation tests or to enhance consistency of the post-packaging device quality. In spite of the difference in the mechanical design of the device, the contact characteristics of the switch are expected to be similar. Section 5.2 addresses some packaging issues of the device and the instrumentation for testing. Sections 5.3 and 5.4 are concerned with the electrical model and mechanical model, respectively of the switch. Comparisons between simulations and measurements are made and discussed. In Section 5.5, a prototype switch is pneumatically actuated while its on-state performance is characterized. Similar actuation testing is performed in Section 5.6 but in an electrostatic fashion. Combined pneumatic and electrostatic actuation is demonstrated and discussed in Section5.7. Section 5.8 is concerned with the on-state contact resistance of the device and its dependency on other parameters. Section 5.9 investigates the switching times of the MEMS switch when electrostatically and pneumatically actuated. The current capacity of a single switch cell is investigated in Section 5.10. Moreover, in Section 5.11 the prototype device is repeatedly operated to understand its performance drift over many cycles of operations. Finally, a brief summary is given in Section 5.12.

5.2 Instrumentation

This section discusses the *post* fabrication treatment of the MEMS switch in preparation for testing, and the hardware and software employed to perform the tests. A PC-based data

acquisition system is built for automatic data collection and better measurement integrity. In addition to a PC, the instrumentation hardware consists of a *Keithley*™ 12-bit data acquisition board and a *National Instruments*™ GPIB board, a *Hewlett-Packard*™ semiconductor analyzer, a *Hewlett-Packard*™ impedance analyzer, and several simple circuits with power operational amplifiers and power supplies. Integration of the individual hardware tools and automation of the testing are realized using *National Instruments*™ *LabVIEW® VI* programming software.

5.2.1 Why dual actuation schemes?

The first task in the characterization study of the MEMS switch is the verification of the mechanical integrity of the movable diaphragm. In situations where a multi-energy-domain transducer deviates from its predicted behavior, the debugging process can be considerably difficult if the different energy-domain physics are coupled. Therefore, it is judicious to separate this mechanical characterization from electrostatic actuation issues by introducing pneumatic actuation as a diagnostic vehicle. The idea is to use pneumatic actuation to study the pressure-deformation behavior of the diaphragm, so that potential *mechanical* problems, if they arise, can be identified and isolated from *electrical* complications. Furthermore, in addition to its diagnostic advantage, pneumatic actuation is a more straightforward approach from the viewpoint of proof-of-concept demonstration.

On the other hand, there are some tricky packaging considerations that must be addressed in order to implement pneumatic actuation and, at the same time, to allow internal lead-out test pads accessible to test probes by keeping a testing window clear from obstruction. These packaging issues are discussed in Subsection 5.2.2.

5.2.2 Packaging issues for pneumatic actuation

On the top surface of the device, there is a testing window and a circular diaphragm, as shown in Figure 5.1. Through the testing window, internal test pads are exposed so that they are accessible to external test probes. These test pads are needed to acquire potentials of contacts to carry out the four-point-probe measurement (Section 5.2.4), and to access the actuation electrode. This testing window has to be left unblocked after packaging, while the circular diaphragm needs to be fully covered and hermetically sealed. In order to enable pneumatic actuation, a leak-free package must be provided and normally this can be achieved by firmly holding down a fitting fixture with an o-ring over the circular diaphragm. However, the clamping force of an o-ring might damage the die, and insufficient clearance exists between the testing window and the diaphragm to allow for an o-

ring. Because of these issues, the proposed packaging scheme, as depicted in Figure 5.2, is to stack a sealing fixture onto a test device and use epoxy in place of *both* the o-ring and the clamping mechanism. Sealing and adhesion between the fixture and the test device can be achieved simultaneously after the epoxy is cured in this scheme. Ideally, the epoxy used in this application should possess properties such as quick curing at room temperature, minimum volume change, and moderate pre-cure viscosity.

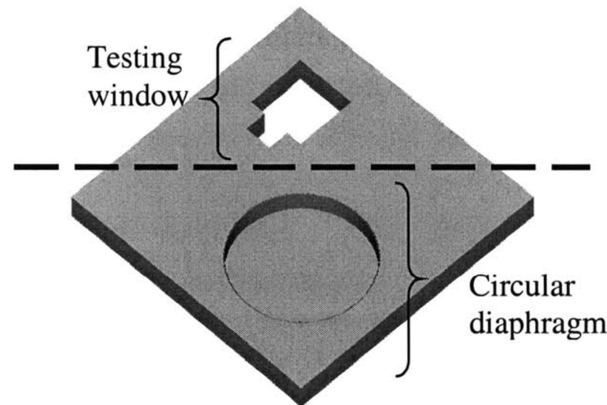

Figure 5.1 Top view of the test device. Testing window needs to be *open* and circular diaphragm needs to be *completely sealed* after packaging.

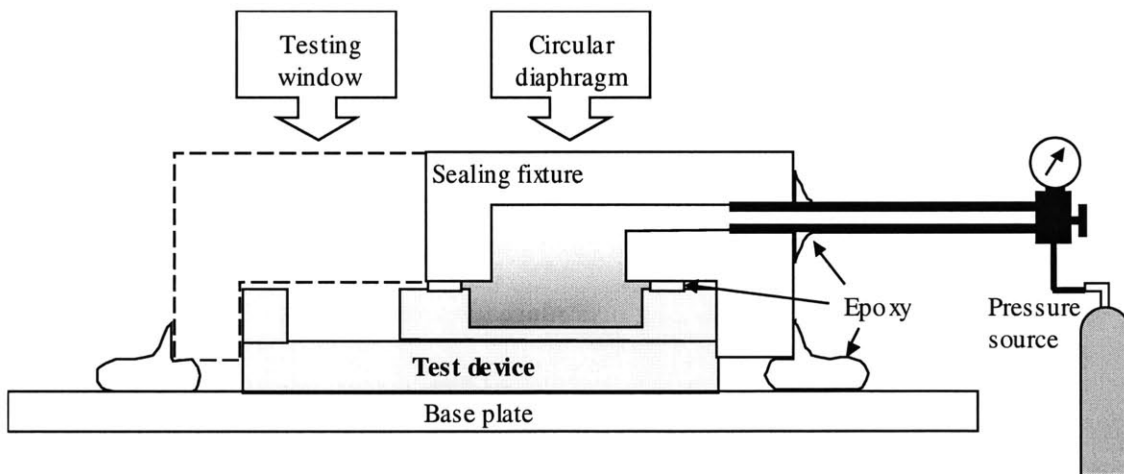

Figure 5.2 Packaging scheme (side view)

In this scheme, a sealing fixture, a conductive base plate, a *scanivalve*® tube, quick-cure epoxy, and a reusable alignment jig are used to package the test device. The geometric designs of the sealing fixture and the alignment jig are provided in Appendix D. In order to leave the testing window clear of obstruction after the hermetic packaging, the sealing fixture is purposely cut on one of the corners, as shown in Figure 5.2 and Figure 5.3. The assembly of the sealing fixture and the test device starts with careful application of the epoxy around the outside ridge of the circular

diaphragm on the device. Before the epoxy cures, the sealing fixture is glued onto the device using a mechanical alignment method. The sealing fixture serves as an interface between the test device and the *scanivalve®* tube and the epoxy provides the sealing function. This mechanical alignment between the sealing fixture and the test device is performed with the help of an alignment jig, as schematically shown in Figure 5.3. The alignment jig is reusable and essentially functions as a position offset reference for the sealing fixture and the test device. After capping the test device with the sealing fixture using epoxy, the stack is then attached onto a conductive base plate for easy handling and, more importantly, electrically connecting to the bottom of the test device, as the bottom surface of the device acts as one electrode and takes part in the testing experiments.

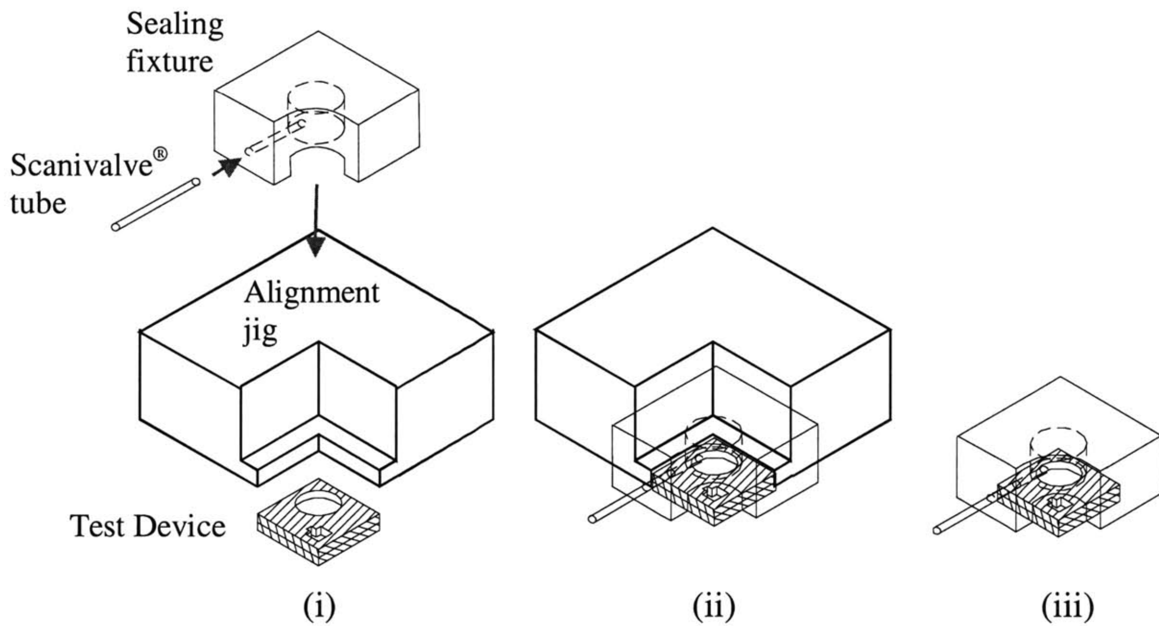

Figure 5.3 Packaging procedure (perspective view)

Figure 5.3 pictorially illustrates the major steps of the new packaging scheme before attaching to a base platform. It is worth mentioning that the use of epoxy in this packaging scheme has both advantages and disadvantages. To its advantage, airtight sealing can be achieved without any clamping mechanism thus eliminates the concern of inducing stresses to the diaphragm. Also, it is possible to dispense the need to thermo-compression-bond the top wafer with the bottom wafer because they can be held together between the sealing fixture and the base plate with this packaging scheme (Figure 5.2). To its disadvantage, this packaging process is time-consuming and highly crafty. For example, the optimal amount of epoxy used to glue the sealing fixture and

the test device together must be learned through practice. The amount of epoxy must be enough to ensure hermetic sealing, but not too much otherwise excess epoxy might wick onto the diaphragm and change its mechanical property or wick into the interface between the top and bottom wafers and change the electrical properties of the device. Moreover, it has to be done in a timely manner because the epoxy hardens in minutes.

Lastly, all packaging issues come about as a consequence of the hermetic sealing requirement to allow pneumatic actuation. The packaging for a pure electrostatic switch *does not* need the sealing and will be as straightforward as ordinary microelectronic packaging.

5.2.3 Software

The programming software used to control the sequence of the electronic variable outputs and measurement data collection is *LabVIEW®* version 4.0 by *National Instruments™*. The details of a *LabVIEW®* program that is used to characterize the on-state performance of the switch while sweeping the actuation voltage at different bias pressures is presented in Appendix F. Other LabVIEW® programs bear similar key block diagrams and therefore are not shown.

5.2.4 Hardware

The characterization of the MEMS switch is carried out through various experiments. These testing experiments focus mainly on air-gap capacitance measurements, pneumatic actuation, electrostatic actuation, contact resistance, current carrying capacity, switching speed, and the cyclic operations of the prototype device. The following is a list of requirements that the design of the instrumentation hardware had to address with a brief discussion provided to explain the approach for the corresponding requirement.

1. Capacitance measurements

   To determine the air gap distance, various capacitance measurements are performed (Section 5.3) using an impedance analyzer (HP4194) that can make impedance measurements while sweeping its DC bias or frequency. The integration of this impedance analyzer with other experimental hardware is done through a GPIB cable and a PC.

2. Pressure control

   A precise and repeatable pressure control is essential in pneumatic actuation tests. An MKS model 640A series differential pressure controller is used for this application.

Manufacturer's specification on pressure control accuracy is ±0.5% of the reading. For a 12-bit digital-to-analog conversion with 100 Torr full-range, the discretization error would be *24.4 mTorr*, or 4.72×10^{-4} *psi*, or 3.2×10^{-5} *Atm*, or *3.25Pa*. The pressure controller features a PI (Proportional-Integral) controller with tunable P gain and I gain. The optimal tuning of the pressure controller gains is a strong function of the gas flow rate, which can be preset with a needle valve downstream as depicted in Figure 5.4.

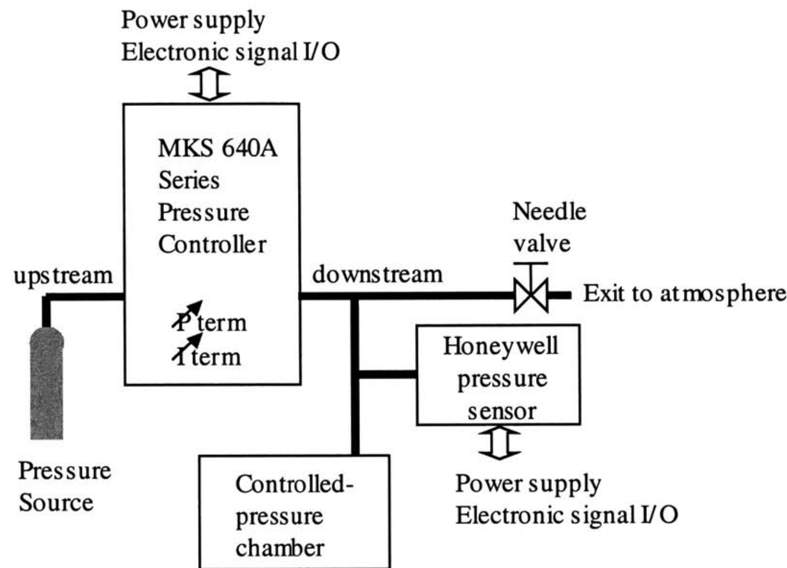

Figure 5.4 Pressure control scheme

3. Pressure measurement

Although the MKS 640 series pressure controller provides access to its internal electronic pressure signal from the transducer, a third-party Honeywell pressure sensor that possesses better signal-to-noise sensing performance at low pressures (less than 0.1 psi) is introduced to the pneumatic network as shown in Figure 5.4. The 0.15% repeatability of the manufacturer's specification with 30 psi full-range results in sensor errors of *0.045 psi* or 3.06×10^{-3} Atm, or 3.1×10^{2} Pa. Considering the 12-bit resolution of the *Keithley™* data acquisition board and the fact that the sensor uses only half of the full 10 V range, the discretization error of pressure sensing is 1.46×10^{-2} psi, or 9.96×10^{-4} Atm, or 1.01×10^{2} Pa.

4. Four-point-probe resistance measurement

The four-point-probe resistance measurement technique is a well-accepted method for resistance measurement because of its independency of the parasitic resistance in the leads. As schematically shown in Figure 5.5 (also refer to Figure 5.7), the contact

resistance of interest R_{12} between contact points 1 and 2 can be detected in the following fashion. By injecting current I into circuit path *T-1-2-B*, a voltage drop V_{12} across points 1 and 2 is created. This voltage can be measured using a high input-impedance voltage sensor through terminals 1' and 2'. The resistance R_{12} can be determined as $\Delta V_{1'2'}/I$. The advantages of such technique are that the parasitic resistance in the test leads, $R_{11'}$ and $R_{22'}$, and the parasitic resistance in the substrates, R_{T1} and R_{B2}, will not *contaminate* the resistance measurement.

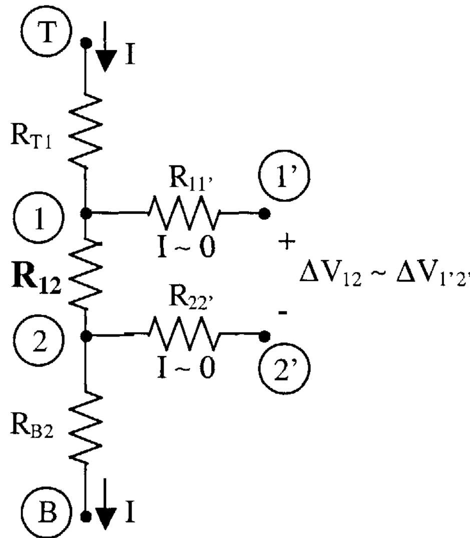

Figure 5.5 Four-point-probe resistance measurement

In order to facilitate the four-point probe measurement technique, the instrumentation must have current supply capability, current measuring capability, and high-impedance voltage measuring capability. The data acquisition board has a *20 mA* limit on its output current channels and does not have current measuring channels. To circumvent these limitations, a current source is provided with a unity-gain operational amplifier and an external power supply. Current measurement is performed by inserting a resistor of known value into the current path, acquiring the voltage drop across the resistor, then calculating the ratio of the measured voltage to the known resistance. Moreover, voltage measurement is carried out using the built-in high-impedance voltage measuring channels of the data acquisition hardware.

5. Actuation voltage output

The voltage output channel of the data acquisition board is limited to *20 V* maximum. The voltage necessary to actuate the diaphragm depends on geometry design and material properties of the diaphragm. However, the actuation voltage is also very sensitive to

uncertainties in the actual air gap separation. In order to account for such uncertainties, it is desirable to have a wide range of voltage output capability. Such voltage amplification is implemented using an operational amplifier with a non-inverting configuration and external power supplies.

6. Test automation

   Test process control and automatic data collection employ a *Keithley*™ *KAS1800* series data acquisition board for direct voltage inputs/outputs and a *National Instruments*™ GPIB board for communications among equipments. The programming is implemented using National Instruments *LabVIEW*® and more details are provided in Appendix F.

Other miscellaneous tests can be performed with standard testing equipments such as an oscilloscope, a multimeter, or a semiconductor analyzer. The integration of the computer, test equipments, electrical hardware, and pneumatic lines are schematically depicted in Figure 5.6.

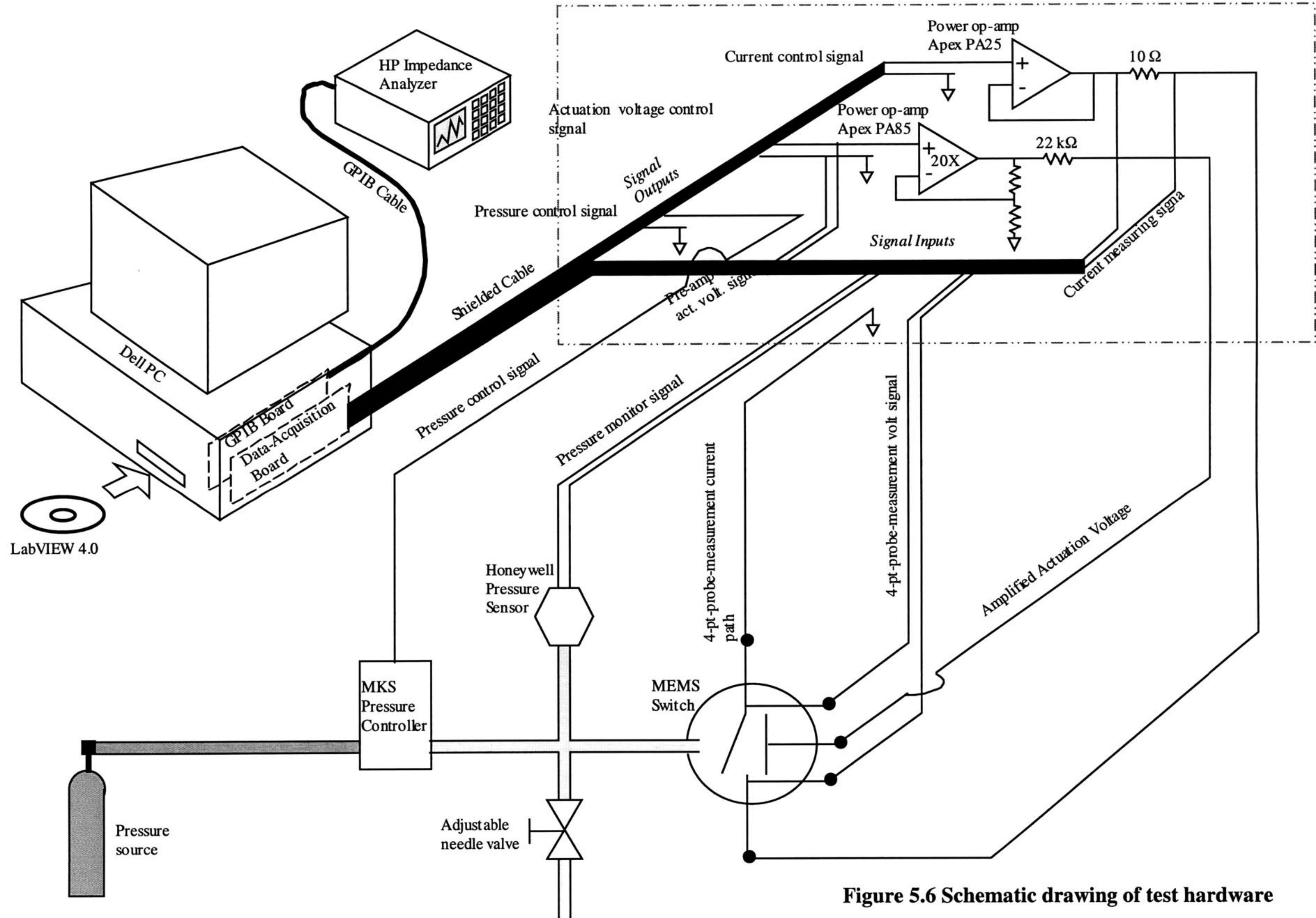

Figure 5.6 Schematic drawing of test hardware

5.3 *Electrical Model*

After a prototype switch is fabricated (Chapter 4) and packaged (Subsection 5.2.2), a series of pre-checks are performed through its terminals to assure device integrity. Figure 5.7 is a cross-section drawing of one MEMS switch cell and it can be seen that there are three electrically isolated parts, namely the top diaphragm (indicated as *1*), the bottom substrate (indicated as *2*), and the poly-silicon actuator encapsulated within oxide layers (indicated as *A*). The first integrity check is to verify that all three terminals are electrically open-circuited. Secondly, a series of capacitance measurements are made to affirm the thickness and dielectric characteristics of the thermally grown oxides as well as to determine the air gap distance between the top diaphragm and the bottom contact. The discussion of how the gap separation is determined starts with an in-depth understanding of the electrical characteristics the device.

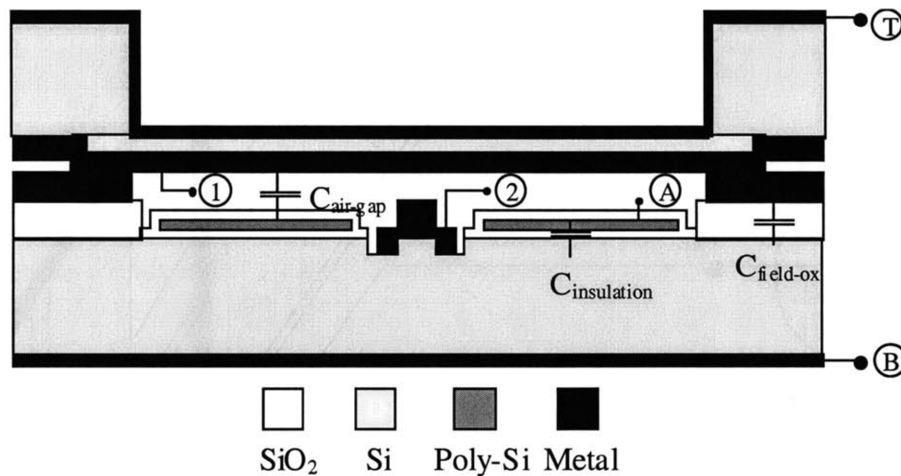

Figure 5.7 Device cross-section drawing of one single switch cell (electrical model)

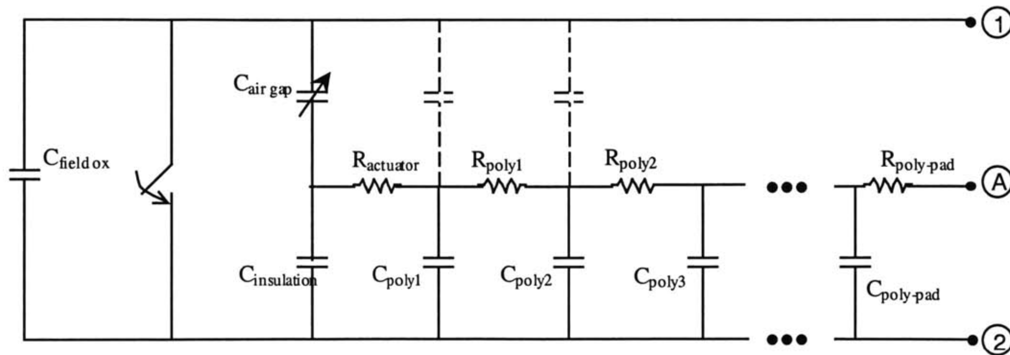

Figure 5.8 Distributed system circuit model of a single switch cell

The distributed system can be treated by solving partial differential equations but this approach is unnecessarily complicated. Figure 5.8 shows a simplified distributed system circuit model of the one single switch cell is depicted. Note that not shown in Figure 5.7 are a long poly-silicon lead-out line and a poly-silicon test pad that are used to allow electrical access to the otherwise-oxide-enclosing poly-silicon actuator. The long lead-out line and test pad are modeled as a long series of *RC* circuits where the *R*'s are the resistors distributed along the line and the *C*'s are the capacitors distributed along the line between the poly-silicon lead-out line and the substrate. Shown in dashed lines in Figure 5.8 are the distributed capacitors between the poly-silicon lead-out and the top diaphragm. Their values are orders of magnitude lower than the other capacitances in the system because of their considerably smaller area and relatively wide air gap distance, and will therefore be neglected. The capacitance between the poly-silicon actuator and the top diaphragm, $C_{air\text{-}gap}$, is variable. Its value depends on the air gap separation and can be used as a measure of diaphragm deflection.

The electrical system model shown in Figure 5.8 is further simplified to the one shown in Figure 5.9 by lumping the long series of *RC*'s in the poly-silicon lead-out line and totally neglecting the capacitance between the lead-out line and top diaphragm. This three-terminal circuit model can be represented in a more generalized format as the one shown in Figure 5.10 where Z_i's are general impedance elements whose definition are given in Figure 5.10.

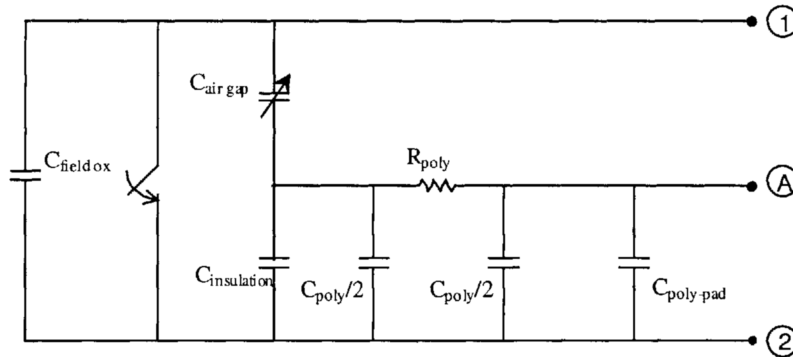

Figure 5.9 Further simplified electrical model of a single switch cell.

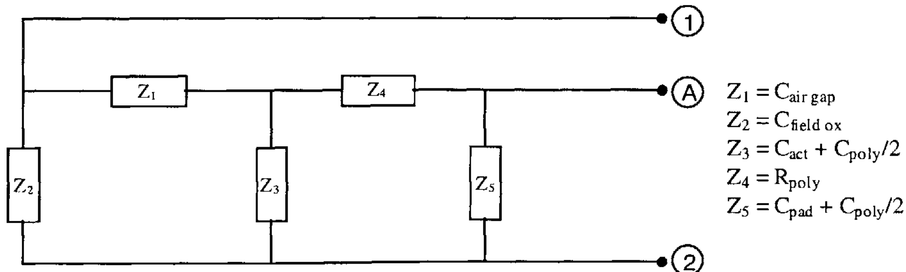

Figure 5.10 Generalized representation of the simplified electrical model

The impedance seen between terminals *1* and *A* is

$$Z_{1A} = \frac{1}{\frac{1-\{left\}}{Z_1} + \frac{1-\{right\}}{Z_2}} \tag{5.1}$$

where

$$\{left\} = (\frac{Z_4}{Z_1 + Z_4})(\frac{Z_3 + Z_2 // Z_5}{Z_1 // Z_4 + Z_3 + Z_2 // Z_5}) + (\frac{Z_5}{Z_2 + Z_5})(\frac{Z_1 // Z_4}{Z_1 // Z_4 + Z_3 + Z_2 // Z_5}),$$

$$\{right\} = (\frac{Z_4}{Z_1 + Z_4})(\frac{Z_2 // Z_5}{Z_1 // Z_4 + Z_3 + Z_2 // Z_5}) + (\frac{Z_5}{Z_2 + Z_5})(\frac{Z_3 + Z_1 // Z_4}{Z_1 // Z_4 + Z_3 + Z_2 // Z_5}).$$

By assuming that $Z_{1A}(j\omega)$, the frequency-dependent impedance element measured between terminals *A* and *1* by the impedance analyzer, is composed of a resistor and a capacitor in series (Figure 5.11), the apparent resistance, *R'*, and the apparent capacitance, *C'*, are then

$$R' = \operatorname{Re}\{Z_{1A}(j\omega)\}, \qquad C' = -\frac{1}{\omega \operatorname{Im}\{Z_{1A}(j\omega)\}} \tag{5.2}$$

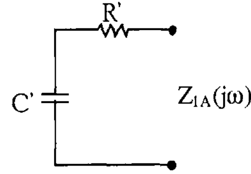

Figure 5.11 Electrical model for impedance analyzer: A resistor and a capacitor in parallel

At very low frequencies, the capacitive impedance becomes dominated and the electrical model degenerates to Figure 5.12 when the switch is in its OFF-state and the apparent capacitance *C'* can be expressed as follows:

$$C' = -\frac{1}{\omega \cdot \operatorname{Im}\{Z_{1A}\}} \approx C'_{air-gap} + \frac{C_{field-ox} \cdot C_{insulation}}{C_{field-ox} + C_{insulation}}, \text{ when the switch is OFF.} \tag{5.3}$$

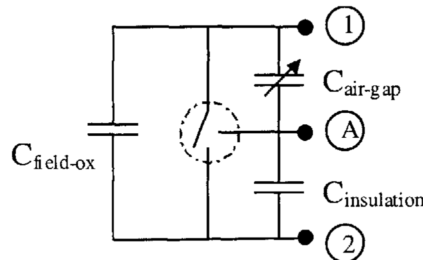

Figure 5.12 Low-frequency circuit model of a single switch cell in OFF-state

The measurements of the impedance Z_{IA} are made at a frequency of *1 kHz*, which is about the lowest end of the available frequency spectrum of the impedance analyzer. Note that $C_{air\text{-}gap}$ is modulated by the air-gap separation between the top diaphragm and the bottom poly-silicon actuator and that the top movable diaphragm can be pneumatically deflected. In order to validate that the low-frequency assumption made in Figure 5.12 holds true for *1 kHz*, the following efforts are made. The resistance of the poly-silicon lead is directly measured (6.9 kΩ) from an un-bonded sample and so are the capacitances of $C_{field\text{-}ox}$ and $C_{insulation}$ (550 pF and 1.12 nF, respectively), and then these measurement values and variable $C_{air\text{-}gap}$ are substituted into Equation (5.1) to calculate $Z_{IA}(j\omega)$. The imaginary part of the $Z_{IA}(j\omega)$ in turn can be employed to calculate the apparent capacitance C' and apparent air-gap capacitance $C'_{air\text{-}gap}$ in Equation (5.3) at *1 kHz*. The fidelity of the low-frequency model can be verified by comparing the numerically varying $C_{air\text{-}gap}$ with the calculated apparent $C_{air\text{-}gap}$, and the results are shown in Figure 5.13. It can be seen from Figure 5.13 that the curve of variable $C_{air\text{-}gap}$ versus apparent air-gap capacitance $C'_{air\text{-}gap}$ is essentially a unity-slope line. The apparent resistance R', however, does vary to some degree but is within 11% of the measured *6.9 kΩ* poly-silicon lead resistance. These results provide the justification for the low-frequency assumption in Figure 5.12.

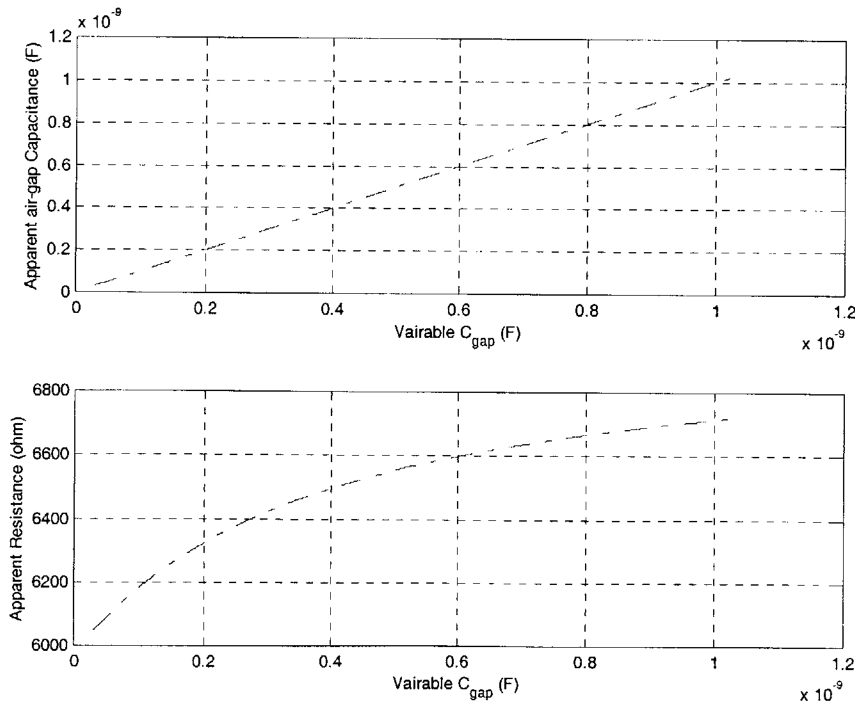

Figure 5.13 Apparent air-gap capacitance $C_{air\text{-}gap}$ vs. variable $C_{air\text{-}gap}$ and apparent resistance R' vs. variable $C_{air\text{-}gap}$ as computed numerically.

In addition, experimental measurements of apparent capacitance *C'* and apparent resistance *R'* are made using *HP-4194* impedance analyzer at *1kHz* from terminals *A* and *1* (Figure 5.7) while deflecting the diaphragm either pneumatically or electrostatically. These measurements are plotted and compared with the simulation curve in Figure 5.14 with frequency as a parameter. As shown in Figure 5.14, the measurement data and the model simulation both display very similar *R'*-*C'* characteristics, except for a horizontal (*R'*-axis) shift due to about 10% deviation in the resistance of the poly-silicon actuation electrode. Note that both *device 1* and *device 2* are fabricated on the same wafer. The actual resistance is linearly dependent on the resistivity of the heavily-doped poly-silicon. The resistivity, ρ, of n-type silicon is formulated as $\rho = \dfrac{1}{q\mu_n N_D}$, where q is the charge of the electron, μ_n the mobility of the electron, and N_D the dopant concentration of the donor. Therefore, the 10% resistance deviation could be due to a 10% variation of dopant concentration across the wafer.

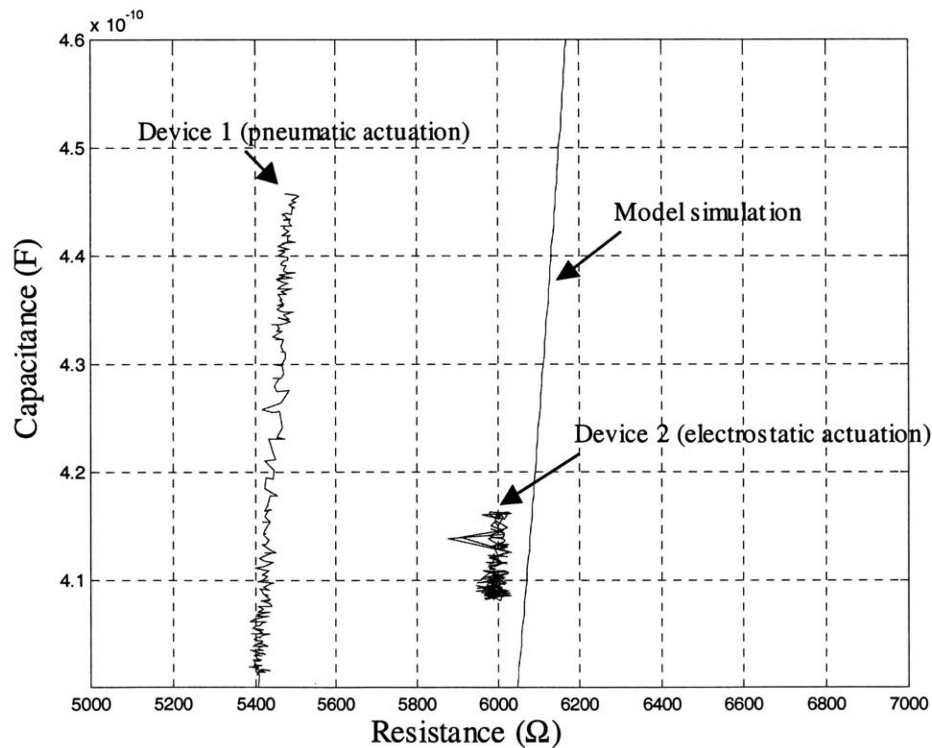

Figure 5.14 Apparent resistance (*R'*) and apparent capacitance (*C'*): Measurement data vs. Model simulation

Now, consider the case when the top diaphragm deflection exceeds the initial air-gap separation resulting in a good electrical contact between the movable diaphragm and the bottom metal pedestal; see Figure 5.7. An electrical contact between terminals *1* and *2* essentially short-circuits

the capacitor $C_{field\text{-}ox}$. Therefore, the impedance seen from terminals A and 1 would be just $C'_{air\text{-}gap}$ and $C_{insulation}$ in parallel at low frequencies as illustrated in Figure 5.15. Now, the expression for the apparent capacitance C' would be the following:

$$C' \approx -\frac{1}{\omega \cdot \mathrm{Im}\{Z_{1A}\}} \approx C'_{air-gap} + C_{insulation} \;, \tag{5.4}$$

when the switch is ON.

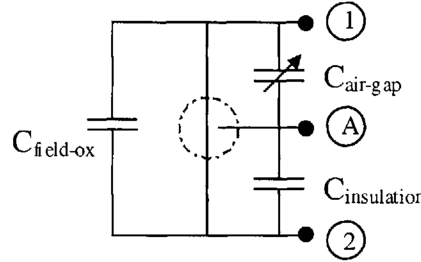

Figure 5.15 Low-frequency circuit model of a single switch cell in ON-state

The deformation of a pneumatically actuated diaphragm is a continuous function of pressure and so is the air-gap capacitance $C_{air\text{-}gap}$. But when an electrical contact is made between terminals 1 and 2, there will be a fundamental change in the low-frequency electrical model, as shown in Figure 5.12 and Figure 5.15, rendering a discontinuity in the measured apparent capacitance C'. The explanation of this phenomenon is given as follows. Revisiting Equations (5.3) and (5.4), it can be observed that the apparent capacitance C' consists of a continuous air-gap capacitance and a switch-state dependent parasitic capacitance. A sudden jump in apparent capacitance when the switch goes from ON-state to OFF-state will take place due to the parasitic capacitance discrepancy in different switch states. Comparing Equations (5.3) and (5.4), it can be anticipated that a capacitance discontinuity of $\left(C_{insulation} - (C_{field\text{-}ox} \cdot C_{insulation}) / (C_{field\text{-}ox} + C_{insulation})\right) \approx 750\ pF$ will be seen in the measurement of apparent capacitance C' from terminals A and 1 when switch state changes. Figure 5.16 shows that such a *750 pF* capacitance discontinuity due to short-circuiting of terminals 1 and 2 does appear in measurement data. This observation, in a sense, affirms the validity of the electrical model of the device. In addition, the capacitance discontinuity can be regarded as an indication of switch state change.

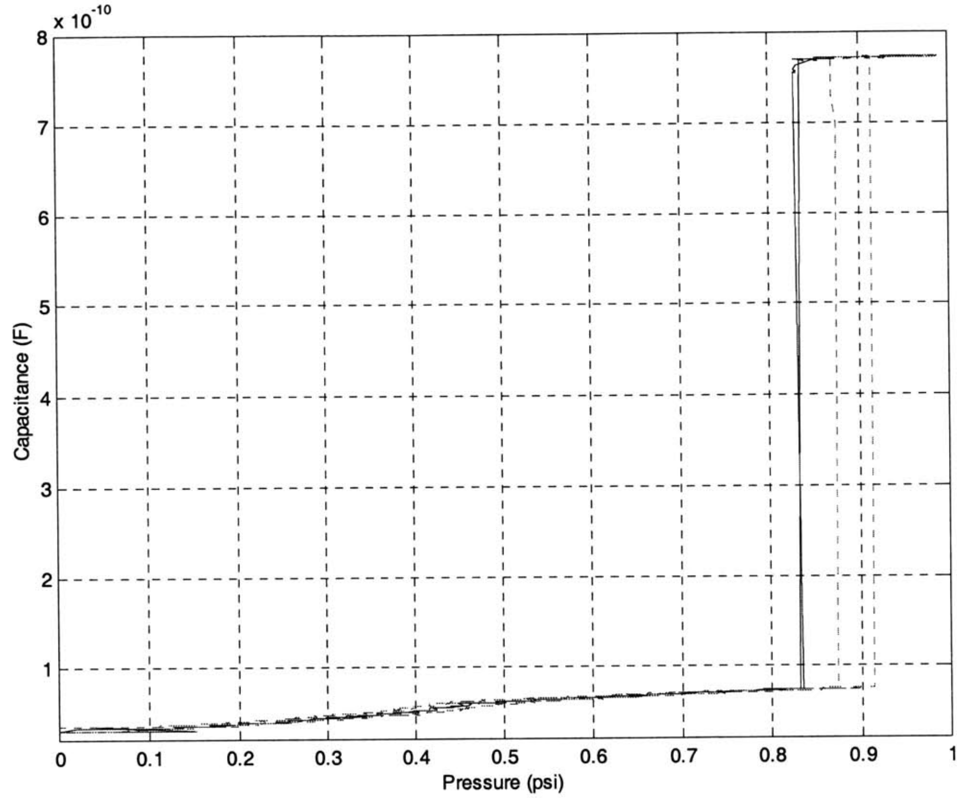

Figure 5.16 Discontinuity in capacitance measurement: An indication of change in switch state

Another consequence of understanding the electrical behavior of the device is the validation of using air-gap capacitance as a measure of initial gap distance with the parallel-plate capacitor model; see Equation (5.5). The dielectrics between the two electrodes of this capacitor comprises of a 1000Å thick thermally grown silicon dioxide and a layer of air whose thickness is to be determined. The area of the capacitor is designed to be A_{poly} = 4.078×10^{-6}m^2. With the measurement of the air-gap capacitance, the gap distance can be determined from

$$C_{air-gap} = \frac{\varepsilon_0 \left(A_{poly}\right)}{\left(x_{air-gap} + {t_{oxide}}/{\varepsilon_r}\right)} \tag{5.5}$$

where $\varepsilon_0 = 8.854\times10^{-12}$ F/m is the permittivity of free space, ε_r=3.8 is the relative permittivity of silicon dioxide, t_{oxide}=$1000Å$ is the oxide thickness, and $x_{air-gap}$ is gap separation variable to be determined from the $C_{air-gap}$ measurement.

In this section, a simplified low-frequency electrical model of the device is established with simulations and measurements made to validate the model. Also, with the help of this electrical model, the initial gap distance between the un-deflected diaphragm and bottom poly-silicon

actuator can be extracted from the capacitance measurements using Equations (5.3), (5.4), and (5.5).

5.4 Mechanical Model

The previous section discusses the pre-test device characteristics from an electrical point of view. The next pre-test characterization presented in this section focuses on the verification the mechanical integrity of the movable diaphragm. The approach of such a mechanical characterization here is to compare the theoretical pressure-capacitance relationship with the measurement data. In order to carry out this task, first a pressure-deflection relationship of the diaphragm is obtained using Timoshenko plate theory [55]. The information of the diaphragm profile can in turn be employed to calculate the capacitance under a prescribed pressure using numerical integration. Finally, just as with the electrical model, a comparison between the model and the measurements are presented and a reconciliation will be made to account for any discrepancy between the two.

5.4.1 Diaphragm deflection profile (Scenario-I)

Figure 5.17 presents in a pictorial way the three sequential steps through which a diaphragm deforms under increasing pressure downward to a stationary bottom ground with a raised pedestal. These steps are collectively referred to as "*Scenario-I*" It is assumed that the surfaces of the plate, the ground electrode, and the top of the raised pedestal are perfectly smooth. As a first-order approximation, the bottom pedestal contacts are jointly model as *one* pedestal contact whose radius is b. Descriptions of these three phases are given below:

- "Approaching" phase. In this phase the clamped circular diaphragm is deformed downward by an increasing and uniformly distributed pressure prior to any *mechanical* contact with the stationary floor or the raised pedestal. See Figure 5.17 *(1)*.
- "Spreading" phase. When the pneumatic pressure reaches a critical value, a *mechanical* contact will be made between the center of the diaphragm and the center of the raised pedestal. This initial contact point will spread out and form a circular contact area on the top surface of the pedestal as the downward pressure keeps rising. During this stage, the diaphragm behaves very much like a touch-mode pressure sensor [83]. See Figure 5.17 *(2)*.

- "Conforming" phase. As soon as the size of the growing contact area reaches that of the pedestal top, under further-increasing downward pressure, the diaphragm will be pushed even harder down and shape itself to conform to the profile topography beneath it. Note that the central part of the diaphragm would be lifted up in this stage due to the slope continuity compliance at the edge of the pedestal. See Figure 5.17 *(3)*.

We will deal with each of these phases separately in this section. For each phase, the diaphragm profile will be calculated using Timoshenko's plate theory [55] with boundary conditions and physical constraints. Then, the profile data will be used to acquire the corresponding capacitance values either analytically or numerically. This work is for the purpose of providing a pressure-capacitance model for each phase using the diaphragm deflection as an intermediate data. The results will be compared with experimental pressure-capacitance measurements.

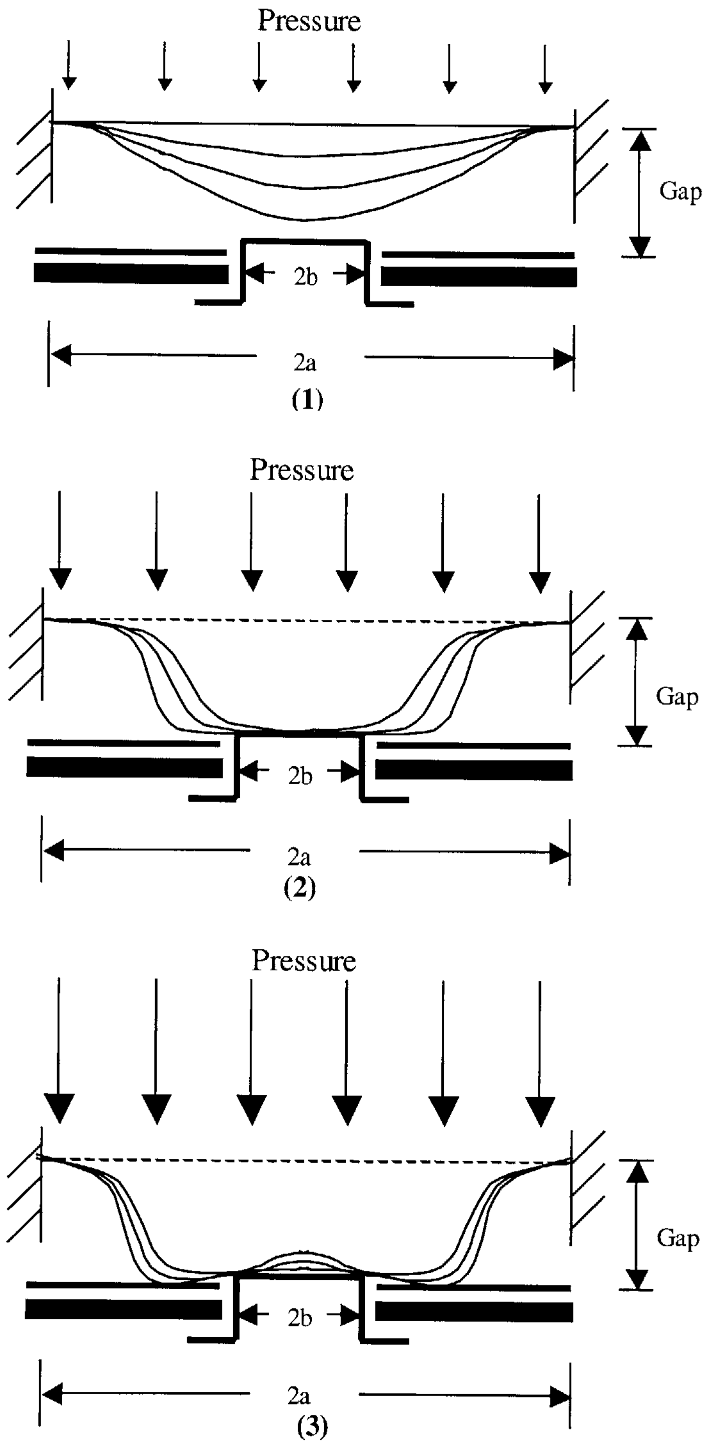

Figure 5.17 The three proposed phases as diaphragm deflecting downward onto a bottom contact pedestal, (1) "approaching", (2) "spreading", and (3) "conforming". (Scenario-I)

"Approaching" phase

The diaphragm of the device can be treated as a thin plate. When the deflection of such thin plate is small in comparison with its thickness, a very satisfactory approximate theory of plate bending under lateral loads has been developed [55] under the following assumptions:

1. There is no stretching deformation in the middle plane of the plate. That is, the middle plane remains neutral during bending.
2. There is no shear force effect. Points of the plate initially lying on a normal-to-the-middle plane remain normal to the middle plane. Therefore an initially straight line normal to the plate remains straight during bending.
3. By definition of a *thin* plate, the normal stresses in the direction transverse to the plane can be disregarded.

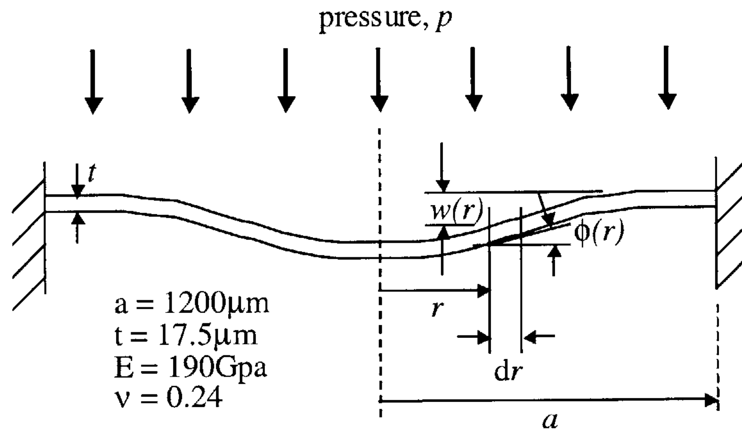

Figure 5.18 Clamped circular thin plate under uniformly distributed pressure

If the load is also symmetrically distributed about the axis perpendicular to the plate, the governing differential equation for a circular plate can be deduced from Newton's 1st Law and is

$$\frac{1}{r}\frac{d}{dr}\left\{r\frac{d}{dr}\left[\frac{1}{r}\frac{d}{dr}\left(r\frac{dw}{dr}\right)\right]\right\}=\frac{q}{D} \tag{5.6}$$

where q is the intensity of load in *Pa* or Nt/m^2, and D is the flexural rigidity of the thin plate. The plate flexural rigidity defined as $D=\frac{Et^3}{12(1-\nu^2)}$ in which E, t, and ν are the Young's modulus, the thickness, and the Poisson ratio of the plate, respectively. Integrating (5.6) four times and using the fact that the shearing force at the center, $r = 0$, must be zero yields an expression for

plate downward deflection w with three integration constants to be determined by boundary conditions. That expression is

$$w(r,p)=\frac{pr^2}{64D}+\frac{C_1r^2}{4}+C_2\ln\frac{r}{a}+C_3\,. \tag{5.7}$$

In the case of clamped circular thin plate, the boundary conditions are that the slope of the deflection surface in the radial direction must be zero for $r = 0$ and $r = a$, and that the deflection at the edge, $r = a$, must be zero. Integrations of Equation (5.6) and incorporation of boundary conditions yields

$$w(r,p)=\frac{p}{64D}(a^2-r^2)^2 \tag{5.8}$$

where the plate deflection, w, is a function of radius r and pressure p.

As can be seen from Equation (5.8), the downward deflection of the plate is proportional to the applied pressure and its maximum value is $w_{\max}=\frac{pr^4}{64D}$ at the center of the plate, $r = 0$. Figure 5.19 shows a family of the profile curves under incrementing pressure from center ($r = 0$) to the edge ($r = 1200\ \mu m$).

The next action is to determine the capacitance between a prescribed plate profile and a stationary ground. Consider an axis-symmetric plate element of infinitesimal width (Figure 5.20), with the assumption that the parallel-plate capacitor model still holds between the ring element and the ground, the incremental capacitance can be found to be

$$dC(r,p)=\frac{\varepsilon_0(2\pi r dr)}{G-w(r,p)} \tag{5.9}$$

where G is the initial gap distance between un-deformed plate and the floor. By design, this initial gap is $1\mu m$. The analytical formulation of plate pressure-deflection relationship, $w(r, p)$, is given in Equation (5.8) and can be substituted into Equation (5.9) for the calculation of the incremental capacitance dC. Carrying out an integration with respect to radius r from $r = 0$ to $r = a$ yields the analytical expression for the capacitance between the deformed plate profile and the floor.

$$C(p)=\int_{r=0}^{r=a}dC(r,p)=\frac{8\pi\varepsilon_0 D}{\sqrt{pGD}}\left[\tanh^{-1}\left(\frac{pa^2}{8\sqrt{pGD}}\right)\right] \tag{5.10}$$

Equation (5.10) is the analytical pressure-capacitance relationship in the "approaching" stage and it is plotted in Figure 5.21. Note that Equation (5.10) assumes that the bottom electrode has the same size of the plate. If the bottom electrode has a radius a_1 which is smaller than the plate radius, $a_1 < a$, then the integration of Equation (5.9) from $r = 0$ to $r = a_1$ yields

$$C(p) = \int_{r=0}^{r=a_1} dC(r,p) = \frac{8\pi\varepsilon_0 D}{\sqrt{pGD}}\left[\tanh^{-1}\left(\frac{pa^2}{8\sqrt{pGD}}\right) - \tanh^{-1}\left(\frac{p\left(a^2 - a_1^2\right)}{8\sqrt{pGD}}\right)\right] \tag{5.11}$$

Also, if there are dielectric materials in the gap other than air, then the gap distance G will have to be adjusted to account for this fact in a fashion similar to the denominator of Equation (5.5).

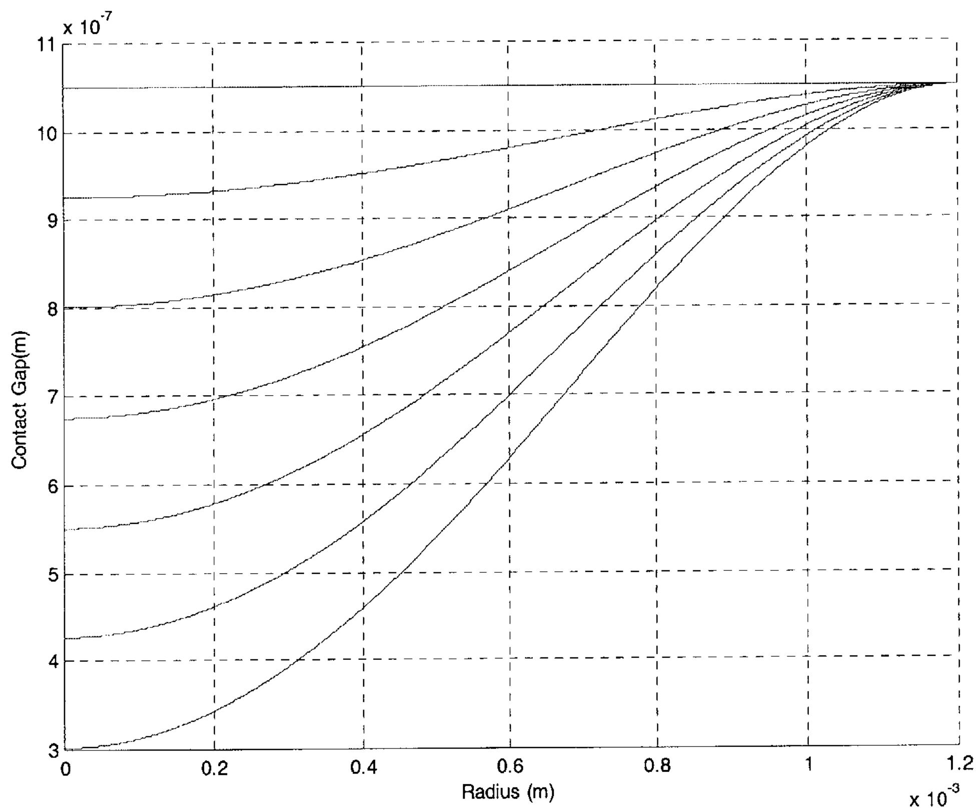

Figure 5.19 Plate deformation profile in "approaching" phase. Each curve represents a 0.05psi pressure increment.

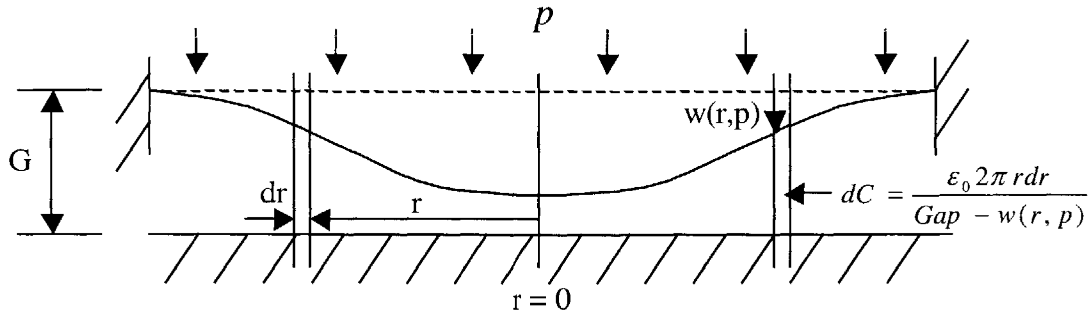

Figure 5.20 Incremental capacitance between deformed plate and ground

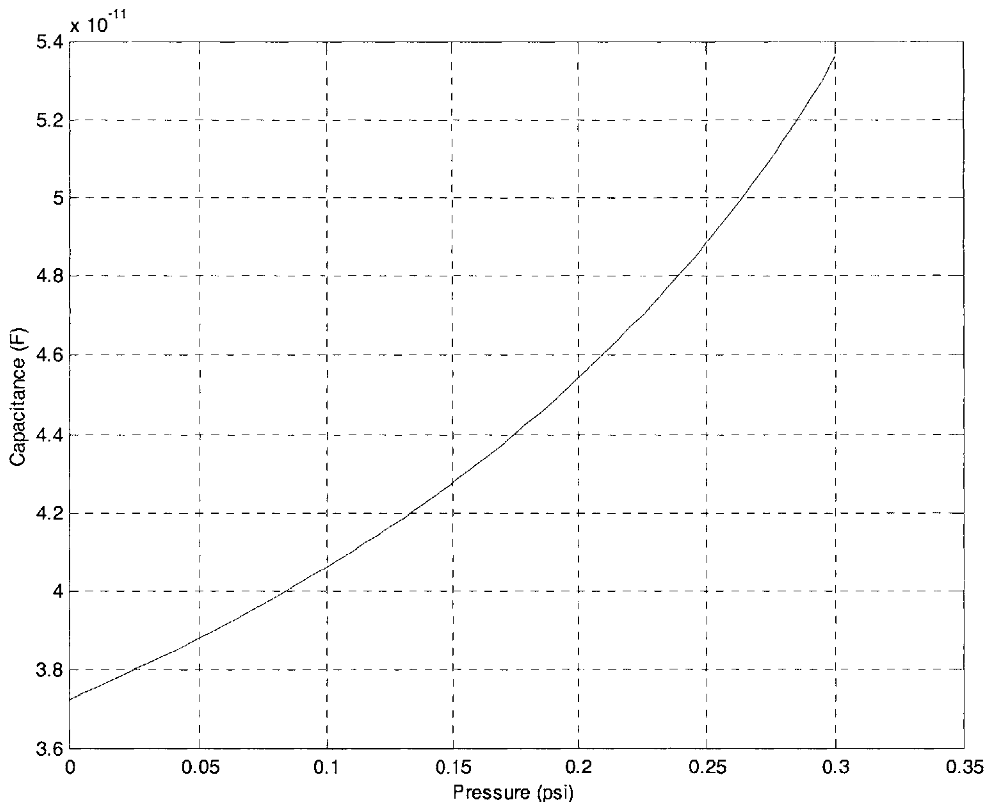

Figure 5.21 Capacitance-pressure curve in "approaching" phase

"Spreading" phase

The onset of the second phase is when the maximum deflection of the circular thin plate, w_{max} from Equation (5.8) at $r = 0$, equals the initial gap distance G. In other words, the "spreading" phase starts when pressure p reaches p_a, where p_a is the pressure that satisfies $w_{\max}(p_a) = G$. The contact spreads out and grows from a contact point to a small circular contact area on the pedestal top as the pressure keeps rising; see Figure 5.17 (2). As a first-order approximation, the

bottom pedestal contacts are jointly model as *one* pedestal contact whose radius is b. This phase ends when the size of the contact area equals that of the pedestal top ($r = b$).

The plate will be divided into two parts for different boundary conditions and constraints. The inner part where the plate is touching the pedestal top and is *flat* ($0 < r < r_i$), and the outer part where the plate deflects but not contacting ($r_i < r < a$); see Figure 5.22.

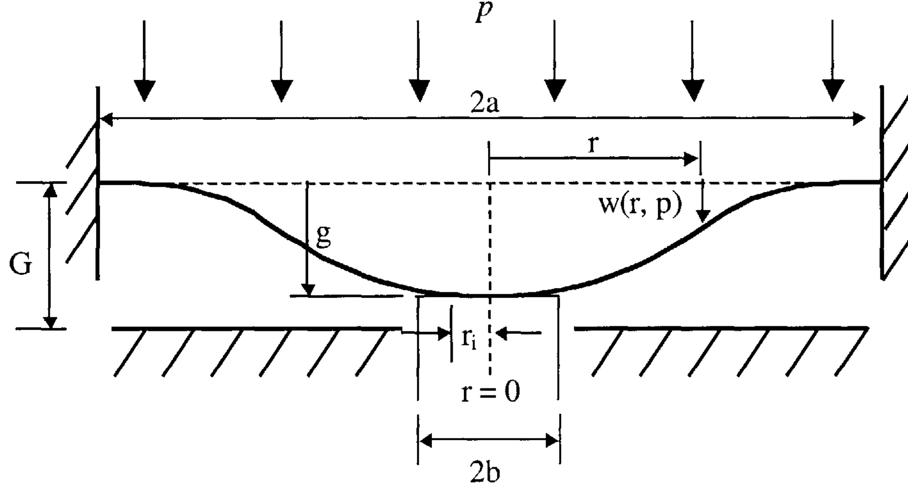

Figure 5.22 Dimension definitions in "spreading" phase.

- Inner region

By assuming that the plate is closely touching the pedestal top, the slope ϕ and deflection w in this region are given by

$$\phi(r) = \frac{dw(r)}{dr} = 0 \text{ and } w(r,p) = g \quad \text{for } 0 < r < r_i. \tag{5.12}$$

- Outer region

The governing differential equation for a circular plate would still be Equation (5.6). The boundary conditions in this case, $\phi(r_i) = 0$, $\phi(a) = 0$, and $w(a) = 0$, can then be substituted into Equation (5.7). The solution becomes

$$w(r,p) = \frac{pr^2}{8D}\left(\frac{r^2}{8} - r_i^2 \ln r + r_i^2\right) + \frac{C_1 r^2}{4} + C_2 \ln r + C_3 \tag{5.13}$$

where $C_1 = \dfrac{a^2 p}{8D\left[\left(r/a\right)^2 - 1\right]}\left[1 - 4\left(\frac{r}{a}\right)^2 \ln a - 3\left(\frac{r}{a}\right)^4 + 4\left(\frac{r}{a}\right)^4 \ln r + 2\left(\frac{r}{a}\right)^2\right]$

$$C_2 = \frac{a^4 \left(\frac{r}{a}\right)^2 p}{16D\left[\left(\frac{r}{a}\right)^2 - 1\right]}\left[\left(\frac{r}{a}\right)^2 - 1 + 4\left(\frac{r}{a}\right)^2 \ln\left(\frac{r}{a}\right)\right]$$

$$C_3 = \frac{a^4 p}{64D\left[\left(\frac{r}{a}\right)^2 - 1\right]}\left[4\left(\frac{r}{a}\right)^2 \ln a - 16\ln^2(a)\left(\frac{r}{a}\right)^4 + 4\ln a\left(\frac{r}{a}\right)^4 - 1 - 2\left(\frac{r}{a}\right)^4\right.$$
$$\left. - 8\left(\frac{r}{a}\right)^4 \ln r + 3\left(\frac{r}{a}\right)^2 + 16\ln a\left(\frac{r}{a}\right)^4 \ln r\right]$$

for $r_i < r < a$.

The results from the inner region and outer region are then combined for the complete plate profile in this phase and are plotted in Figure 5.23.

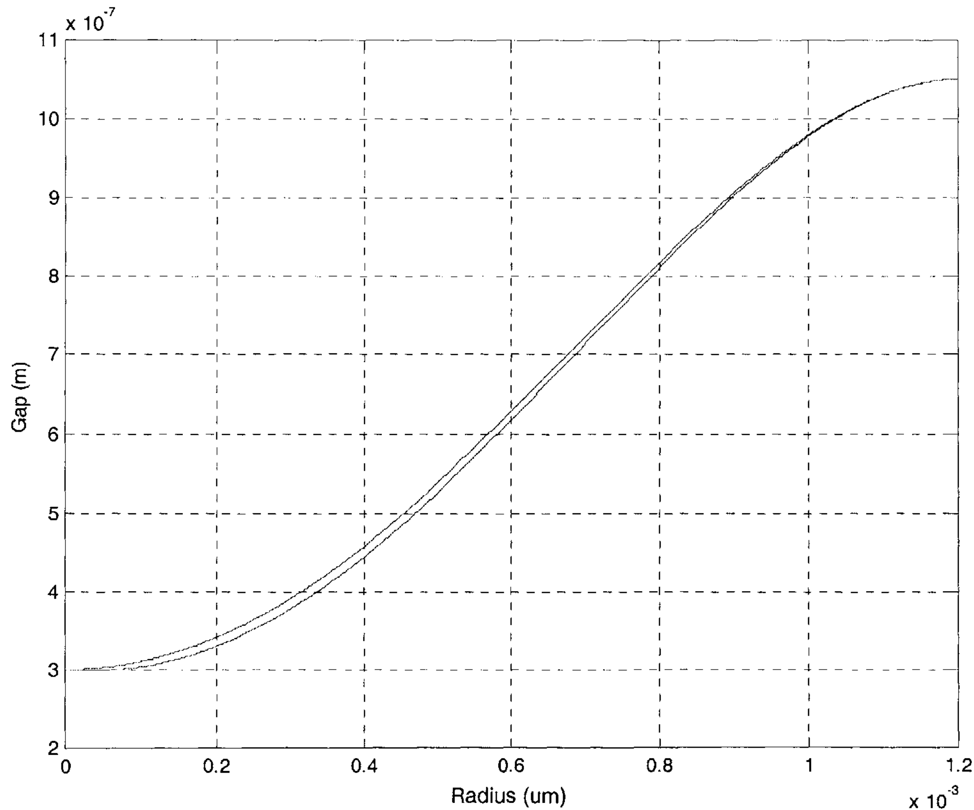

Figure 5.23 Plate deformation profile in "spreading" phase.

The analytical formulation for the capacitance between the deformed plate and the ground could be obtained by integrating Equation (5.9) with Equations and (5.12) and (5.13) substituted in.

However, numerical integration will be performed instead to avoid the tremendous algebraic complication in the execution of the analytical integration. In Figure 5.24, the numerical integration capacitance-pressure results in the "spreading" phase are plotted in solid line while the analytical results in the "approaching" phase are plotted in dash-dot line.

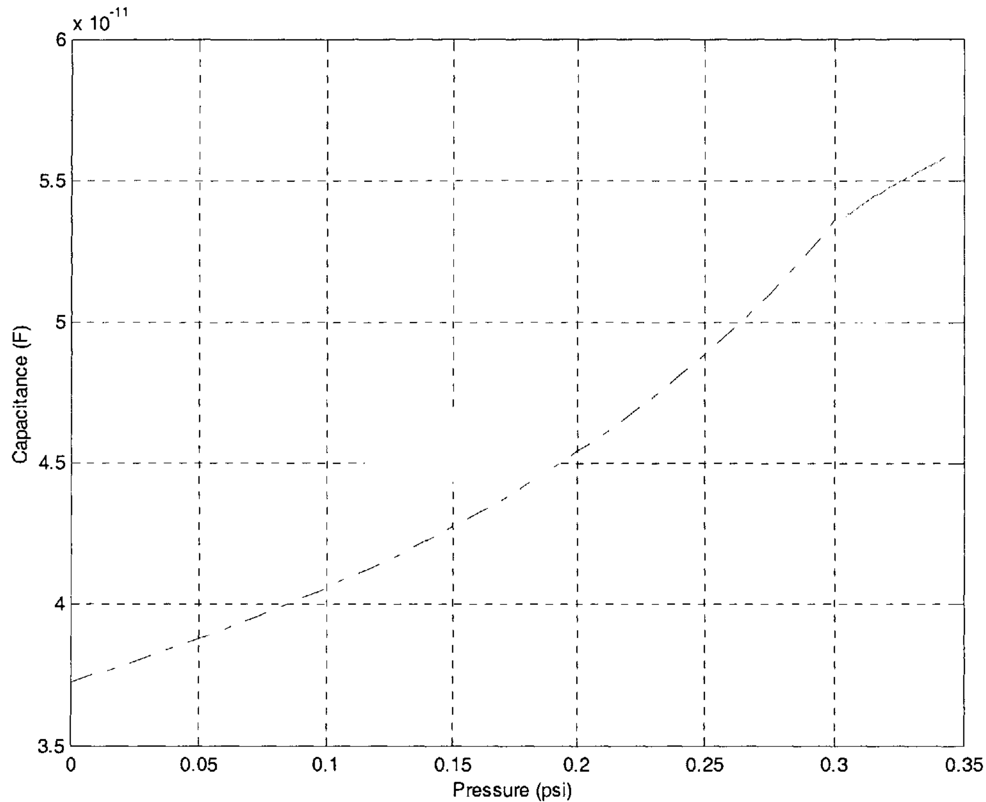

Figure 5.24 Capacitance-pressure curve in "spreading" phase (solid line) and "approaching" phase (dash-dot line).

"Conforming" phase

Under this scenario, the "conforming" phase starts when the pressure rises to a point ($p > p_b$) such that the size of the contact area goes beyond that of the pedestal top and the plate begins to conform to the topography of the ground. The mathematic treatment in this phase is very similar to the case in "spreading" phase, except for some adjustments on the boundary conditions and constraints. As a first-order approximation, the bottom pedestal contacts are jointly model as *one* pedestal contact whose radius is b.

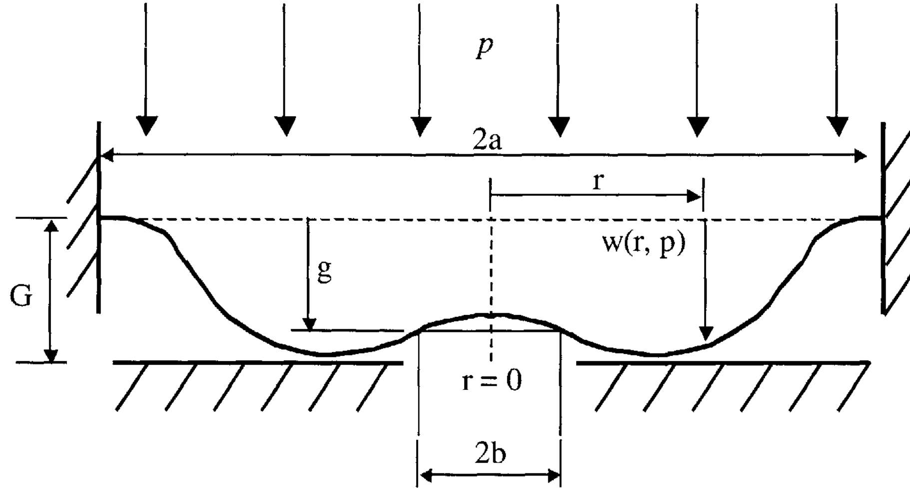

Figure 5.25 Dimension definitions in "conforming" phase.

Again, the Timoshenko plate model will be adopted. The governing differential equation for the clamped circular thin plate under uniform pressure remains the same as in Equation (5.6). The following discussion addresses the plate deformation profiles in two different regions: (1) the inner region ($0 < r < b$), and (2) the outer region ($b < r < a$), where b is the radius of the top surface on the pedestal.

- Inner region

Equation (5.7) is rewritten as

$$w_I(r,p) = \frac{pr^2}{64D} + \frac{C_{I1}r^2}{4} + C_{I2}\log\frac{r}{a} + C_{I3} \tag{5.14}$$

with the slightly changed notation on the integration constants and variables to differentiate them from the ones for outer region. The boundary conditions in the inner region are

$$\begin{cases} \phi_I(0) = 0\,, \\ w_I(0) = 0\,. \end{cases} \tag{5.15}$$

- Outer region

Equation (5.7) is rewritten as

$$w_O(r,p) = \frac{pr^2}{64D} + \frac{C_{O1}r^2}{4} + C_{O2}\log\frac{r}{a} + C_{O3} \tag{5.16}$$

with the slightly changed notation on the integration constants. The boundary conditions in the outer region are

$$\begin{cases} \phi_O(0) = 0 \,, \\ w_O(0) = 0 \,. \end{cases} \tag{5.17}$$

There are six integration constants, C_{I1}, C_{I2}, C_{I3}, C_{O1}, C_{O2}, and C_{O3}, in Equations (5.14) and (5.16) but only four boundary conditions in Equations(5.15) and (5.17). The two additional constraints necessary to solve for all unknowns come from the continuity and moment balance of the thin plate on the edge of the pedestal top, $r = b$. These are

$$\begin{cases} w_I(b) = w_O(b) \,, \\ M_I(b) = D\left(\dfrac{1}{r}\dfrac{dw_I(b)}{dr} + \dfrac{d^2 w_I(b)}{dr^2}\right) = -M_O(b) = -D\left(\dfrac{1}{r}\dfrac{dw_O(b)}{dr} + \dfrac{d^2 w_O(b)}{dr^2}\right). \end{cases} \tag{5.18}$$

With the four boundary conditions, one continuity constraint, and one moment balance equation, all six integration constants are completely determined and are

$$C_{I1} = \frac{-a^2 p}{16D\left(r/a\right)^2\left[-\left(r/a\right)^2 + 2\ln\left(r/a\right) + 1\right]}\left[-3\left(\frac{r}{a}\right)^2 + 13\left(\frac{r}{a}\right)^4 + 1 - 11\left(\frac{r}{a}\right)^6 + 24\left(\frac{r}{a}\right)^4 \ln\left(\frac{r}{a}\right) - 4\left(\frac{r}{a}\right)^2 \ln\left(\frac{r}{a}\right)\right],$$

$$C_{I2} = 0 \,,$$

$$C_{I3} = \frac{-a^4 p}{16D\left(r/a\right)\left[-\left(r/a\right)^2 + 2\ln\left(r/a\right) + 1\right]}\left[-4\left(\frac{r}{a}\right)^2 \ln\left(\frac{r}{a}\right) - 10\left(\frac{r}{a}\right)^6 - 3\left(\frac{r}{a}\right)^2 + 12\left(\frac{r}{a}\right)^4 + 1 + 22\left(\frac{r}{a}\right)^4 \ln\left(\frac{r}{a}\right)\right],$$

$$C_{O1} = \frac{a^2 p}{16D\left[-\left(r/a\right)^2 + 2\ln\left(r/a\right) + 1\right]}\left[-4\ln\left(\frac{r}{a}\right) + \left(\frac{r}{a}\right)^4 - 1\right],$$

$$C_{O2} = \frac{a^4 p}{32D\left[-\left(r/a\right)^2 + 2\ln\left(r/a\right) + 1\right]}\left[2\left(\frac{r}{a}\right)^2 - \left(\frac{r}{a}\right)^4 - 1\right], \text{ and}$$

$$C_{O1} = \frac{a^4 p}{64D\left[-\left(\frac{r}{a}\right)^2 + 2\ln\left(\frac{r}{a}\right) + 1\right]}\left[2\ln\left(\frac{r}{a}\right) + 2\left(\frac{r}{a}\right)^4 - \left(\frac{r}{a}\right)^4\right].$$

With all integration constants solved, Equation (5.14) can be employed to calculate the plate deformation profile for the inner region ($0 < r < b$) and Equation (5.16) for the outer region ($b < r < a$). Combination of inner-region and outer-region results renders the full plate profile in this "conforming" phase. The profiles are plotted in Figure 5.26.

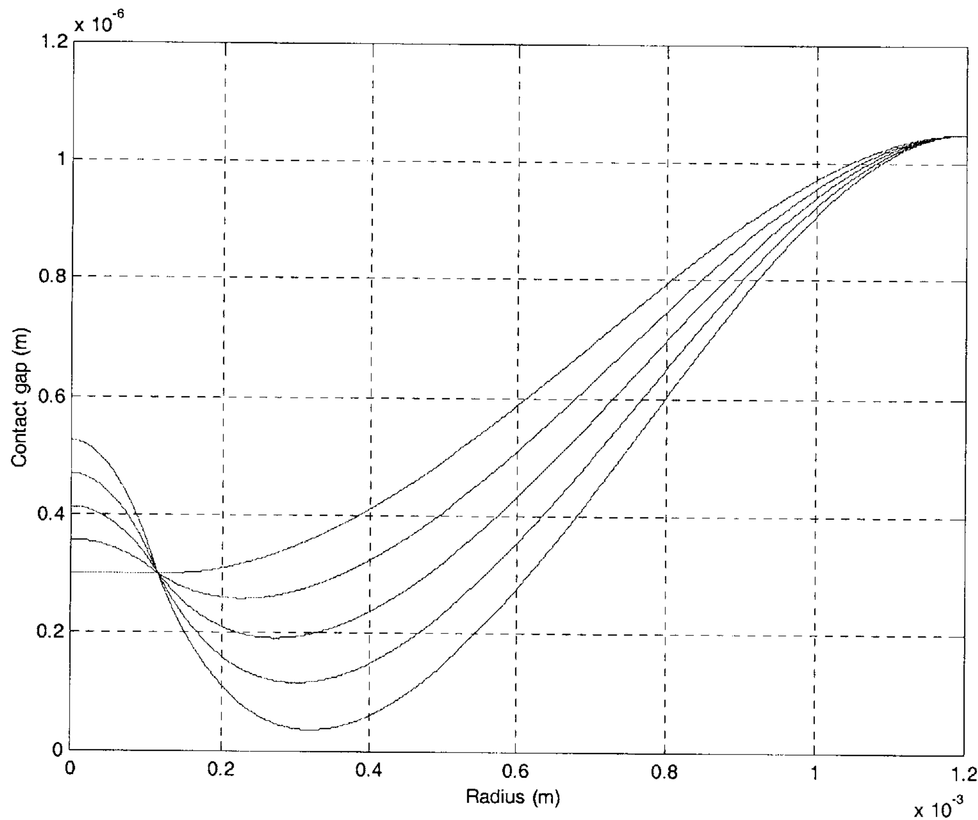

Figure 5.26 Plate deformation profile in "conforming" phase. Each curve represents a 0.05psi pressure increment.

The final step in this analysis is the computation of the capacitance between the deformed plate and the ground. Instead of carrying out analytical integration, numerical integration of Equation (5.9) with Equations (5.14) and (5.16) substituted in will be performed. Figure 5.27 shows the numerical integration capacitance-pressure results in the "conforming" phase.

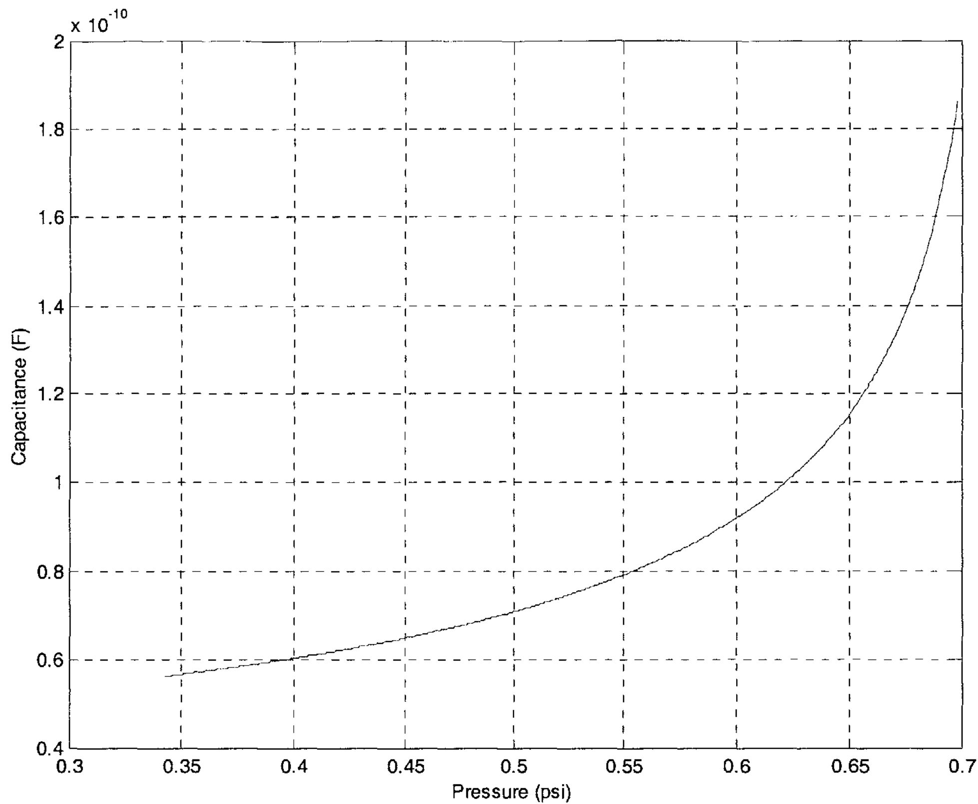

Figure 5.27 Capacitance-pressure curve in "conforming" phase.

In this subsection, mechanical modeling of the diaphragm using Timoshenko plate theory [55] is carried out to acquire the theoretic pressure-deformation-capacitance relationships. Depending on the pressure level, mechanical design of the thin plate, and ground electrode profile, the deformation of the thin plate could be in an "approaching", "spreading", or "conforming" phase, and the mathematical derivation can be executed analytically or numerically. The logical step following this analysis is a comparison between the model and experimental data and will be discussed next.

5.4.2 Pressure-capacitance model and discussions (Scenario-I)

Under the *smooth* surface assumption in the scenario, the complete pressure-capacitance curve shown in Figure 5.28 can be constructed by combining Figure 5.21, Figure 5.24 and Figure 5.27.

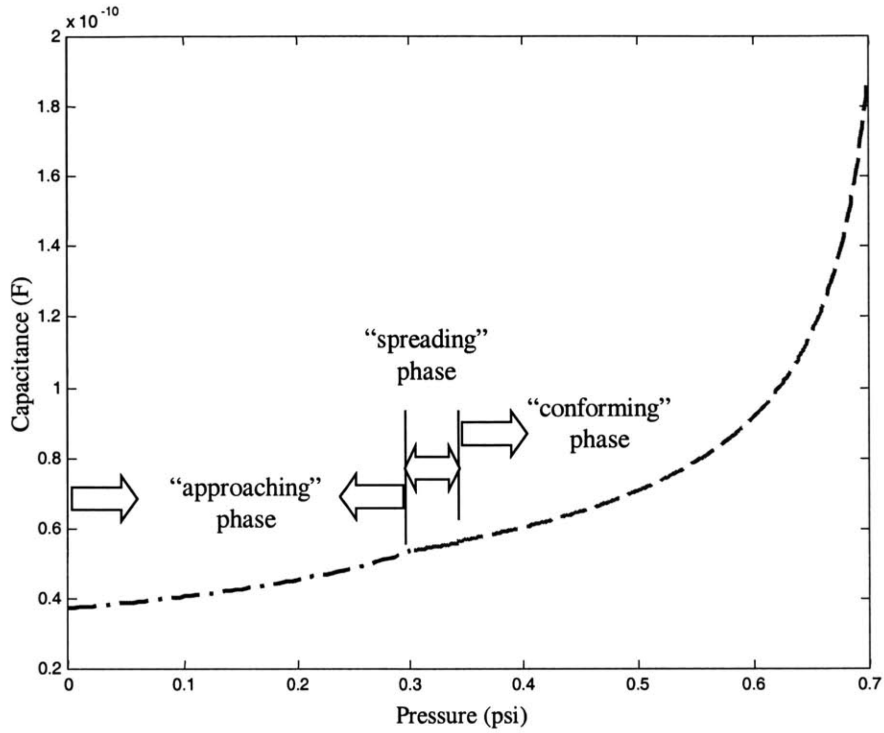

Figure 5.28 Complete capacitance-pressure plot in Scenario-I.

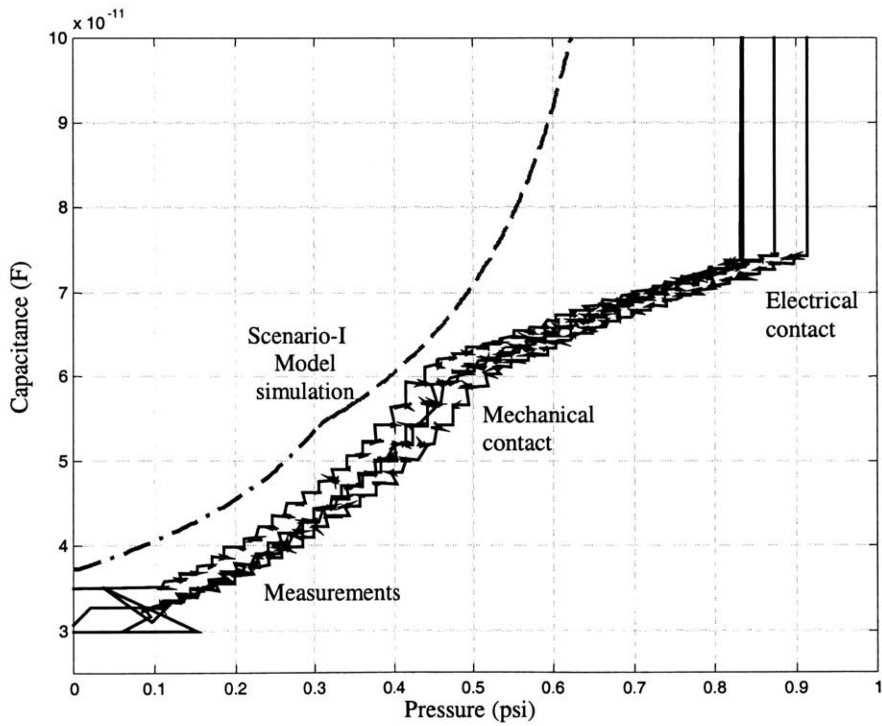

Figure 5.29 Pressure-capacitance curve comparison: Experimental data (solid lines) vs. Scenario-I model (dashed line)

Figure 5.29 shows the experimental measurements of the pressure-capacitance curves with the Scenario-I model simulation. Note that the sudden capacitance jump in the measurement data is an indication of the electrical contact between the top diaphragm and the pedestal as explained in Section 5.3. It can be seen in Figure 5.29 that the mechanical contact, indicated by a bend in the pressure-capacitance curve, and the electrical contact, indicated by a capacitance jump, do not take place at the same pressure and this could be caused by a number of reasons. First, the pedestal height is designed to be 0.2 mm higher than the ground level and is determined by the thickness of a metal layer, as illustrated in Figure 5.7. It is plausible that non-uniform metal deposition or inadequate thickness control might have caused insufficient pedestal height. Secondly, the first contact is supposed to be between the center of the thin plate and the center of the pedestal top assuming that the top wafer and the bottom wafer are perfectly aligned. If, however, they are misaligned by more than the radius of the top pedestal radius, the first contact point might not occur at the expected locations. Additionally, surface roughness on the plate, the ground, or the pedestal top will change the contact behavior of the device.

From Figure 5.29, a few similarities between the model simulation and the experimental data can be seen as listed below.

- The model predicts a bend in the pressure-capacitance curve in the transition from "approaching" phase to "spreading" phase and such bend can be observed in the measurement curves above approximately 0.45 psi..
- The slopes of the pressure-capacitance in the "spreading" phase for both cases are in close agreement.
- There is a decent match between the curvatures in the simulation and measurements in the low-pressure-range.

On the other hand, dissimilarities can be observed as listed below.

- There is an initial capacitance mismatch between the two curves at zero pressure. This indicates that there can be a discrepancy between the design gap distance and the actual post-packaging gap distance.
- The onset of the "spreading" phase occurs at different pressures. Again, this can result from the mismatch in the initial gap distance.
- The experimental curves are missing the "conforming"-phase curve that features a noticeable upward concavity. This is the *most* striking difference between the simulation

curve and the experimental data. One possible physical explanation for this is that the presence of some sort of unexpected objects prevents the plate from completely conforming to the bottom electrode. The source of such unexpected objects could be either external particle contaminants or surface roughness due to material agglomeration.

In this subsection, comparison between the model simulation of the pressure-capacitance characteristics of the device and experimental data is made. Similarities and dissimilarities are discussed and plausible explanations are given. Further modification of the model will be presented in the next subsection in an effort to achieve better agreement between the model and the measurements.

5.4.3 Diaphragm deflection profile (Scenario-II)

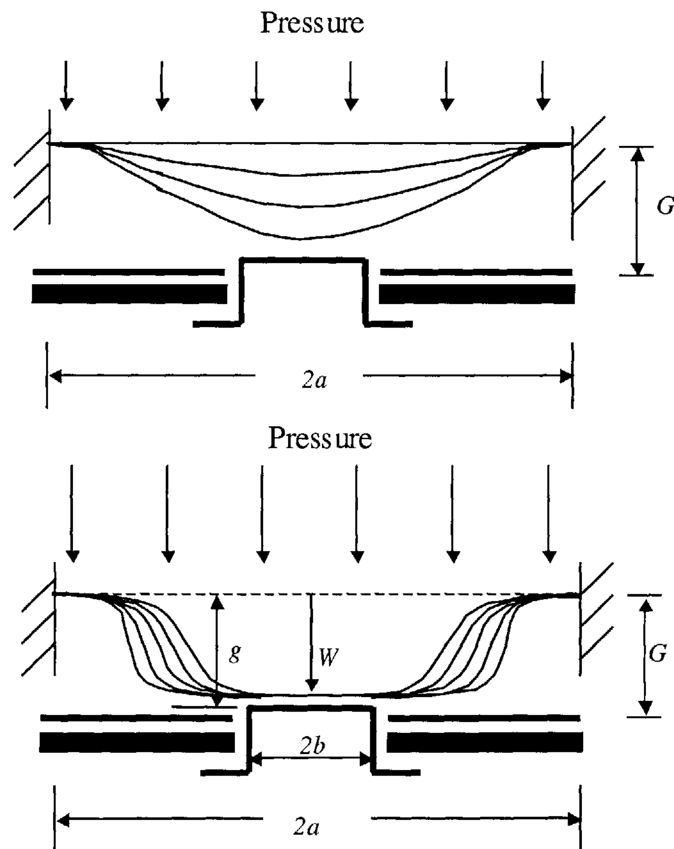

Figure 5.30 The two phases of diaphragm deflecting downward onto a bottom contact pedestal, (1) "approaching", (2) and "spreading". (Scenario-II)

To model and explain the dissimilarities observed in Scenario-I (Subsection 5.4.2), the following adjustments will be made to modify the thin plate deformation model, resulting in *Scenario-II*.

- Instead of using the design gap distance, the initial gap will be determined by the capacitance measurement with no pressure applied.
- To account for the fact that the upwardly-concave part of the "conforming" phase pressure-capacitance curve is missing in the measurement data, an additional assumption is made that somehow the plate deformation is restricted by unexpected obstacles that prevent the plate from completely conforming to the bottom profile. For analysis simplification, we will assume that such obstacles are uniformly distributed.

Again, as a first-order approximation, the bottom pedestal contacts are jointly model as *one* pedestal contact whose radius is b. Under Scenario-II, the sequence of the thin plate deflecting under increasing downward pressure is depicted in Figure 5.30. The most significant differences from Scenario-I model (Figure 5.17) are: (1) the third "conforming" phase no longer exists, and (2) in the second "spreading" phase, the maximum deflection of the thin plate is restricted to W, while $W \leq g$.

The plate deformation equations for clamped circular thin plate developed in Subsection 5.4.1 using Timoshenko's plate model [55] are still applicable in this scenario and therefore will be presented without repeating the derivations.

"Approaching" phase

This phase is exactly the same as in Scenario-I and therefore the pressure-deflection formulation, Equation (5.8), and pressure-capacitance expression, Equation (5.10) still hold.

$$w(r,p) = \frac{p}{64D}(a^2 - r^2)^2 \tag{5.8}$$

$$C(p) = \int_{r=0}^{r=a} dC(r,p) = \frac{8\pi\varepsilon_0 D}{\sqrt{pGD}}\left[\tanh^{-1}\left(\frac{pa^2}{8\sqrt{pGD}}\right)\right] \tag{5.10}$$

"Spreading" phase

Similarly, the equations for the plate deflection are repeated below for the inner region and outer region. The only minor difference is that the maximum deflection in the inner region is now W, instead of g. The equations for the outer region remain unchanged. Together, the equations are:

- inner region

$$\phi(r) = \frac{dw(r)}{dr} = 0 \text{ and } w(r,p) = g$$

(5.19)

for $0 < r < r_i$;

- outer region

$$w(r,p) = \frac{pr^2}{8D}\left(\frac{r^2}{8} - r_i^2 \ln r + r_i^2\right) + \frac{C_1 r^2}{4} + C_2 \ln r + C_3 \tag{5.13}$$

where

$$C_1 = \frac{a^2 p}{8D\left[\left(r/a\right)^2 - 1\right]}\left[1 - 4\left(\frac{r}{a}\right)^2 \ln a - 3\left(\frac{r}{a}\right)^4 + 4\left(\frac{r}{a}\right)^4 \ln r + 2\left(\frac{r}{a}\right)^2\right]$$

$$C_2 = \frac{a^4 \left(r/a\right)^2 p}{16D\left[\left(r/a\right)^2 - 1\right]}\left[\left(\frac{r}{a}\right)^2 - 1 + 4\left(\frac{r}{a}\right)^2 \ln\left(\frac{r}{a}\right)\right]$$

$$C_3 = \frac{a^4 p}{64D\left[\left(r/a\right)^2 - 1\right]}\left[4\left(\frac{r}{a}\right)^2 \ln a - 16\ln^2(a)\left(\frac{r}{a}\right)^4 + 4\ln a\left(\frac{r}{a}\right)^4 - 1 - 2\left(\frac{r}{a}\right)^4 \right.$$
$$\left. - 8\left(\frac{r}{a}\right)^4 \ln r + 3\left(\frac{r}{a}\right)^2 + 16\ln a\left(\frac{r}{a}\right)^4 \ln r\right]$$

for $r_i < r < a$.

The diaphragm deformation profiles based on above equations are plotted in Figure 5.31, with the "approaching"-phase curves in dashed lines and the "spreading"-phase curves in solid lines.

The gap distance for the computation of capacitance can be determined from these deformations. Note that the maximum deflection possible in the "spreading" phase is $G = 1.25\mu m$, i.e. $W \leq 1.25\mu m$. This maximum deflection can only happen in the case when all surfaces are perfectly smooth and free of particle contaminants. In the presence of any non-smoothness, such as surface roughness asperities, material crystal grain agglomeration, and/or extrinsic solid contaminants, the plate motion is restricted by such non-smoothness and the deflection is *less* than this maximum value. Figure 5.32 shows the model pressure-capacitance simulation curves for several different deflection limits. It can be observed from the model simulations that, in the presence of such plate-motion-limiting non-smoothness, the mechanical contact takes place earlier than

theoretically predicted, and that the slope of the pressure-capacitance curve exhibits a slower rate in the "spreading" phase. Also shown in Figure 5.32 are the experimental pressure-capacitance curves. As discussed earlier in Section 5.3, due to the *electrical* contact of he plate and bottom pedestal, there is a capacitance discontinuity in the capacitance measurements as predicted. Moreover, the experimental curves and the model curve corresponding to $W = 1.1\ \mu m$ have a very good agreement.

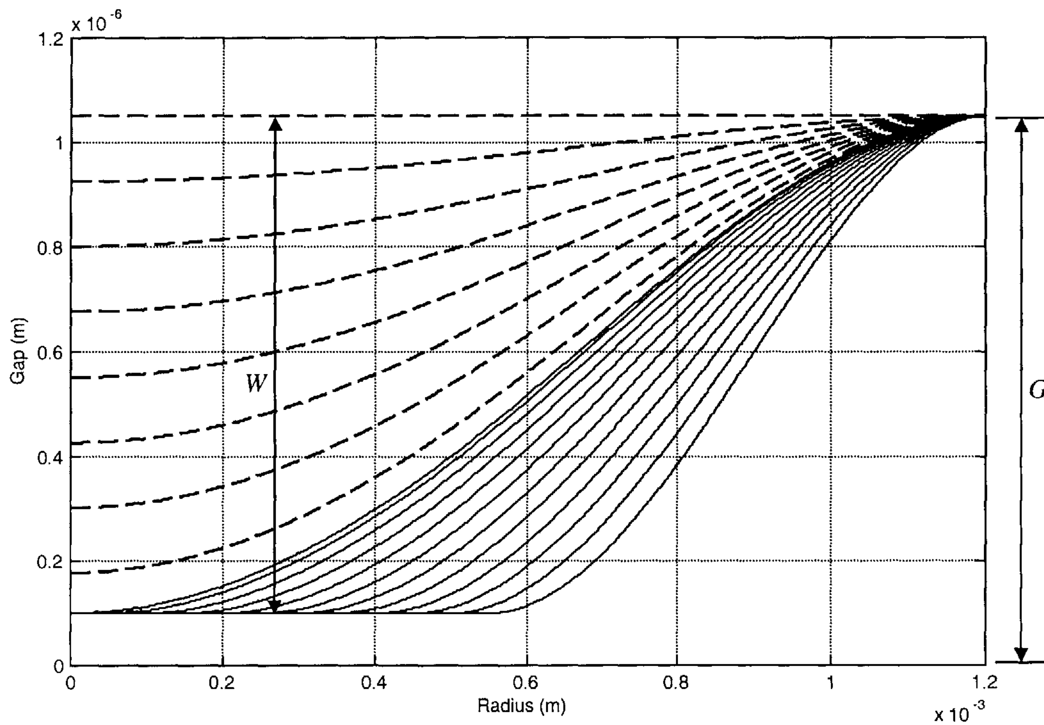

Figure 5.31 Plate deformation in Scenario-II.
"Approaching" phase (dashed): each curve represents 0.05psi increment. "Spreading" phase (solid): each curve represents 50μm increment in touchdown radius.

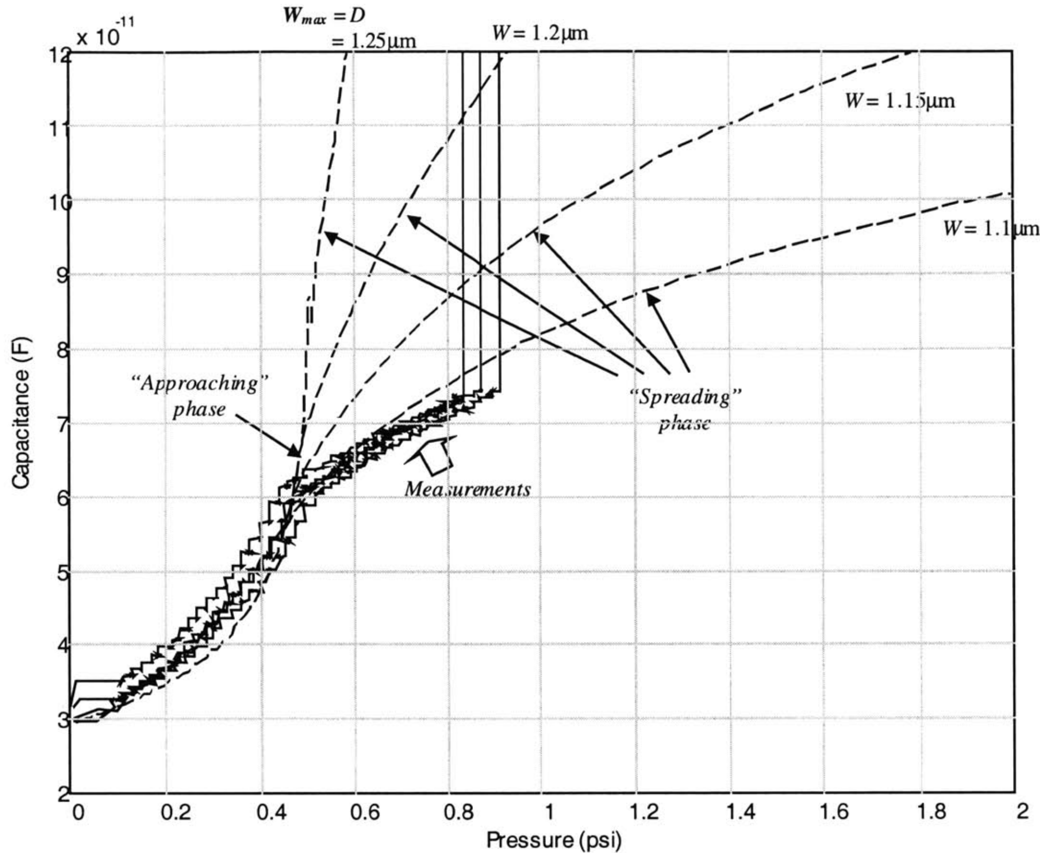

Figure 5.32 Pressure-capacitance curve comparison:
Experimental data (solid lines) vs. Scenario-I model (dashed line)

Observation of the pressure-capacitance curves in Figure 5.32 suggest that the thin top plate and the ground electrode are kept from being brought into close contact by some objects that are *0.15 μm* (= *1.25 μm* – *1.1 μm*) in their dimensional size. Inaccessibility of the post-packaging contact surface within the gap poses difficulties in the diagnosis of sources of such unexpected objects. However, roughness measurements on un-packaged bottom poly-silicon actuators were made with the help of an optical interferometry surface profiler (see Appendix E), and the roughness asperity height is found to be *148nm*, which is on the same order of the dimensional size of these *0.15μm* objects that limit the plate deflection.

5.5 Pneumatic Actuation

The pneumatic actuation capability that the MEMS power switch features not only facilitates the characterization tasks discussed in Sections 5.3 and 5.4, but also provides the device a secondary functionality as a pressure switch. The device studied here has an LPCVD stoichiometric silicon nitride (Si_3N_4) top diaphragm of *1500 Å* in thickness and sixteen *30 μm*-diameter bottom pedestal

contacts. The pressure actuation experiments are carried out by monitoring both the contact resistance and the electrical current-flow through the device as the actuation pressure sweeps. The hardware described in Subsection 5.2.4 is employed to perform the experiments and the results for this device are plotted in Figure 5.33. Note that the resistance axis is in logarithm scale and the current axis is in linear scale.

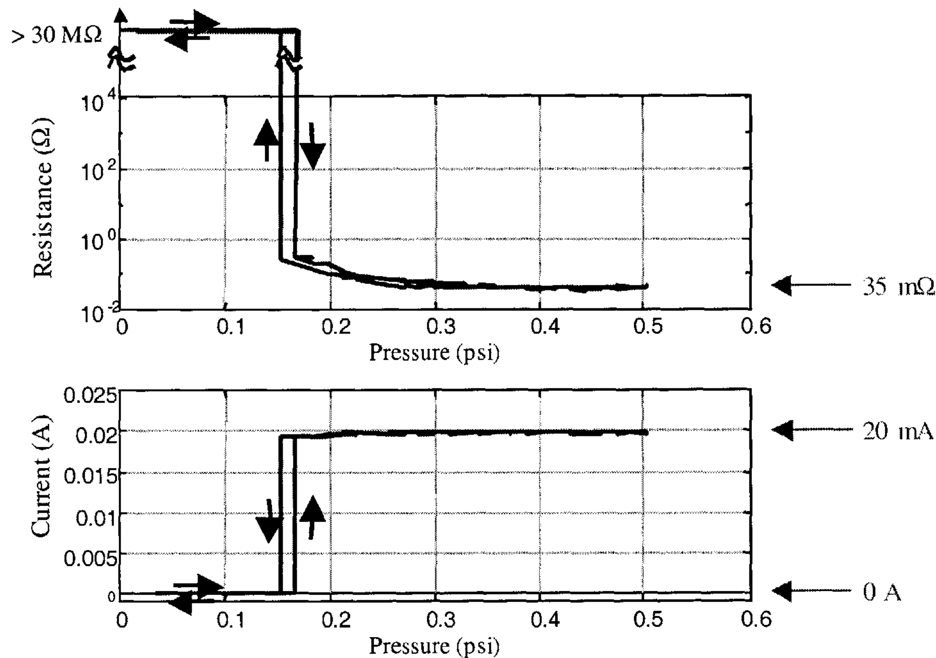

Figure 5.33 Pneumatic actuation test result

With no pneumatic pressure applied, the MEMS pressure switch exhibits a contact resistance higher than the *30MΩ* limit of the measuring ohmmeter. As the pressure goes beyond the turn-on threshold, the contact resistance, measured with the four-point-probe technique discussed in Subsection 5.2.4, starts out with a sub-ohm value and settles down to *35mΩ* with high enough pressure. The on-state current level in this experiment is *20mA*. The experimental turn-on pressure, *0.16psi* or *1103Pa*, is within 7% of the theoretical turn-on pressure, *0.15psi* or *1036Pa*, obtained using Equation 3.62 [61]. Pressure switches of different threshold pressures can be fabricated with different diaphragm thickness, diaphragm material, residual-stress level, and/or gap separation distance. Moreover, what makes the type of pressure switch interesting is that the threshold pressure can also be dynamically tuned with a voltage bias. A discussion of the MEMS switch under combined actuation is given in Section 5.7.

5.6 *Electrostatic Actuation*

The demonstration of electrostatic actuation is first presented by performing a capacitance-voltage measurement on a switch cell that has a *17.5 μm* single-crystal silicon diaphragm (Figure 5.34). As discussed in Section 5.3, a capacitance jump is an indication of electrical contact and is a result of successful electrostatic actuation. Based on the initial air-gap capacitance of *21.5 pF*, the gap distance of the device is determined to be *1.6 μm*. Using Equation (3.12), the estimated pull-in voltage is 22.7 V. The capacitance jump occurs at *24.6 V* as observed from capacitance-voltage curve of the device in Figure 5.34. Also shown in the plot is a simulation of the capacitance-voltage curve using a *MATLAB®* script (Appendix G) that will be discussed in more detail in Section 5.7.

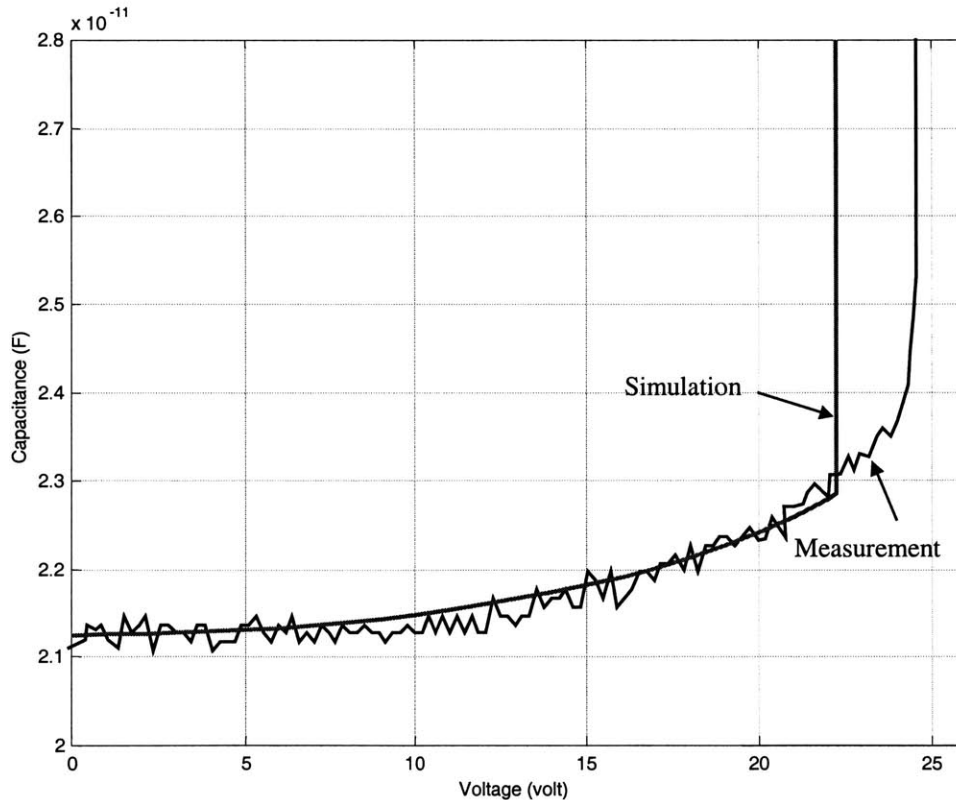

Figure 5.34 Electrostatic actuation: capacitance vs. actuation voltage

The actuation current I_A is also measured after the switch cell is electrostatically turned *on*. This actuation current is virtually negligible (less than *40 pA* in magnitude) as shown in Figure 5.35. This is expected since low actuation power is one of the characteristics of electrostatic actuation.

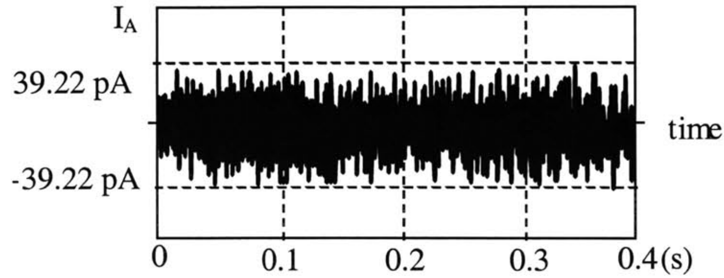

Figure 5.35 Actuation current of the switch

Another demonstration of electrostatic actuation is presented with the switch cell that has a 1500 Å thick LPCVD nitride diaphragm and sixteen 30 μm-diameter pedestal contacts. This same device was tested in pneumatic actuation in Section 5.3. The pull-in voltage estimate based on Equation (3.12) for this device is *19.92 V*. Similar to the experiment with pneumatic actuation, contact resistance and current through the device are monitored as the actuation voltage sweeps. The results are shown Figure 5.36. The pull-in occurs at a voltage of *19.9 V* and release at *14.7 V*. The on-state characteristics of *35 mΩ* contact resistance and *20 mA* on-state current are consistent with these observed in the pneumatic actuation test.

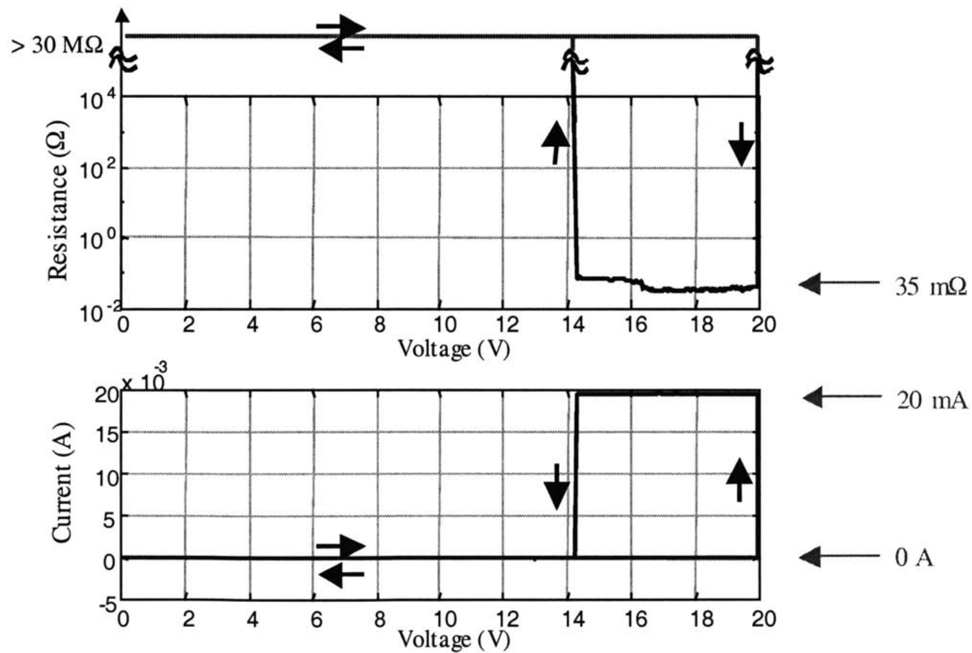

Figure 5.36 Electrostatic test result

5.7 Combined Actuation

This section discusses the situation when the MEMS switch is actuated with pneumatic pressure *and* electrostatic voltage. The demonstrative device has a *17.5 μm*-thick single-crystal silicon

diaphragm and seven *3 μm*-diameter bottom pedestal contacts. Based on the *25.8 pF* gap capacitance measurement, the post-packaging gap distance of the device is estimated to be *1.6 μm*. The theoretical closing pressure is predicted at *0.64 psi* but the switch closes at *0.12 psi*, which is less than 20% of predicted pressure. A possible explanation for this early switch closure is that conductive particle contaminants might be present in the contact area shorting the device at a lower pressure. Predicted electrostatic pull-in voltage is 22.7V and the switch closes at 23.7V, a reasonable 4.2% mismatch. The electrostatic pull-in voltage would be unaffected by the particles since the actuation voltage must reach the snap-through pull-in voltage before the diaphragm is significantly deflected. The measured pull-in voltages at various pneumatic pressure biases are listed in the first two columns in Table 5.1 below.

Pressure bias (psi)	Measured pull-in voltage (V)	Simulated pull-in voltage (V)	Simulation/measurement mismatch (%)
0	23.7	22.7367	4.2
0.013	21.1	20.8618	1.1
0.013	21.8	20.8618	4.5
0.040	20.1	17.1442	17.2
0.041	19.6	17.0112	15.2
0.067	18.2	13.6781	33.0
0.067	17.3	13.6781	26.5
0.085	16.9	11.5166	46.7
0.085	16.1	11.5166	39.8
0.103	13.9	9.4829	46.6

Table 5.1 Electrostatic pull-in voltage under pneumatic pressure bias

Listed in the third column in Table 5.1 are the simulated pull-in voltages, acquired by numerically solving

$$D\nabla^4 g - T_d \nabla^2 g = -\frac{\varepsilon_0 V^2}{2g^2} - p \tag{5.20}$$

for the clamped circular diaphragm over ground plane [52], where g is the gap, D is the flexural rigidity as defined in Equation (5.6), ε_0 is the permittivity of vacuum, $T_d = \sigma_0 t$ = (*residual stress*) × (*diaphragm thickness*), V is the applied voltage, and p is the downward distributed pressure load. This differential equation can be approximated using centered finite difference formulation and is solved iteratively in *MATLAB®* (Appendix G). During each Newton iteration, the system matrices are first set up using previously updated gaps. Then the program solves for the new $\Delta g_{i\text{-}updated}$ using Gauss elimination, and updates the gaps, $g_{i\text{-}updated} = g_{i\text{-}previous} + \Delta g_{i\text{-}updated}$. This procedure is iterated until convergence is attained, i.e. when the $\Delta g_{i\text{-}updated}$'s get sufficiently small.

The gaps determined in this manner yield the desired self-consistent solution satisfying Equation (5.20). An erratic solution of the gaps indicates that the diaphragm is beyond the pull-in point and that the pull-in condition has been reached. With different pressure biases, different initial diaphragm profiles are numerically obtained to calculate the initial gaps to start the iterations under the corresponding pressures.

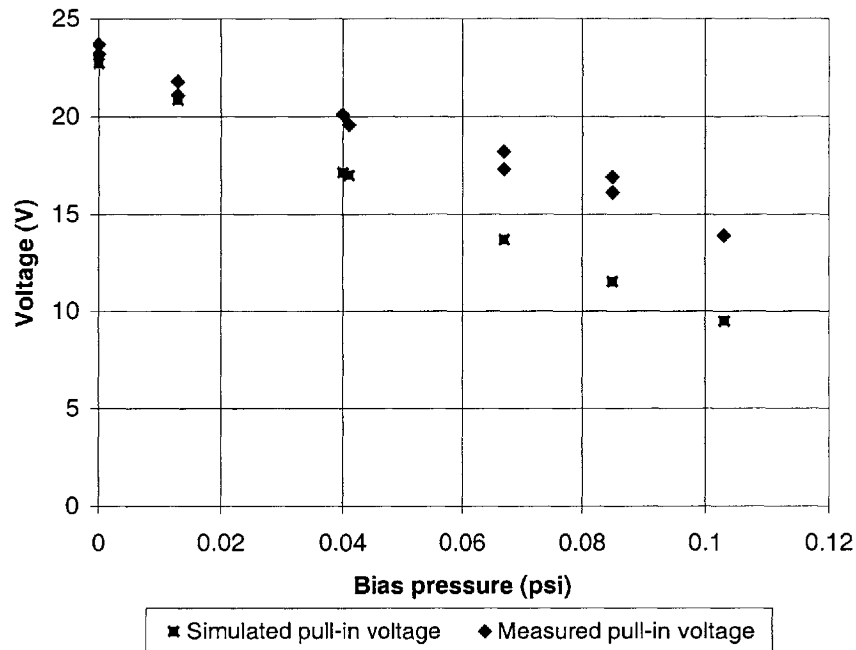

Figure 5.37 Combined actuation: Simulated $V_{pull-in}$ (squares) vs. measured $V_{pull-in}$ (diamonds)

As shown in Figure 5.37 or Table 5.1, at higher-pressure biases, the measured pull-in voltages are about 35-45% higher than the simulated values. An explanation for this disagreement is that the simulation does not consider the opening in the center region of the poly-silicon actuator. This opening in the bottom actuator electrode is purposely made to give room for the pedestal contacts; see the mask layouts in 0. In the simulation, as the diaphragm deflects downward pneumatically, the center portion is deformed closer to the bottom electrode and a significantly higher electrostatic force is generated because of the inverse-proportionality dependence of electrostatic force on the gap. However, in reality, such augmentation of the electrostatic force in the central diaphragm portion when pneumatically biased is substantially diminished because of the loss of the central portion of actuator electrode. A higher pressure-bias will heighten this difference between simulation and reality and widen the mismatch. Another plausible reason for this disagreement is that the same particle contamination problem causing early switch closure pneumatically might have limited the diaphragm motion and resulted in higher pull-in voltage.

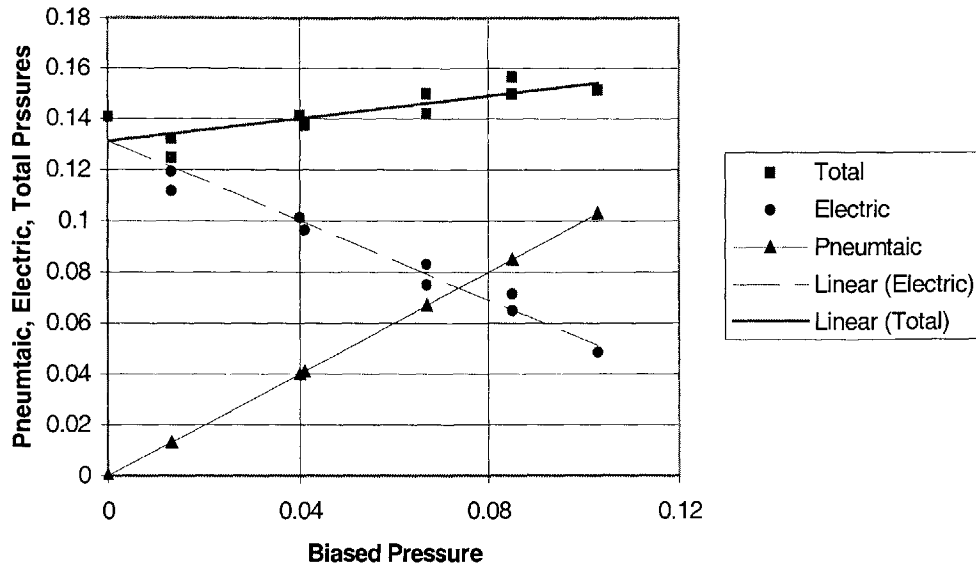

Figure 5.38 Pneumatic pressure, electrostatic pressure, and total pressure under combined actuation

Another analysis approach that is less susceptible to the complications caused by the absence of the central portion of the actuation electrode is to employ the idea of electrostatic pressure defined in Equation (3.11).

$$p_{electrostatic} = \frac{1}{2}\varepsilon_0 E^2 = \frac{1}{2}\varepsilon_0\left(\frac{V}{g}\right)^2 \tag{3.11}$$

Theoretically, the electrostatic pressure exerted on the diaphragm is *higher* in the center than in the periphery due to the inverted-bell shape of the diaphragm under deformation. We will neglect such non-uniform gap distribution and assume that it can be approximated as a parallel-plate capacitor model because:

(1) the electrostatic pull-in is an instable snap-through motion and deflections before pull-in are only a fraction of the full gap; and

(2) there is *no* electrostatic pressure in the center where the diaphragm deflects the most because of the opening.

Figure 5.38 shows the relationship between the pneumatic pressure, the equivalent electrostatic pressure, and the sum of the two. The experimental closing pressure for the device is *0.12 psi* with no voltage applied. It does show that the total pressure of the combined actuation stays

within *20%* of *0.12 psi*, i.e. $p_{pneumatic} + p_{electrostatic} \approx p_{total}$. This is a better match than the previous analysis.

5.8 Contact resistance

As shown in the device cross-section drawing in Figure 3.14, the height of the pedestal contact is set by the thickness of the metal film and it is designed to be higher than the actuation electrode by *2000 Å*. However, due to the setup in the metal evaporation process, there will always be a certain degree of non-uniformity in metal thickness, and, in some cases, the pedestal might not be tall enough to stick out. The consequence of insufficient metal height is poor contact force resulting in less-optimal contact resistance. Figure 5.39 shows measurements made on a device with insufficient metal height.

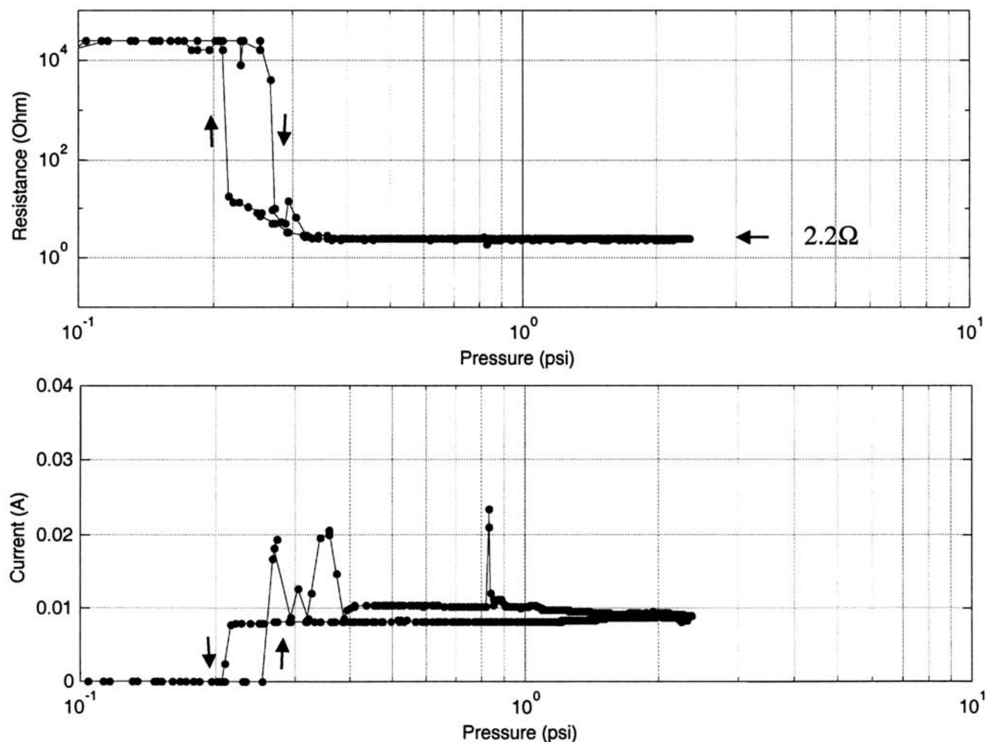

Figure 5.39 Resistance measurements of a device with insufficient metal height

The contact metal was gold, with chromium or titanium as an adhesion layer between the gold and the substrate. With sufficient metal height and fresh gold, the contact resistance of the MEMS switch is well below *0.1Ω*, normally around *50mΩ*, and as low as *14 mΩ.*

The contact resistance dependence on pressure is not always apparent in our experimental observations, nor consistent. Figure 5.40 shows the results of one of the devices that exhibit a

stronger resistance dependence on pressure. This device has a *10 μm* thick single-crystal silicon diaphragm and 16 *3μm*-diameter pedestal contacts. The top four plots are *I-V* scans of the device using four-point-probe technique at different applied pressures. The slopes of the *IV* curves represent the contact resistance and a *500 mΩ* dash-line is plotted as a reference slope for comparison purpose. It can be seen that, as pressure rises, the slope of the *IV* curve gets slower indicating a lower contact resistance. The bottom two plots are the resistance-pressure and conductance-pressure relationships for this device.

Figure 5.41 presents another interesting result in which the contact resistance is measured as a function of current level and directionality. The switch cell being investigated has a *10 μm* thick single-crystal silicon diaphragm and sixteen *30 μm*-diameter pedestal contacts. The threshold pneumatic pressure for the device is *0.12 psi*, but the device is actuated at constant *1 psi* pressure to ensure tight contact closure and to exclude pressure dependence during the test. The sign convention for the current flow is such that *positive* current flows from *bottom* contacts into *top* diaphragm. The experiment is carried out with the computer-controlled instrumentation described in Section 5.2 and current sweeps from most negative to most positive for one run. Five rounds of current sweep are made and contact resistances are detected using four-point-probe technique. One of the noticeable characteristics is the significantly higher contact resistance at low current. This is not a surprising phenomenon if part of the electrical contact area is *quasi-metallic* and covered by insulating films sufficiently thin to be penetrated by electron current by means of tunneling [42]. If this is the case, lower contact resistance can be expected at higher currents since a higher electric field will enhance the electron tunneling and essentially increase the conducting contact area. Another observation is the slight asymmetry of the resistance with respect to current polarity. The resistance measured with negative current is about 10-*20%* higher than that with positive current in this experiment. This could be due to unexpected Schottky diodes formed at the semiconductor-metal interface. An ideal ohmic contact at the semiconductor-metal interface can be achieved only if the semiconductor is *degenerately* doped. For this particular device, the ohmic contact might be imperfect leading to a slightly rectifying semiconductor-metal interface. Also interesting to note is the ultra low *5 mΩ* contact resistance for positive currents higher than *20 mA*.

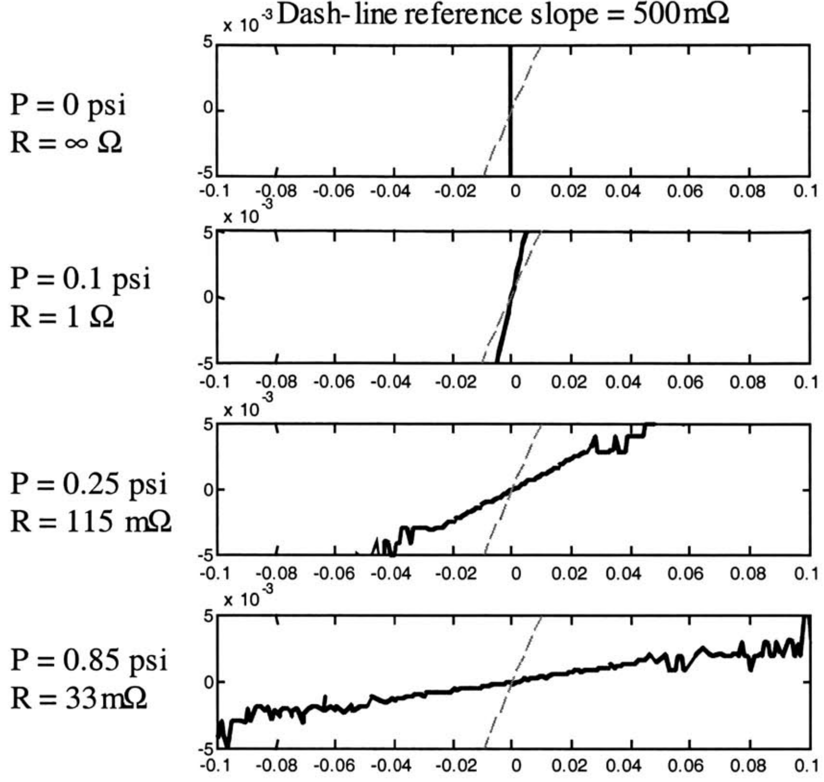

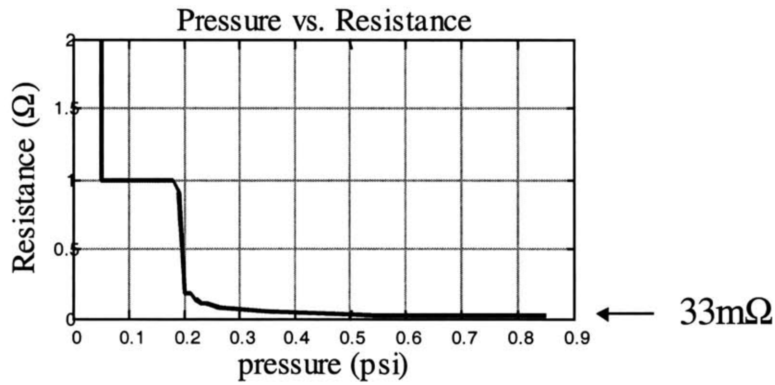

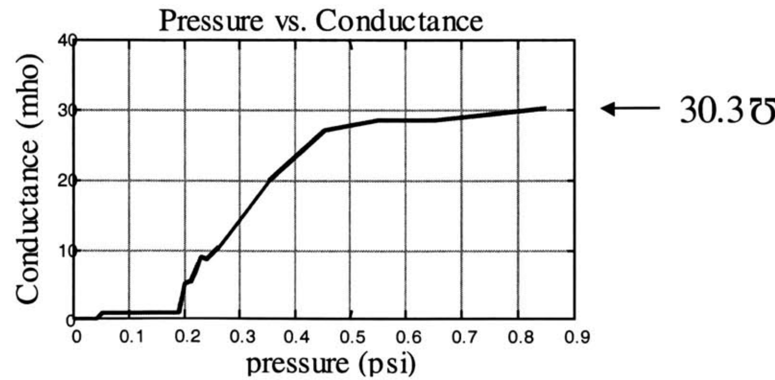

Figure 5.40 Contact resistance vs. pressure

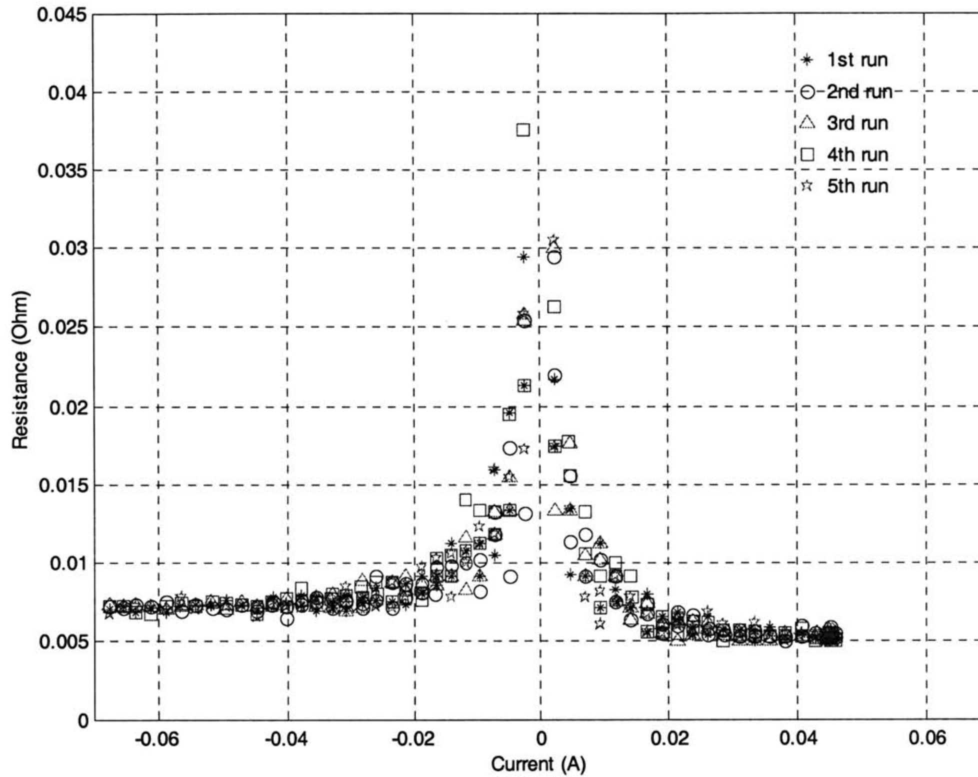

Figure 5.41 Contact resistance vs. current (positive current flows from bottom to top)

5.9 Switching time

One of the key aspects of a switching device is how fast it can switch states. Therefore an experiment was designed to investigate the switching time of the power MEMS switch. The setup with which the test is carried out is depicted in Figure 5.42. The idea is to use a load resistor whose resistance is significantly larger than the on-resistance of the device. When the switch is turned *on*, most of the potential drop will take place across the load resistor and the voltage output, V_{out}, will be essentially ground zero. If the switch is in *off* state, there will be no current flowing through the load resistor and the voltage output will be the source voltage. In this way, the state change of the switch can be captured with an oscilloscope and then compared to the change of the actuation signal.

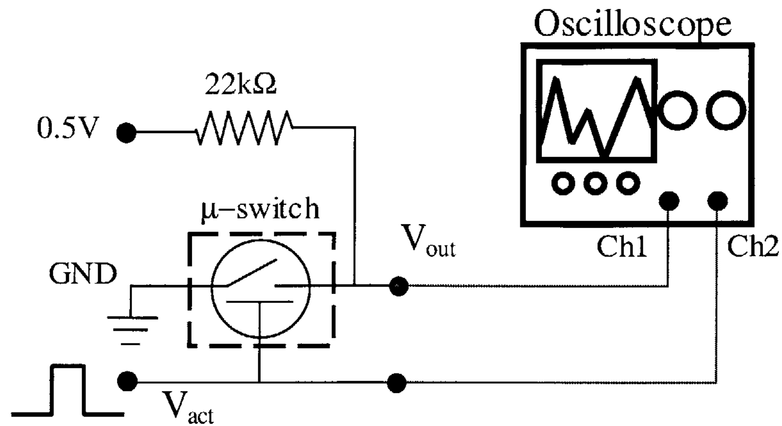

Figure 5.42 Hardware setup for switching time test

5.9.1 Electrostatic switching

The device used in this test is one with a 1500 Å nitride diaphragm. The switching time can be determined by measuring the time delay between the change of the actuation voltage V_{act} and that of the switch state V_{out}. Both signals are fed into an oscilloscope and the screen shot is shown in Figure 5.43. The switch-*on* time is *5ms* and switch-*off* time is *30ms*. Another interesting observation is that when the device operates for a certain length of time, the switch-*off* time can drift by an amount as high as *600 ms*. This is believed to be an oxide charging effect. A suggestion to alleviate the charging complications is to pattern the insulating oxide film above the poly-silicon actuation electrode. This turns the solid oxide film into small oxide stops. With this additional patterning, the problematic oxide in some actuation area is removed leaving air as the only separation between the diaphragm and the poly-silicon.

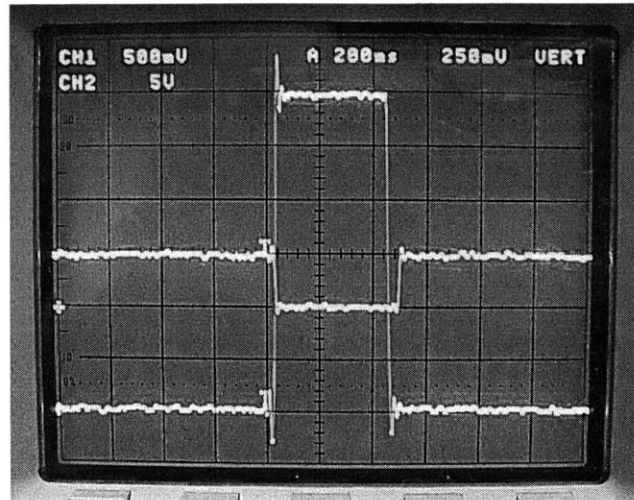

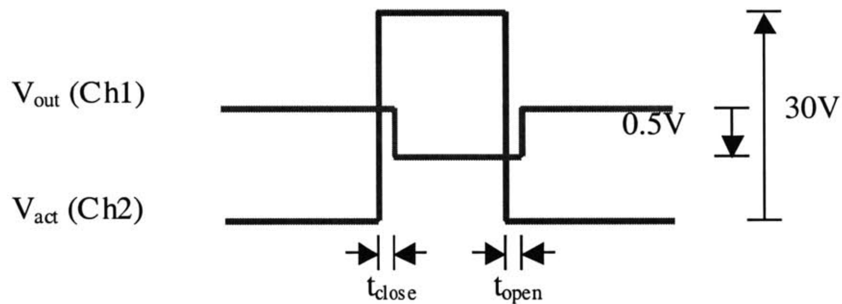

Figure 5.43 Switching time (device switching electrostatically)

5.9.2 Pneumatic switching

The same device studied in Subsection 5.9.1 is used for the pneumatic switching time test. The experiment is performed in a similar way except the actuation voltage is replaced with the pressure output signal. Again, the switching time can be detected by measuring the time delay between the change of the pressure sensor signal and the change of the device output voltage. The results are shown in Figure 5.44 and both switch-*on* and switch-*off* times are found to be *50ms*.

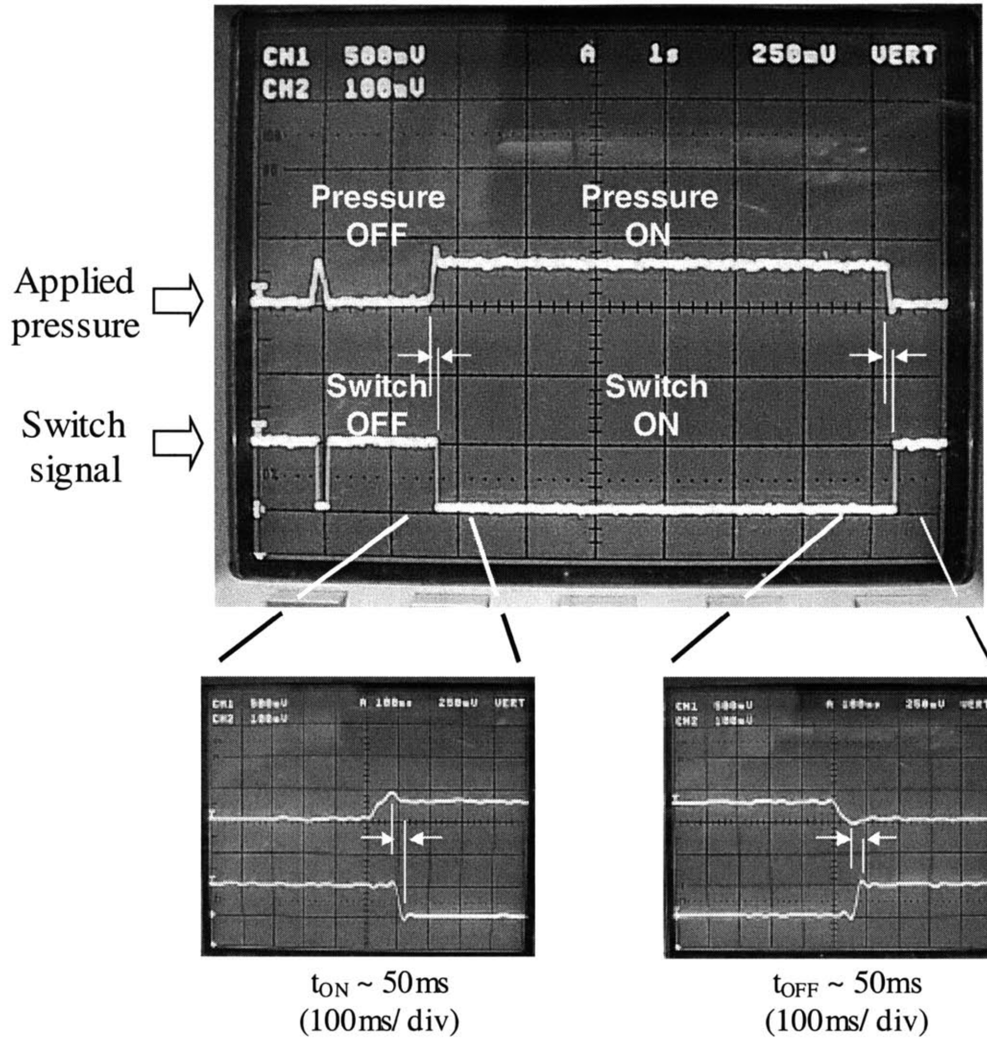

Figure 5.44 Switching time (device switching pneumatically)

Because the switch is operating in atmospheric environment, the design of the device is such that its switching speed is limited by the squeeze-film damping effects (Subsection 3.6.2). The exact switch switching speed depends not only on the squeeze-film damping but also on the diaphragm characteristics and the actuation forces. The governing equation of parallel rigid-body plates under squeeze-film effects is the compressible isothermal Reynold's equation, Equation (3.78). As discussed in Subsection 3.6.2, the characteristic time constant in the compressible isothermal Reynold's equation is used as a quick estimation of the effects of squeeze-film damping without solving the nonlinear partial differential equation. This characteristic time is repeated below

$$\tau_{sqfm} = \frac{48\mu_a a^2}{p_a h_0^{\ 2}}. \tag{3.79}$$

The gap separation of the device studied here is *2.79 μm* based on capacitance measurements (Section 5.3). Therefore the characteristic time of squeeze-film damping in this air gap is on the order of *15.8 ms*. These *5 ms*, *20 ms*, and *50 ms* switching time measurements are on the same order-of-magnitude of the characteristic time.

5.10 Current capacity

The *cold*-switching current capacity of one single switch cell is investigated in this section. The experiment is carried out by performing four-point-probe resistance measurements at different current levels then checking the integrity of the device immediately thereafter. The device under investigation had a 1500 Å thick LPCVD silicon nitride and sixteen *30 μm*-diameter pedestal contacts. The results are plotted in Figure 5.45.

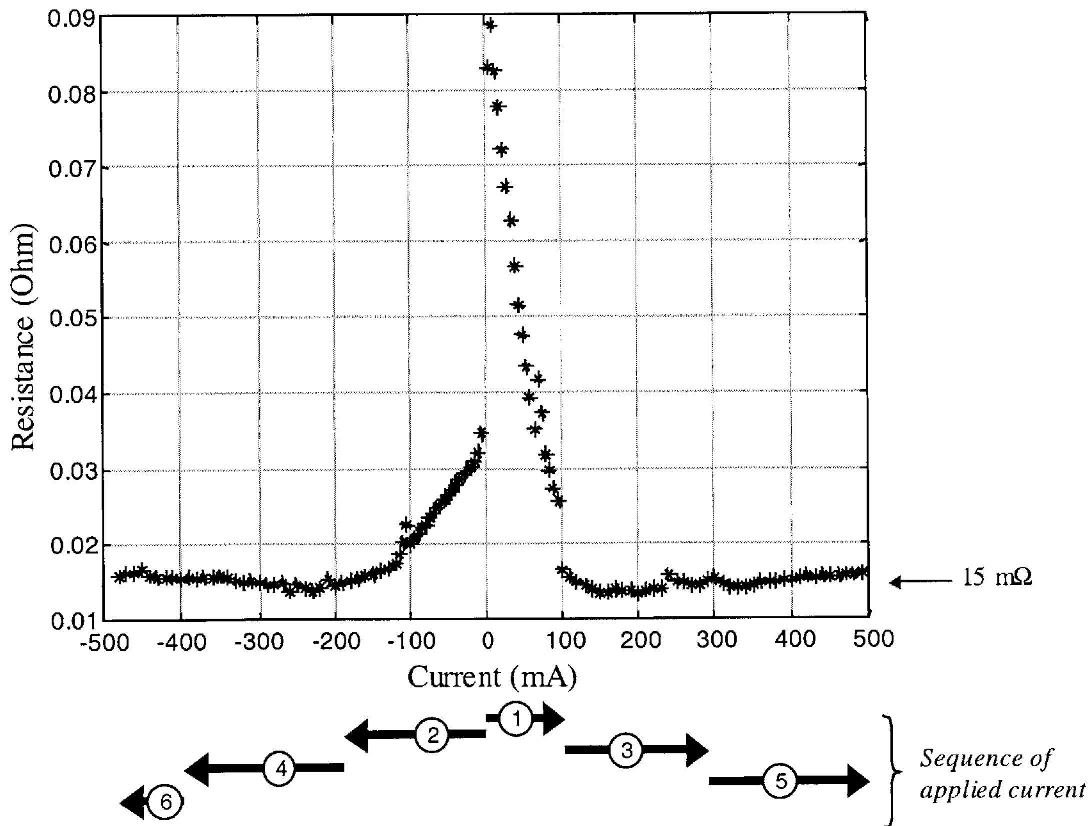

Figure 5.45 Current capacity for one single switch cell

The current starts from zero and increments at 5mA, and the direction of the current is alternated every 100 mA or 200 mA. The arrows and corresponding numbers in the bottom of Figure 5.45

indicate the exact sequence of current supply in this test. For this switch cell, contact sticking does not occur until ***+490mA*** or ***–480mA*** and the device is still operational after the contacts are re-opened with back pressure.

5.11 Cyclic Operation

In addition to demonstrating repeated operations of the device, it is of our interest to examine if material failures, such as fatigue and creep, take place under cyclic operation and to investigate the device performance over time. The same switch cell tested for current capacity (1500Å nitride diaphragm with sixteen *30µm* contacts) is employed in this experiment. Figure 5.46 shows the contact resistance of the device at a current load of *20mA* over many cycles.

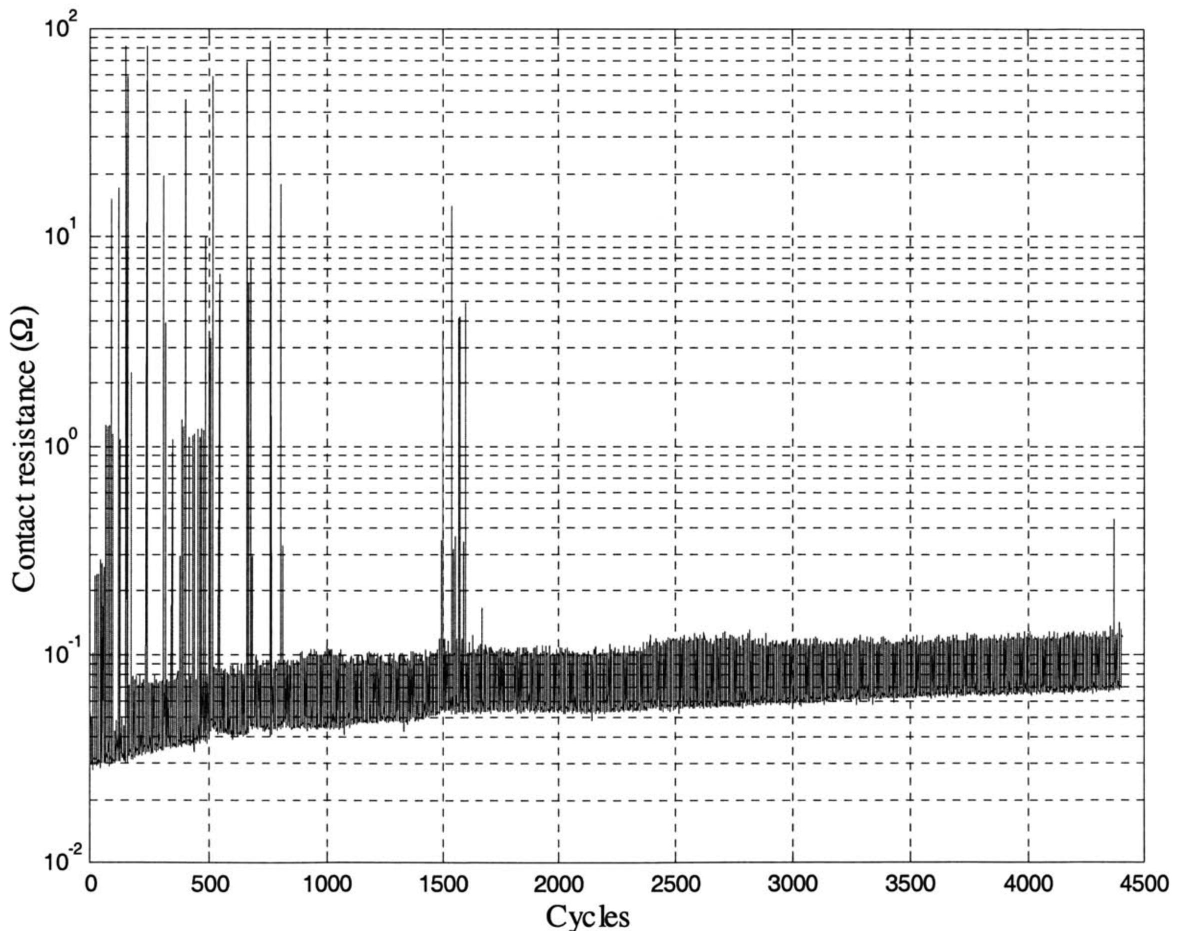

Figure 5.46 Contact resistance vs. cycles

For the first few hundreds of cycles, the contact resistances exhibit some *spikes* and then settles to around *100 mΩ*. These resistance spikes indicate that there might be a process of burning off chemisorbed and/or physisorbed films and re-deposition of the products on the metal contact surface in the early cycles. This process is stabilized after the "*burn-in*" period. This test experiment is performed using the hardware described in Section 5.2 and Figure 5.47 shows the first thirty cycles of the test results.

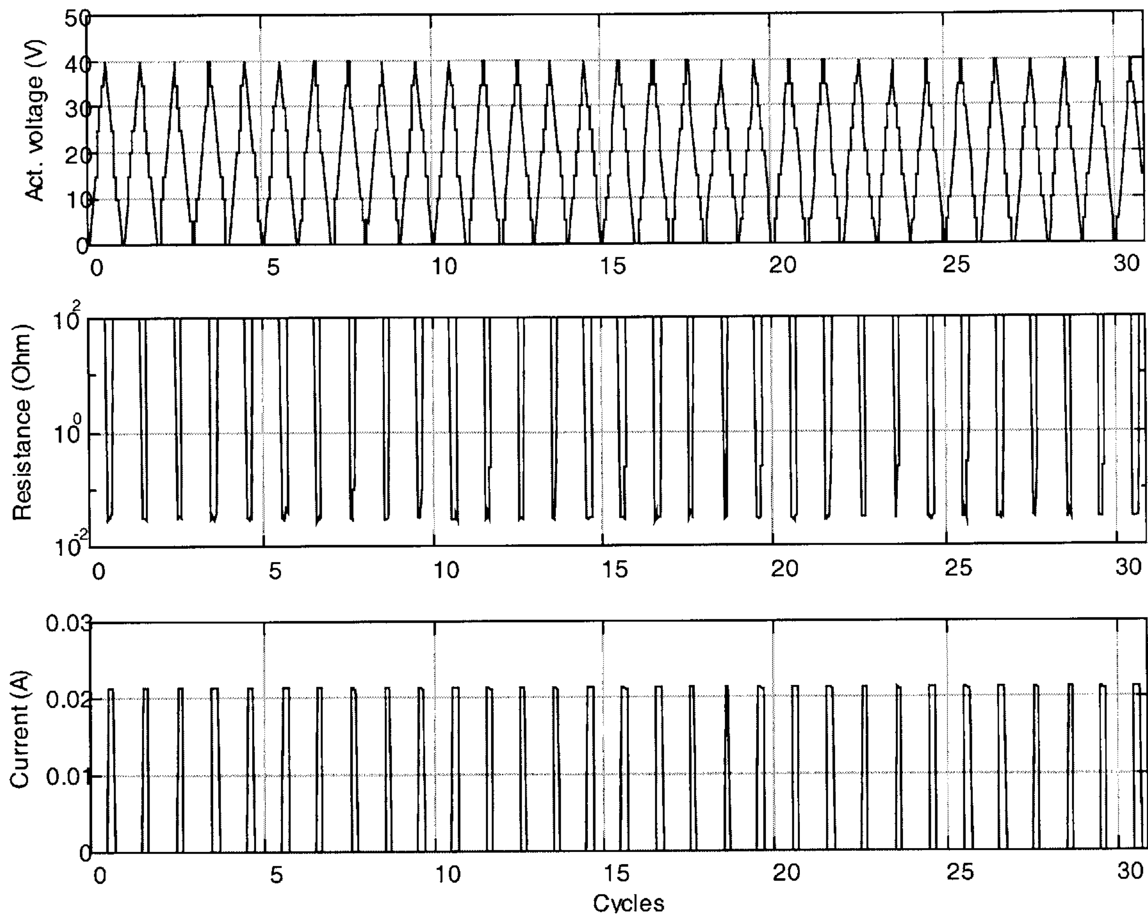

Figure 5.47 First 30 cycles in cyclic operation test

Insulation oxide breakdown

The cyclic operation test ends after *4404* cycles because of a device failure. The failure mode is an unexpected electrical breakdown at *40V* in the insulation oxide that covers the poly-silicon actuation electrode. The *1000 Å* insulation oxide is grown thermally on poly-silicon. For oxides thermally grown on single-crystal silicon, a thickness of *1000 Å* should be able to sustain a potential as high as *100 V* without breaking down. However, this value might be optimistic in this case because (1) the top insulation oxide layer covering poly-silicon actuator is grown from poly-

silicon and such oxide might have a higher defect density, and (2) the relatively large actuator area, $4.532 \times 10^{-6} m^2$, enhances the likelihood of having a weakening defect in the area. Therefore, an experiment was carried out to test the breakdown strength of the top insulation oxide. In Figure 5.48, two devices that have been heat-treated for 2 minutes at *350°C* to simulate the thermal cycle of thermo-compression bond are tested and breakdown voltages of the oxide are recorded at *66 V* and *64 V*. Two devices without the thermal treatment are tested and their oxide breakdown strengths are *105 V* and *62 V*, as shown in Figure 5.49. The following lessons are learned from this experiment

- *1000 Å* thick silicon dioxide grown on poly-silicon has a breakdown strength of about *60 V*. Taking a safety factor of three, the devices should not run above *20 V*.
- The thermal cycle of thermo-compression bonding does not have much adverse effect on the oxide breakdown strength.

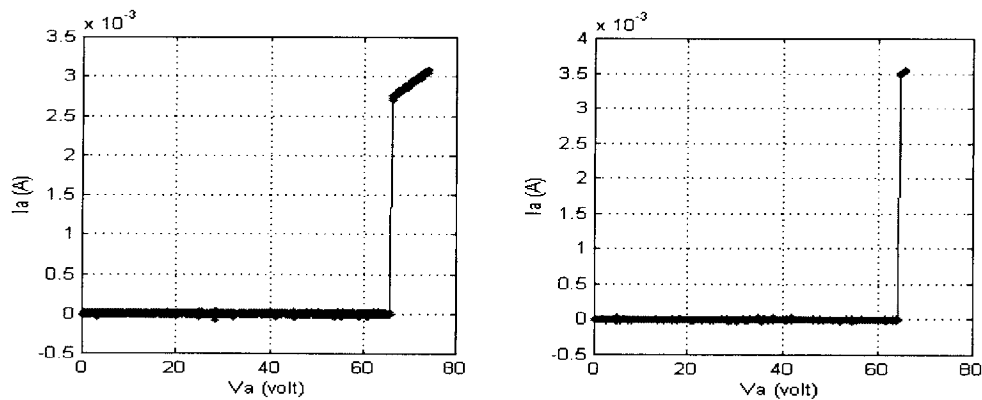

Figure 5.48 Insulation oxide breakdown test (350°C, 2min. thermal treatment)

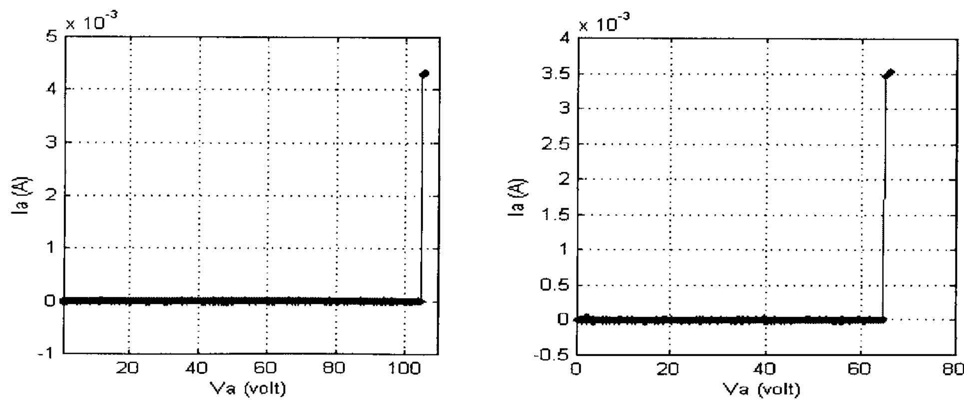

Figure 5.49 Insulation oxide breakdown test (no thermal treatment)

5.12 Summary

In this chapter, packaging issues of a single MEMS switch cell and test results of the prototype are discussed. Test hardware, software and instrumentation limitations are first addressed. Electrical modeling of the device and mechanical modeling of the diaphragm deflection are provided. The MEMS switch is aimed to replace existing *power* switches, therefore the focus of the device testing is on its on-state resistance performance. Low on-state contact resistance has been consistently observed and contact resistance as low as *5 mΩ* has been measured. The resistance dependency on pressure and current are also investigated. Pneumatic actuation at *0.16 psi* and electrostatic actuation at *20 V* are both demonstrated with reasonable agreement between model and experimental data. Combined actuation of the device is also performed and the results are compared with MATLAB simulations. Current capacity for a single switch cell is explored under cold-switching condition and is found to be about *480 mA*. Switching times are measured to be in the *30-50 ms* range. Finally, cyclic operation of the device is executed and the failure mode of the device is discussed.

Chapter 6 SUMMARY, CONCLUSIONS, AND SUGGESTIONS FOR FUTURE WORK

This closing chapter provides a summary, conclusions, and suggestions for future work beyond the thesis. Section 6.1 briefly summarizes each chapter. Major conclusions are presented in Section 6.2, and Section 6.3 contains the suggestions for future improvements and the continuation of this thesis.

6.1 Summary

This thesis has developed an electrostatically-actuated power MEMS switch. As outlined in Chapter 1, the complete power switch prototype consists of an array of switch cells and is paralleled with a protecting circuit for *arcless* switching; see Section 1.5. Such a system design enables this thesis to focus on the development of a normally-open *SPST* switch cell that operates under *cold switching* conditions, and leaving the arcing-related problems and other more complicated switch configurations to a higher system-level arrangement that will be part of future work. Other topics included in Chapter 1 are the historic background of micro switching devices, discussions on their attributes and applications in Section 1.1, and a brief literature survey in Section 1.2.

Chapter 2 is primarily concerned with the understanding and characterization of the physics of electrical breakdown phenomena in micron-scale air gaps. These are important subjects for the development of the MEMS switch because they dictate the *off-state* blocking voltage of the switch. Townsend and Streamer electrical breakdown theories are discussed in Section 2.3. Because of the micron-scale geometries of MEMS devices, the Townsend breakdown model, which applies to electrical breakdown systems of lower pressure-separation product (*pd*), is believed to provide a more applicable breakdown model. Special considerations for micro-scale air breakdown strength are addressed in Section 2.4 and the argument is advanced that electrical

breakdown in narrowly separated air gaps is *more* dependent on the electrode surface roughness. An empirical investigation of achievable standoff voltages in such narrow air gaps and its results are presented in Section 2.5. The experimental results are promising because breakdown voltages exceeding *300 V* are achieved for air gaps as small as *0.5 μm*. A die-level metal-to-metal thermo-compression bond process protocol is also established to minimize the diesaw slurry/dust contamination that otherwise leads to very low breakdown voltages.

Chapter 3 discusses the theories and considerations used in the design of the MEMS power switch. Commonly seen actuation schemes in MEMS devices are briefly introduced and a justification for selecting an electrostatic scheme is given in Section 3.2. Formulated predictions of the *pull-in* voltage and *release* voltage for the electrostatic actuation of clamped circular diaphragm are also provided. Discussion and analysis of two different mechanical diaphragm structures, a bossed circular diaphragm and a uniform-thickness circular diaphragm, are given in Section 3.3. Metal-to-metal contact characteristics are discussed in Section 3.5. Seemingly straightforward electrical contact systems are actually fairly involved physical phenomena. In addition to contact size and contact force, contact surface tribology characteristics, thermoelectric effects, contact surface cleanliness, and arrangement of contact patterns all have non-trivial effects on the contact resistance. As a result, accurate contact resistance prediction is *not* practically attainable. Nevertheless, this is discussed in Section 3.7. The squeeze damping of the air film bounded between the moving diaphragm and the stationary bottom substrate and its effects on the device switching speed are examined in Section 3.6.

In Chapter 4, the fabrication details of the MEMS switch and other relevant issues are discussed. The device consists of a bottom wafer and a top wafer bonded together. Fabrication processes for both bottom and top wafers are compatible with that for silicon based integrated-circuits until metallization. For the bottom wafer, a 5-mask process is designed bearing similarity with mainstream microelectronics processes. The top wafer, which is fabricated with a 3-mask process, features classic bulk-micromachined diaphragm structures, and so extreme handling care must be taken once these delicate structures are formed.

Chapter 5 contains various characterization results of the MEMS switch. The prototype switch has gone through several evolutions, described in Chapter 4, and not all tests are performed with the same type of switch. Some design modifications are made to facilitate some actuation tests or to enhance the consistency of the post-packaged device quality. In spite of the differences in the mechanical designs, the contact characteristics of the switches are expected to be similar. Packaging issues and the instrumentation for device testing are addressed in Section 5.2.

Electrical model and mechanical model of the device are established and comparisons between model simulations and measurements are made and discussed in Section 5.3 and Section 5.4. The comparison generally shows very good agreement. A prototype device is pneumatically actuated while its on-state performance is characterized in Section 5.5. Similar characterization is performed electrostatically in Section 5.6. Combined pneumatic and electrostatic actuation is demonstrated and discussed in Section 5.7. The on-state contact resistance of the device and its dependence on other parameters are investigated in Section 5.8. The switching times of the MEMS switch when electrostatically and pneumatically actuated are investigated in Section 5.9. The current capacity of a single switch cell is explored in Section 5.10. The prototype device is repeatedly operated to understand its performance drift over 4000 cycles of operations in Section 5.11.

6.2 Conclusions

The primary contribution of this thesis is the realization of design theories through the experimental characterization of a micro-fabricated power MEMS switch. Experiences and conclusions are gained along the course of the analysis, design, fabrication, and testing of the device and are presented in this section.

In Chapter 2, based on the test results of the device off-state electrical breakdown performance, it is concluded that *300 V* is an achievable off-state standoff voltage in micron-scale air gaps. Particle contamination, which induces post-packaged device shorting, becomes an issue due to the *die-level* thermocompression bond process, unless a thorough solvent clean is performed before bonding. When a reliable and well-accepted *wafer-level* thermocompression bond process becomes available, this contamination problem should be eliminated. Paschen's law predicts similarities between electrical breakdown of narrow air gaps at atmospheric pressure and that of wide gaps at vacuum pressure. However, deviation of experimental results from the theoretical prediction is observed. To account for the mismatch, a hypothesis is argued that electrical breakdown of narrow gaps is more dependent on the secondary ionization at the cathode surface and therefore is more sensitive to the surface roughness condition, which is not considered in a Paschen breakdown model.

Chapter 3 reaches a conclusive design of the power MEMS switch. Actuation methods commonly implemented in micro actuators are critiqued on their suitability for automotive power switching applications and their MEMS processing facility. The choice of actuation scheme for the MEMS switch is electrostatics. Its advantages are low power consumption and CMOS compatible

materials and processes. The major disadvantages are the requirements of a large area and a close gap separation to generate a significant closing force. The moving structure of the actuator is chosen to be a bulk-micromachined clamped circular diaphragm. Key device specifications such as, actuation pull-in/release voltage, actuation pressure, off-state standoff voltage, maximum allowable actuation voltage, on-state resistance, and switch time are calculated.

Chapter 4 focuses on the fabrication of the MEMS switch and the process-relevant complications. Early generations of the switch having a bossed structure are introduced and their design considerations and fabrication difficulties are explained. A bossed diaphragm has several desirable features such as simplification in device modeling and straightforward contact force calculations but is prohibited due to stress-related fabrication issues. Therefore, a uniform-thickness diaphragm structure with minimal high-temperature processing is found to be easier to fabricate and, more importantly, less stress-troubled. Moreover, a highly tensile-stressed LPCVD nitride diaphragm device is proposed so that the diaphragm structure is *less* susceptible to stress problems.

Chapter 5 provides conclusions learned from the experimental characterization of the device. Pneumatic actuation of the device requires an airtight package and the quick-cure epoxy is found to be a very useful experimental tool. Electrical modeling and mechanical modeling of the device behaviors are made, and most mismatches between model predictions and actual measurements are explained. The surface roughness of the poly-silicon actuation electrode is identified as the cause. Agreements between the estimations and experimental measurements in both electrostatic actuation test and pneumatic actuation test validate the understanding of the device physics. The MEMS switch cell displays promising on-state performance as a power switch, specifically in resistance measurement and current capacity tests. For example, *400 mA* is passed through contacts having on-state resistance between $5\ m\Omega$ and $50\ m\Omega$. Also, the switching time of *30-50 ms* is adequate for power switching applications. But *oxide charging* effects are observed and need more investigation to understand their physics and to remedy the problems they cause. Preliminary results show that the MEMS switch can be operated repeatedly for over 4000 cycles.

6.3 Recommendations for Future Work

This section suggests directions for further investigations of the development of the power MEMS switch. Subsection 6.3.1 offers suggestions for off-state performance improvement. Subsections 6.3.2 and 6.3.3 are concerned with switch development from a system viewpoint. Subsection 6.3.4 recommends a way to allow higher electrostatic actuation voltage, and

Subsection 6.3.5 proposes an alternative design that could potentially exhibit better on-state performance.

6.3.1 Ultra-high standoff voltage

The *270 V* standoff voltage of the device is sufficient for most power applications. However, even-higher off-state blocking voltage may be required in certain applications, In response, this subsection suggests future directions to take. Our experiments with electrical breakdown strength in narrow gaps are carried out exclusively in atmospheric air, mostly because the current metal-to-metal thermocompression bonding technology does not assure hermetic sealing. Potentially, a gas-sealing metal-to-metal wafer bonding technology or packaging scheme would facilitate the use of other dielectric gases at different pressures bringing forth a new dimension in terms of improving breakdown strength of the MEMS switches.

According to what Paschen law predicts, pumping up the gas pressure inside the gap has the same effect on electrical breakdown as does raising the gap separation distance in a linearly proportional manner. Therefore, it can be argued that either increasing or decreasing the gap pressure can be implemented to move further away from the *pd* point corresponding to the minimum breakdown potential in the Paschen breakdown curve (Figure 2.1) and thus improves the breakdown strength.

Other dielectric gases than air may be used to improve the breakdown strength of the switch. Possible dielectric gases that can used to improve electrical breakdown are simple gases, such as nitrogen, hydrogen, helium, or oxygen; oxide gases, such as carbon dioxide and sulfur dioxide; Hydrocarbon gases, such as methane, ethane, propane, butane, and hexane; and electronegative gases such as sulfur hexafluoride (SF_6), dichlorodifluoromethane (CCl_2F_2, Freon 12, Genetron 12) and so on.

6.3.2 Protection arcless-switching circuit

It is believed that the lifetime of the mechanically moving MEMS switch is dictated more by the wear of its contacts than by the failure of the diaphragm itself. Since arcing is a well-known cause of contact wear, a protective circuit is proposed to parallel with the power MEMS switch device to limit the potential across the switch contacts under a design value. Such a parallel protection circuit turns on before/turns off after the MEMS switch. This way, the contacts of the switch are protected from being brought into close vicinity at high voltage.

A successful development of this protective circuit and its integration with the switch can greatly improves the switch life time, current capacity, and its high-voltage performance.

6.3.3 Switch cell array

The purpose of the switch cell array design is *two-fold.* First if offers an apparent current capacity boost through parallelism. Also, it allows complex switch configurations to be built from arrays of a simple SPST switch cell. This leaves more complicated switch configurations to packaging-level arrangements. Furthermore, the protective/control circuit can be implemented by replacing one of the cells in the array with a circuit cell.

6.3.4 Thicker insulation oxide

As discussed in Subsection 3.4.2, the thickness of the insulation oxide above the poly-silicon actuation electrode is directly linked to the achievable maximum actuation voltage. To raise this achievable actuation voltage without electrical breakdown in oxide, a thicker insulation layer is proposed.

6.3.5 Other design possibilities

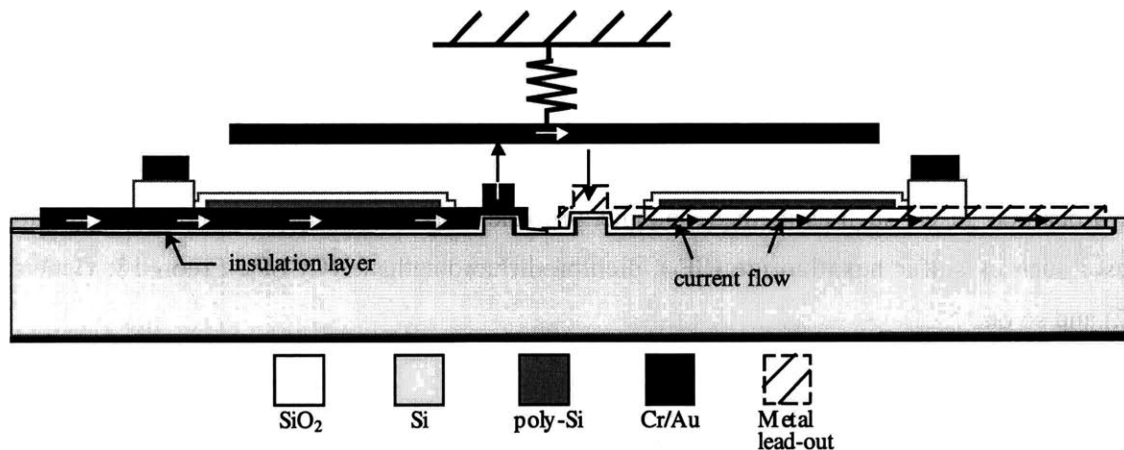

Figure 6.1 Other MEMS switch design: A vertically-moving structure deflects down and electrically connects with two pedestal contacts.

The on-state resistance of the device comprises a series of resistances along the current path and the bulk resistance has a dominant contribution. The apparent approaches to reducing the bulk resistance are (1) lowering the resistivity of the starting substrates, and (2) thinning the thickness

of the starting substrates. Another way to lower the total on-state resistance is proposed in Figure 6.1. Two electroplated *thick* metal lines are isolated and open in the center of the device; a vertically-moving structure is deflected downward electrostatically and connects the two metal lines. The current flows horizontally in this case. There are two metal-to-metal contacts in this design, but our analysis shows that very low constriction resistance in metal-to-metal contacts can be achieved. On the other hand, the resistivity of metals are orders of magnitude lower than heavily-doped semiconductors and, as a result, ultra-low resistance in the metal lines can be achieved with proper geometric design of the metal lines.

Appendix A DIAPHRAGM BUCKLING

The flatness of the diaphragm structures is inspected under a *WYKO™* surface profiler that uses optical interferometry technologies. The plot in Figure A.1 shows that buckling is apparent for a bossed silicon diaphragm featured in Generation 3 of the switch; refer to Section 4.2.4. A tensile-stressed nitride film is added to help stretch the diaphragm flat but no improvement is observed. The profile of a silicon bossed diaphragm coated with nitride is shown in Figure A.2. As discussed in Section 4.2.4, thermal expansion coefficient mismatch and stress gradients are conjectured to be the cause of the buckling. The fact that adding a tensile nitride film does not reduce the diaphragm buckling supports the argument that a *stress-gradient,* instead of absolute *stress* level, is the cause of the buckling.

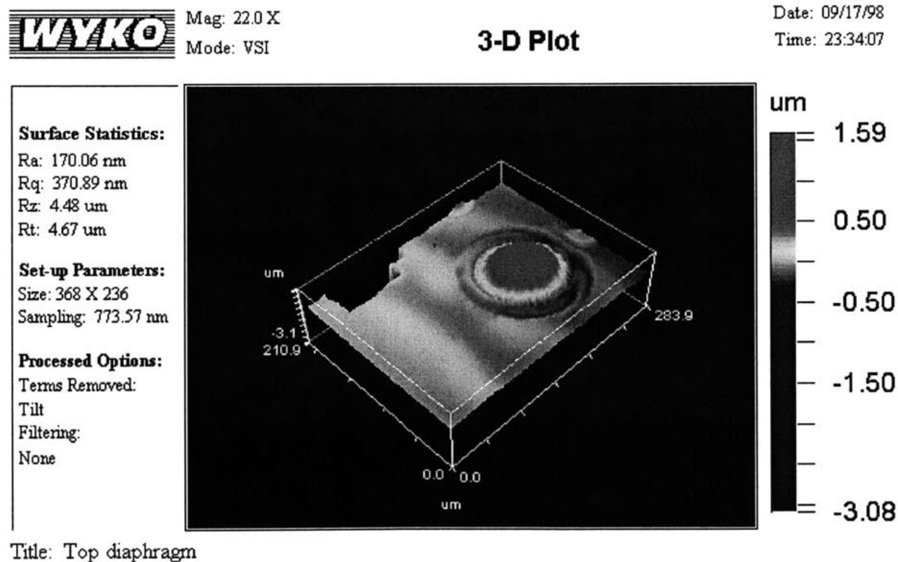

Figure A.1 Buckling of thin bossed silicon diaphragms.

Mag: 22.0 X
Mode: VSI

3-D Plot

Date: 09/17/98
Time: 22:55:55

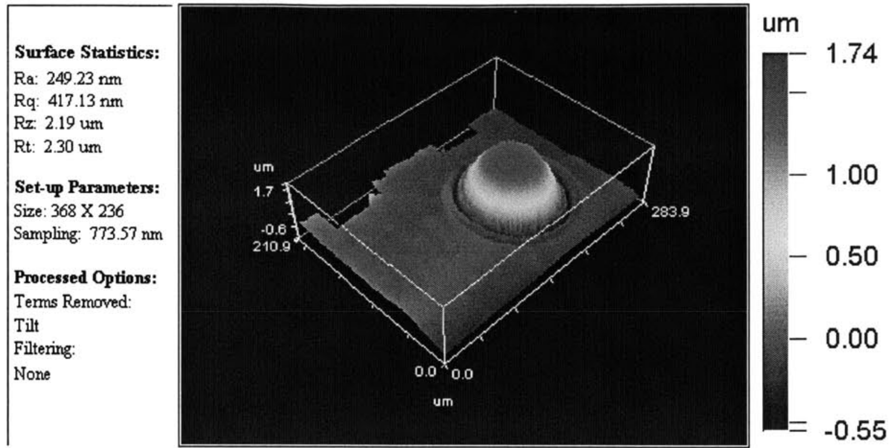

Title: Top diaphragm

Figure A.2 Buckling of thin bossed silicon diaphragms coated with nitride film

Appendix B Detailed Process Travelers

§B.1 Traveler report for bottom wafers

```
Traveller Report for Lot: relay_lower

Description:      PFR file for electro-static microrelay

**** 1. Opset Task: STRESS-RELIEF-OXIDE   Opset: dsro430

MACHINE:  ICL rca              USER: joeywong
SPECIAL INSTRUCTIONS:
**RCA CLEAN IS REQUIRED**
Step 1a:  SC1 - 10mins.
Step 1b:  Dump Rinser 1.
Step 2a:  HF Dip - 15secs.
Step 2b:  Dump Rinser 1.
Step 3a:  SC2 - 15mins.
Step 3b:  Dump Rinser 2 - until 9Mohms is achieved.
Step 4:  Spin Dry - 60sec rinse, 240sec dry.
---------------------------------

MACHINE:  ICL tubeA1           USER: joeywong
Settings
           RECIPE                        210

**** 2. Opset Task: IMPLANT   Opset: NOT AN OPSET

MACHINE:  ICL implanter
SPECIAL INSTRUCTIONS:
Do N+-ION-IMPLAN on the front side.
Settings
           ELEMENT                       Arsenic
           DOSE                          1.0E16
           ENERGY                        90keV
           TIME                          > 20 Seconds

**** 3. Opset Task: IMPLANT   Opset: NOT AN OPSET

MACHINE:  ICL implanter

SPECIAL INSTRUCTIONS:
Do N+-ION-IMPLAN on the backside.

Settings
           ELEMENT                       Arsenic
           DOSE                          1.0E16
           ENERGY                        90keV
```

TIME > 20 Seconds

**** 4. Opset Task: GROW-10K-OXIDE Opset: dox10k

MACHINE: ICL rca USER: joeywong

SPECIAL INSTRUCTIONS:
RCA CLEAN IS REQUIRED
Step 1a: SC1 - 10mins.
Step 1b: Dump Rinser 1.
Step 2a: HF Dip - 15secs.
Step 2b: Dump Rinser 1.
Step 3a: SC2 - 15mins.
Step 3b: Dump Rinser 2 - until 9Mohms is achieved.
Step 4: Spin Dry - 60sec rinse, 240sec dry.

MACHINE: ICL tubeB1 USER: joeywong
Settings
RECIPE 223

MACHINE: ICL ellipsometer USER: joeywong
WAFERSETS: Lot relay_lower: relay_lower
FILM-TYPE K2 (oxide)

**** 5. Opset Task: GENERIC-TRL-PHOTO Opset: generic-trl-photo-joeywong

MACHINE: TRL HMDS
Settings
RECIPE Standard HMDS
MATERIAL HMDS
TIME 25 minutes
TEMP 150C

MACHINE: TRL coater USER: joeywong
Settings
MATERIAL OCG 825-34 cSt. safe resist
RECIPE 11

MACHINE: TRL prebakeovn USER: joeywong
Settings
TEMP-C 90
TIME 30 minutes

MACHINE: TRL ksaligner1 USER: joeywong
Settings
MASK-ID BTM-NI
Readings
EXPOSURE_TIME 1.5 sec

MACHINE: TRL photo-wet USER: joeywong

Readings

DEVELOP_TIME	1 min

MACHINE: TRL postbake USER: joeywong

Settings

TEMP-C	120
TIME	30 minutes

MACHINE: TRL microscope USER: joeywong

SPECIAL INSTRUCTIONS:

Center Wafer Inspect Wafer Alignment (Flat Away)

Spec +/-.5u:

**** 6. Opset Task: WET-ETCH-10K-OXIDE Opset: wox10k

MACHINE: ICL oxide USER: joeywong

Settings

SINK	Oxide-Sink
TANK	1
ACID	7-1boe
TIME	5 Minutes

MACHINE: ICL ellipsometer USER: joeywong

SPECIAL INSTRUCTIONS:

Test wafer oxide THICKNESS (5 readings). Spec: < 25A

Settings

FILM-TYPE	K2 (oxide)

**** 7. Opset Task: RESIST-ASH Opset: phash ****

MACHINE: ICL asher USER: joeywong

SPECIAL INSTRUCTIONS:

Bright light inspect all wafers after completion.

Settings

PROGRAM	endpoint
SET	30:20

**** 8. Opset Task: 1K-OXIDE-BEDDING Opset: dox-bed

MACHINE: ICL rca USER: joeywong

SPECIAL INSTRUCTIONS:

RCA CLEAN IS REQUIRED

Step 1a: SC1 - 10mins.

Step 1b: Dump Rinser 1.

Step 2a: HF Dip - 15secs.

Step 2b: Dump Rinser 1.

Step 3a: SC2 - 15mins.

Step 3b: Dump Rinser 2 - until 9Mohms is achieved.

Step 4: Spin Dry - 60sec rinse, 240sec dry.

MACHINE: ICL tubeA2 USER: joeywong
Settings
RECIPE 228

MACHINE: ICL ellipsometer USER: joeywong
SPECIAL INSTRUCTIONS:
Center Wafer oxide THICKNESS (5 readings). Spec: 1000 +/- 50A

Settings
FILM-TYPE K2 (oxide)

**** 9. Opset Task: LPCVD-POLYSILICON Opset: dpoly3k

MACHINE: ICL rca USER: joeywong

SPECIAL INSTRUCTIONS:
NO IONIC CLEAN REQUIRED IF WITHIN 24 HOURS OF FURNACE OPERATION
Step 1a: SC2 - 15mins.
Step 1b: Dump Rinser 2 - until 9Mohms is achieved.
Step 2: Spin Dry. - 60sec rinse, 240sec dry.

MACHINE: ICL tubeA6 USER: joeywong
Settings
RECIPE 428

Readings
HUMIDITY NIL

MACHINE: ICL nanospec USER: joeywong
PECIAL INSTRUCTIONS:
Test Wafer polysilicon THICKNESS (5 readings). Spec: 3000 +/- 210A

Settings
FILM-TYPE 4
LENS-TYPE 2

Readings
Test wafer id-1 monitor
Test Wafer:top-1 3100.0S0
Test Wafer:center-1 3098.0S0
Test Wafer:left-1 3197.0S0
Test Wafer:right-1 3094.0S0
Test Wafer:bottom-1 3092.0S0
Test wafer id-2 sample1
Test Wafer:top-2 3117.0S0
Test Wafer:center-2 3116.0S0
Test Wafer:left-2 3120.0S0
Test Wafer:right-2 3119.0S0
Test Wafer:bottom-2 3123.0S0

**** 10. Opset Task: GENERIC-TRL-PHOTO Opset: generic-trl-photo-joeywong

MACHINE: ICL HMDS USER: joeywong

Settings

RECIPE	Standard HMDS
MATERIAL	HMDS
TIME	25 minutes
TEMP	150C

MACHINE: ICL coater USER: joeywong

SPECIAL INSTRUCTIONS:
Be sure to use Focus-Exposure wafer to determine the appropriate settings.

Settings

MATERIAL OCG 825-34 cSt. safe resist

RECIPE 11

MACHINE: TRL prebakeovn USER: joeywong

Settings

TEMP-C	90
TIME	30 minutes

MACHINE: TRL ksaligner1 USER: joeywong

Settings

MASK-ID BTM-ND

Readings

EXPOSURE_TIME 1.8

MACHINE: TRL photo-wet USER: joeywong

Readings

DEVELOP_TIME 1 min 40 sec

MACHINE: TRL postbake USER: joeywong

Settings

TEMP-C	120
TIME	30 minutes

MACHINE: TRL microscope USER: joeywong

SPECIAL INSTRUCTIONS:
Center Wafer Inspect Wafer Alignment (Flat Away)
Spec +/-.5u:

**** 11. Opset Task: POLYSILICON-PLASMA-ETCH Opset: plpoly5k

MACHINE: ICL oxide USER: joeywong

Settings

SINK	Oxide-Sink
TANK	NIL
ACID	7-1BOE
TIME	5 Seconds

MACHINE: ICL etcher-1 USER: joeywong

Settings

CHEMISTRY	CCl4
RECIPE	10

Readings

ETCH_TIME/WAFER_[SEC	1:30

MACHINE: ICL nanospec USER: joeywong

SPECIAL INSTRUCTIONS:
Center wafer polysilicon THICKNESS (5 readings). Spec: 50A<
thick <240A

**** 12. Opset Task: BKSIDE-POLY-PLASMA-ETCH Opset:
plpolyback5k

MACHINE: ICL etcher-1 USER: joeywong

SPECIAL INSTRUCTIONS:
Backside etch, load wafers resist-side down.
Afterward, inspect all wafers for residual poly nucleations.

Settings

CHEMISTRY	CCl4
RECIPE	12

Readings

ETCH_TIME/WAFER_[SEC	1 min 30 sec

**** 13. Opset Task: RESIST-ASH Opset: phash

MACHINE: ICL asher USER: joeywong

SPECIAL INSTRUCTIONS:
Bright light inspect all wafers after completion.
Settings

PROGRAM	endpoint
SET	30:20

**** 14. Opset Task: IMPLANT Opset: NOT AN OPSET

MACHINE: ICL implanter

Settings

ELEMENT	Arsenic
DOSE	7.0E15
ENERGY	90keV
TIME	> 20 Seconds

**** 15. Opset Task: 1K-OXIDE-COVER   Opset: dox-cover

MACHINE: ICL rca   USER: joeywong

SPECIAL INSTRUCTIONS:

RCA CLEAN IS REQUIRED

Step 1a: SC1 - 10mins.

Step 1b: Dump Rinser 1.

Step 2a: HF Dip - 15secs.

Step 2b: Dump Rinser 1.

Step 3a: SC2 - 15mins.

Step 3b: Dump Rinser 2 - until 9Mohms is achieved.

Step 4: Spin Dry - 60sec rinse, 240sec dry.

MACHINE: tubeA2

Settings

RECIPE	228

MACHINE: ellipsometer

SPECIAL INSTRUCTIONS:

Center Wafer oxide THICKNESS (5 readings). Spec: 1000 +/- 50A

Settings

FILM-TYPE	K2 (oxide)

**** 16. Opset Task: GENERIC-TRL-PHOTO   Opset: generic-trl-photo-joeywong

MACHINE: HMDS

Settings

RECIPE	Standard HMDS
MATERIAL	HMDS
TIME	25 minutes
TEMP	150C

MACHINE: coater

SPECIAL INSTRUCTIONS:

Be sure to use Focus-Exposure wafer to determine the appropriate settings.

Settings

MATERIAL	OCG 825-34 cSt. safe resist
RECIPE	11

MACHINE: prebakeovn

Settings

TEMP-C 90

TIME 30 minutes

MACHINE: ksaligner1 ksaligner2 ksaligner3

Settings

MASK-ID BTM-NB

MACHINE: photo-wet

MACHINE: postbake

Settings

TEMP-C 120

TIME 30 minutes

MACHINE: microscope

Spec +/-.5u:

**** 17. Opset Task: WET-ETCH-5K-OXIDE Opset: wox5k

MACHINE: oxide

Settings

SINK Oxide-Sink

TANK 1

ACID 7-1boe

TIME 2 Minutes 30 Seconds

MACHINE: ellipsometer

Settings

FILM-TYPE K2 (oxide)

**** 18. Opset Task: RESIST-ASH Opset: phash

MACHINE: asher

Settings

PROGRAM endpoint

SET 30:20

**** 19. Opset Task: GENERIC-TRL-PHOTO Opset: generic-trl-photo-joeywong

MACHINE: HMDS

Settings

RECIPE Standard HMDS

MATERIAL HMDS

TIME 25 minutes

TEMP 150C

MACHINE: coater
SPECIAL INSTRUCTIONS:
Be sure to use Focus-Exposure wafer to determine the appropriate settings.

Settings
MATERIAL OCG 825-34 cSt. safe resist
RECIPE 11

MACHINE: prebakeovn

Settings
TEMP-C 90
TIME 30 minutes

MACHINE: ksaligner1 ksaligner2 ksaligner3
Settings
MASK-ID BTM-NG

MACHINE: photo-wet

MACHINE: postbake

Settings
TEMP-C 120
TIME 30 minutes

MACHINE: microscope

SPECIAL INSTRUCTIONS:
Center Wafer Inspect Wafer Alignment (Flat Away)
Spec +/-.5u:

**** 20. Opset Task: SILICON-PLASMA-ETCH Opset: plsilicon-20k

MACHINE: etcher-1

SPECIAL INSTRUCTIONS:
RECIPE 19 STEP 7: Change TIME = 6 min

Settings
CHEMISTRY SF6
RECIPE 19

MACHINE: dektak

SPECIAL INSTRUCTIONS:
Center Wafer oxide THICKNESS (5 readings). Spec: 20000 +/- 1000A

Settings

FILM-TYPE	oxide

**** 21. Opset Task: RESIST-ASH Opset: phash

MACHINE: asher

Settings

PROGRAM	endpoint
SET	30:20

**** 22. Opset Task: GENERIC-TRL-PHOTO Opset: generic-trl-photo-joeywong

MACHINE: HMDS
Settings

RECIPE	Standard HMDS
MATERIAL	HMDS
TIME	25 minutes
TEMP	150C

MACHINE: coater
Settings

MATERIAL	OCG 825-34 cSt. safe resist
RECIPE	11

MACHINE: prebakeovn
Settings

TEMP-C	90
TIME	30 minutes

MACHINE: ksaligner1 ksaligner2 ksaligner3
Settings

MASK-ID	BTM-NM

MACHINE: photo-wet

MACHINE: postbake
Settings

TEMP-C	120
TIME	30 minutes

MACHINE: microscope
SPECIAL INSTRUCTIONS:
Center Wafer Inspect Wafer Alignment (Flat Away)
Spec +/-.5u:

**** 23. Opset Task: METAL-EVAPORATION Opset: mevap

MACHINE: e-beam
Settings

MATERIAL	Cr-Au
THICKNESS	10000.0

**** 24. Opset Task: TRL-METAL-STRIP Opset: wstrip

MACHINE: photo-wet

MACHINE: dektak
WAFERSETS: Lot relay_lower: relay_lower
Settings

FILM-TYPE	oxide

**** 25. Opset Task: METAL-EVAPORATION Opset: mevap

MACHINE: e-beam

Settings

MATERIAL	Al-Si
THICKNESS	5000.0

**** 26. Opset Task: SAW-WAFERS Opset: saw

MACHINE: diesaw
WAFERSETS: Lot relay_lower: relay_lower

SPECIAL INSTRUCTIONS:
Saw wafers into individual cells.

§B.2 Traveler report for top wafers

```
Traveller Report for Lot: relay_upper1

Description:      PFR file for electro-static microrelay

**** 1. Opset Task: PIRANHA-CLEAN-OPERATION   Opset: pirhana-
clean-operation

     Machine:  pre-metal
     Settings:   SINK ..................... "pre-metal"
                 TANK ..................... 1
                 ACID ..................... "3:1 H2SO4:H2O2"
                 TIME ..................... "10 minutes"

**** 2. Opset Task: TOP-RESIST-COAT   Opset: top-resist-coat

 HMDS
     Machine:  HMDS
     Settings:   RECIPE ................... "Standard HMDS
recipe#1"
                 MATERIAL ................. "HMDS"
                 TIME ..................... "30 minutes"
                 SET ...................... ""

  RESIST-COAT
     Machine:  coater
     Settings:   MATERIAL ................. "OCG 825-35 cSt.
safe resist"
                 RECIPE ................... 11

  HARD-BAKE
     Machine:  developer
     Settings:   RECIPE ................... 43

**** 3. Opset Task: GENERIC-TRL-PHOTO   Opset: generic-trl-
photo-joeywong

MACHINE:  TRL HMDS
Settings
           RECIPE                        Standard HMDS
           MATERIAL                      HMDS
           TIME                          25 minutes
           TEMP                          150C

---------------------------------

MACHINE:  TRL coater           USER: joeywong
Settings
           MATERIAL                      OCG 825-34 cSt. safe
resist
           RECIPE                        11
---------------------------------

MACHINE:  TRL prebakeovn       USER: joeywong
Settings
           TEMP-C                        90
```

TIME 30 minutes

MACHINE: TRL ksaligner1 USER: joeywong

Settings

MASK-ID TOP-NI

Readings

EXPOSURE_TIME 1.5 sec

MACHINE: TRL photo-wet USER: joeywong

Readings

DEVELOP_TIME 1 min

MACHINE: TRL postbake USER: joeywong

Settings

TEMP-C 120

TIME 30 minutes

MACHINE: TRL microscope USER: joeywong

SPECIAL INSTRUCTIONS:

Center Wafer Inspect Wafer Alignment (Flat Away)

Spec +/-.5u:

**** 4. Opset Task: SILICON-PLASMA-ETCH Opset: plsilicon-20k

MACHINE: etcher-1

SPECIAL INSTRUCTIONS:

RECIPE 19 STEP 7: Change TIME = 6 min

Settings

CHEMISTRY SF6

RECIPE 19

MACHINE: dektak

SPECIAL INSTRUCTIONS:

Center Wafer oxide THICKNESS (5 readings). Spec: 20000 +/- 1000A

Settings

FILM-TYPE oxide

**** 5. Opset Task: PIRANHA-CLEAN-OPERATION Opset: piranha-clean-operation

Machine: pre-metal

Settings: SINK .... "pre-metal"

TANK 1

ACID .... "3:1 H2SO4:H2O2"

TIME .... "10 minutes"

**** 6. Opset Task: GENERIC-TRL-PHOTO   Opset: generic-trl-photo-joeywong

MACHINE: TRL HMDS
Settings

RECIPE	Standard HMDS
MATERIAL	HMDS
TIME	25 minutes
TEMP	150C

MACHINE: TRL coater   USER: joeywong
Settings

MATERIAL	OCG 825-34 cSt. safe resist
RECIPE	11

MACHINE: TRL prebakeovn   USER: joeywong
Settings

TEMP-C	90
TIME	30 minutes

MACHINE: TRL ksaligner1   USER: joeywong
Settings

MASK-ID	TOP-NM

Readings

EXPOSURE_TIME	1.5 sec

MACHINE: TRL photo-wet   USER: joeywong
Readings

DEVELOP_TIME	1 min

MACHINE: TRL postbake   USER: joeywong
Settings

TEMP-C	120
TIME	30 minutes

MACHINE: TRL microscope   USER: joeywong
SPECIAL INSTRUCTIONS:
Center Wafer Inspect Wafer Alignment (Flat Away)
Spec +/-.5u:

**** 7. Opset Task: SILICON-PLASMA-ETCH   Opset: silion-plasma-etch

PLASMA-ETCH
Machine: TRL sts1
Settings: CHEMISTRY SF6, CCL4
RECIPE STS56

INSPECT-THICKNESS
    Machine: nanospec
    Settings: FILM-TYPE 1
    Spec: "--"

**** 8. Opset Task: TOP-RESIST-COAT Opset: top-resist-coat

HMDS
    Machine: HMDS
    Settings: RECIPE .... "Standard HMDS recipe#1"
        MATERIAL .... "HMDS"
        TIME .... "30 minutes"
        SET .... ""

RESIST-COAT
    Machine: coater
    Settings: MATERIAL .... "OCG 825-35 cSt. safe resist"
        RECIPE 11

HARD-BAKE
    Machine: developer
    Settings: RECIPE 43

**** 9. Opset Task: GENERIC-TRL-PHOTO Opset: generic-trl-photo-joeywong

MACHINE: TRL HMDS
Settings
    RECIPE Standard HMDS
    MATERIAL HMDS
    TIME 25 minutes
    TEMP 150C

MACHINE: TRL coater USER: joeywong
Settings
    MATERIAL AZ4620. thick resist
    RECIPE 11

MACHINE: TRL prebakeovn USER: joeywong
Settings
    TEMP-C 90
    TIME 60 minutes

MACHINE: TRL ksaligner2 USER: joeywong
Settings
    MASK-ID TOP-NB
Readings
    EXPOSURE_TIME 600 sec

MACHINE: TRL photo-wet USER: joeywong
Readings

DEVELOP_TIME 3 min

MACHINE: TRL postbake USER: joeywong

Settings

TEMP-C 120

TIME 30 minutes

MACHINE: TRL microscope USER: joeywong

SPECIAL INSTRUCTIONS:

Center Wafer Inspect Wafer Alignment (Flat Away)

Spec +/-.5u:

**** 10. Opset Task: SILICON-PLASMA-ETCH Opset: silion-plasma-etch

PLASMA-ETCH

Machine: TRL sts1

Settings: CHEMISTRY SF6, CCL4

RECIPE STS56

INSPECT-THICKNESS

Machine: nanospec

Settings: FILM-TYPE 1

Spec: "--"

**** 10. Opset Task: PIRANHA-CLEAN-OPERATION Opset: piranha-clean-operation

Machine: pre-metal

Settings: SINK .... "pre-metal"

TANK 1

ACID .... "3:1 H2SO4:H2O2"

TIME .... "10 minutes"

**** 11. Opset Task: BUFFERED-OXIDE-ETCH Opset: buffered-oxide-etch

OXIDE-BOE-ETCH

Machine: oxide

Settings: SINK .... "Oxide-Sink"

TANK 2

ACID .... "7-1boe"

TIME .... "35 Seconds"

INSPECT-THICKNESS

Machine: nanospec

Settings: FILM-TYPE 1

Spec: "3500<<5000"

INSPECT-THICKNESS

Machine: ellipsometer

Settings: FILM-TYPE .... "K2 (thin oxide)"

Spec: "<25"

**** 12. Opset Task: TRL-METAL-STRIP Opset: wstrip

MACHINE: photo-wet

MACHINE: dektak

Settings

FILM-TYPE	oxide

**** 13. Opset Task: METAL-EVAPORATION Opset: mevap

MACHINE: e-beam

Settings

MATERIAL	Cr-Au
THICKNESS	10000.0

**** 14. Opset Task: SAW-WAFERS Opset: saw

MACHINE: diesaw

SPECIAL INSTRUCTIONS:

Saw wafers into individual cells.

Appendix C Mask Layouts

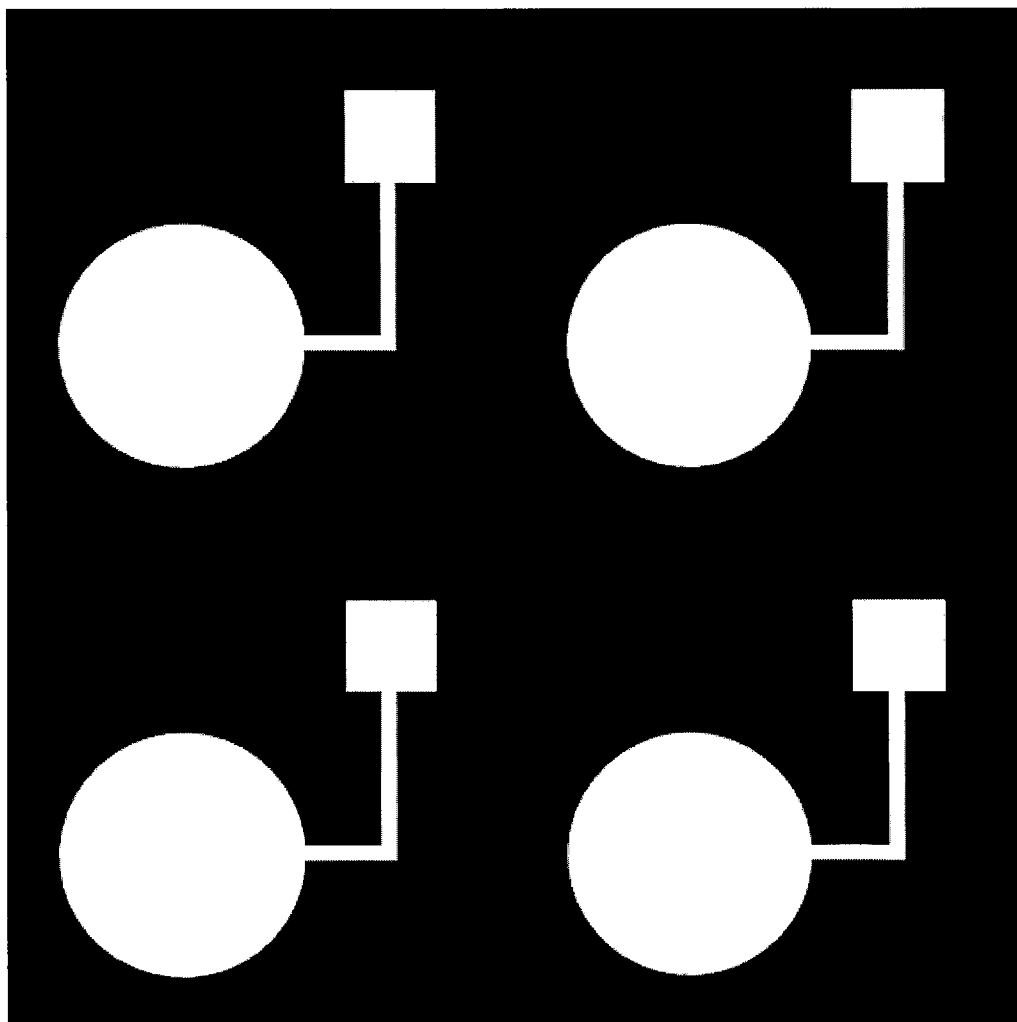

Figure C.1 Mask ID: BTM-NI

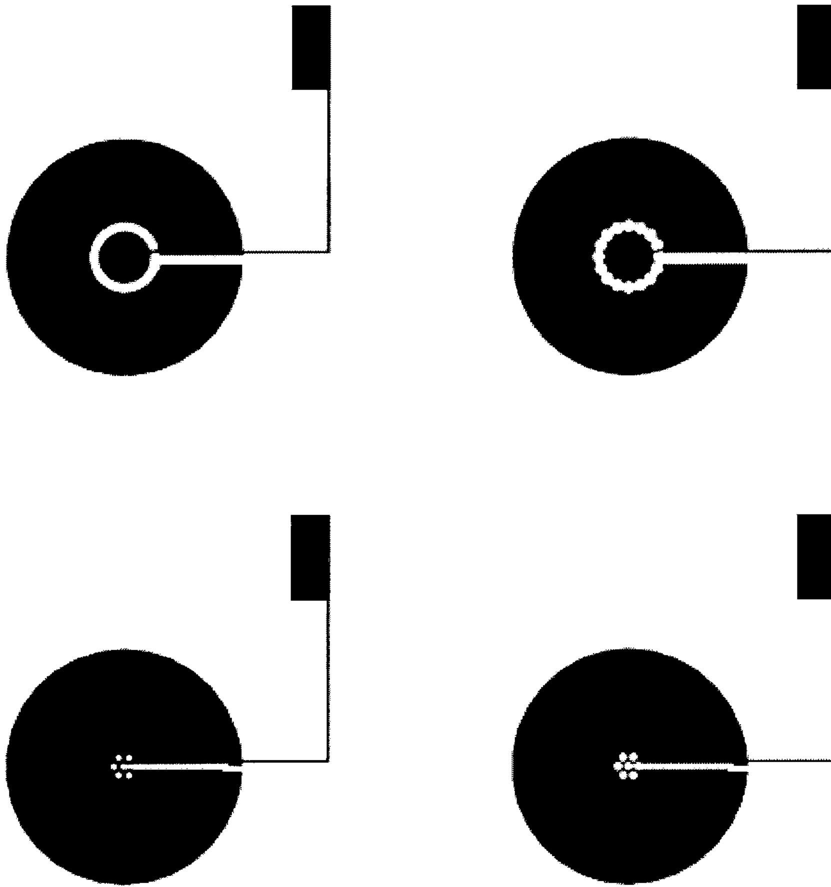

Figure C.2 Mask ID: BTM-ND

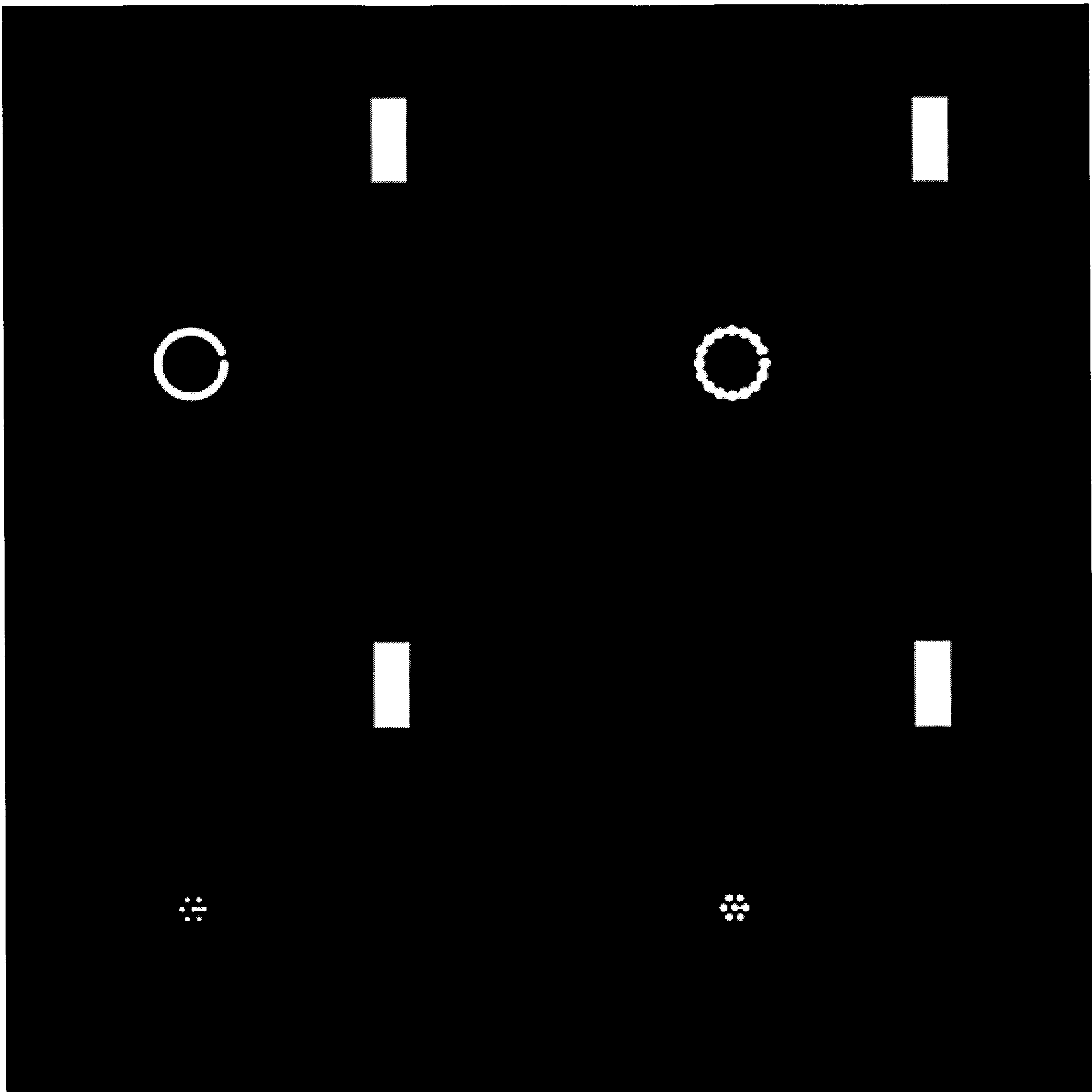

Figure C.3 Mask ID: BTM-NB

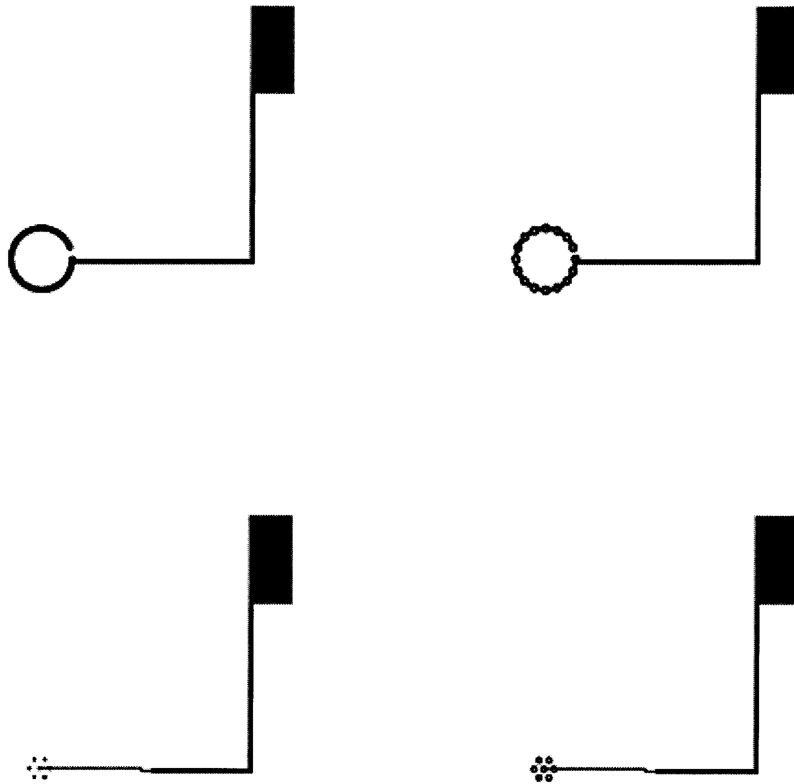

Figure C.4 Mask ID: BTM-NG

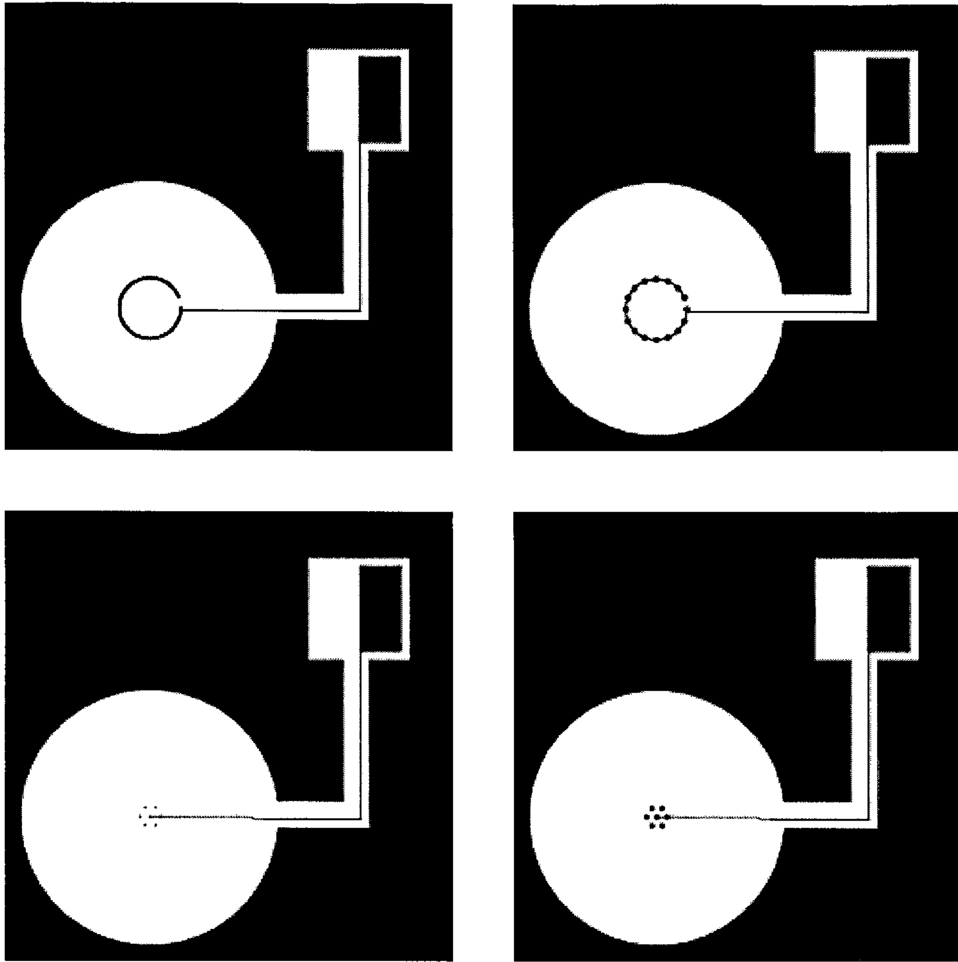

Figure C.5 Mask ID: BTM-NM

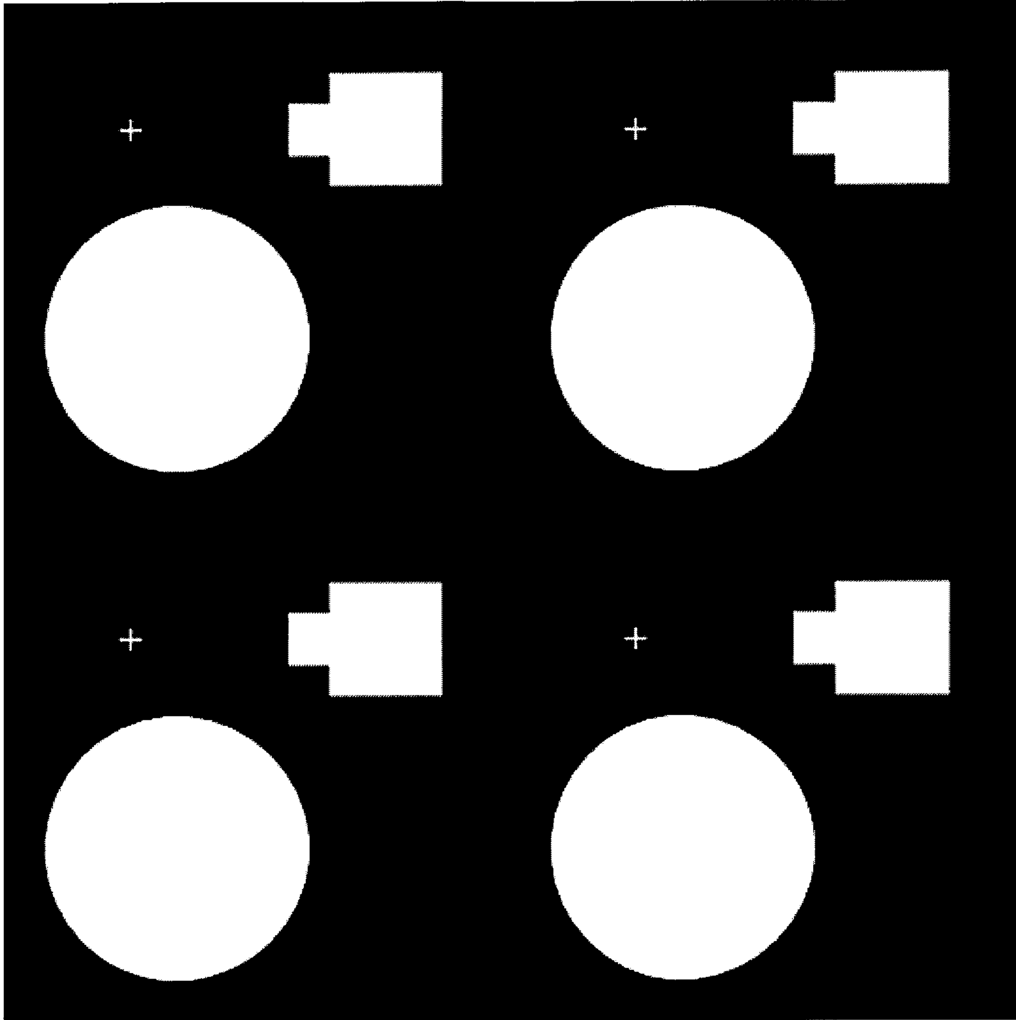

Figure C.6 Mask ID: TOP-NB

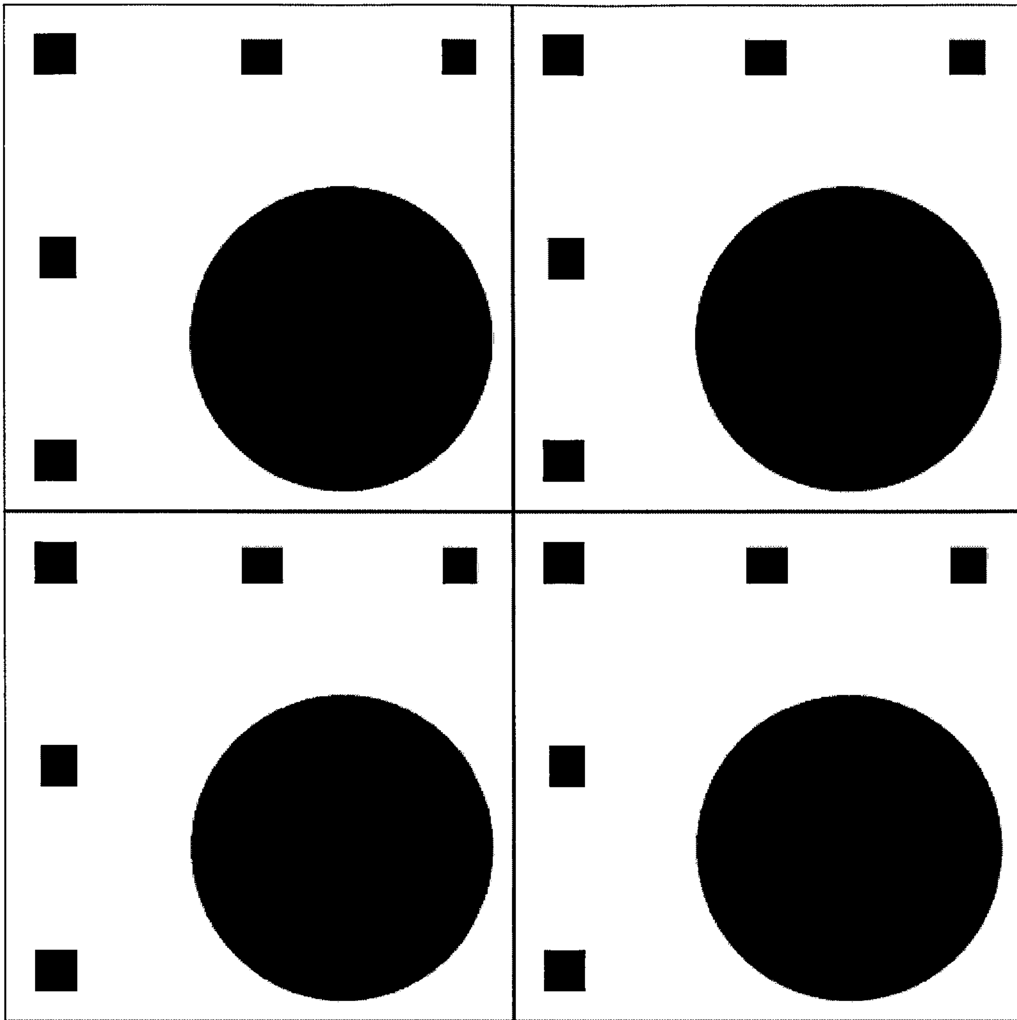

Figure C.7 Mask ID: TOP-NM

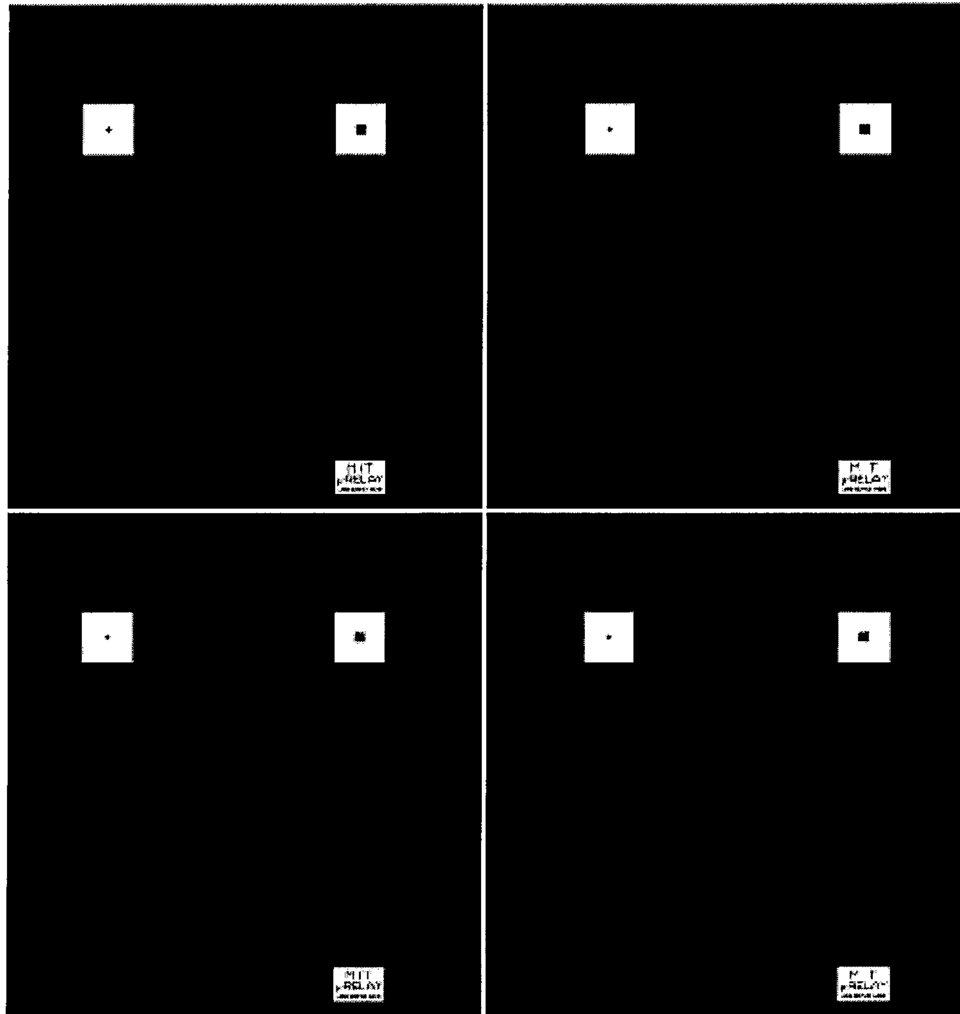

Figure C.8 Mask ID: TOP-NI

Appendix D Test fixture design

Included in this appendix are the design drawings for the sealing fixture and alignment jig. The material of choice is plexiglass because of its good machinability and electrical insulation. For the sealing fixture (Figure D.1), there are two raised ridges on two adjacent sides for easy alignment between the device and the fixture. The alignment jig (Figure D.2) serves as a position reference when assembling the device with the sealing fixture and is reusable.

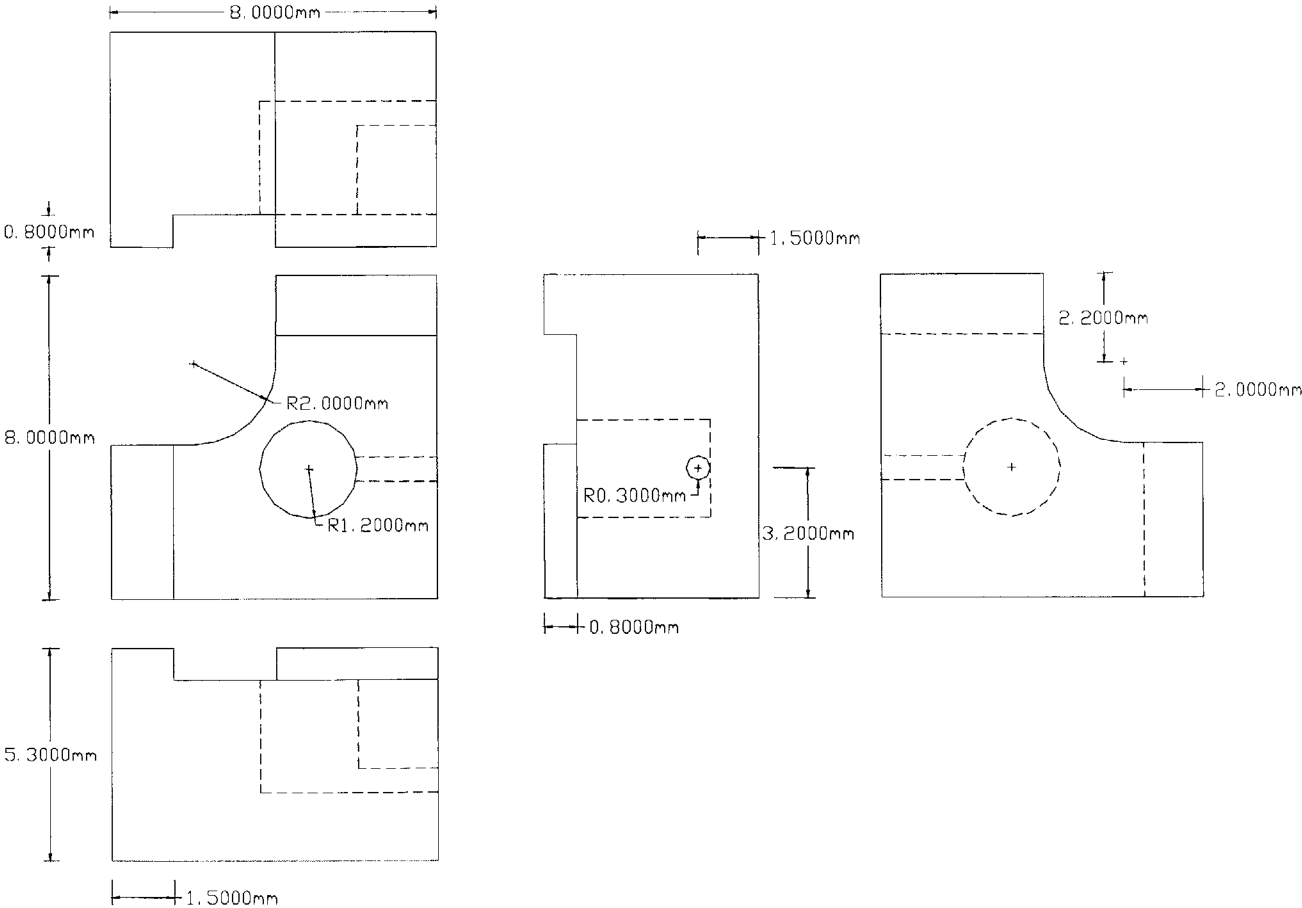

Figure D.1 Drawing for the sealing fixture design

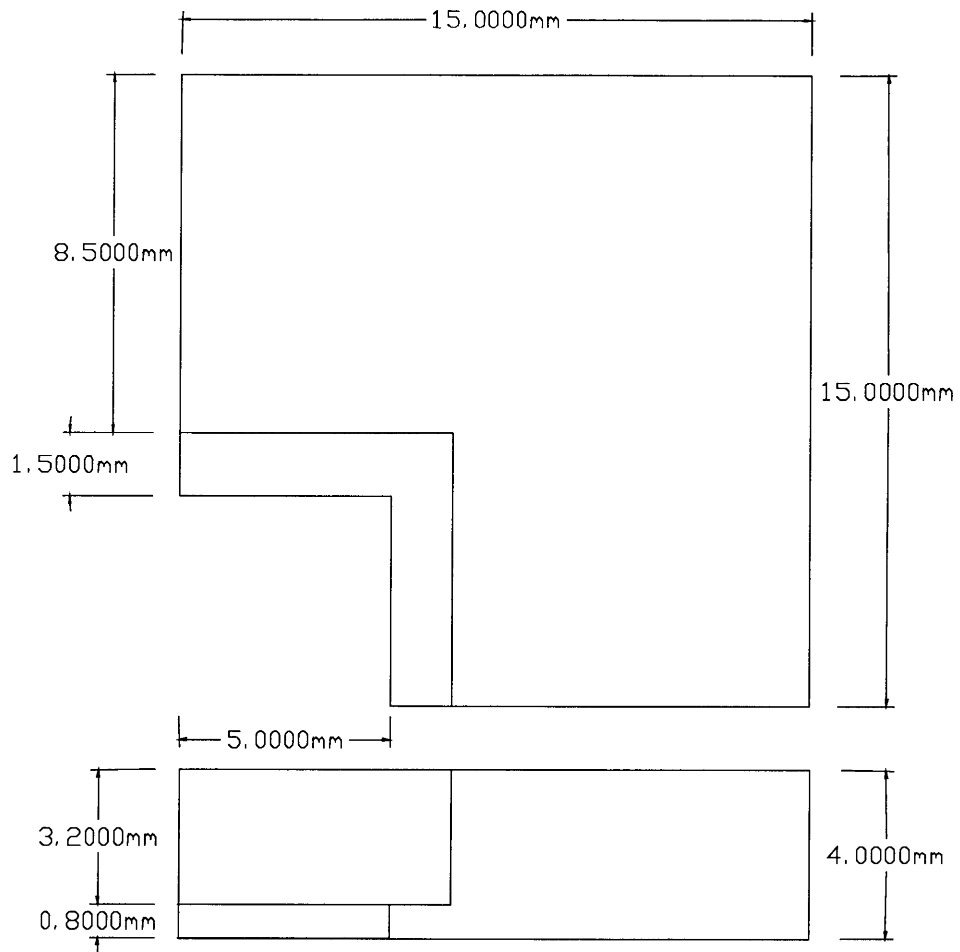

Figure D.2 Drawing for the alignment jig design

Appendix E POLY-SILICON SURFACE ROUGHNESS MEASUREMENT

As discussed in Section 5.4, which concerned the modeling of the mechanical contacts of the devices, a mismatch arises between the prediction and the experimental gap closure. Surface roughness is one of the possibilities that could have prevented the diaphragm from closely approaching the bottom wafer. This appendix presents the surface profile measurements of the bottom substrate inspected under a *WYKO™* surface profiler using optical interferometry technology. These measurements are used in Subsection 5.4.3 to demonstrate that the unexpected un-smoothness could be resulted from surface roughness of the poly-silicon actuation electrode.

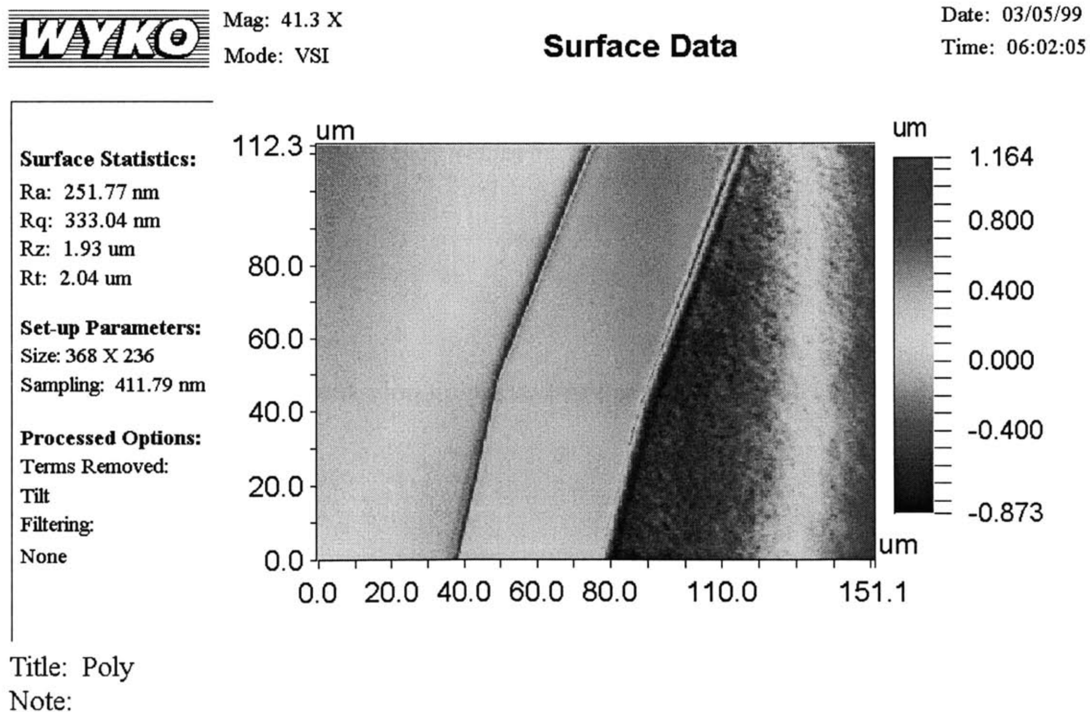

Figure E.1 Surface condition of bottom substrate (measured by *WYKO* surface profiler)

Figure E.1 shows the surface condition of the poly-silicon actuation electrode on the right and that of the field oxide area on the left. It can be clearly seen that the poly-silicon surface on the right has a much *rougher* surface condition. In Figure E.2, a roughness measurement is made on the poly-silicon surface. The global dishing of the surface profiles is due to the fact that the sample is *not* perfectly level and has nothing to the with the real surface profile. According to the measurements, the average roughness of the poly-silicon surface is in the range of *27.9nm* to *64.9nm* and the peak and valley of the surface is on the order of ±*145nm*. These roughness values are on the same order of magnitude of the size of the extrinsic object size that the model of Section 5.4.3 predicts (*1500 Å*).

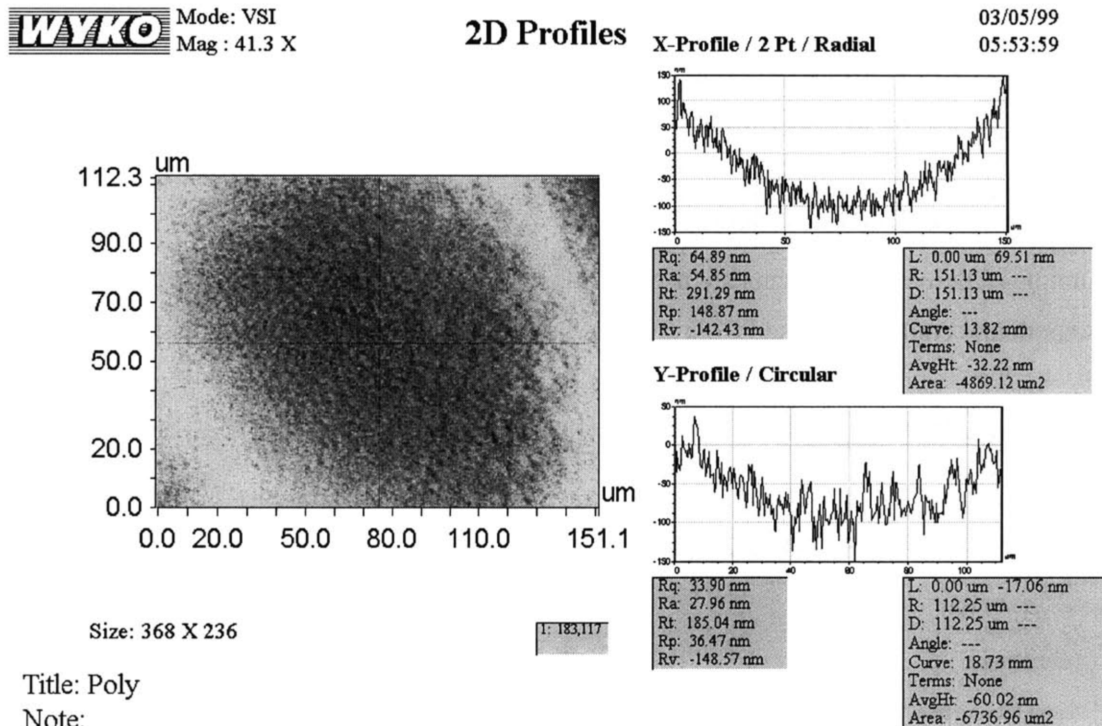

Figure E.2 Surface roughness of the top surface on poly-silicon actuation electrode

Appendix F LabVIEW® PROGRAMS

As discussed in Subsection 5.2.3, this appendix contains a LabVIEW® program used in the testing of the switch. Specifically, the program presented here performs a four-point-probe resistance measurements, measures the current through the device and monitors the real-time actuation pressure while sweeping the actuation voltage at biased pressures. When the experiment is completed, the program also saves the data to a file.

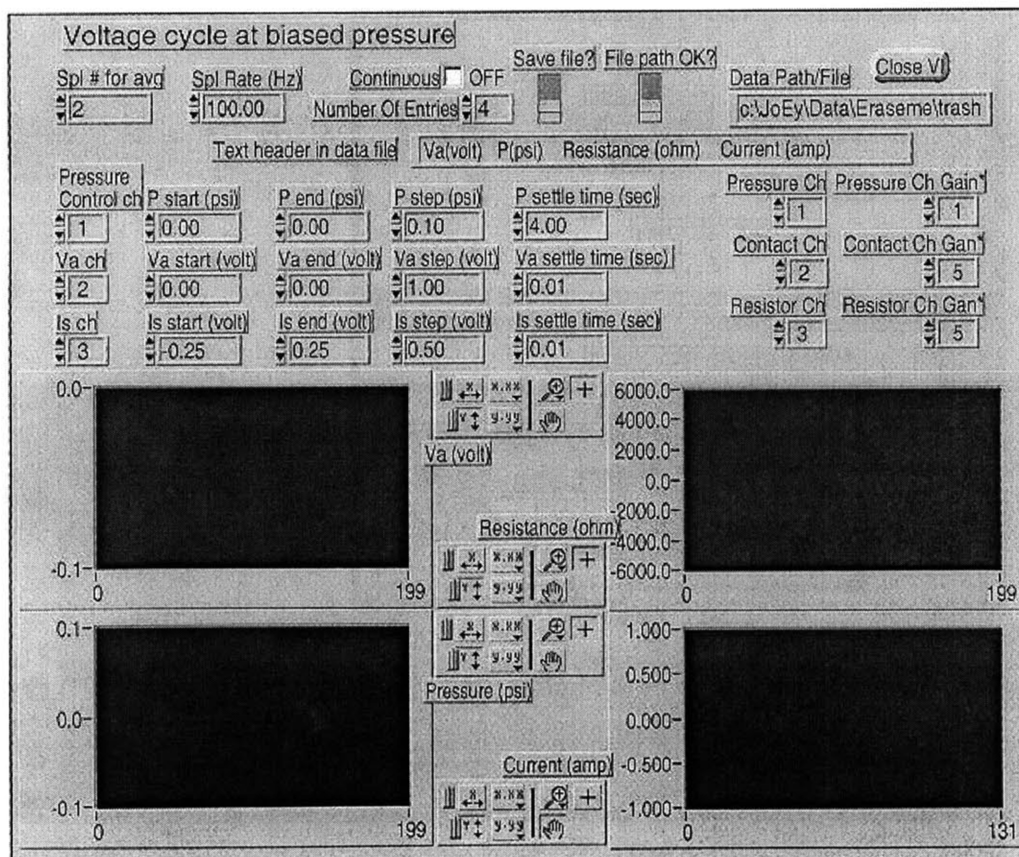

Figure F.1 Front panel of a LabVIEW® program used for device characterization while sweeping actuation voltage at biased pressures.

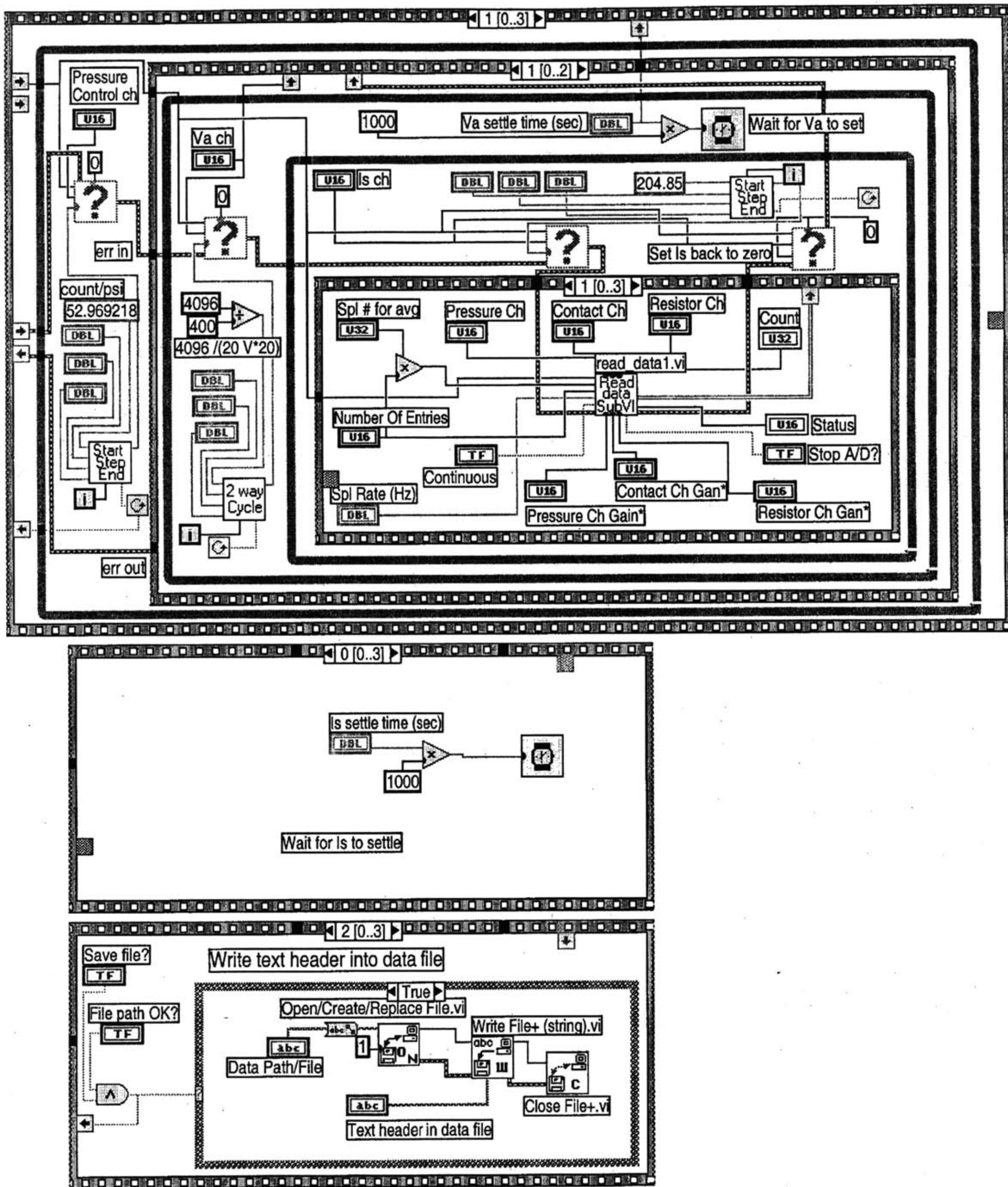

Figure F.2 Block diaphragm of the LabVIEW® program shown in Figure F.1. (1 of 5)

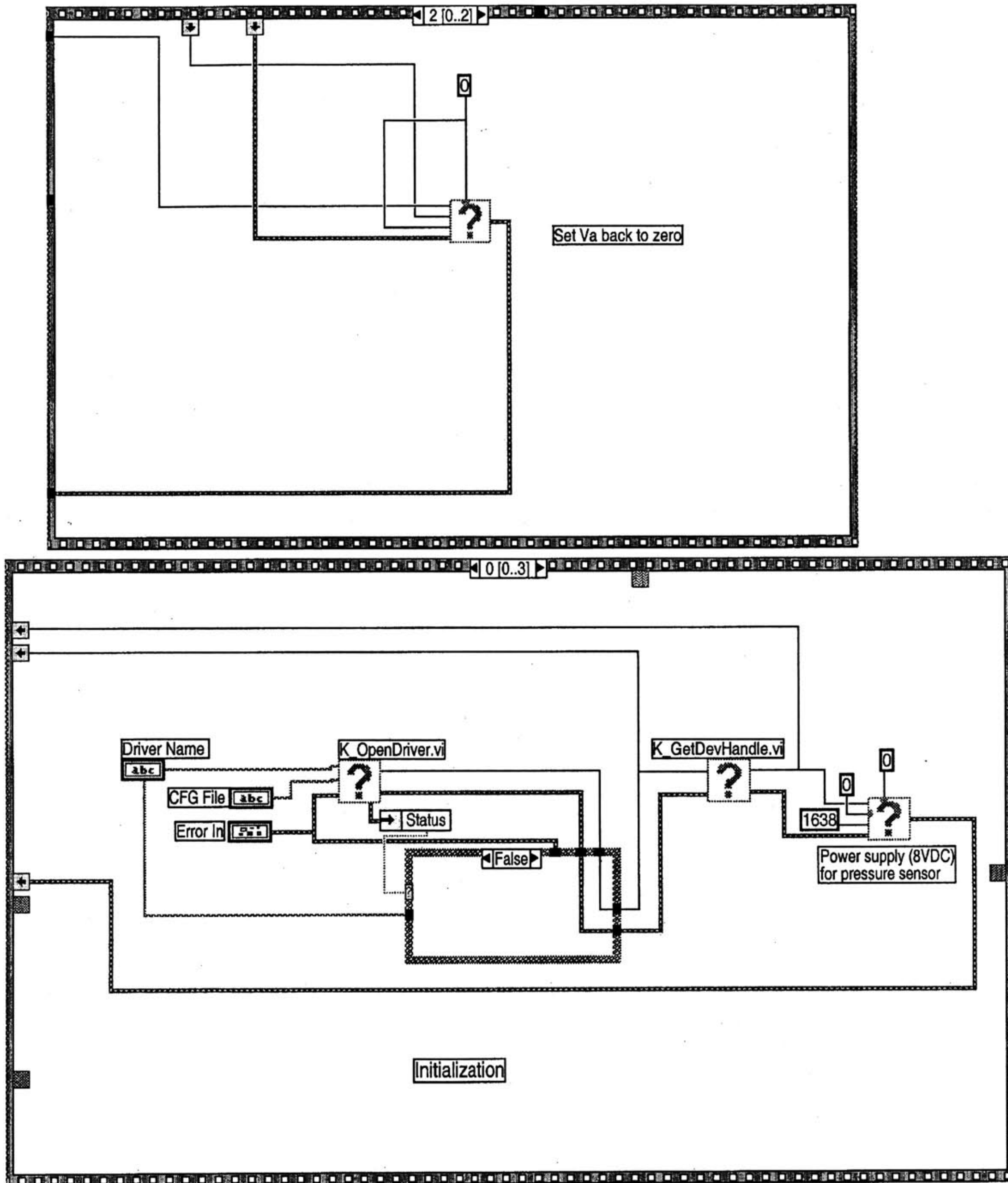

Figure F.3 Block diaphragm of the LabVIEW® program shown in Figure F.1. (2 of 5)

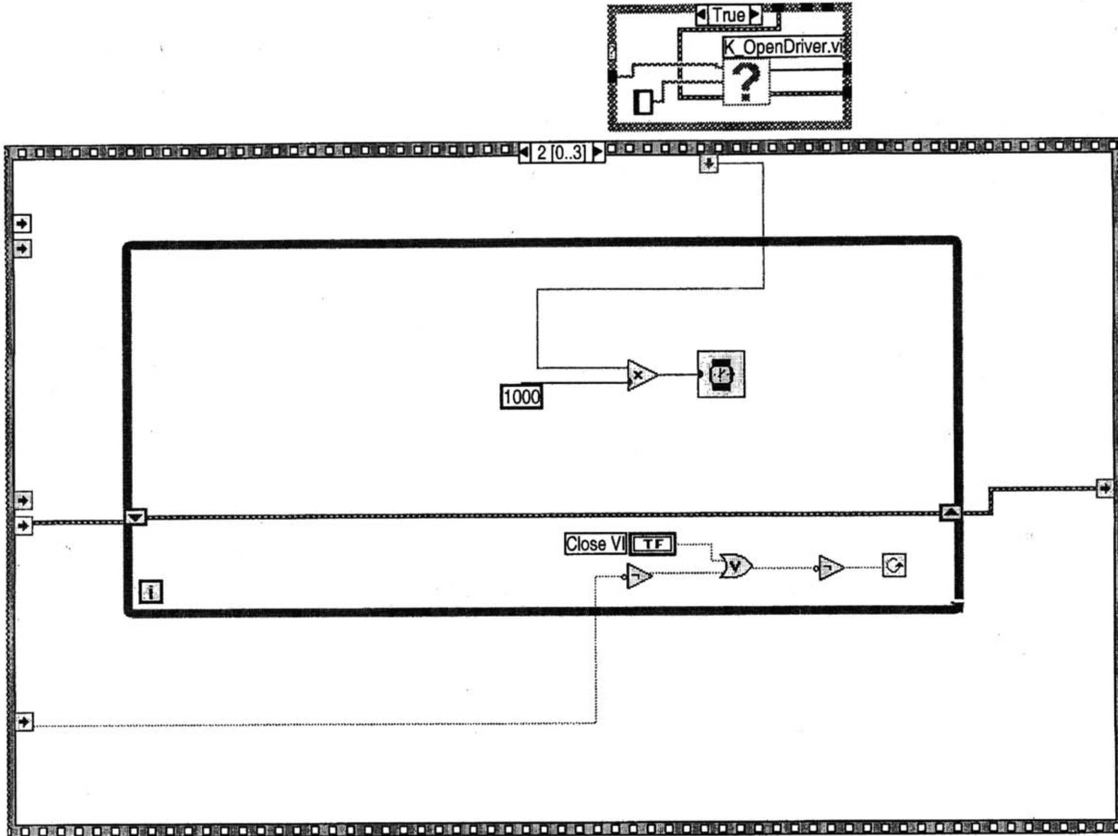

Figure F.4 Block diaphragm of the LabVIEW® program shown in Figure F.1. (3 of 5)

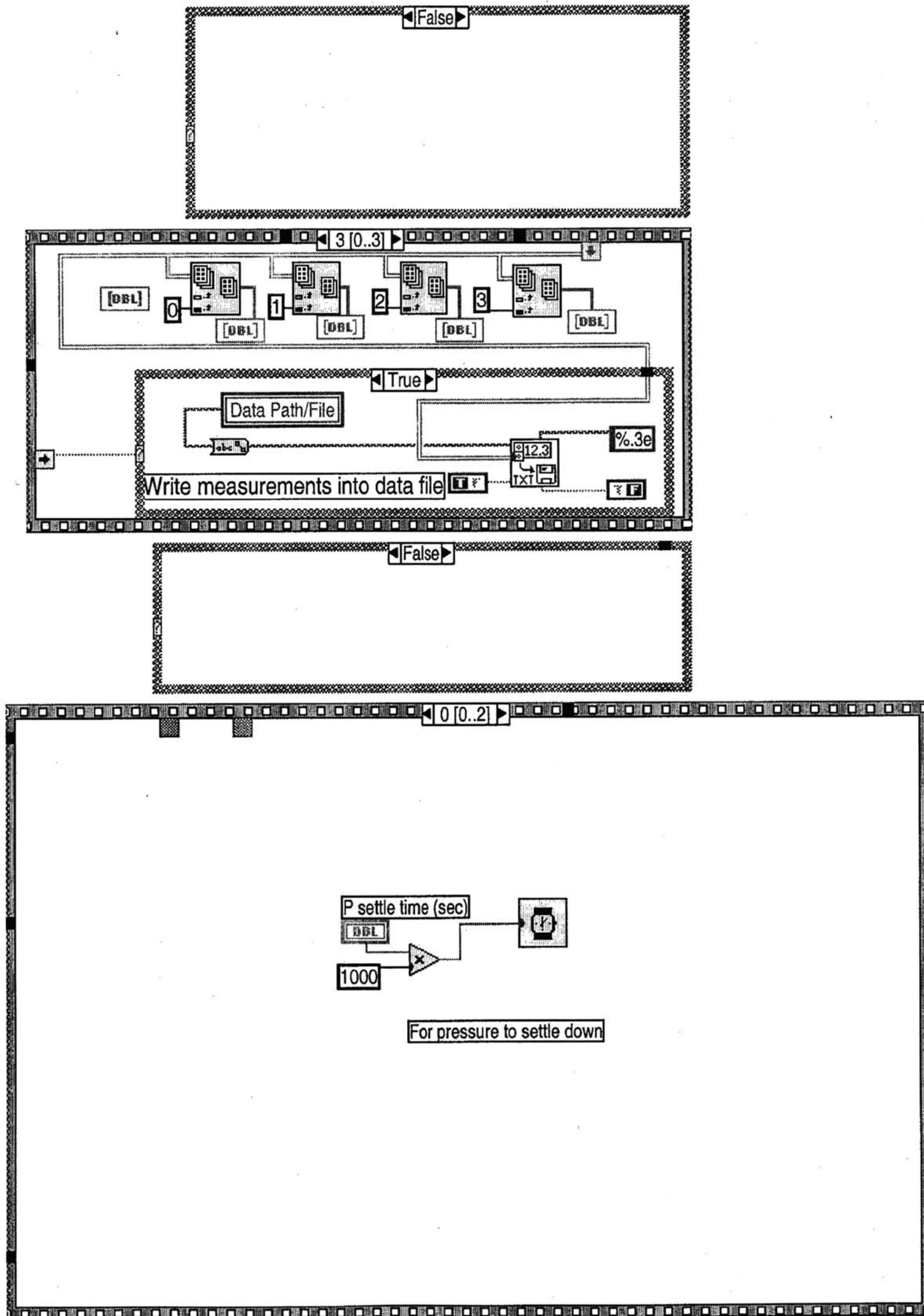

Figure F.5 Block diaphragm of the LabVIEW® program shown in Figure F.1. (4 of 5)

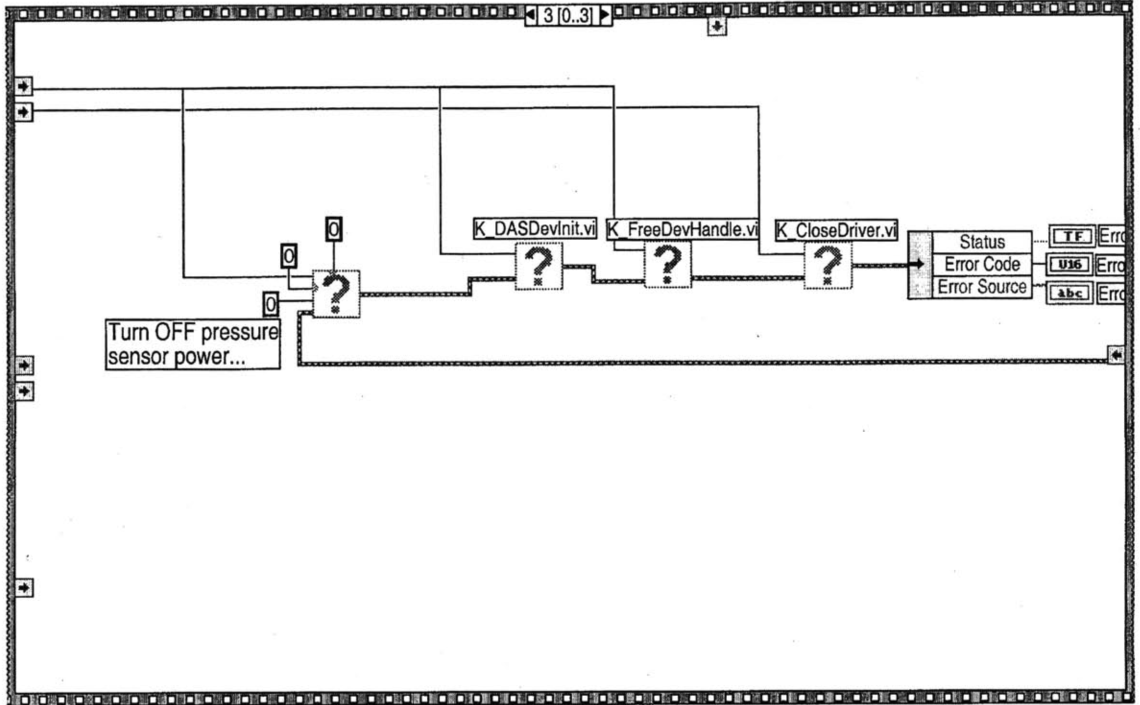

Figure F.6 Block diaphragm of the LabVIEW® program shown in Figure F.1. (5 of 5)

Appendix G MATLAB® SCRIPT FOR CIRCULAR CLAMPED DIAPHRAGMS

The MATLAB® script presented in this appendix is the finite difference formulation for the self-consistent electromechanical solution for clamped circular diaphragms. The simulation of the pressure-capacitance relationship in Section 5.6 and the prediction of electrostatic pull-in voltages under pressure bias in Section 5.7 are attained using this code.

This script is adapted and modified from class notes [84] of MIT course 6.971 in Fall term, 1997.

```
clear;

d=input('Enter discretization number (50 to 100 range is suggested): ');
d=120;
N=d+3;
Z=input('Enter newton iteration number (5 to 10 range is suggested): ');
R=1e-6*input('Enter movable conductor radius in um: ');
RF=1e-6*input('Enter fixed ground conductor radius in um: ');
if RF >= R    RF=R; end

t=1e-6*input('Enter movable conductor thickness in um: ');
g=1e-6*input('Enter gap in um: ');
E=1e9*input('Enter movable conductor youngs modulus in GPa: ');
nu=input('Enter movable conductor poisson ratio: ');
s=1e6*input('Enter movable conductor residual stress in MPa: ');
P=input('Enter applied pressure in Pa:');
h=R/(d-1);
D=E*t^3/(12*(1-nu^2));
T=s*t;
a=T/D;
```

```
e=8.8541878e-12;

g1 = 1.55;
g2 = 1.65;
g3 = 0.00;
S3 = s*t*g^3;
B3 = E/(1-nu^2)*t^3*g^3;
u3 = (12*S3/B3)^(1/2) * g2 * R/2;
D3 = 1 + (2*(1-cosh(u3))/u3/sinh(u3));
V_pull_in_HH=real(g1*S3/(e*R^2*D3))^(1/2)
g1a = 1.55;
g2a = 1.63978;
u3a = (12*S3/B3)^(1/2) * g2a * R/2;
D3a = 1 + (2*(1-cosh(u3a))/u3a/sinh(u3a));
V_pull_in_HH2=real(g1a*S3/(e*R^2*D3a))^(1/2)
Bckl_stress_in_MPa = -14.682*E*t^2/12/R^2/1e6

b=P/D;
A=zeros(N,N);
C=zeros(N,1);

A(1,1)=-1;
A(1,3)=1;
A(2,2)=-1;
A(2,3)=3;
A(2,4)=-3;
A(2,5)=1;
A(N-1,N-2)=1;
A(N,N-3)=-1;
A(N,N-1)=1;

for i=3:N-2
   r=(i-2)*h;
   A(i,i-2)=1-h/r;
   A(i,i-1)=-4+2*h/r-h^2*(1/r^2+a)-.5*h^3*(1/r^3-a/r);
   A(i,i)=6+2*h^2*(1/r^2+a);
   A(i,i+1)=-4-2*h/r-h^2*(1/r^2+a)+.5*h^3*(1/r^3-a/r);
   A(i,i+2)=1+h/r;
```

```
   C(i)=b*h^4;
end

ig=A\C;

% V=input('Enter applied voltage: ');
V =0;
b=-e*V^2/(2*D);
c=P/D;

y=g*ones(N,1);
y=y+ig;
A=zeros(N,N);
C=zeros(N,1);
cap=zeros(N,1);
y1p=zeros(N,1);
y2p=zeros(N,1);
y3p=zeros(N,1);
y4p=zeros(N,1);

PN=round((RF/R)*d+1);

A(1,1)=-1;
A(1,3)=1;
A(2,2)=-1;
A(2,3)=3;
A(2,4)=-3;
A(2,5)=1;
A(N-1,N-2)=1;
A(N,N-3)=-1;
A(N,N-1)=1;

for j=1:Z

   for i=3:PN
      y1p(i)=(-y(i-1)+y(i+1))/(2*h);
      y2p(i)=(y(i-1)-2*y(i)+y(i+1))/h^2;
      y3p(i)=(-y(i-2)+2*y(i-1)-2*y(i+1)+y(i+2))/(2*h^3);
      y4p(i)=(y(i-2)-4*y(i-1)+6*y(i)-4*y(i+1)+y(i+2))/h^4;
      r=(i-2)*h;
      A(i,i-2)=1-h/r;
```

```
        A(i,i-1)=-4+2*h/r-h^2*(1/r^2+a)-h^3*(1/r^3-a/r)/2;
        q=2*h^4/y(i)*(y4p(i)+2*y3p(i)/r-y2p(i)*(1/r^2+a)+y1p(i)*(1/r^3-a/r)-c);
        A(i,i)=6+2*h^2*(1/r^2+a)+q;
        A(i,i+1)=-4-2*h/r-h^2*(1/r^2+a)+h^3*(1/r^3-a/r)/2;
        A(i,i+2)=1+h/r;
        C(i)=h^4*(b/y(i)^2-y4p(i)-2*y3p(i)/r+y2p(i)*(1/r^2+a)-y1p(i)*(1/r^3-
a/r)+c);
    end

    for i=PN+1:N-2
        y1p(i)=(-y(i-1)+y(i+1))/(2*h);
        y2p(i)=(y(i-1)-2*y(i)+y(i+1))/h^2;
        y3p(i)=(-y(i-2)+2*y(i-1)-2*y(i+1)+y(i+2))/(2*h^3);
        y4p(i)=(y(i-2)-4*y(i-1)+6*y(i)-4*y(i+1)+y(i+2))/h^4;
        r=(i-2)*h;
        A(i,i-2)=1-h/r;
        A(i,i-1)=-4+2*h/r-h^2*(1/r^2+a)-h^3*(1/r^3-a/r)/2;
        q=2*h^4/y(i)*(y4p(i)+2*y3p(i)/r-y2p(i)*(1/r^2+a)+y1p(i)*(1/r^3-a/r)-c);
        A(i,i)=6+2*h^2*(1/r^2+a)+q;
        A(i,i+1)=-4-2*h/r-h^2*(1/r^2+a)+h^3*(1/r^3-a/r)/2;
        A(i,i+2)=1+h/r;
        C(i)=h^4*(-y4p(i)-2*y3p(i)/r+y2p(i)*(1/r^2+a)-y1p(i)*(1/r^3-a/r)+c);
    end

    f=A\C;
    y=y+f;
end

cap(3)=e*pi*h^2/y(2);
for i=4:PN
    r=(i-2)*h;
    cap(i)=cap(i-1)+e*pi*h^2*(2*i-5)/(.5*(y(i)+y(i-1)));
end

y=1e6*y;
cap=1e12*cap;
f=1e6*f;

plot(y);
axis([2 d+1 0 g*2e6]);
xlabel('Discretization in x');
```

```
ylabel('Gap (um)');
Center_gap=y(2)
%Center_gap_estimate=1e6*(g+P/k)
Error=f(2)
Cap_pF=cap(PN)
k1=16*E*t^3/(3*R^4*(1-nu^2));
k2=4*T/R^2;
k=k1+k2;
V_pull_in_estimate=((8*k*(g+P/k)^3)/(27*e))^.5
```

BIBLIOGRAPHY

[1] Forester, T.,*The microelectronics revolution*, Cambridge, MA: MIT Press.1981 .

[2] Kassakian, J.G., Schlecht, M.F., and Verghese, G.C.,*Principles of power electronics*, : Addison-Wesley Publishing Company, Inc.1992 .

[3] Heumann, K.,*Basic principles of power electronics*, : Springer-Verlag Berlin Heidelberg.1986 .

[4] Petersen, K.E., "*Silicon as a mechanical material*", Proceedings of the IEEE, 1982. 70(5): p. 420-456.

[5] Petersen, K.E., "*Micromechanical Membrane Switches on Silicon*", I.B.M. Journal of Research and Development, 1979. 23(4): p. 376-385.

[6] Drake, J., Jerman, H., Lutze, B., and Stuber, M., "*An Electrostatically Actuated Micro-Relay*", in *Transducers '95, The 8th International Conference on Solid-State Sensors and Actuators, and Eurosensors IX*. 1995. Stockholm, Sweden. p.380-383

[7] Zavracky, P.M., Majumder, S., and McGruer, N.E., "*Micromechanical switches fabricated using nickel surface micromachining*", Microelectromechanical Systems, Journal of, 1997. 6(1): p. 3-9.

[8] Fullin, E., Gobet, J., Tilmans, H.A.C., and Bergqvist, J., "*A new basic technology for magnetic micro-actuators*", in *Micro Electro Mechanical Systems, 1998. MEMS 98. Proceedings., The Eleventh Annual International Workshop on*. 1998. p.143-147

[9] Sakata, M., Komura, Y., Seki, T., Kobayashi, K., Sano, K., and Horiike, S., "*Micromachined Relay which Utilizes Single Crystal Silicon Electrostatic Actuator*", in *Micro Electro Mechanical Systems, 1999. MEMS '99. Twelfth IEEE*. 1999. p.21-24

[10] Tilmans, H.A.C., *et al.*, " *A fully-packaged electromagnetic microrelay*", in *Micro Electro Mechanical Systems, 1999. MEMS '99. Twelfth IEEE International Conference on*. 1999. p.25-30

[11] Hannoe, S., Hosaka, H., Kuwano, H., and Yanagisawa, K., "*Mechanical and Electrical Characteristics of Ultra-low-force contacts Used in Micromechanical Relays*", in *Proceedings of the 17th International Conference on Electrical Contacts*. 1994. Nagoya, Japan. p.185-191

[12] Yao, J.J. and Chang, M.F., "*A Surface Micromachined Miniature Switch for Telecommunications Applications with Signal Frequencies from DC up to 4 GHz*", in *Transducers '95, The 8th International Conference on Solid-State Sensors and Actuators, and Eurosensors IX*. 1995. Stockholm, Sweden. p.384-387

[13] Schiele, I., Huber, J., Evers, C., Hillerich, B., and Kozlowski, F., "*Micromechanical relay with electrostatic actuation*", in *Solid State Sensors and Actuators, 1997. TRANSDUCERS '97 Chicago., 1997 International Conference on*. 1997. p.1165 - 1168

[14] Brown, E.R., "*RF-MEMS switches for reconfigurable integrated circuits*", Microwave Theory and Techniques, IEEE Transactions on, 1998. 46(11): p. 1868-1880.

[15] Goldsmith, C.L., Yao, Z., Eshelman, S., and Denniston, D., "*Performance of Low-Loss RF MEMS Capacitive Switches*", IEEE Microwave and Guided Wave Letters, 1998. 8(8): p. 269-271.

[16] Nguyen, C.T.-C., "*Microelectromechanical devices for wireless communications*", in *Micro Electro Mechanical Systems, 1998. MEMS 98. Proceedings., The Eleventh Annual International Workshop on*. 1998. p.1-7

[17] Hyman, D., *et al.*, "*GaAs-compatible surface-micromachined RF MEMS switches*", Electronics Letters, 1999. 35(3): p. 224-226.

[18] Zhou, S., Sun, X.-Q., and Carr, W.N., "*A Monolithic Variable Inductor Network Using Microrelays with Combined Thermal and Electrostatic Actuation*", Journal of Micromechanics and Microengineering, 1999. 9: p. 45-50.

[19] Hirata, A., Machida, K., Kyuragi, H., and Maeda, M., "*A micromechanical switch as the logic elements for circuits in multi chip mudule on Si (MCM-Si)*", in *Micro Electro Mechanical Systems, 1999. MEMS '99. Twelfth IEEE*. 1999. p.582-587

[20] Sakata, M., "*An Electrostatic Microactuator for Electro-Mechanical Relay*", in *Micro Electro Mechanical Systems, 1989, MEMS '89, Proceedings. IEEE*. 1989. p.149-151

[21] Hashimoto, E., Uenishi, Y., and Watabe, A., "*Thermally Controlled Magnetization Microrelay*", in *Solid-State Sensors and Actuators, 1995 and Eurosensors IX.. Transducers '95. The 8th International Conference on*. 1995. p.361-.364

[22] Rogge, B., Schulz, J., Mohr, J., Thommes, A., and Menz, W., "*Fully Batch Fabricated Magnetic Microactuators Using A Two Layer Liga Process*", in *Solid-State Sensors and Actuators, 1995 and Eurosensors IX.. Transducers '95. The 8th International Conference on*. 1995. p.320-323

[23] Roy, S. and Mehregany, M., "*Fabrication of electrostatic nickel microrelays by nickel surface micromachining*", in *Micro Electro Mechanical Systems, 1995, MEMS '95, Proceedings. IEEE*. 1995. p.353-357

[24] Gretillat, M.-A., Yang, Y.-J., Hung, E.S., Rabinovich, V., Ananthasuresh, G.K., De Rooij, N.F., and Senturia, S.D., "*Nonlinear electromechanical behaviour of an electrostatic microrelay*", in *Solid State Sensors and Actuators, 1997. TRANSDUCERS '97 Chicago., 1997 International Conference on*. 1997. p.1141 - 1144

[25] Simon, J., Saffer, S., Sherman, F., and Kim, C.-J., "*Lateral polysilicon microrelays with a mercury microdrop contact*", Industrial Electronics, IEEE Transactions on, 1998. 45(6): p. 854-860.

[26] Taylor, W.P., Brand, O., and Allen, M.G., "*Fully integrated magnetically actuated micromachined relays*", Microelectromechanical Systems, Journal of, 1998. 7(2): p. 181-191.

[27] Gretillat, M.-A., Thiebaud, P., de Rooij, N.F., and Linder, C., "*Electrostatic polysilicon microrelays integrated with MOSFETs*", in *Micro Electro Mechanical Systems, 1994, MEMS '94, Proceedings, IEEE Workshop on*. 1994. p.97 - 101

[28] Goldsmith, C., Randall, J., Eshelman, S., Lin, T.H., Denniston, D., Chen, S., and Norvell, B., "*Characteristics of micromachined switches at microwave frequencies*", in *Microwave Symposium Digest, 1996., IEEE MTT-S International*. 1996. p.1141-1144

[29] Seki, T., Sakata, M., Nakajima, T., and Matsumoto, M., "*Thermal Buckling Actuator for Micro Relays*", in *Solid State Sensors and Actuators, 1997. TRANSDUCERS '97 Chicago., 1997 International Conference on*. 1997. p.1153-1156

[30] Taylor, W.P. and Allen, M.G., "*Integrated magnetic microrelays: normally open, normally closed, and multi-pole devices*", in *Solid State Sensors and Actuators, 1997. TRANSDUCERS '97 Chicago., 1997 International Conference on*. 1997. p.1149-1152

[31] *Sun, X.-Q., Farmer, K.R., and Carr, W.N.*, "*A bistable microrelay based on two-segment multimorph cantilever actuators*", in *Micro Electro Mechanical Systems, 1998. MEMS 98. Proceedings., The Eleventh Annual International Workshop on*. 1998. p.154 - 159

[32] Paschen, F., "*Ueber die xum Funkenubergang in Luft, Wasserstoff und Kohlensaure bei verschiedenen Drucken erforderliche Potentialdifferenz*", Annalen der Physik, 1889. 37: p. 69-96.

[33] Townsend, J.S.,*The Theory of Ionization of Gases by Collision*, London: Constable & Co. Ltd.1910 .

[34] E. E. Kunbardt, L.H.L.,*Electrical Breakdown and Discharges in Gases - Part A, Fundamental Processes and Breakdown*, : Plenum Press.1981 .

[35] Meek, J.M. and Craggs, J.D.,*Electrical Breakdown of Gases*, : Oxford at the Clarendon Press.1953 .

[36] Brown, S.C.,*Introdution to Electrical Discharges in Gases*, New York: Wiley.1966 .

[37] Raether, H., Arch. Elektrotech, . 34: p. 49.

[38] Wolf, S. and Tauber, R.N., *Chapter 3: Vacuum Technology for VLSI Applications*, in *Silicon Processing for the VLSA Era - Volume 1, Process Technology*. 1986. p. 75.

[39] Germer, L.H. and Haworth, F.E., "*A low voltage discharge between very close electrodes*", Physical Reviews, 1948. 73: p. 1121.

[40] Shugg, W.T.,*Handbook of Electrical and Electronic Insulating Materials*, : IEEE Press.1995 .

[41] Suh, N.P.,*The principles of design*, : Oxford University Press.1990 .

[42] Holm, R.,*Electric Contacts: Theory and Application*, : Springer-Verlag.1967 .

[43] Zemansky, M.W. and Dittman, R.H.,*Heat and Thermodynamics*, New York: McGraw-Hill.1981 .

[44] Lienhard, J.H.,*A Heat Transfer Textbook*, Englewood Cliffs, New Jersey: Prentice-Hall.1987 .

[45] Wright, J.A., Tai, Y.-C., and Chang, S.-C., "*A large-force, fully-integrated MEMS magnetic actuator*", in *Solid State Sensors and Actuators, 1997. TRANSDUCERS '97 Chicago., 1997 International Conference on*. 1997. p.793-796

[46] Herbert H. Woodson and Melcher, J.R.,*Electromechanical Dynamics, Part II: Fields, Forces, and Motion*, New York: J. Wiley.1968 .

[47] W. K. Schomburg, R. Ahrens, W. Bacher, S. Engemann, and P. Krhl, J.M., "*Long-term performance Analysis of Thermo-Pnuematic Micropump Actuators*", in *International Conference on Solid-State Sensors and Actuators, Tranducers '97*. 1997. Chicago. p.361-364

[48] Simon, J., Saffer, S., and Kim, C.-J., "*A liquid-filled microrelay with a moving mercury microdrop*", Microelectromechanical Systems, Journal of, 1997. 6(3): p. 208-216.

[49] A. D. Johnson, J. D. Busch, C. A. Ray, and Sloan, C., "*Fabrication of Silicon-Based Shape Memory Alloy Microactuators*", in *Material Research Society Symposium.* 1992.
[50] K. D. Skrobanek, M. Kohl, and Miyazaki, S., "*Stress-optimized shape memory devices for the use in microvalves*", in *IEEE MEMS Workshop, 1997, MEMS '97.* 1997. Nagoya, Japan. p.256-261
[51] M. Kohl and Skrobanek, K.D., "*Linear Microactuators Based on the Shape Memory Effect*", in *International conference on Solid-state Sensor and Actuator.* 1997. Chicago, IL. p.785-788
[52] Osterberg, P.M. and Senturia, S.D., "*M-TEST: A Test Chip for MEMS Material Property Measurement Using Electrostatically Actuated Test Structures*", Journal of Microelectromechanical Systems, 1997. 6(2): p. 107-118.
[53] Microcosm Technologies, I.,*MEMCAD 4.0 User Guide*, .1998 .
[54] Connally, J.A., "*Micromechanical Fatique Testing*", 1992, Massachusetts Institute of Technology: Cambridge, MA.
[55] Timoshenko, S.P. and Woinowsky-Krieger, S.,*Theory of Plates and Shells*, : McGraw-Hill Book Company.1959 .
[56] Seidel, H., "*The mechanism of anisotropic electrochemical silicon etching in alkaline solutions*", in *IEEE solid state sensor and actuator workshop.* 1990. Hilton Head Island, SC. p.86-91
[57] Tilmans, H.A.C., "*Micro-mechanical sensors using encapsulated built-in resonant strain gauges*", 1993, University of Twente: Enschede, The Netherlands.
[58] Huff, M.A., "*Silicon micromachined wafer-bonded valves*", 1993, Massachusetts Institute of Technology: Cambridge, MA.
[59] Giovanni, M.D.,*Flat and corrugated diaphragm design handbook*, New York and Basel: Marcel Dekker, Inc.1982 .
[60] Pettersson, O., "*Circular plates subjected to radially symmetrical transverse load combined with uniform compression or tension in the plane of the plate*", Acta Polytechnica, 1954. 138: p. 1-31.
[61] Lin, P., "*The in-situ measurement of mechanical properties of multi-layer coatings*", 1990, Massachusetts Institute of Technology: Cambridge, MA.
[62] O'Dwyer, J.M.,*The theory of electrical conduction and breakdown in solid dielectrics*, London, UK: Clarendon.1973 .
[63] Hyman, D. and Mehregany, M., "*Contact physics of gold microcontacts for MEMS*", in *Electrical Contacts, 1998. Proceedings of the Forty-Fourth IEEE Holm Conference on.* 1998. p.133-140
[64] Hosaka, H., Kuwano, H., and Yanagisawa, K., "*Electromagnetic microrelays: concepts and fundamental characteristics*", in *Micro Electro Mechanical Systems, 1993, MEMS '93, Proceedings.* 1993. p.12-17
[65] Majumder, S., McGruer, N.E., Zavracky, P.M., and adams, G.G., "*Measurement and modelling of surface micromachined, electrostatically actuated microswitches*", in . 1997. p.1145-1148
[66] Schimkat, J., "*Contact materials for Microrelays*", in *Micro Electro Mechanical Systems, 1998. MEMS 98. Proceedings., The Eleventh Annual International Workshop on.* 1998. p.190-194
[67] Greenwood, J.A. and Willamson, J.B.P., "*Contact of nominally flat surfaces*", in *Proceedings of the Royal Society.* 1966. London, UK. p.300-319
[68] Timoshenko, S. and Goodier, J.N.,*Theory of elasticity*, New York: McGraw-Hill.1951 .
[69] Chang, W.R., Etsion, I., and Bogy, D.B., "*An elastic-plastic model for the contact of rough surfaces*", Journal of Tribology, 1987. 109: p. 257-263.
[70] Tabor, D.,*The hardness of metals*, : Oxford University Press.1951 .
[71] Strang, G.,*Introduction to applied mathematics*, : Wellesley-Cambridge Press.1986 .
[72] Meirovitch, L.,*Analytical methods in vibrations*, New York: Macmillan.1967 .
[73] Langlois, W.E., "*Isothermal squeeze films*", Quarterly Applied Mathematics, 1962. XX(2): p. 131-150.
[74] Griffin, W.S., Richardson, H.H., and Yamanami, S., "*A study of squeeze film damping*", Journal of Basic Engineering, June, 1966: p. 451-456.
[75] Blech, J.J., "*On isothermal squeeze films*", Journal of Lubrication Technology, 1983. 105: p. 615-620.
[76] Andrews, M., Harris, I., and Turner, G., "*A comparison of squeeze-film theory with measurements on a microsctructure*", Sensors and Actuators A, 1993. A36(2): p. 79-87.
[77] Yang, Y.-J. and Senturia, S.D., "*Numerical simulation of compressible squeezed-film damping*", in *Solid-State Sensor and Actuator Workshop.* 1996. Hilton head, South Carolina. p.76-79
[78] Epstein, A.H., Senturia, S.D., Anathasuresh, G., Ayon, A., and Breuer, K., "*Power MEMS and microengines*", in *International conference on solid-state sensors and actuators, Tranducers 97.* 1997. Chicago, IL. p.753-756

[79] Neudeck, G.W.,*The PN junction diode*, : Addison-Wesley Publishing Company.1989 .
[80] Finne, R.M. and Klein, D.L., "*A water-amine-complexing agent system for etching silicon*", Journal of Electrchemical Society, 1967. 114(965).
[81] Mehregany, M., "*Application of Micromachined Structures to the study of mechanical properties and adhesion of thin films*", 1985, Massachusetts Institute of Technology: Cambridge, MA.
[82] Senturia, S.D., Schmidt, M.A., and Harrison, D.J., "*Microsystems: mechanical, chemical, optical*", 1995.
[83] Ko, W.H. and Wang, Q., "*Touch mode capacitive pressure sensors*", Sensors AND Actuators A-Phisical, 1999. 175(3): p. 242-251.
[84] Osterberg, P., "*Electrostatically actuated microelectromechanical test structures for material property measurement*", 1995, Massachusetts Institute of Technology: Cambridge, MA.